Deep and Periodically Driven Optical Lattices for Fundamental Physics
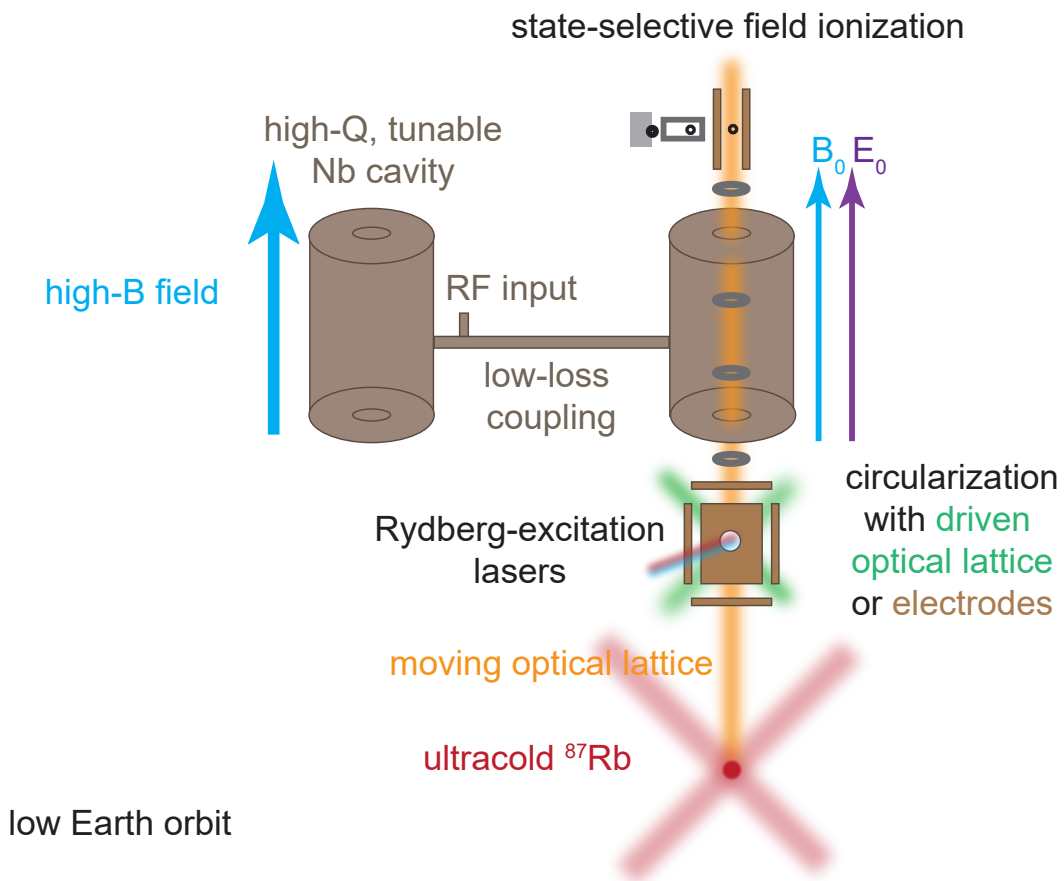
by

Ryan James Cardman

A dissertation submitted in partial fulfillment
of the requirements for the degree of
Doctor of Philosophy
(Physics)
in The University of Michigan
2023

Doctoral Committee:

       Professor Georg A. Raithel, Chair
       Assistant Professor Alexander P. Burgers
       Professor Timothy E. Chupp
       Professor Steven T. Cundiff
       Dr. Vladimir S. Malinovsky, Army Research Lab

state-selective field ionization

high-Q, tunable
Nb cavity

B_0 E_0

high-B field

RF input

low-loss
coupling

circularization
with driven
optical lattice
or electrodes

Rydberg-excitation
lasers

moving optical lattice

ultracold ^{87}Rb

low Earth orbit

A space-based apparatus for fundamental physics with Rydberg atoms.

Ryan James Cardman

rcardman@umich.edu

ORCID iD: 0000-0002-4418-8776

For my loving family

ACKNOWLEDGEMENTS

When I first arrived in the sub-basement six years ago, I quickly realized how much optics, instrumentation, quantum physics, and programming I still had to master throughout my graduate career. Luckily, I've had the company of very clever colleagues to turn the difficulty knob from "insurmountable" to "challenging." In these pages, I would like to show my gratitude to them.

I first would like to thank my advisor, Georg Raithel, for the countless project meetings and trips to SB149 to lend me helpful advice when I was trying to tame my unruly apparatus. Georg is a model physicist and has showered me with his encyclopedic knowledge on the workings of any aspect of experimental physics from vacuum pumps to nifty optics tricks needed for quick alignment, making any technical procedure look much easier than it actually was for me. His scientific curiosity and love for the field, however, were truly the things that gave me that post-meeting energy and ambition in the lab.

I would like to thank the fellow grad students in the group along whom I've had the pleasure to brainstorm and discuss projects: Andira Ramos, Jamie MacLennan, Alisher Duspayev, Bineet Dash, Xiaoxuan Han, Lu Ma, Michael Viray, Lefeng Zhou, and Carlos Owens. Thank you both Andira and Jamie for welcoming me into the lab, teaching me the ins and outs of your experiments (in person or through massively long email exchanges), and quickly finding me tasks in which I could contribute when I first joined the group. You both had very methodical and careful ways of planning to make changes to the experiment, an admirable trait of a good scientist that I am working to perfect. Also, thank you for the chocolates and the cannoli from Silvio's! Alisher, thank you for taking over the deep-lattice experiment and the long hours planning and carrying-out projects with me in the lab (especially keeping the cavity locked during my data acquisition so that we could have Figs. 3.10-3.12). I have been amazed at your efficiency, depth of knowledge, and how quickly you were able to learn the intricacies of the apparatus. Bineet, thank you for the friendly conversations and immense curiosity demonstrated by your many questions. Your questions and eagerness to think deeply about every piece of equipment have prodded me to also learn more about them. Additionally, I would like to thank you for the many car rides, coffee breaks, and lunch discussions. Xiaoxuan, I want to thank you for the year you spent with

our group so many miles away from your own lab and your ability to adjust to a new setting so quickly. You are a dedicated researcher who was able to adapt to new trajectories on various plans we had for the deep-lattice experiment. Thank you also for monitoring the bake-out of my primary MOT chamber while I was away. Lu, I have always been amazed at your vast knowledge in electronics and experimental planning (everything you built looked of commercial quality), as well as grateful for your willingness to take time out of your busy days to provide wise input in all of my queries about a piece of electronics I wanted to build/troubleshoot. Michael, thank you for also being so welcoming to me when I first joined the group, the interesting lunch conversations, and the numerous Department events you helped organize through the Graduate Council! Lefeng and Carlos, I know you both first joined the group in my final semester, but I want to thank you both for the large contributions to the BEC and EIT experiments you've made in such a short time. Thank you also to the very talented undergraduates with whom I've had overlap in the group: Ansh Shah, Abby Pan, and Eric Peterson!

I want to thank other past members of the group who graduated before my time but with whom I've collaborated on papers and projects: David Anderson, Rachel Sapiro, Nithiwadee Thaicharoen, Kaitlin Moore, Eric Paradis, Yun-Jhih Chen, and Sarah Anderson. In particular, I'd like to thank Dave and Rachel, along with Luís F. Gonçalves, for allowing me to have the awesome experience of interning at Rydberg Technologies as a graduate student. At Rydberg, I was exposed to the astounding physics of "hot" atoms, and the clever engineering required to deploy them as a valuable piece of equipment. The experience influenced my choice of industry over academia as a career path, and I am wholeheartedly grateful for the opportunity.

I would like to thank the other members of my committee: Alex Burgers, Tim Chupp, Steve Cundiff, and Vlad Malinovsky for their edits and commentary to the work contained in the following pages.

I'd like to thank the various sources of my funding over the past six years: NASA, the NSF, and the Rackham Predoctoral Fellowship.

Finally, I would like to thank my parents for their sacrifices and unstoppable drive to ensure that I always received the best education possible. From a young age, they hammered into me the dedicated work ethic that is requisite for adapting to the many roadblocks in running a physics experiment. Also, I thank them for their immense love (which no physical apparatus can ever measure).

TABLE OF CONTENTS

LIST OF FIGURES

xi

xiii

LIST OF TABLES

ABSTRACT

Fundamental physics is concerned with the problems of defining fundamental constants, units of measurement, and searching for new forces and aspects of matter. Usually, the best way to resolve these inquiries is to have a precise knowledge of atomic energy levels and the transition frequencies in order for their quantum states to be manipulated. Spectroscopy is a tool that probes these atomic energy levels by observing the atom's response as the energy of the applied radiation is varied. Over the past century, spectroscopy using electromagnetic radiation has involved direct interactions with the atom's electric and magnetic multipole moments via the $\mathbf{A} \cdot \mathbf{p}$ term of the minimal coupling Hamiltonian. The work presented in this thesis utilizes such interactions with laser fields and goes a step further by exploring a novel light-matter interaction via the A^2 term.

Leading problems in the field of fundamental physics include the commercialization of optical frequency standards with short-term stabilities beating $10^{-11}/\sqrt{\tau}$ and the discovery of new science arising from competitive precision measurements of the Rydberg constant and the detection of axion dark matter. Ultracold rubidium atoms subject to periodic optical potentials in standing waves of light known as optical lattices offer solutions to these problems. Rubidium atoms contained in miniaturized, glass vapor cells can be probed with a 778-nm laser in order to obtain the $|5S\rangle \rightarrow |5D\rangle$ transition frequency as a portable optical frequency standard. Optical traps can induce shifts that compensate those incurred by the probing lasers and confine the atoms to prevent residual Doppler effects, both of which would otherwise hamper the clock stability. Addressing the other two problems mentioned, circular-state Rydberg atoms that are able to be manipulated with optical lattices introduce a platform for high-resolution spectroscopy of their electronic transitions using very weak microwave fields. The long lifetimes of circular states, which approach 1 s, extend the probing times for a measurement of the Rydberg constant (10^{-12} uncertainty) insensitive to the proton charge radius, and the existence of microwaves generated by axion couplings to the electromagnetic field. This dissertation explores the functionality of optical lattices as a

tool that can contribute to the advancement of these aforementioned endeavors.

In the first implementation of optical lattices for these goals, a measurement of the Rb $|5D_{3/2}\rangle$ AC polarizability and photoionization cross section is performed using a cavity-enhanced optical lattice with an ultra-deep depth on the order of $\sim 10^5$ single-photon recoils. The lattice wavelength is $\lambda = 1.064~\mu$m, which induces shifts on $|5D_{3/2}\rangle$ that can be characterized by the measured scalar polarizability of $\alpha^S_{5D_{3/2}} = -524(17)$ atomic units. I choose this wavelength because it is commonly available as a narrow-linewidth, high-powered laser. At this wavelength, photoionization induces decay of this energy level and broadening of spectral lines as evidence of the significant measured cross section $\sigma_{PI} = 44(1)$ Mb.

The secondary use of lattices as a tool for fundamental physics concerns periodically driven ponderomotive potentials for the effort of initializing the circular states required for a Rydberg constant measurement and dark-matter detection. Experimentally, the principles are discussed in a newly developed lattice phase-modulation technique, where the $|46S_{1/2}\rangle \rightarrow |46P_{1/2}\rangle$ and $|48S_{1/2}\rangle \rightarrow |49S_{1/2}\rangle$ transitions were spectrocscopically measured with this driving mechanism. Additionally, the importance of cancelling stray electric and magnetic fields for this mechanism to be efficient is also demonstrated. The applicability of ponderomotive light-matter interactions for obtaining circular states is discussed in a theoretical proposal of all-optical circularization techniques.

CHAPTER I

Introduction

1.1 Standing-Waves of Light: Optical Lattices

We encounter standing waves on a daily basis. They appear in your life whenever you listen to music and hear the perturbations they make in the air around them as sound. Guitars, pianos, violins, cellos, etc. are all instruments that operate on a vibration in a string that travels back and forth to make an interference pattern known as a standing wave. The pegs that make the strings taut form a cavity for the vibration that allows certain standing wavelengths, and consequently notes, to propagate on the string. Another commonplace instance of standing waves is a microwave oven, which consists of a cavity that traps electromagnetic waves with a frequency of 2.5 GHz. The resulting interference pattern enhances the microwave power and makes spatial regions of local minima and maxima in the electromagnetic field.

This work deals with standing waves of laser light in the visible to infrared region of the electromagnetic spectrum. More specifically, through both theory and experiment, I will discuss the underlying physics that takes place when matter is in the presence of this sort of standing wave. The matter studied will be a dilute gas of alkali-metal (rubidium) atoms at a temperature below 1 mK; in this work, each atom can more or less be considered as an isolated particle, unless otherwise stated. A standing wave of coherent light effects a sinusoidal potential, much like the crystalline lattice potential famously studied by Felix Bloch [11; 12]. For this reason, the laser's interference pattern is considered an *optical lattice.*

On an alkali-metal atom in its ground state, the light mainly exerts two forces: a conservative, electric-dipole force and a frictional scattering force that opposes the center-of-mass (CM) velocity, $\mathbf{V}_0$. The latter force is only significant when light is near the resonance of a transition between two electronic quantum states while the former, based on the orientation of induced electric-dipole moments on the electronic wave function by the incident field,

dominates for light at far-off-resonant (FOR) frequencies. Optical lattices based on inter-play between the scattering and electric-dipole forces were initially studied experimentally in [13; 14; 15; 16]. However, in this work, these near-resonant optical lattices are only used for cooling the atomic sample to temperatures on the order of the Doppler limit and are not the subject of discussion for this thesis. Optical lattices around which this thesis is centered are at wavelengths of $\lambda = 1064$ nm and 532 nm, sufficiently FOR from any electronic transition in rubidium.

FOR optical lattices can trap and control the motion of atoms quite well, isolating them from environmental perturbations like gravity. As a result, the trapped atom's energy levels can be probed with external electromagnetic fields for prolonged periods of time. Knowledge of these levels unravels ultra-precise measurements of fundamental constants (e.g., the Rydberg constant [17; 18], the fine-structure constant [19], the mass of an electron [20], etc.) used by all physicists. Atomic structure can provide definitions for units of measurement like the second [21] , the meter [22], and a volt [23], which are frequently jotted down in lab notebooks by all researchers. There has been a growing push to replace the classical definitions of these units with ones based on quantized atomic energy levels, and, consequently, the removal of uncertainties on fundamental constants based on quantum measurements (e.g., Planck's constant, fundamental charge, Boltzmann's constant, etc.) [24]. Uncovering new particles, seeing if their physical properties behave symmetrically with other known matter, and learning about the forces they bring to observable matter is another hallmark of fundamental physics. This work is focused on using optical lattices as a tool to further the progress of specific experiments belonging to each of the three aforementioned sectors of fundamental physics.

Specifically, the problems in fundamental physics I seek to address in this thesis using FOR optical lattices involve a two-photon frequency standard in the infrared spectrum [25], made possible by the interrogation of the forbidden $5S \rightarrow 5D$ transition of Rb, and using circular-state Rydberg atoms to search for axionic dark matter [1] and a precision measurement from the Rydberg constant [26], removed from perturbations that are now under question [27]. All of these mentioned problems have a connection in the sense that their effects can be easily read-out by the energies of atomic states, making the use of FOR optical lattices a necessity. For the case of the infrared frequency standard of Rb using the $5S \rightarrow 5D$ clock transition, an ultra-deep, FOR lattice at the commonly available wavelength of 1.064 μm, above the $5D$ photoionizaiton threshold, is used to make a measurement of the state's dynamic polarizability, adding to the experimental efforts in understanding its light shifts at various wavelengths [28]. Inelastic ponderomotive interactions on Rydberg electrons by deep 532-nm and 1.064-μm optical lattices are studied in the context of driving

2

their transitions and performing high-precision spectroscopy for the purpose of initializing a sample of circular-state Rydberg atoms used for detecting dark matter and measuring the Rydberg constant. This thesis spends time discussing the principles of implementing deep and periodically driven ponderomotive optical lattices through experiment [7] and simulation [5; 9]. Also, methods of electromagnetic-field control for an experiment requiring a driven ponderomotive optical lattice are demonstrated with high-precision spectroscopy of Rydberg hyperfine structure [8].

1.2 A Portable Rubidium Optical Clock

In fundamental physics, atomic clocks seek to answer the question of how long a second is. A second must be calibrated by the period of a system that is oscillatory with time: a swinging pendulum and an orbiting planet suffice to yield an interval of time for wrist watches and grandfather clocks, but are inappropriate for satellites and the experiments performed in this thesis. Instead, they use the frequency separation between two long-lived electronic states of an atom to define the interval of a second.

Before the development of the laser, RF and microwave radiation was used to probe these stable atomic energy levels. The ammonia (NH_3) clock was based on the absorption of 23.870 GHz radiation by the molecule, which is the same frequency at which the nitrogen atom in the molecule oscillates above and below the plane at which the hydrogen atoms lie [29]. It was the first clock based on the oscillations predicted by quantum mechanics, but had a humble systematic uncertainty around 10^{-8} based in part by collisional broadening and first-order Doppler effects [29]. The molecular beam absorbed the microwaves head-on inside a waveguide, making the microwave frequency seen in the molecule's frame of reference velocity dependent.

Rather than a molecule, an alkali-metal, ^{133}Cs, was a subsequent atom to be used for a clock transition. The hyperfine structure splitting of cesium (between $F = 3$ and $F = 4$) is in the microwave X-band (9.19263177 GHz) [30], and the $F = 4$, hyperfine level decays to $F = 3$ in first-order perturbation theory by means of a magnetic-dipole/electric-quadrupole (M1/E2) transition, making the level metastable. Initial experiments of the cesium clock, which reached a measurement uncertainty of 10^{-10}, involved using magnetic filters to initialize F, m_F Cs atoms with a thermal beam in a Stern-Gerlach apparatus and passing them through a microwave waveguide twice [21]. Considering a given mean speed of the beam, the shape of the waveguide formed two instances of a fixed pulse area of $\theta = \pi/2$, both separated by a speed-dependent delay time T. After measuring the population that made the transition to the other hyperfine state, a series of fringes appear as a function of microwave frequency,

with the central fringe determining the resonant transition frequency. PID circuits, using the clock signal, then stabilized the microwave generator's frequency.

I want to also mention another notable atomic reference based on an M1 microwave transition developed by Norman F. Ramsey's group, a maser operating on the ground-state hyperfine transition of hydrogen ($|F = 1, m_F = 0 > \to |F = 0, m_F = 0 >$ at $\omega_0 = 2\pi \times 1.420405$ GHz with a width on the order of 1 Hz) [31; 32]. For the first hydrogen maser, Stern-Gerlach selector magnets guided atoms in the $m_F = 0$ and $m_F = 1$ Zeeman sublevels of $F = 1$ towards the aperture of a paraffin-coated bulb located inside a TE_{011} microwave cavity of $Q = 60000$; the maser's output power was measured to be a humble pW after being mixed with a cesium-referenced signal generator (NC Atomichron) [31; 32].

For the cesium clock, the invention of lasers allowed optical pumping of the cesium atoms to the magnetically-insensitive ground state, $m_F = 0$, laser cooling, and optical fluorescence detection of the atoms. As a result, removal of line pulling, first- and second-order Doppler effects, and first-order Zeeman effects enhanced the clock stability to $3 \times 10^{-13}\tau^{-1/2}$ (τ is the total time the clock is averaging its frequency per time of an experimental cycle) with a systematic lower limit at 10^{-15} due to density-dependent shifts and blackbody radiation [33].

A clock's statistical fluctuation $\sigma_y(\tau)$ (a.k.a. the Allan deviation) [33] scales as the the inverse of the transition's quality factor Q and the inverse of the signal-to-noise ratio (SNR):

$$\sigma_y(\tau) = \frac{\Delta\omega_0}{\omega_0} \frac{\tau^{-1/2}}{SNR}, \tag{1.1}$$

where the transition frequency ω_0 and linewidth $\Delta\omega_0$ both define Q as $Q = \omega_0/\Delta\omega_0$. Ideally, this uncertainty will vanish as $\tau \to \infty$, but systematic effects usually cause it to deviate from its linear dependence on $\tau^{-1/2}$ and plateau or rise as τ gets larger. The systematic shifts and uncertainties from atom-atom interactions as well as stray DC and thermal electromagnetic fields need to be well known and minimized in order to get long-term stability.

Alkaline-earth atoms have a unique quantum structure in their valence electrons that allow very narrow $^1S_0 \to ^3P_0$ transitions to be made through state mixing of dipole-allowed transitions by spin-orbit coupling and hyperfine mixing. These doubly forbidden transitions are in the optical spectrum and yield quality factors on the order of 10^{14}. When considering the absorption of the probing laser by an ensemble of non-interacting atoms, $SNR = \sqrt{N_{at}}$, where N_{at} is the number of atoms probed in a single experimental cycle. Maximizing N_{at} requires probing three-dimensional arrays of atoms confined to inhibit first-order Doppler effects; what better system is there to do this than an optical lattice? Vigorous study of the differential polarizability in the ^{87}Sr $5s5s^1S_0 \to 5s5p^3P_0$ transition has led to the discovery of wavelength-dependent zero crossings that give rise to a magic optical lattice which leaves

the transition unperturbed by the second-order AC Stark effects [34]. As a result, JILA's SrI and SrII optical clocks of ^{87}Sr trapped inside a $\lambda = 813$ nm lattice were able to obtain uncertainties of 2.0×10^{-18} [35] and 6.4×10^{-18} [36], respectively. The fractional uncertainty in such a clock has gotten so good that gravitational redshifts within the atomic sample can be imaged with an uncertainty of 7.6×10^{-21} after 92 h of averaging time [37].

1.2.1 Rubidium $5S_{1/2} \to 5D_j$ Transitions

While the electronic instrumentation and quantum-mechanical tools needed to obtain the same accuracy as a ^{87}Sr optical lattice clock are elegant, the strontium clock is not yet compact enough to be sold to labs across the globe as a stable frequency reference to which all lasers and synthesizers can be locked. Compact, commercial frequency references that provide a stable 10 MHz signal output can be based on the ^{87}Rb hyperfine transition, $F = 1 \to F = 2$, which is similar to the one in the Cs clock. These clocks consist of isotopically pure vapor cells that are optically pumped by light from a rubidium lamp and probed by a magnetic-dipole transition from microwaves contained within a cavity. A typical rubidium frequency produced by Stanford Research Systems (SRS) has a specified short-term stability of $2 \times 10^{-11} \tau^{-1/2}$.

Replacing the microwave transition with one that can be probed with lasers can reduce this value and relieve the burden of having to obtain a high SNR. The most favorable optical transition from the rubidium ground state is $\left| 5S_{1/2} \right\rangle \to \left| 5D_{5/2} \right\rangle$, which can be probed with two counter-propagating $778-$nm laser beams [25; 28; 38; 39]. To date, the demonstrated short-term stability is $1.8 \times 10^{-13} \tau^{-1/2}$ [39]. Decay to the $5S_{1/2}$ results in the emission of fluorescence at 5.2 μm and 420 nm, with the latter detectable by a photomultiplier tube (PMT). The $\left| 5S_{1/2} \right\rangle \to \left| 5D_{3/2} \right\rangle$ transition is also suitable for a frequency standard. A 1556-nm laser, located within the telecommunications C-band, can be frequency doubled to produce the probing beams and stabilized to the atomic transition, meaning an ultra-stable C-band frequency reference can be made available for applications in fiber-optic communications [40]. Fig. 1.1 shows the energy level structure relevant for a $\left| 5S_{1/2} \right\rangle \to \left| 5D_j \right\rangle$ clock.

For longer measurement times, the two-photon optical rubidium standard reaches a systematic uncertainty limited by the 778-nm field's AC Stark shifts. Power fluctuations in the probing laser are therefore translated into frequency jitters in the vapor-cell based clock. Described in [28], it is therefore of interest to find an additional "mitigation" laser with an ultra-narrow linewidth < 1 kHz, FOR from any electronic transition, having the sole purpose of AC Stark shifting the transition back into its unperturbed frequency. Calculations in [28] indicate that one such wavelength exists at 785 nm. With miniaturized laser cooling setups becoming more common [41; 42], a portable clock based on slowed atoms is not unforesee-
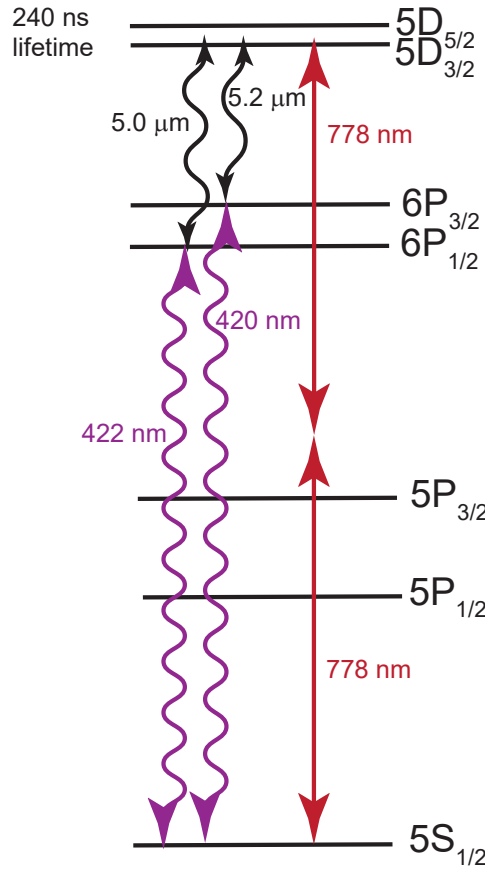
Figure 1.1: Relevant energy levels participating in $|5S\rangle \rightarrow |5D\rangle$ clock transitions.

able. Therefore, this additional laser can also be used to craft optical lattices and dipole traps to confine the atoms for longer measurement times.

1.2.2 Ultra-Deep Optical Lattices for Polarizability Measurements

Precision spectroscopy of the $5D$ level's AC polarizabilities at various wavelengths is therefore of interest. A "mitigation" laser in the infrared beyond 1.251 μm induces strong positive or negative AC Stark shifts within narrow < 10 MHz frequency windows that correspond to resonances with Rydberg states. In this work, the polarizability at the widely used wavelength $\lambda = 1.064$ μm is measured.

In this work, to perform the measurement of the $5D_{3/2}$ energy response to this wavelength, an optical lattice at λ with a depth $\sim 10^5$ single-photon recoils is implemented through an optical field-enhancement cavity [43] that features a laser-cooled sample of ^{85}Rb in its geometric center. A large lattice depth is required to obtain enough measurements on the line shifts so that the statistical uncertainty can be minimized.

Two-step laser spectroscopy through the Rb D_1 line to the $5D_{3/2}$ is performed on the lattice trapped atoms in order to measure the light shifts on the transition frequencies without having to calibrate the lattice field (two transitions measure two unknowns simultaneously: the lattice field and AC polarizability). A similar technique was performed in [44] to measure the AC polarizability for the $5P_{3/2}$ level of rubidium with the upper level being a Rydberg state for which $\lambda = 1064$ nm is the tune-out wavelength along its quantization axis.

Being above the $5D$ ionization threshold in frequency, potential mitigation wavelengths below 1.251 μm need to be characterized for how strongly they couple the $5D$ electron to a unbound continuum state $|\epsilon', l', j', m_j'\rangle$ of energy $\epsilon' = W_{5D_{3/2}} + \hbar\omega_L$ in a process known as *photoionization* (PI), as this process is responsible for a reduction in the clock's SNR and contributes to line broadening. Measurement of the PI cross section σ is also performed in this work at $\lambda = 1064$ nm.

1.3 A Circular-State-Rydberg-Atom Apparatus for Fundamental Physics

The second and third sectors of fundamental physics upon which this dissertation touches involve the goal of obtaining high-precision spectroscopy on circular-state (CS) Rydberg atoms [45]. A Rydberg state of an atom is one in which an electron occupies a large principal quantum number $n \geq 20$. We determine what "large" is by how well the physical properties of the atom scale with n. For extended wave functions of the atom's electron, quantum theory arrives at several of its properties (e.g., size, electric-dipole moment, lifetime, energy-level structure, electric polarizability, etc.) having a dependence on n; such properties will be discussed in detail throughout this thesis.

In terms of quantum numbers, the circular states occupy $|n, l = n - 1, |m_l| = n - 1\rangle$. CS atoms are an interesting platform to study fundamental physics due to their enhanced sensitivity to background RF and magnetic fields. They are also the longest lived Rydberg state within the n manifold. Research described in [46] has, in fact, demonstrated their sensitivity to RF fields at the single- to few-quanta level. Their lifetimes scale as n^5, chiefly as a consequence of the limited spontaneous decay channels for the atom. Thus, high-precision Rabi spectroscopy with interaction times on the order of ~ 50 ms and ~ 20 Hz linewidths are conceivable with these systems.

Another favorable feature of the CS Rydberg atom is the interesting and simplistic shape of its wave function. The wave lies primarily on a plane perpendicular to the atom's quantization axis and forms a three-dimensional torus about the nucleus and inner-shell electrons. This "bagel" shape arises from the angular structure of a spherical harmonic with maxi-

mum l and $|m_l|$ both equal to $n-1$. As n increases in magnitude, the inner radius of this "bagel" wave function widens, i.e., it becomes less like a New-York-style bagel and more like a Montreal bagel! The radial charge distribution of the electron also vanishes rapidly as r_e^{2l}, with r_e being the radial distance from the atom's center-of-mass. Therefore, in the vicinity of the CS atom's nucleus, there are no observable charge interactions among the protons, inner-shell electrons, and the Rydberg electrons. This annular electron wave function makes the CS one of the pieces of matter that most closely resemble the Bohr model of the atom.

Because the CS atom closely resembles the Bohr model and has a long lifetime sufficient for spectroscopic probing times at the order of ~ 50 ms, it is an attractive system for obtaining a competitive measurement of the Rydberg constant down to a relative uncertainty of 10^{-12} [26]. The Rydberg constant, R_∞, is one of the most precisely known fundamental constants, but nearly all of its measurements have been performed through spectroscopy of low-l atomic states, where there is significant interaction of the probed electron with the nuclear charge. It is desirable to make a measurement of R_∞ without such interactions mainly due to the ongoing "proton radius puzzle," [27; 17; 18; 47; 48] where over the past decade there has been an unusual bimodal distribution of rms proton charge radius measurements, $\sqrt{r_p^2}$, with the most precisely measured value from the Lamb shift of muonic hydrogen [27] having a value below the previously accepted CODATA value [49].

Overlap of the rms proton charge radius with the electronic wave function yields a systematic effect in spectroscopic measurement, as shown below in the formula for an energy level of hydrogen [17],

$$W_{n,l,j} = -\frac{hcR_\infty}{n^2}\frac{m_p}{m_p+m_e} + \frac{4cR_\infty\delta_{l,0}}{3n^3}\left(\frac{m_p}{m_p+m_e}\right)^3\left(\frac{\alpha r_p}{\lambda_c}\right)^2 + \Delta W_{QED}(n,l,j), \qquad (1.2)$$

where m_p is the mass of the proton, $\lambda_C = 2.42631023867(73) \times 10^{-12}$ m is the Compton wavelength [49], and $\Delta W_{QED}(n,l,j)$ are relativistic, quantum electrodynamic (QED) corrections to the energy that are minimized for high-l atomic states. The finite-proton-charge correction arises from the second term in the above equation and can also be ignored for high-l atomic states. High-resolution spectroscopy between a CS (labeled in this section as state $|0\rangle$) and another high-l Rydberg state (state $|1\rangle$) would rely chiefly on the first term and yield a "clean" measurement

Because they are long-lived, CSs can also partake in an experiment designed to detect axions where long wait times for detection are required. Axions are spinless particles that are considered to make up low-energy dark matter [50]. Their rest energy equates to photons with energies in the ultra-low frequency to microwave portion of the electromagnetic spectrum,

and it turns out that this rest-mass energy can be converted to photon energy through an interesting phenomenon known as *Primakoff conversion* [51; 52]. In the Lagrangian $\mathcal{L}$ for the axion scalar field a, there is a term [51; 52],

$$\mathcal{L}_{a\gamma\gamma} = \epsilon_0 g_{a\gamma\gamma} a \mathbf{E} \cdot \mathbf{B}, \tag{1.3}$$

where $g_{a\gamma\gamma}$ is the axion-two-photon coupling strength, $\mathbf{E}$ is the converted electromagnetic field, and $\mathbf{B}$ is an intense, DC magnetic field. The axion mass, m_a, is related to the constant $g_{a\gamma\gamma}$ through the following relation, $0.14 m_a \text{ GeV}^{-2} < g_{a\gamma\gamma} < 0.38 m_a \text{ GeV}^{-2}$, where the lower- and upper-bounds come from the models proposed in [53; 54] and [55; 56], respectively. Here, the mass of the axion takes into account a lifetime-dependent scalar f_a [57], in the relation,

$$m_a = 6 \ \mu\text{eV} 10^{12} \text{GeV} / f_a. \tag{1.4}$$

Given an axion energy of 120 μeV, the converted microwave field would have a frequency of $\omega_\mu/(2\pi) \sim 30$ GHz, near the resonance of the $|0\rangle \rightarrow |1\rangle$ transition for a $n = 48$ CS. A magnetic field to convert this would need to be on the order of $B \sim 10$ T, afforded by superconducting magnets surrounding a niobium microwave cavity with Q of 10^{10} near the resonance of the 30-GHz microwave field [1]. Axion densities hovering around 0.45 GeV/cm^3 and the resulting $g_{a\gamma\gamma} = 10^{-15} \text{ GeV}^{-1}$ at 120 μeV [1] elicit these constraints on B and Q from the following relation [58; 59]

$$P_\mu = g_{a\gamma\gamma}^2 \rho_{DM} \hbar^3 \omega_\mu B^2 vQ, \tag{1.5}$$

where P_μ is the microwave power of the resulting field of the converted axion, $\rho_{DM} = 0.45 \text{ GeV/cm}^3$ is the energy density of axions, and v is the cavity volume ($\sim 10^{-4} \text{ m}^3$). Converted power P_μ is above the limit of noise from blackbody photons that the Rydberg atoms would detect in the environmental conditions given above [60; 1].

For this apparatus to have a dual functionality of measuring the Rydberg constant and detecting dark matter, the CSs need to be cold at the order of ~ 1 μK and easily transportable with external laser fields. An optical lattice with its nodes and antinodes moving at a speed of $V_{lat} = 1$ m/s acts as a "conveyor" belt for the atoms and can transport them long distances, through one vacuum chamber to another, and even through a microwave cavity. This moving optical lattice is shown in Fig. 1.2 and is realized by two ultra-stable, counter-propagating laser beams phased locked with an offset frequency equal to V_{lat}/λ. For a laser at $\lambda = 2000$ nm, this corresponds to an offset-frequency lock of 0.5 MHz between the two beams. One does not want the optical lattice potential to over-perturb the Rydberg states

such that the experiments contain large systematic errors, yet one also does not want effects of gravity, which the lattice force counteracts, to contribute systematic effects as well. A suitable solution is to have the apparatus in a microgravity environment such as the low Earth orbit, where the lattice depth can be on the order of a single-photon recoil [26].
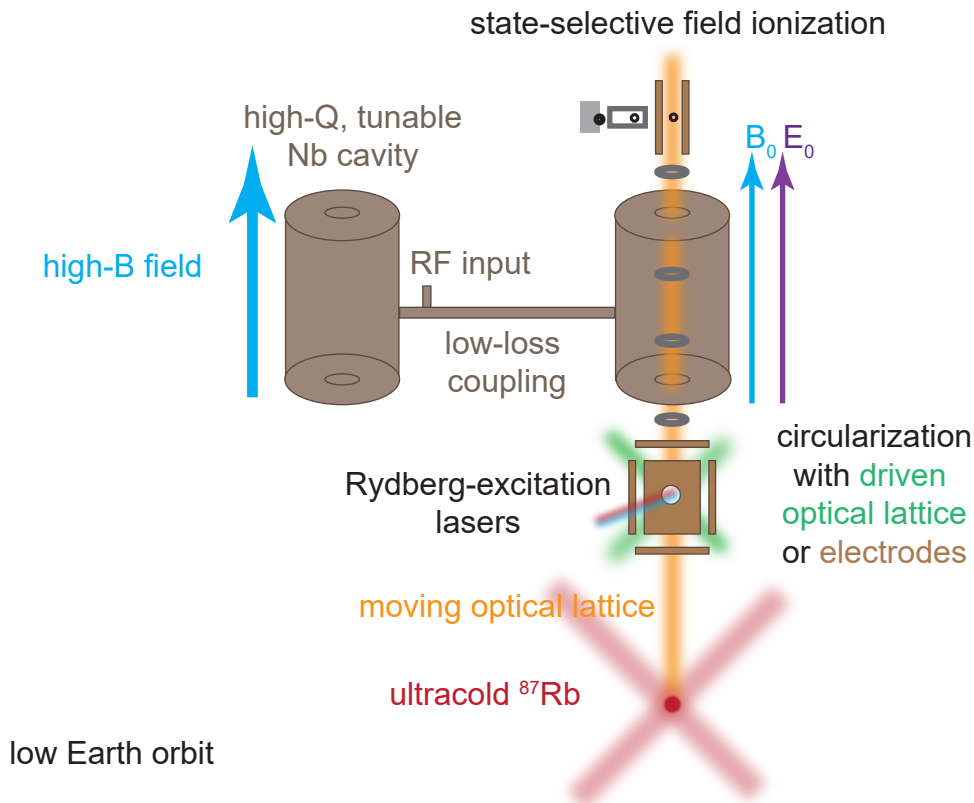
Figure 1.2: The proposed circular-state-Rydberg-atom apparatus located in the low Earth orbit. Optical lattices needed for transporting and circularizing the atoms (gray rings) are shown. An additional lattice (not shown) may be used for spectroscopically measuring R_∞. The niobium cavities may be tuned into resonance with the Rydberg state using a protruding rod (not shown) or an adjustable aperture. Background DC fields in the detection cavity are required to make the hydrogenic manifold nondegenerate. Figure adapted from [1].

The proposed apparatus features a lower cooling vacuum chamber ($\sim 10^{-9}$ Torr) of ^{87}Rb atoms that brings their temperature down to 1 μK. Atoms are then loaded into the moving optical lattice described above and transported into a "circularization" chamber, where they are first excited into a low-l Rydberg state with resonant laser fields and then circularized with either of the two methods from [61] or [9] (this work). The atoms can be probed spectroscopically in this chamber for the Rydberg constant measurement [26] using an amplitude-modulated optical lattice [62; 63] or external microwave radiation [26; 64; 8].

For axion dark matter detection, they can be moved further upwards with the moving optical lattice into a detection cavity that is coupled to an identical niobium cavity where the axion is converted into a microwave. For diagnostic purposes, microwaves can be fed into the waveguide coupling the two cavities. In order to assess if a CS made a transition into $|1\rangle$, a state-selective field ionization (SSFI) apparatus is placed in the final chamber [60]. The following sub-sections briefly describe the quantum mechanics behind the two fundamental-physics experiments with CSs.

1.3.1 Measuring the Rydberg Constant

The Rydberg constant measurement (RCM) experiment has been proposed in great detail in [26; 6]. Two methods exist for probing the energy levels of these high-l Rydberg states. Avoiding systematic uncertainties from first-order DC Zeeman and Stark effects requires a wise choice of two states for which the transition frequencies have no linear dependencies on external electric and magnetic fields. A transition can be made insensitive to background magnetic fields in first-order perturbation theory by choosing states with the same m_l and probing them with π-polarized couplings. Certain high-angular-momentum states in the diagonalized DC Stark Hamiltonian, which are superpositions of high-l Rydberg states have no net electric-dipole moments and experience no level shifts proportional to $\mathbf{E}$. They are the states with equal parabolic quantum numbers $n_1 = n_2$ [60; 65] and have same expectation values of the parity operator as the CS. For this reason, the transition must be electric-dipole-forbidden. Chosen in [26], the states of interest are $|0\rangle = |n = 51, n_1 = 0, n_2 = 0, m_l = 50\rangle$ (the CS) and $|1\rangle = |53, 1, 1, 50\rangle$ (a nearly CS), which are separated in energy by $h \times 93.6$ GHz and shown in Fig. 1.3.

High-frequency microwaves (also known as mm-waves) in the V band and polarized along the quantization axis can be generated from a horn antenna. The frequency of theses waves would be centered around 46.8 GHz, and they would probe the $|0\rangle \to |1\rangle$ transition through an electric-dipole transition in the second order. This type of transition is also called a Raman transition [66]; first-order Doppler shifts as a consequence of this off-resonant transition can be removed from the measurement by using 46.8 GHz, mm-waves from two counter-aligned antennas. Exemplary cases of Doppler-free spectroscopy using counter-aligned fields and off-resonant Raman transitions were spectroscopic studies of the hydrogen $\left|1^2S_{1/2}\right\rangle \to \left|2^2S_{1/2}\right\rangle$ [67] and $\left|1^2S_{1/2}\right\rangle \to \left|3^2S_{1/2}\right\rangle$ transitions [18]. In this case, mm-waves are used instead of laser beams, so the Doppler-free technique suffers from the imperfect directionality of the antennas, the scattering off metal pieces of the apparatus, and a diffraction limit above the size of the atomic sample.

One circumvents the three issues described above by replacing the mm-waves with laser

high-precision spectroscopy for RCM
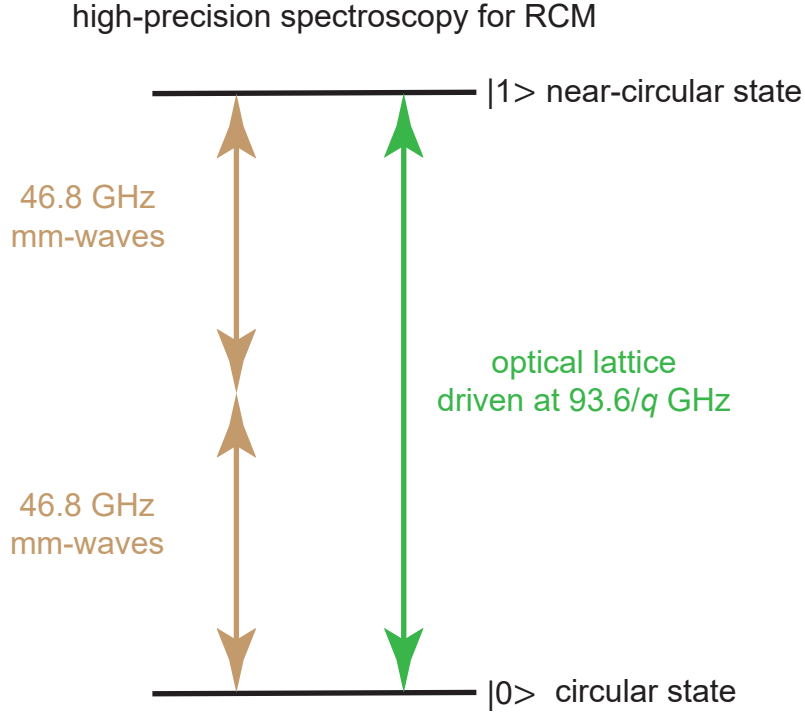
Figure 1.3: Level structure and spectroscopic methods for a Rydberg constant measurement (RCM). Here, $|0\rangle = |n = 51, n_1 = 0, n_2 = 0, m_l = 50\rangle$ and $|1\rangle = |53, 1, 1, 50\rangle$.

fields. The counter-propagating beams create an optical lattice that varies spatially throughout the Rydberg electron's wave function due to the exaggerated size of the atom. If the lattice's intensity gradient has some periodic dependence on time with a frequency that is a subharmonic q of 93.6 GHz, an internal-state transition of the Rydberg atom is driven. This transition is in first-order perturbation theory and governed by the $eA^2/(2m_e)$ term of the Hamiltonian, where A is the magnitude of the vector potential and and m_e is the electron rest mass. As a result, one obtains a Doppler-free spectral line at the Fourier limit with minimal inhomogeneous broadening from stray fields with the latter benefit being a consequence of the high spatial selectivity the laser can provide. Techniques for periodic driving of the lattice can come from amplitude modulation [26; 62; 63], phase modulation [9; 7], and bichromatic lattices [9], with the latter two methods studied in this work.

The proposed CS apparatus is fully equipped to accommodate both methods of spectroscopy (mm-wave and laser). Both methods would contribute their own unique uncertainties to the budget outlined in [26].

1.3.2 Searching for Dark Matter

When the CS atoms are transferred through the high-Q cavity (TE$_{121}$ mode) [68] in state $|0\rangle = |n = 48, n_1 = 0, n_2 = 0, m_l = 47\rangle$, the axion-converted microwave at ~ 30 GHz is coupled to the cavity through which the CS atoms in $|0\rangle$ pass. Considering the mode number of the microwave photon in the Hamiltonian; the "bare" states [69; 66] to the system are a product space between the electronic states $|0\rangle$ or $|1\rangle$, another high-l Rydberg state that the ~ 30 GHz field is resonant with, and the photon states consisting of the vacuum state $|0\rangle$ and $|1\rangle$, the $N = 1$ Fock state, which signifies the presence of a microwave photon. There are two relevant bare states for this experiment: $|01\rangle$, the electron in the CS and the presence of an axion microwave field, and $|10\rangle$, the electron in the nearly CS and a vacuum state of the ~ 30 GHz field. Both states are separated in energy by the detuning of the generated microwave field from the electronic resonance, as shown in the left level scheme in Fig. 1.4.
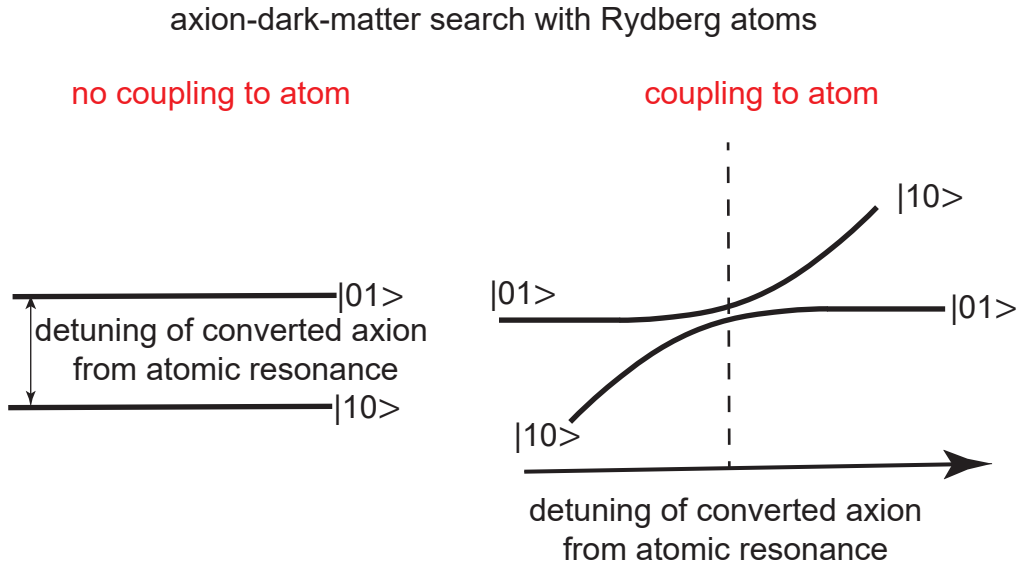
Figure 1.4: Detection scheme for sensing an axion-converted microwave field by varying the Rydberg transition frequency. The dashed line on the right is the point where the axion-converted microwave is resonant with the Rydberg-Rydberg transition.

When the atom-field interaction is included, the "bare" states no longer are diagonal to the Hamiltonian, and the new eigenstates are "dressed" states [69; 66]. Dressed states

are detuning-dependent superpositions of the bare eigenkets. Their energy separation varies with detuning as shown in the right level scheme of Fig. 1.4. Using several tuning "knobs" to tune the energy separation between the two Rydberg states into resonance with the axion-converted microwave (e.g., an electric field E_0 or the moving optical lattice intensity), sweeping the energies over the resonance, allows an atom initially in bare state $|01\rangle$ to adiabatically follow into $|10\rangle$, the nearly circular Rydberg state. Because of the internal state's entanglement with that of the microwave's, detection of an atom with Rydberg state $|1\rangle$ verifies the existence of an axion that was converted in the left cavity of Fig. 1.2.

1.3.3 Deep, Periodically Driven Optical Lattices for Obtaining Circular States

The above apparatus for the Rydberg experiments I proposed will take a decade to implement (to put it mildly), and it is mostly suitable for a medium-sized collaboration among AMO and particle physicists. Many optical lattices required for this experiment were also just discussed above. The latter part of this dissertation focuses on developing time-modulation techniques of the optical lattices for the purpose of engineering the Rydberg electron's wave function into a CS from a laser-excitable, low-l Rydberg state.

Initializing a sample of CSs is not a trivial matter. Traditional laser excitation prohibits the preparation of states with $|m_l| \sim n$ by parity rules. The addition of an electric field, as was done in only induces l mixing of low- and high-l states, but the quantum state is still at a low, fixed-$|m_l|$ [70]. Proposed in [71] and demonstrated in [72; 73; 74], including a magnetic field transverse to the electric field causes further mixing of low- and high-$|m_l|$ states to adiabatically prepare the atoms in the CS. Other methods of circularization include using adiabatic rapid passage [45; 75; 61] of many RF-driven transitions using radio waves resonant with the Stark and Zeeman splittings of a hydrogenic manifold under parallel DC electric and magnetic fields aligned along the atom's quantization axis. Both methods require advanced control of stray electric and magnetic fields down to the $\sim 100~\mu$V/cm and $\sim$mG levels, respectively, and long adiabatic ramping times on-the-order or above the lifetime of a low-l state. Furthermore, adding > 1 W of RF frequencies on the order of ~ 100 MHz to an ultra-high-vacuum chamber's internal electrodes elicits great difficulty in impedance matching, avoiding cross-talk with other electronics, and adding DC offset voltages to the RF.

Both methods are the more traditional ways of preparing CSs and can be described theoretically with the $e\mathbf{A}\cdot\mathbf{p}_e/m_e$ term of the minimum coupling Hamiltonian. Afforded by the $e^2A^2/2m_e$ part, where $\mathbf{A}$ is the vector potential of a laser field in the form of an optical lattice, the atom-field interaction from this term allows Δl-independent transitions to be made from one Rydberg state to another, provided that there is enough spatial variation of the laser

intensity in the frame of the Rydberg wave function (for angular-momentum conservation) and that the deep lattice (10^3 photon recoils) is varying with time at a frequency that is a subharmonic of the atomic transition frequency (for energy conservation). For optical lattices, angular-momentum conservation is independent of the change of l brought on by the transition thanks to the sinusoidal matrix elements provided. In the context of a laser beam exerting a force on a Rydberg atom, the $e^2A^2/2m_e$ term describes *ponderomotive* interactions [76; 77; 78; 79], where the electron quiver under a laser beam pushes the quasi-free particle towards regions of intensity minima. In this work, techniques of lattice-laser modulation are presented and different from periodically varying the standing-wave peak intensity that was performed in [62; 63]. Ponderomotive laser spectroscopy of the Rydberg atom through lattice shaking (phase modulation) is experimentally demonstrated in this work for two-level systems separated in energy by $\sim h \times$ 40-70 GHz. Its significance in the all-optical initialization of CSs for fundamental physics is thereafter discussed theoretically in the context of the hydrogenic manifold split up in energy by $\sim h \times$ 100 MHz; additional methods for obtaining CSs by periodic driving of the lattice are also presented.

1.4   Outline of Dissertation

The dissertation is outlined in the following way. Chapter II discusses light-matter interactions, forces, and energy shifts for deeply bound atomic states (binding energy > $h \times$ 200 THz). Chapter III discusses precision measurements of the Rb $5D_{3/2}$ polarizability and photoionization cross section at $\lambda =$ 1.064 μm obtained by laser spectroscopy of Rb atoms in an ultra-deep optical lattice ($\sim 10^5$ photon recoils). Chapter IV introduces a theoretical background concerning weakly bound Rydberg states and the circular state in non-optical electromagnetic fields. Chapter V discusses the ponderomotive light force on Rydberg atoms. Chapter VI discusses the experimental apparatus constructed for studying Rydberg atoms in periodically driven optical lattices. Chapter VII describes a precision measurement of the $nP_{1/2}$ hyperfine structure made possible by the stray field control of the apparatus. Chapter VIII introduces an experimental demonstration of Δl-independent, Rydberg-Rydberg transitions driven through optical-lattice phase modulation. Chapter IX then proposes methods of obtaining CSs by this modulation technique, along with procedures that use lattices created by interfering laser beams of two frequencies. Chapter X discusses future possibilities of experiments and applications of the ideas I conveyed in this work.

CHAPTER II

Interactions between Deeply Bound Electronic States and Light

Every study discussed in this thesis explores the dynamics of atoms in optical fields: i.e., the changes optical fields incur on the internal states of the bound electrons and the forces they apply on the center-of-mass (CM) motion. In this chapter, I will start by discussing the theory of optical forces on CM motion and how they relate to light scattering in matter using the context of a single, two-level atom. The first section will focus on the case when the field is nearly resonant (NR) with an atomic transition while the second will investigate FOR optical fields using a multi-leveled alkali atom with a single valence electron. In the third section, I will lay out the theory of FOR optical lattices, standing waves of light that confine and trap the atoms' CM in the nodes and antinodes by means of the conservative dipole force. Following this discussion, I will explain how, at some optical wavelengths, the valence electron is ejected from the atom by the light, forming an ion and a free-electron state (FES).

2.1 Atoms in Near-Resonant Optical Fields

In this section, I will use a two-level atom with electronic states $|1\rangle$ and $|2\rangle$. More in depth discussions with similar content can be found in [66; 80]. State $|1\rangle$ is stable and has a negligible energy width, state $|2\rangle$ is at an energy of $\hbar\omega_0$ above $|1\rangle$ and decays back to $|1\rangle$ at a rate of Γ. I am assuming that there is no collisional decoherence γ or inhomogeneous broadening of energy levels in this system.

The vector potential $\mathbf{A}(\mathbf{r} = \mathbf{R}_0 + \mathbf{r}_e, t)$ of the optical field for a small atom in a low-lying atomic state is

$$\mathbf{A}(\mathbf{r} = \mathbf{R}_0 + \mathbf{r}_e, t) \simeq \hat{\epsilon}\frac{\mathcal{E}(\mathbf{R}_0)}{\omega_L} \sin\left(\mathbf{k}_L \cdot \mathbf{R}_0 - \omega_L t\right), \tag{2.1}$$

from this point onward, $\hat{\epsilon}$ will denote the polarization unit vector of the field, ω_L, the light field's angular frequency, $\mathbf{k}_L = \omega_L \hat{k}_L / c$, its wave vector pointing along its propagation direction $\hat{k}_L$, and $\mathcal{E}(\mathbf{R}_0)$, the field amplitude. The expression $\mathbf{r} = \mathbf{R}_0 + \mathbf{r}_e$ is the atomic electron's position vector in the laboratory frame. This is the vector sum of the atom's CM position $\mathbf{R}_0$ and coordinate relative to the CM $\mathbf{r}_e$. These coordinates correspond to canonical momenta $\mathbf{P}_0$ and $\mathbf{p}_e$, respectively. I will use this convention throughout this thesis.

The total Hamiltonian $\hat{H}$ for the atom (of mass M) in the presence of this light field can be expressed as

$$\hat{H} = \frac{P_0^2}{2M} + \hat{H}_e(\mathbf{R}_0, \hat{\mathbf{r}}_e, t), \tag{2.2}$$

where the CM kinetic energy $\frac{P_0^2}{2M}$ is treated classically here and $\hat{H}_e(\mathbf{R}_0, \hat{\mathbf{r}}_e, t)$, the electron's Hamiltonian, must be treated quantum-mechanically. There are instances where it is appropriate to treat $\mathbf{P}_0$ and $\mathbf{R}_0$ as quantum operators, namely in the scenarios where the atom's de Broglie wavelength becomes significant and P_0^2 is small, such is the case for quantum degenerate gases of bosonic [81; 82] and fermionic [83; 84] atoms. Another necessity of quantizing the CM motion is when the system's trajectory is highly dependent on the changing internal state of the electron [85]. In Section 2.3, I will discuss how CM quantization is done in the case of optical lattices.

As explained in the Appendix, the Hamiltonian for the valence electron is, in the velocity gauge,

$$\hat{H}_e(\mathbf{R}_0, \hat{\mathbf{r}}_e, t) = \frac{\hat{p}_e^2}{2m_e} + \frac{e}{m_e} \mathbf{A}(\mathbf{R}_0 + \hat{\mathbf{r}}_e, t) \cdot \hat{\mathbf{p}}_e + \frac{e^2 A^2(\mathbf{R}_0 + \hat{\mathbf{r}}_e, t)}{2m_e} + \hat{U}_C - e\phi(\mathbf{R}_0 + \hat{\mathbf{r}}_e), \tag{2.3}$$

where, $\hat{U}_C$ is the Coulomb interaction with the nucleus and all other electrons, in the absence of static electric fields, the scalar potential ϕ vanishes in the velocity gauge. Using the following gauge transformation rules (l denotes length gauge):

$$\mathbf{A}_l = \mathbf{A} + \nabla \Lambda \tag{2.4}$$

$$\phi_l = \phi - \frac{\partial \Lambda}{\partial t} \tag{2.5}$$

and function $\Lambda = -\mathbf{r} \cdot \mathbf{A}$, as was done in [86] where the resulting Hamiltonian was proven to be gauge invariant under this transformation, I arrive at

$$\mathbf{A}_l = -\hat{k}_L \frac{(\hat{\epsilon} \cdot \mathbf{r})\mathcal{E}(\mathbf{r})}{c} \cos\left(\mathbf{k}_L \cdot \mathbf{r} - \omega_L t\right) \tag{2.6}$$

$$\phi_l = -(\hat{\epsilon} \cdot \mathbf{r})\mathcal{E}(\mathbf{r}) \cos\left(\mathbf{k}_L \cdot \mathbf{r} - \omega_L t\right). \tag{2.7}$$

Note that the $\mathbf{A} \cdot \hat{\mathbf{p}}_e$ and A^2 terms of Eq. 2.3 are now suppressed by a factor of c and c^2 respectively and can be neglected for a non-relativistic electron. Then, I get

$$\hat{H}_e(\mathbf{R}_0, \hat{\mathbf{r}}_e, t) = \frac{\hat{p}_e^2}{2m_e} + \hat{U}_C + \frac{e}{2} \langle 2| \, \hat{\epsilon} \cdot \hat{\mathbf{r}}_e \mathcal{E}(\mathbf{R}_0 + \hat{\mathbf{r}}_e) e^{i(\mathbf{k}_L \cdot (\mathbf{R}_0 + \hat{\mathbf{r}}_e) - \omega_L t)} |1\rangle \, |2\rangle \langle 1|$$
$$+ \frac{e}{2} \langle 1| \, \hat{\epsilon} \cdot \hat{\mathbf{r}}_e \mathcal{E}(\mathbf{R}_0 + \hat{\mathbf{r}}_e) e^{-i(\mathbf{k}_L \cdot (\mathbf{R}_0 + \hat{\mathbf{r}}_e) - \omega_L t)} |2\rangle \, |1\rangle \langle 2| . \quad (2.8)$$

For a small atom at an electronic energy level near its ground state, I can make the electric-dipole approximation (EDA), where $e^{\pm i(\mathbf{k}_L \cdot (\mathbf{R}_0 + \hat{\mathbf{r}}_e)} \simeq e^{\pm i \mathbf{k}_L \cdot \mathbf{R}_0}$ and consequently, $\mathcal{E}(\mathbf{R}_0 + \hat{\mathbf{r}}_e) \simeq \mathcal{E}(\mathbf{R}_0)$.

To simplify the form of the Hamiltonian, it is often useful to introduce the angular Rabi frequency Ω(in units of rad/s or $2\pi \times$Hz) given by

$$\Omega(\mathbf{R}_0) = \frac{e\mathcal{E}(\mathbf{R}_0)}{\hbar} \langle 2| \, \hat{\epsilon} \cdot \hat{\mathbf{r}}_e |1\rangle . \quad (2.9)$$

In the field-interaction picture, the Hamiltonian $\hat{\tilde{H}}_e$ is, in matrix notation,

$$\hat{\tilde{H}}_e = \frac{\hbar}{2} \begin{bmatrix} \delta_L - \mathbf{k}_L \cdot \mathbf{V}_0 & |\Omega(\mathbf{R}_0)| \\ |\Omega(\mathbf{R}_0)| & -\delta_L + \mathbf{k}_L \cdot \mathbf{V}_0 \end{bmatrix} \quad (2.10)$$

where $\delta_L = \omega_L - \omega_0$, $\mathbf{V}_0$ is the CM velocity vector of the atom, and the upper-left corner of the matrix corresponds to the $|1\rangle$ state. Because the field is near-resonant, δ_L is at the order of Γ and Ω. The interaction $\hbar \mathbf{k}_L \cdot \mathbf{V}_0$ corresponds to Doppler shifts of the field's wavelength as seen by the moving atom. In order to learn about this near-resonant field's effects on the CM dynamics, one must obtain the state populations and coherences in the steady-state regime $(1/t << \Gamma, \Omega, \delta_L)$ from solving the optical Bloch equations (OBEs).

2.1.1 Optical Bloch Equations

The OBEs are a consequence of the following master equation in the field-interaction picture:

$$\frac{d\hat{\tilde{\rho}}(\mathbf{R}_0, \mathbf{V}_0, t)}{dt} = -\frac{i}{\hbar}[\hat{\tilde{H}}_e(\mathbf{R}_0, \mathbf{V}_0, t), \hat{\tilde{\rho}}(\mathbf{R}_0, \mathbf{V}_0, t)] + \begin{bmatrix} \Gamma \rho_{22} & -\Gamma \tilde{\rho}_{12}/2 \\ -\Gamma \tilde{\rho}_{21}/2 & -\Gamma \rho_{22}, \end{bmatrix} \quad (2.11)$$

where $\hat{\tilde{\rho}}$ is the density matrix operator defined as

$$\hat{\tilde{\rho}} = \begin{bmatrix} |c_1(\mathbf{R}_0, \mathbf{V}_0, t)|^2 & c_1(\mathbf{R}_0, \mathbf{V}_0, t)c_2^*(\mathbf{R}_0, \mathbf{V}_0, t)e^{-i[\omega_L t - \mathbf{k}_L \cdot \mathbf{R}_0 - \eta]} \\ c_2(\mathbf{R}_0, \mathbf{V}_0, t)c_1^*(\mathbf{R}_0, \mathbf{V}_0, t)e^{i[\omega_L t - \mathbf{k}_L \cdot \mathbf{R}_0 - \eta]} & |c_2(\mathbf{R}_0, \mathbf{V}_0, t)|^2 \end{bmatrix},$$
(2.12)

with c_i being the CM position- and velocity-dependent probability amplitude for state $i = 1$ or 2 in the Schrōdinger picture. The generalized quantity η consists of the remaining phases imparted by the laser field, which I will assume are negligible in the following discussion. In the steady-state regime, the following OBEs are obtained,

$$0 = \text{Im}(\tilde{\rho}_{12})|\Omega(\mathbf{R}_0)| - \Gamma\rho_{22} \tag{2.13}$$

$$0 = i(\delta_L - \mathbf{k}_L \cdot \mathbf{V}_0)\tilde{\rho}_{21} - \frac{i}{2}|\Omega(\mathbf{R}_0)|(1 - 2\rho_{22}) - \Gamma\tilde{\rho}_{21}/2 \tag{2.14}$$

$$\rho_{11} = 1 - \rho_{22} \tag{2.15}$$

$$\tilde{\rho}_{12} = \tilde{\rho}_{21}^*, \tag{2.16}$$

which yields

$$\rho_{22}(\mathbf{R}_0, V_{0z}, t) = \frac{\Omega^2(\mathbf{R}_0)/4}{\Gamma^2/4 + (\delta_L - k_L V_{0z})^2 + \Omega^2(\mathbf{R}_0)/2} \tag{2.17}$$

$$\text{Re}(\tilde{\rho}_{12}) = \text{Re}(\tilde{\rho}_{21}) = \frac{\Omega(\mathbf{R}_0)(\delta_L - k_L V_{0z})/2}{\Gamma^2/4 + (\delta_L - k_L V_{0z})^2 + \Omega^2(\mathbf{R}_0)/2} \tag{2.18}$$

$$\text{Im}(\tilde{\rho}_{12}) = -\text{Im}(\tilde{\rho}_{21}) = \frac{\Gamma\Omega(\mathbf{R}_0)/4}{\Gamma^2/4 + (\delta_L - k_L V_{0z})^2 + \Omega^2(\mathbf{R}_0)/2}, \tag{2.19}$$

and $\rho_{11} = 1 - \rho_{22}$ for a wave propagating along the z-axis.

When the light is near resonance with the electronic transition of the atom, the atom will fluoresce at angular frequency ω_L. What is happening here is that the incident optical field is scattering off the atom at a random direction. The probability that this scattering event will occur is proportional to ρ_{22}, and the rate at which the photons of the field scatter is given by $\Gamma_{sc} = \Gamma\rho_{22}$. For a single scattering event, an energy $\hbar\omega_L$ taken from the entire optical field is dissipated into the surrounding vacuum. Therefore, the total amount of energy lost from the field by the isotropic thermal sample of atom density N at temperature T per unit

length and time is given by

$$dw(\delta_L)/(dtdZ_0) = -N\hbar\omega_L \int\limits_{-L/2}^{L/2} \int\limits_{-L/2}^{L/2} \int\limits_{-\infty}^{\infty} \Gamma_{sc}(X_0, Y_0, \delta_L, V_{0z}) f(V_{0z}, T) dX_0 dY_0 dV_{0z} \qquad (2.20)$$

$$f(V_{0z}, T) = \sqrt{\frac{M}{2\pi k_B T}} e^{-MV_{0z}^2/2k_B T}, \qquad (2.21)$$

where L here is the transverse dimension of the volume containing the atom sample. The convolution of the Maxwell distribution f and the scattering rate yields a Voigt profile as a function of δ_L. At low temperatures, the Doppler broadening of the absorption profile is negligible, and the above integral results in a Lorentzian function of δ_L. However, for temperatures even as low as liquid nitrogen (77 K), the Doppler broadening exceeds 100 MHz and the profile resembles a Gaussian. As an example of these features in the context of resonant light incident on ^{85}Rb atoms (I approximate it as a two-level atom in this example), Fig. 2.1 exhibits a plot of optical power density scattered by the atoms for common temperatures: 300 K (room-temperature), 77 K (liquid N$_2$), 4 K (liquid He), 1 K (1-K pot), 0.1 mK (laser cooling). Clearly, the colder and, consequently, slower the atom, the sharper and stronger the absorption profile is.

From Eq. 2.20, one can back out an expression for the intensity lost due to the scattering of the incident light. If we assume a very weak incident field polarized along x, the scattering rate is

$$\Gamma_{sc} \simeq \Gamma \frac{I(\mathbf{R}_0) d_x^2/2c\epsilon_0}{\Gamma^2/4 + (\delta_L - k_L V_{0z})^2}. \qquad (2.22)$$

Therefore, the intensity as a function of Z_0 is the solution to the following differential equation,

$$dI/dZ_0 = -\frac{N\hbar\omega_L \Gamma d_x^2}{2c\epsilon_0} \sqrt{\frac{M}{2\pi k_B T}} \int\limits_{-\infty}^{\infty} \frac{e^{-MV_{0z}^2/2k_B T}}{\Gamma^2/4 + (\delta_L - k_L V_{0z})^2} dV_{0z} I(\mathbf{R}_0) = -a(\delta_L) I(\mathbf{R}_0),$$

$$(2.23)$$

where $a(\delta_L) = n''(\delta_L)\omega_L/c$ is the Beer's absorption coefficient, which is proportional to the imaginary component of the refractive index. The recoil energy this two-level atom of mass M receives during a scattering event is two times $E_r = \hbar^2 k_L^2/2M$. This quantity is known as the single-photon recoil energy. In order to understand the momentum shift of the atom under this scattering interaction, one must obtain the expectation value of the force associated with this recoil $\langle \mathbf{F} \rangle$.
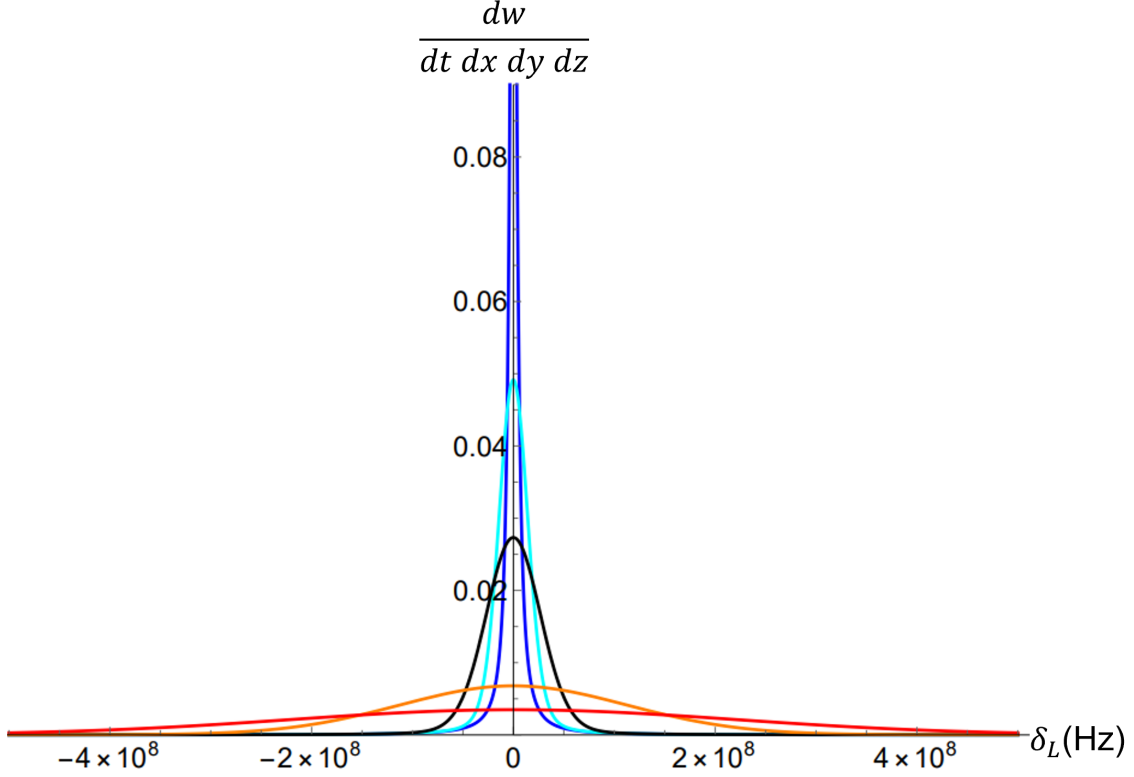
Figure 2.1: Power per unit volume $dw/(dt\,dx\,dy\,dz)$ in units of $N\hbar\omega_L\Gamma$ for 780-nm light scattered by rubidium atoms as a function of detuning from the cycling transition for the following temperatures: 300 K (red), 77 K (orange), 4 K (black), 1 K (cyan), 0.1 mK (blue).

2.1.2 Conservative and Dissipative Optical Forces

The force $\langle \mathbf{F} \rangle$ exerted on the atom by the optical field is given by

$$
\begin{aligned}
\langle \mathbf{F} \rangle &= -\langle \hat{\mathbf{d}} \cdot \hat{\epsilon} \vec{\nabla}_0 \mathcal{E}(\mathbf{R}_0) \cos\left(\mathbf{k}_L \cdot \mathbf{R}_0 - \omega_L t\right)\rangle \\
&= -\frac{\langle 1|\, \hat{\mathbf{d}} \cdot \hat{\epsilon}\, |2\rangle}{2}\left[\tilde{\rho}_{12}\left(\vec{\nabla}_0 \mathcal{E}(\mathbf{R}_0) + i\mathbf{k}_L \mathcal{E}(\mathbf{R}_0) \right) + \tilde{\rho}_{21}\left(\vec{\nabla}_0 \mathcal{E}(\mathbf{R}_0) - i\mathbf{k}_L \mathcal{E}(\mathbf{R}_0) \right) \right] \\
&= \hbar\Omega(\mathbf{R}_0)\left[\mathrm{Im}(\tilde{\rho}_{12})\mathbf{k}_L - \mathrm{Re}(\tilde{\rho_{12}})\vec{\nabla}_0 \mathcal{E}(\mathbf{R}_0)/\mathcal{E}(\mathbf{R}_0) \right] \\
&= \hbar\mathbf{k}_L\Gamma_{sc} - \frac{\hbar\Omega^2(\mathbf{R}_0)(\delta_L - k_L V_{0z})/2}{\Gamma^2/4 + (\delta_L - k_L V_{0z})^2 + \Omega^2(\mathbf{R}_0)/2}\left(\frac{\vec{\nabla}_0 \mathcal{E}(\mathbf{R}_0)}{\mathcal{E}(\mathbf{R}_0)} \right) = \mathbf{F}_{sc} + \mathbf{F}_{grad}. \quad (2.24)
\end{aligned}
$$

The first force term is a dissipative scattering force that induces an average momentum change of $\hbar\mathbf{k}_L$ on the atom, as can be seen in Fig. 2.2. The second is a conservative force

that pushes the atom towards regions of high or low field intensities depending on δ_L. This force is known as the *dipole force*, and was the mechanism for the first experiments involving the trapping of dielectric nanospheres in a highly-focused single beam [87]. In the case that the applied optical field resembles a plane wave, where there is no intensity gradient, the dipole force is negligible.
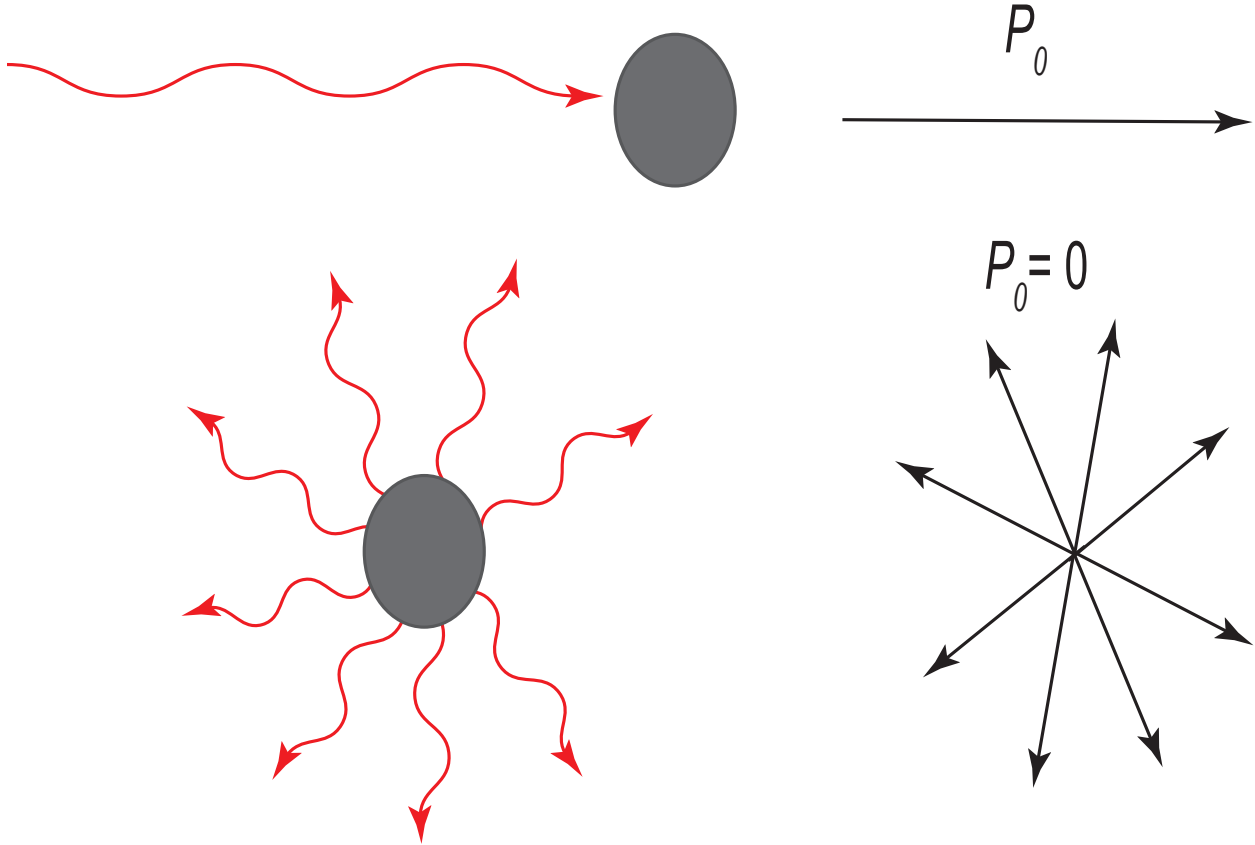
Figure 2.2: A scattering event on an atom by a co-linear laser field. In the top figure, the incident field causes a momentum recoil P_0 in the direction of the black arrow. The bottom figure shows the outgoing field in a random direction that is opposite to the atom's momentum vector. Over many scatters, the net recoil from the outgoing field averages to zero, leaving the total change in the atom's momentum to be $N\hbar\mathbf{k}_L$, where N is the number of events.

In Fig. 2.3, the velocity dependence of the dissipative scattering force is displayed for $\delta_L = -\Gamma/2$ in a scenario where two plane-wave laser beams of the same frequency and intensity are counter-propagating. In the limit of small $|k_L V_{0z}|$ towards the origin of the

plot, a linear dependence on V_{0z} is observable. Such a dependence attests to the dissipative nature of the scattering force, as it behaves like a frictional force with a linear dependence on the atom's velocity.
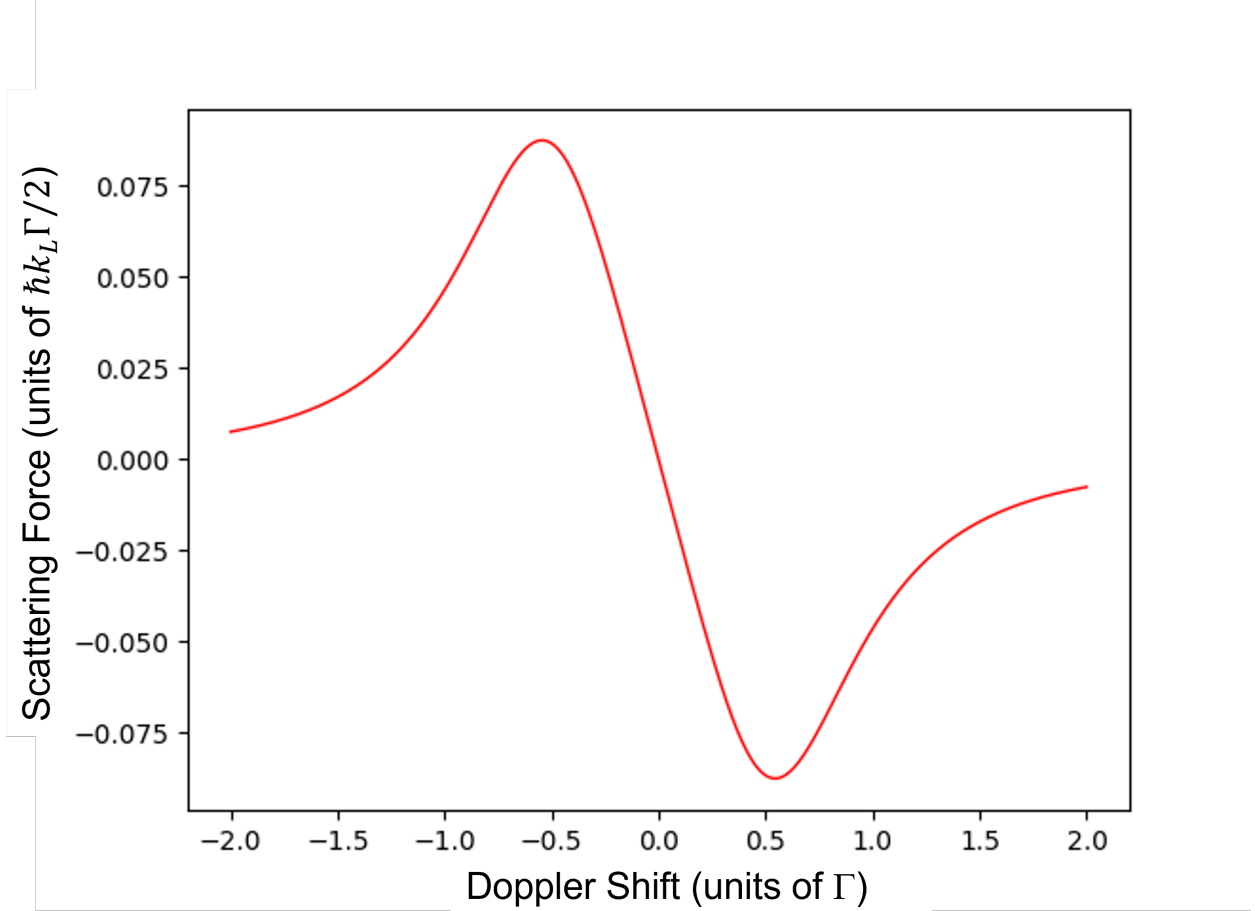
Figure 2.3: The dissipative scattering force on an atom as a function of Doppler shift ($k_L V_{0z}$). Here, $\Omega = 0.25\Gamma$ and $\delta_L = -\Gamma/2$.

An effective damping coefficient may be derived in this limit where $k_L V_{0z} << \Omega, \Gamma, \delta_L$. As shown in Ref. [88], binomial expansion of the scattering force from two counter-propagating, plane-wave-like laser beams with the same intensities and frequencies in the limit $k_L V_{0z} << \Gamma$ yields

$$\mathbf{F}_{sc} = \hbar \mathbf{k}_L \Gamma \left[\frac{\Omega^2(\mathbf{R}_0)/4}{\Gamma^2/4 + (\delta_L - k_L V_{0z})^2 + \Omega^2(\mathbf{R}_0)/2} - \frac{\Omega^2(\mathbf{R}_0)/4}{\Gamma^2/4 + (\delta_L + k_L V_{0z})^2 + \Omega^2(\mathbf{R}_0)/2} \right],$$
$$(2.25)$$

leads to the following damping coefficient α

$$\alpha = -\frac{\hbar k_L^2 \Gamma \delta_L \Omega^2}{(\Gamma^2/4 + \Omega^2/2 + \delta_L^2)^2}. \tag{2.26}$$

Therefore, it can be concluded that using six, intersecting laser beams with the same frequencies and intensities, this frictional force brought on by the near-resonant scattering of the laser fields off the atom can dampen its translational motion, cooling it to a temperature approaching absolute zero, with limits shown below. This technique of cooling is analogous to placing a macroscopic particle in molasses. Hence, this described system is famously referred to as *optical molasses*.

2.1.3 Laser Cooling

It appears at first glance that the atom placed in the optical molasses would eventually reach absolute zero. However, this conjecture violates many principles of thermodynamics and statistical mechanics. In actuality, the atom in the optical molasses exhibits diffusion in a similar manner as the Brownian motion of particles placed in a viscous fluid [89]; that is to say, the atom will never become stationary.

From the Langevin equation [90; 91] for an atom experiencing a frictional force $-\alpha V_0$ and a random force F with the property $\langle F(t) \rangle = 0$ over time,

$$\dot{P}_0 = -\alpha P_0/M + F(t), \tag{2.27}$$

the variance in P_0, $\sigma_{P_0}^2$ can be obtained using the identity for the random force $\langle F(t)F(t') \rangle = 2D\delta(t - t')$, where D is a normalization constant known as the *momentum-diffusion coefficient*. Using Eq. 2.27, the following expression is obtained for $\sigma_{P_0}^2$,

$$\sigma_{P_0}^2 = \frac{DM}{\alpha}\left(1 - e^{-2\alpha t/M}\right). \tag{2.28}$$

At timescales on the order of a single scattering event $t << M/2\alpha$ much faster than the time the system reaches equilibrium, the variance reduces to

$$\sigma_{P_0}^2 \simeq 2Dt, \tag{2.29}$$

whereas it reduces to

$$\sigma_{P_0}^2 = \langle P_0^2 \rangle \simeq DM/\alpha, \tag{2.30}$$

when $t \to \infty$. Using the equipartition theorem in 3D ($\langle P_0^2 \rangle/2M = 3k_BT/2$, as $t \to \infty$, the

lower temperature limit of the atom is derived

$$T = \frac{D}{3\alpha k_B}. \tag{2.31}$$

In order to get a result for the coldest temperature obtained from a three-dimensional scattering force, with a damping coefficient α, I will detail the causes of momentum diffusion D from the random force $F(t)$.

During a scattering event, the incident direction of the laser field is fixed, but the scattered direction is random under the assumption that the atom nor incident field are polarized. Over many events, the average momentum kick from this scattered field is zero, leaving the net momentum kick in the propagation direction of the incident field. However, the mean-square of the momentum, $\langle P_0^2 \rangle$ is nonzero and equal to the squared momentum of the outgoing field, $\hbar^2 k_L^2$. The momentum variance from this random kick is summed over the total number of scattering events within a short time interval, $\Gamma_{sc} t$. Thus, when using Eq. 2.29, the momentum diffusion from the random recoil of the atom is

$$D_{recoil} = \frac{\hbar^2 k_L^2 \Gamma \Omega^2}{8(\Omega^2/2 + \delta_L^2 + \Gamma^2/4)}. \tag{2.32}$$

An additional mechanism for momentum diffusion arises from the uncertainty in photon mode number, δN, from the coherent laser field incident on the atom, which leads to a variance in the total momentum kick in the direction of the incident field. This variance can be described by

$$\hbar^2 k_L^2 \sigma_N^2 = \hbar^2 k_L^2 \langle N \rangle, \tag{2.33}$$

true for Poissonian photon statstics, which is what a coherent radiation field follows. The average photon mode number of the light imparting this momentum kick on the atom after a duration t is given by $\Gamma_{sc} t$. Thus, the diffusion coefficient from the incident laser field is also

$$D_{laser} = \frac{\hbar^2 k_L^2 \Gamma \Omega^2}{8(\Omega^2/2 + \delta_L^2 + \Gamma^2/4)}. \tag{2.34}$$

If the laser field has a significant intensity gradient, an additional term calculated in [90; 69] is added to D_{laser} resulting from random fluctuations in the dipole force. However, we are investigating the lowest temperature limit laser cooling from the scattering force can provide in a two-level atom, so here I am assuming a plane-wave approximation to the radiation field.

The sum of the two contributions to momentum diffusion for six incident plane waves of

the same frequency and intensities in the limit of $\delta_L = -\Gamma/2$ and $\Omega << \Gamma$ results in

$$D = D_{recoil} + D_{laser} = \frac{3\hbar^2 k_L^2 \Omega^2}{\Gamma}. \tag{2.35}$$

In the same limit, the three-dimensional damping coefficient that the atom sees from six intersecting plane-wave laser fields reaches its maximum value, $\alpha \simeq 2\hbar k_L^2 \Omega^2/\Gamma^2$, and the lower temperature limit, known as the Doppler temperature, T_D, becomes

$$T_D = \frac{\hbar\Gamma}{2k_B}. \tag{2.36}$$

For two alkali atoms commonly used in laser cooling, Rb and Na, the Doppler temperatures are 146 μK and 235 μK, respectively [92; 93]. The first experiment of three-dimensional laser cooling towards the Doppler temperature was performed in [94] at Bell Labs using Na and a tunable dye laser operating at 589 nm. Surprisingly, a later experiment [13] demonstrated that a similar apparatus could reach temperatures much lower than T_D based on an improved theoretical model [2] that derived a larger α.

2.1.4 Magneto-Optical Trap (MOT)

While the scattering force from near-resonant light works well in slowing down atoms to temperatures prohibited by Newton's law of cooling, inspection of Eq. 2.25 implies that the atom will not necessarily be spatially trapped near the intersection point of all six beams from such a force. Experiments that rely on the production of highly dense atomic samples, such as the generation of Bose-Einstein condensates [81; 82] and Fermi degenerate gases [83; 84], therefore cannot be performed from six intersecting, red-detuned laser beams alone; the scattering force must exhibit a spatial dependence that allows it to act like a restoring force. For some time, it was believed that optical fields could not confine neutral atoms under the scattering force in all three-dimensions due to the optical Earnshaw theorem [95]; the flaw in this belief came from the fact that atoms have several magnetic suborbitals that can be populated depending on the presence of a magnetic field and the polarization of the incident light. In this sub-section, I will explore the *magneto-optical trap* (known by all atom trappers as a MOT), a cooling and trapping method I use in all of my experiments.

Alkali atoms, such as Rb, Cs, and Na, are not two-level systems. Magnetic-dipole interactions between the valence electron's total magnetic moment and that of the nucleus results in a net atomic angular momentum quantized as the hyperfine quantum number F. The ground state's magnetic suborbitals therefore range from $m_F = -F$ to F. For the excited state used in the MOT, the hyperfine quantum number is usually $F' = F + 1$. For the

example in my description of the MOT, I will use the simple case of $F = 0$ and $F' = 1$. This case is "simple" because there are no optical pumping effects needed to be taken into account, as the ground state here is spinless.

The MOT requires the application of a magnetic quadrupole field $\mathbf{B}_q$ around the origin of the apparatus, where the six laser beams meet. This field is generated by two parallel loops of current in the anti-Helmholtz configuration. At the origin, the quadrupole magnetic field is zero. Small distances from the origin yield a magnetic field directly proportional to the CM displacement. Thus, along the z-axis,

$$\mathbf{B}_q \simeq \beta Z_0 \hat{k}, \tag{2.37}$$

where β is the magnetic-field gradient, typically on the order of 10 G/cm, not strong enough to trap atoms at thermal temperatures, but enough to give Zeeman shifts on the order of the laser field's detuning from resonance. The Zeeman shift $\hbar\Delta_Z(m_F, m_{F'}, Z_0)$ on the atomic levels is

$$\Delta_Z(m_F, m_{F'}, Z_0) = (g_{F'}m_{F'} - g_F m_F)\mu_B \beta Z_0/\hbar, \tag{2.38}$$

where $m_F = 0$ in this case, $g_{F'}$ is the gyromagnetic ratio factor of the F' state, and $\mu_B = h \times 1.39$ MHz/G. A plot of the Zeeman shifts under $\mathbf{B}_q$ for states $F' = 1$ and $F = 0$ is shown in Fig. 2.4(a) with the coil configuration shown in Fig. 2.4(b).

Along the z-direction there are two counter-propagating laser beams of equal intensities and frequencies. Propagating in the direction of positive Z_0, the laser beam is σ^+-polarized with respect to the Z_0-axis, which allows transitions only to the $m_{F'} = 1$ sublevel. In the direction of negative Z_0, the laser beam is σ^--polarized with respect to Z_0, so a transition to $m_{F'} = -1$ is allowed. When a hot atom moves away from the origin and counter to the direction of one of the beams, the Doppler shift and position-dependent Zeeman shift both tune the energy splitting into resonance, which optimizes the scattering rate. As the atom keeps moving in the same direction while being slowed by the beam, the Doppler shift is reduced while the Zeeman shift is enhanced from the quadrupole field, keeping the resonance condition met and optimizing the scattering rate. Quantitatively, this force is approximated as

$$\mathbf{F}_{\mathrm{MOT}} = \hbar \mathbf{k}_L \Gamma \left[\frac{\Omega^2(\mathbf{R}_0)/4}{\Gamma^2/4 + (\delta_L - k_L V_{0z} - g_{F'}\mu_B \beta Z_0/\hbar)^2 + \Omega^2(\mathbf{R}_0)/2} \right.$$
$$\left. - \frac{\Omega^2(\mathbf{R}_0)/4}{\Gamma^2/4 + (\delta_L + k_L V_{0z} + g_{F'}\mu_B \beta Z_0/\hbar)^2 + \Omega^2(\mathbf{R}_0)/2} \right], \tag{2.39}$$

making it position-dependent, and in a limiting form, similar to a damped harmonic oscillator
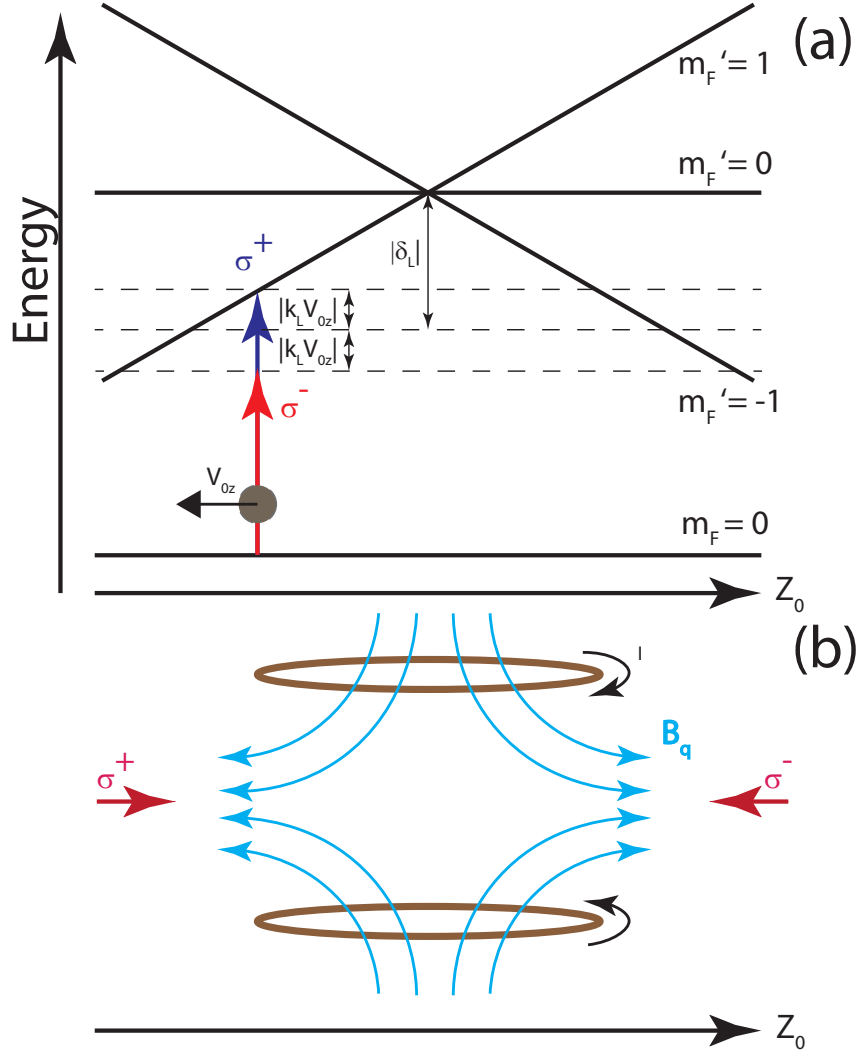
Figure 2.4: (a) Energy level structure for the MOT apparatus. For an atom in the position shown, with a negative velocity with respect to Z_0, the σ^+-polarized is tuned into resonance while the σ^- light is tuned out. This leads to a stronger net kick by the laser field, opposing the atom's motion and confining it near the origin. Note that these polarizations are defined with respect to the quantization axis (z), which defines the m_F basis; thus, they are both the same polarization (LCP) in the optical field's frame of reference. (b) Coil, current (I), and beam configuration in one dimension of the MOT. The blue magnetic-quadrupole-field lines are shown.

that settles near the equilibrium position (the origin) [88].

For ^{85}Rb, the species used in this thesis, $F = 3$ and $F' = 4$. The σ-polarized lasers for this alkali additionally optically pump [66; 92] the valence electron into either the $m_F = 3$ or $m_F = -3$ state, making the relevant transitions for photon scattering to occur between

$m_F = \pm 3$ and $m_{F'} = \pm 4$. It also happens that this transition is not entirely closed. As can be seen in Fig. 2.5, the nearby hyperfine state of the $\left|5P_{3/2}, F' = 4\right\rangle$ level is only 121 MHz away [92]. Atoms can still be off-resonantly excited into the $F' = 3$ level and decay into the $\left|5S_{1/2}, F = 2\right\rangle$ level, which cannot be accessed by the cooling laser due to the excessive 3 GHz detuning from resonance. An additional laser at a frequency resonant with the $\left|5S_{1/2}, F = 2\right\rangle \rightarrow \left|5P_{3/2}, F' = 2\right\rangle$ or $\left|5P_{3/2}, F' = 3\right\rangle$ transitions is typically irradiated on the MOT in order to pump atoms back into the $F = 3$ hyperfine state. This laser is referred to as the *repumper* in this thesis.
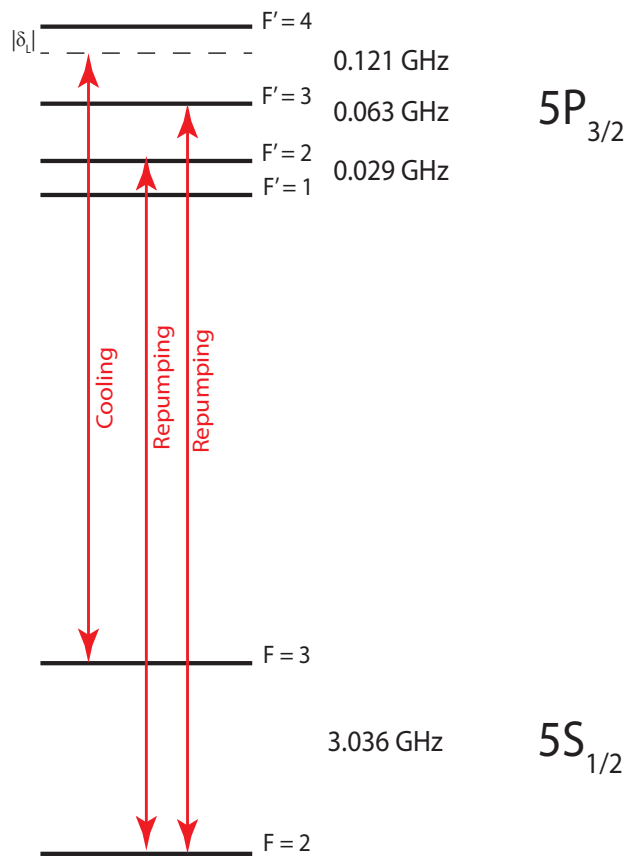
Figure 2.5: Diagram of relevant ^{85}Rb energy levels and laser fields (at 780 nm) used in laser cooling. Two repumping transitions are permissible to make the D_2 line closed.

The first MOT was performed with Na atoms in [96]. Typical MOT densities are at

the order of $\sim 10^{10}$ atoms/cm³, making them suitable for studying interactions involving atomic collisions, such as the measurement of the C_6 Van der Waals coefficient [97] and the formation of Rydberg-ground and Rydberg-Rydberg molecules [98; 99]. MOTs are sometimes not suitable for experiments involving a magnetic-field-free environment, such as the ones I perform in Chapters VII-VIII, as it is experimentally complicated to exterminate $\mathbf{B}_q$ in time for the measurements to be performed due to induced eddy currents [68]. Furthermore, a MOT usually can only provide a sample with a minimum temperature of T_D. Another method of laser cooling, known as *polarization-gradient (PG) cooling* is required to achieve temperatures lower than T_D [2].

2.1.5 Polarization-Gradient (PG) Cooling

The scattering force derived earlier in this section made two approximations in the model. First, I assumed that the atom has exactly two energy levels. Furthermore, I made the assumption that the two, counter-propagating laser beams do not form an interference pattern. These two approximations contribute to the reason why Eq. 2.26 was found to be an underestimate [13; 2].

The counter-propagating laser beams of opposite helicity with respect to the quantization axis form a linear polarization rotating along the direction of the beam propagation axis (shown in Fig. 2.6(a)) that yields empirically a stronger α than the two-level model of Eq. 2.26 predicts when $\mathbf{B}_q = 0$. Optical pumping of hyperfine magnetic suborbitals and the rotating polarization of the laser field both create a velocity-dependent redistribution of populations in m_F. As a consequence of this imbalance of m_F distribution, the scattering force of the counter-propagating beams is unbalanced due to the differing coupling strengths among the $F, m_F \to F', m_{F'}$ transitions [2]. It is this effect that makes the original two-level model of the optical molasses invalid.

Mathematically, the gradient of linear polarizations resultant to the superposition of the σ^+- and σ^--polarized counter-propagating beams of equal intensity, are depicted in the laser field as

$$\mathbf{E}(Z_0, t) = \frac{-i\mathcal{E}_0}{\sqrt{2}}\left[\hat{\epsilon}_x \sin\left(k_L Z_0\right) + \hat{\epsilon}_y \cos\left(k_L Z_0\right)\right] e^{-i\omega_L t} + c.c., \tag{2.40}$$

as was derived in [2], where $\hat{\epsilon}_x$ and $\hat{\epsilon}_y$, are the linear polarization vectors in the laboratory frame of reference. Larmor's theorem dictates that this rotating polarization seen in the rotating frame of the moving atom with velocity V_{0z} has the same effect as a DC magnetic field pointing along the laser propagation axis with a corresponding Zeeman interaction,

$$\hat{U}_r = k_L V_{0z} \hat{J}_z, \tag{2.41}$$
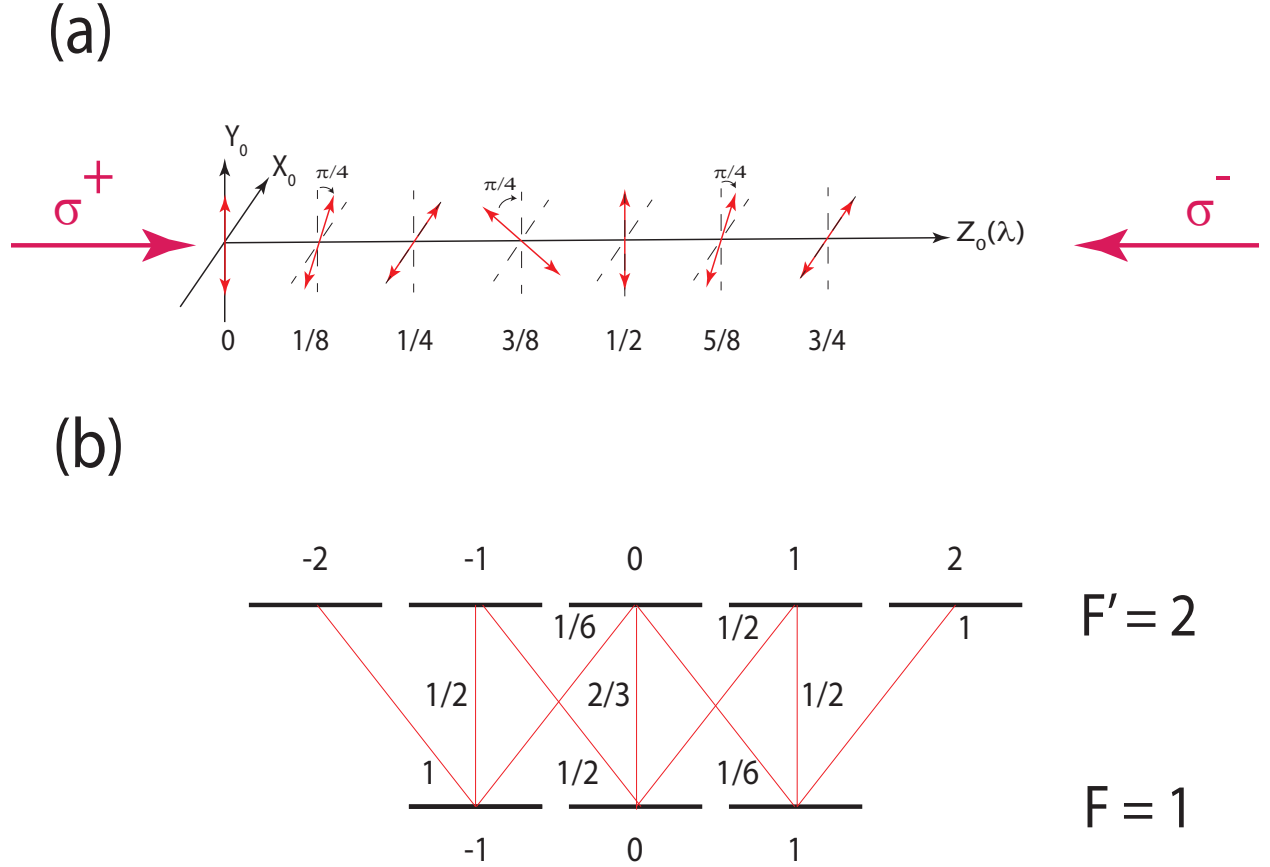
Figure 2.6: (a) The interference pattern between counter-propagating σ^+ and σ^- beams (both are LCP in the field's reference frame) results in a rotating linear polarization along the Z_0-axis in the rotating-wave approximation. (b) Clebsch-Gordan coefficients for all couplings among m_F and m'_F. Figure loosely adapted from [2].

for a stationary atom.

   In this discussion, following the reasoning in [2], I will use the case of $F = 1$ and $F' = 2$, which has Clebsch-Gordan coefficients presented for all possible optical transitions in Fig. 2.6(b). These factors show the relative Rabi frequencies of each transition for a given laser field strength $\mathcal{E}_0$. Optical dipole shifts in the energy levels therefore vary among m_F,

$$\hbar\Delta(|m_F| = 1) = \frac{\hbar\Omega^2}{8\delta_L} \tag{2.42}$$

$$\hbar\Delta(m_F = 0) = \frac{\hbar\Omega^2}{6\delta_L} \tag{2.43}$$

at $Z_0 = 0$, where Ω is the reduced Rabi frequency here and the atom's quantization direction is set to the y-axis, making the laser field π-polarized. For PG cooling, $\delta_L = -4\Gamma$ typically

and Ω is reduced such that $\Delta(m_F) >> \Gamma_{sc}$, with Γ_{sc} being the photon scattering rate averaged over all m_F [2]. Optical pumping with a π-polarized laser field induces the following respective populations for the $|m_F| = 1$ states and $m_F = 0$ state: 4/17 and 9/17 [2; 66]

The effective Zeeman interaction, $\hat{U}_r$, mixes the m_F states, since the angular momentum operator is transverse to the quantization axis. First-order corrections are given by

$$|F = 1, m_F = 0\rangle^{(1)} = |1, 0\rangle + \frac{24\delta_L k_L V_{0z}}{\sqrt{2}\Omega^2} |1, 1\rangle + \frac{24\delta_L k_L V_{0z}}{\sqrt{2}\Omega^2} |1, -1\rangle \qquad (2.44)$$

$$|F = 1, m_F = 1\rangle^{(1)} = |1, 1\rangle - \frac{24\delta_L k_L V_{0z}}{\sqrt{2}\Omega^2} |1, 0\rangle \qquad (2.45)$$

$$|F = 1, m_F = -1\rangle^{(1)} = |1, -1\rangle - \frac{24\delta_L k_L V_{0z}}{\sqrt{2}\Omega^2} |1, 0\rangle \qquad (2.46)$$

calculated from nondegenerate perturbation theory in the limit $k_L V_{0z} << \Delta(m_F)$. Under this sort of weak mixing, the perturbed basis states are still nearly orthogonal and part of a complete Hilbert space. Furthermore, the population distribution of m_F states does not deviate significantly from the unmixed case. Therefore, I can express the total quantum state $|\psi\rangle$ as

$$|\psi\rangle = c_z(F = 1, m_F = 0) |F = 1, m_F = 0\rangle_z + c_z(1, 1) |1, 1\rangle_z + c_z(1, -1) |1, -1\rangle_z$$
$$\simeq \sqrt{9/17} |F = 1, m_F = 0\rangle^{(1)} + \sqrt{4/17} \big[|1, 1\rangle^{(1)} + |1, -1\rangle^{(1)} \big], \quad (2.47)$$

where $c_z(F, m_F)$ and $|F, m_F\rangle$ are the probability amplitudes and eigenkets of the system when taking the laser propagation axis (z-axis) as the quantization direction.

One can arrive at the velocity-dependent polarization of the atoms when choosing z as the quantization axis,

$$_z\langle 1, 1|1, 1\rangle_z - _z\langle 1, -1|1, -1\rangle_z \simeq \frac{240\delta_L k_L V_{0z}}{17\Omega^2} \qquad (2.48)$$

which is directly proportional to the expectation value of the $\hat{J}_z$ operator. The right-hand side is the expression obtained when calculating $\langle \hat{J}_z \rangle$ with the basis states quantized along the y-axis.

An atom with $V_{0z} > 0$ will most likely be polarized in the $m_F = -1$ state and receive a stronger force from the scattering of a counter-propagating σ^--polarized photon. Thus, the frictional force is proportional to the atomic polarization, yielding a new expression for the damping coefficient,

$$\alpha \propto -\hbar\delta k_L^2 \Gamma_{sc}/\Omega^2, \qquad (2.49)$$

which, in the limit of $\delta >> \Gamma, \Omega$, enhances α by δ_L^2/Ω^2 when ignoring numerical factors. In PG cooling, the detuning is increased more towards the red and the laser power is reduced in order to optimize α and lower the equilibrium temperature of the atom. For ^{85}Rb, this reasoning, first presented in [2], works well for $F = 3$ and $F' = 4$. Exact values of α and T can be obtained by solving the OBEs tailored to the hyperfine structure of the alkali in question and utilizing Monte-Carlo wave function algorithms [100]. In most cases, PG cooling can cool atoms to below 50 μK.

The first experiment demonstrating three-dimensional laser cooling [94] did not feature a magnetic quadrupole field, yet only achieved temperatures at the Doppler limit. However, a nearly identical experiment [13] reported Na cooling down to 50 μK and noticed changes in the molasses temperatures as a function of external magnetic fields and laser polarizations. It turns out that the ion pumps for the vacuum in [94] were providing external magnetic fields that surprisingly heated the molasses to T_D [101]. For the interference of two laser counter-propagating laser beams of orthogonal, linear polarizations, PG cooling can also provide temperatures below T_D, as described in [2].

Laser cooling neutral atoms with optical fields slightly detuned from resonance remains to be one of the most outstanding tools in physics, for one can enhance electromagnetic radiation's interaction time with matter and, in most cases, eliminate noticeable Doppler effects shown in Fig. 2.1. For these reasons, laser cooling has been a critical piece of technology for obtaining time standards with unprecedented accuracy [21; 36; 35; 37], as well as simulating complicated problems in condensed-matter physics [102]. Furthermore, it has permitted extended coherence times for manipulating atomic qubits with optical and microwave radiation in quantum gates [103; 104; 105].

2.2 Far-Off-Resonant Optical Fields

As δ_L is increased, the scattering rate is significantly lowered and the dissipative force is reduced. At the same time, the conservative dipole force exerted on the atom can still induce observable effects if there is an appreciable gradient in the optical field distribution. In this regime, $\delta_L >> \Omega, \Gamma$, the FOR laser field induces AC Stark shifts in the atomic energy level that can be derived from second-order, time-dependent perturbation theory. Complying with physically realizable systems, I have included the multilevel structure of a typical alkali atom in this discussion; i.e., each atomic state now has n, l, j, m_j quantum numbers.

For a given atomic state of n, l, j, m_j quantum numbers, the FOR laser field induces, in its probability amplitude c_{n,l,j,m_j}, a small perturbation in the second order of the atom-field

potential $\hat{U}_{AF}$,

$$
\begin{aligned}
c_{n,l,j,m_j} = c_{n,l,j,m_j}^{(0)} &- \frac{1}{\hbar^2} \int\limits_0^t dt' \int\limits_0^{t'} dt'' \Bigg[\sum_{n',l',j',m_j'} \langle nljm_j | U_{AF}^\dagger(\mathbf{R}_0,\hat{\mathbf{r}}_e,t') \left| n'l'j'm_j' \right\rangle \\
&\times \left\langle n'l'j'm_j' \right| U_{AF}(\mathbf{R}_0,\hat{\mathbf{r}}_e,t'') | nljm_j \rangle \, e^{i\omega_{nlj}^{n'l'j'}(t''-t')} \\
&+ \sum_{l'j'm_j'} \text{p.v.} \int\limits_0^\infty d\epsilon' \rho(\epsilon') \langle nljm_j | U_{AF}^\dagger(\mathbf{R}_0,\hat{\mathbf{r}}_e,t') \left| \epsilon'l'j'm_j' \right\rangle \\
&\times \left\langle \epsilon'l'j'm_j' \right| U_{AF}(\mathbf{R}_0,\hat{\mathbf{r}}_e,t'') | nljm_j \rangle \, e^{i\omega_{nlj}^{\epsilon'}(t''-t')} \Bigg], \quad (2.50)
\end{aligned}
$$

where $c_{n,l,j,m_j}^{(0)} = 1$, $\rho(\epsilon')$ is the density of FESs, $\left| \epsilon',l'j'm_j' \right\rangle$ of kinetic energy ϵ', $\omega_{nlj}^{n'l'j'} = (W_{n'l'j'} - W_{nlj})/\hbar$, $\omega_{nlj}^{\epsilon'} = (\epsilon' - W_{nlj})/\hbar$, and

$$
U_{AF}(\mathbf{R}_0,\hat{\mathbf{r}}_e,t) = -e(\hat{\mathbf{r}}_e \cdot \hat{\epsilon})\mathcal{E}(\mathbf{R}_0)/2[e^{i(\mathbf{k}_L \cdot \mathbf{R}_0 - \omega_L t)} + e^{-i(\mathbf{k}_L \cdot \mathbf{R}_0 - \omega_L t)}]. \quad (2.51)
$$

Eq. 2.50 often is written, incorrectly, without the second term. Electric-dipole couplings to the FESs, where the electron has a kinetic energy above the ionization threshold and is no longer bound by the electrostatic potential of the ionic core, are possible. Because there is no binding, the states form a continuous distribution where $\rho(\epsilon') = 1$ per unit energy. Resonant couplings, in fact, are the mechanism for which photoionization (PI) of the atom can occur (see Section 1.4) [106; 5; 3]. The energy shift $\Delta W_{n,l,j,m_j}$ on the atomic state is given by $i\hbar \frac{\dot{c}_{n,l,j,m_j}}{c_{n,l,j,m_j}}$, where, in the denominator, it is good enough to write $c_{n,l,j,m_j} = 1$. One can write a simple relation between the AC Stark shift on energy W_{nlj} and the optical field strength $\mathcal{E}$

$$
\Delta W_{n,l,j,m_j}(\mathbf{R}_0) = -\frac{1}{4}\alpha_{n,l,j,m_j}(\omega_L)\mathcal{E}(\mathbf{R}_0)^2, \quad (2.52)
$$

where α no longer is used to represent the damping coefficient on the atom, but the polarizability of the atom in light of angular frequency ω_L. This quantity describes how strongly and in what direction an electric dipole moment can be induced in the neutral atom by the laser field. It is typically written in atomic units (multiply by $4\pi\epsilon_0 a_0^3$ to get to SI units). Explicitly, the polarizability is obtained after Eq. 2.50 is integrated over t' and t'' and terms

oscillating faster than the motion of the atom are neglected,

$$\alpha_{n,l,j,m_j}(\omega_L) = \frac{2}{\hbar}\left[\sum_{n',l',j',m_j'}|\langle n',l',j',m_j'|\,\hat{\epsilon}\cdot\hat{\mathbf{d}}\,|n,l,j,m_j\rangle|^2\frac{\omega_{nlj}^{n'l'j'}}{(\omega_{nlj}^{n'l'j'})^2 - \omega_L^2}\right.$$

$$\left. + \text{p.v.}\sum_{l',j',m_j'}\int_0^\infty d\epsilon'\rho(\epsilon')|\langle \epsilon',l',j',m_j'|\,\hat{\epsilon}\cdot\hat{\mathbf{d}}\,|n,l,j,m_j\rangle|^2\frac{\omega_{nlj}^{\epsilon'}}{(\omega_{nlj}^{\epsilon'})^2 - \omega_L^2}\right]. \quad (2.53)$$

Note that $\alpha_{n,l,j,m_j}(\omega_L)$ depends on the magnetic suborbital m_j and the laser polarization $\hat{\epsilon}$. This is an inconvenience when making measurements and obtaining estimates of the polarizability because every experiment is different; i.e., the laser polarizations differ from lab to lab and the m_j distribution can vary based on optical pumping and Zeeman effects. In order to avert inconsistencies, after some nontrivial tensor algebra [107], Eq. 2.53 is written in terms of polarization-independent parameters $\alpha_{n,l,j}^S(\omega_L)$, $\alpha_{n,l,j}^V(\omega_L)$, and $\alpha_{n,l,j}^T(\omega_L)$. These are known as the *scalar, vector,* and *tensor* polarizabilities, respectively. When the laser polarization has no circular component, which is the case in this thesis, $\alpha_{n,l,j,m_j}(\omega_L)$ has no dependence on $\alpha_{n,l,j}^V(\omega_L)$, so

$$\alpha_{n,l,j,m_j}(\omega_L) = \alpha_{n,l,j}^S(\omega_L) + \frac{3m_j^2 - j(j+1)}{j(2j-1)}\alpha_{n,l,j}^T(\omega_L), \quad (2.54)$$

and, in the F, m_F basis, which is the hyperfine-structure dominated Hilbert space, one simply swaps j for F and m_j for m_F in the prefactor of the second term.

When $j \geq 1$, sufficiently strong AC-Stark interactions can induce a breakdown in the hyperfine structure, and the $|m_F|$ splitting brought on by the nonzero tensor polarizability reorders into a $|m_j|, m_I$ pair state. Interestingly, you may find a parallel here with the Zeeman and Paschen-Back regimes, where the nuclear spin $\mathbf{I}$ and the electron's total angular momentum $\mathbf{J}$ precess about a magnetic field at independent rates when the $\mathbf{B}$-field interaction is stronger than the hyperfine structure. This reordering was experimentally observed in [44; 108] for rubidium in the $5P_{3/2}$ state.

2.2.1 Polarizability of the $5D_{3/2}$ State in Rb: an Example

Portions of this section are based on Ref. [3].

Polarizabilities pertaining to the states involved in D1 & D2 lines in Rb are precisely calculated and indexed by [109]. What is not as well understood, however, are the polarizabilities of the $5D_j$ states, which have metrological applications in compact, portable time

standards [25; 28] and the atomic redefinition of the meter [22]. Therefore, I the use the $5D_{3/2}$ level in Rb as the exemplary state when showing the estimated polarizability's behavior at a variety of optical wavelengths. Common wavelengths of interest are 532 nm, 778 nm, 1064 nm, 1251 nm, and 10 μm, as they are widely used wavelengths produced by commercially available lasers. In this work, the FOR wavelength I use for all experimental work is 1064 nm; 10 W of narrow-linewidth (< 100 kHz) light can easily be generated by a Fiber YAG laser.

Fig. 2.7 depicts the $5D_{3/2}$ scalar and tensor polarizabilities' response to optical wavelengths from the UV regime to the NIR to mid-infrared portions. The dipersive-like features in the curves correspond to resonant transitions of the atom's internal state from the $5D_{3/2}$ level. Here the resonance to $5P_{1/2}$ is at 762 nm, and the transition to $5P_{3/2}$ is at 776 nm. At 1251-nm to 2 μm, there are clusters of resonances from the $5D_{3/2}$ level; these are couplings to Rydberg nP_j and nF_j states all the way up to the photoionization (PI) threshold at 1251 nm. As can be seen from these dispersive-like curves, at red detunings, the polarizability becomes positive, making the atom high-laser-field seeking; the opposite is true for the blue-detunings. Intercepts of the horizontal axis correspond to *tune-out* wavelengths, where the atom no longer feels a conservative force from the optical field.

At wavelengths below ~ 600 nm, it can be seen that the scalar polarizability mimics the $1/\omega_L^2$ dependence of the free-electron polarizability, $\alpha_e = -\frac{e^2}{m_e \omega_L^2}$, derived from the eigenvalue of a Volkov state [110](explained in Chapter V). Expansion of the polarizability's energy dependence makes this behavior very apparent when $\omega_L >> \omega_{nlj}^{n'l'j'}$, the case in the context of the Rb $5D_{3/2}$ state when $\lambda << 762$ nm,

$$\frac{\omega_{nlj}^{n'l'j'}}{(\omega_{nlj}^{n'l'j'})^2 - \omega_L^2} = -\omega_{nlj}^{n'l'j'}/\omega_L^2 \left[1 + \frac{(\omega_{nlj}^{n'l'j'})^2}{\omega_L^2} + ...\right]. \tag{2.55}$$

A detailed comparison of α_e with α_{n,l,j,m_j} is provided in [86].

In the long-wavelength limit, as can be seen in Fig. 2.8 there is one last strong resonance to the $4F_{5/2}$ level at around 10 μm, the wavelength of a CO_2 laser. When $\lambda \to \infty$, the scalar and tensor polarizabilites approach their DC values of 18012 and -1093 respectively, at least 10^8 times smaller than that of a Rydberg state.

2.3   Optical Lattices

Atoms in a standing-wave laser field can be periodically trapped or antitrapped in the hills and valleys of the sinusoidal optical potential. For the one-dimensional case, the adiabatic
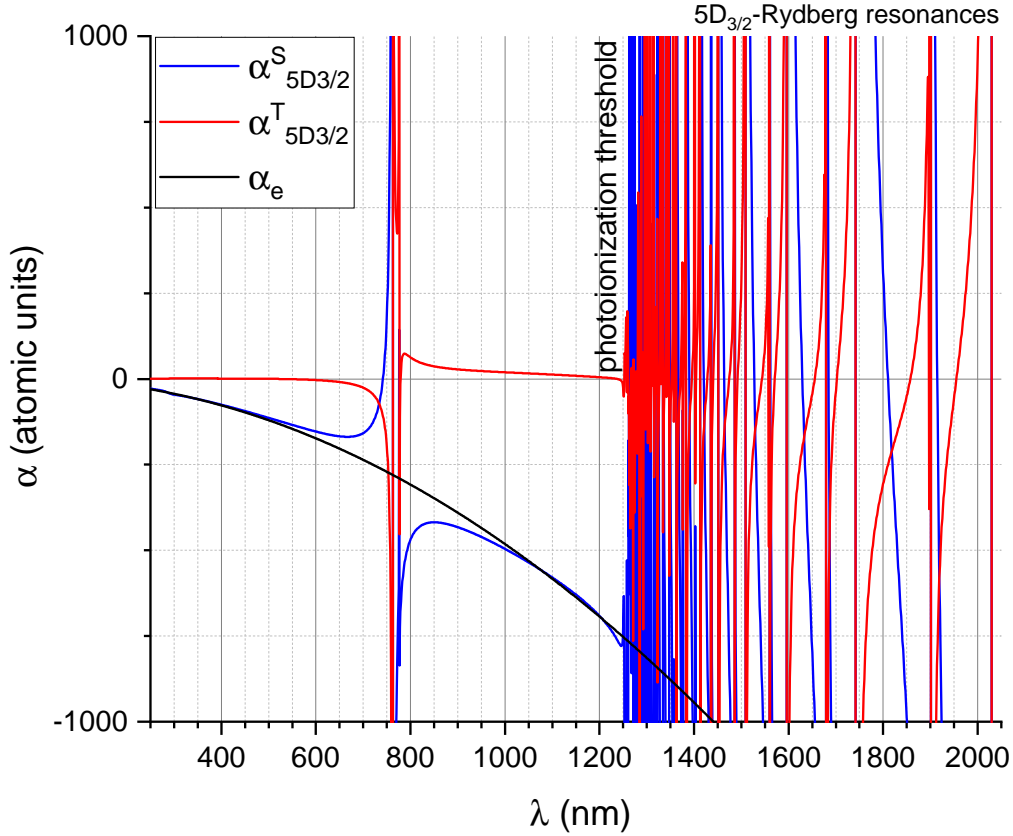
Figure 2.7: Behavior of scalar and tensor polarizability for Rb $5D_{3/2}$ level at short wavelengths. Comparison with the free-electron polarizability α_e is depicted. Figure adapted from [3].

potential on the CM coordinate, $\mathbf{R}_0$, is given by

$$U_{ad}(\mathbf{R}_0) = \frac{U_0}{2} + \frac{U_0}{2}\cos(2\mathbf{k}_L \cdot \mathbf{R}_0), \tag{2.56}$$

where U_0 is the lattice depth, a parameter directly proportional to $-\alpha_{n,l,j,m_j}(\omega_L)$, and $U_0 < 0(> 0)$ means the atom will be high(low)-laser-field seeking.

U_{ad} can be thought of as a classical potential or a quantum operator. Typically, when U_0 is very low in magnitude, or the atomic ensemble's de Broglie wavelength is significant, $\mathbf{R}_0$ becomes an operator. This quantum treatment of the CM coordinate is *always* correct no matter the lattice depth or the de Broglie wavelength, but the number of relevant basis states scales as $\sqrt{u_0}$, where $u_0 = U_0/E_{2r}$. The parameter $E_{2r} = 2\hbar^2 k_L^2/M$ is the two-photon
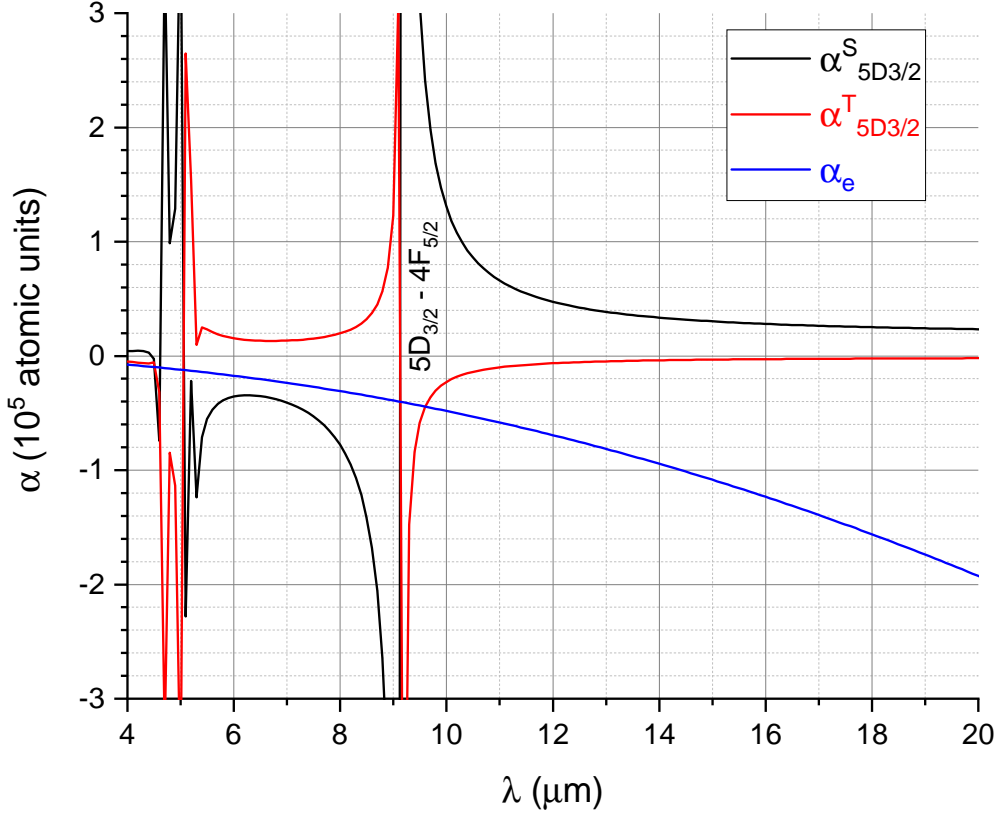
Figure 2.8: Behavior of scalar and tensor polarizability for Rb $5D_{3/2}$ level at wavelengths above 4 μm is shown. Comparison with the free-electron polarizability α_e is depicted, and the convergence to the static scalar and tensor polarizabilities is apparent. Figure adapted from [3].

recoil energy ($E_{2r} = h \times 8.3$ kHz for ^{85}Rb in 1064 nm). Thus, it becomes computationally unfeasible in this regime to calculate the band structure when the classical potential is a good enough approximation to the one where CM is quantized, as the number of eigenstates scales as $\sqrt{U_0/E_{2r}}$.

For the one-dimensional case using the quantum model for a single atom or coherent matter wave, where the lattice-propagation direction is chosen as the quantization axis (Z_0), the Hamiltonian for the CM coordinate Z_0 becomes

$$\hat{H} = \frac{\hat{P}_{0z}^2}{2M} + \frac{U_0}{2}\hat{\mathbb{1}} + \frac{U_0}{2}\cos\left(2k_L\hat{Z}_0\right), \tag{2.57}$$

where $\hat{P}_{0z}$ is the CM momentum operator along the z-axis in SI units and $\hat{\mathbb{1}}$ is an identity operator. It is easier to scale the parameters as

$$\hat{H} = \hat{h} E_{2r} \tag{2.58}$$

$$\hat{P}_{0z} = 2\hbar k_L \hat{p}_{0z} \tag{2.59}$$

$$U_0 = u_0 E_{2r} \tag{2.60}$$

$$\hat{Z}_0 = \hat{\theta}_0 / (2k_L). \tag{2.61}$$

Now the Hamiltonian is scaled down to

$$\hat{h} = \hat{p}_{0z}^2 + (u_0/2)\hat{\mathbb{1}} + (u_0/2)\cos\hat{\theta}_0, \tag{2.62}$$

and the eigenbasis consists of the following Fourier components that have a phase periodicity of π,

$$b_{m,k_0}(\theta_0) = e^{ik_0\theta_0/2} \begin{cases} \sqrt{\pi^{-1}}, & m = 0 \\ \sqrt{2\pi^{-1}} \sin\left[(m+1)\theta_0/2\right], & \text{odd } m \\ \sqrt{2\pi^{-1}} \cos\left[m\theta_0/2\right], & \text{even } m \end{cases} \tag{2.63}$$

where k_0 is the quasimomentum ($-1 < k_0 < 1$ is the first Brillouin zone), and m is the band index. Note that this Hamiltonian parallels that of the electron in a crystalline solid, where the wave function is perturbed by a periodic lattice of positively charged ions.

As an example, Fig. 2.9 shows the eigenvalues (a) and the probability distribution of the CM matter wave (b) for a lattice depth of $u_0 = 20$. The diagonalized band index is denoted by ν, and the eigenfunctions are Bloch waves denoted by

$$\psi_{\nu,k_0}(Z_0) = \sum_{\nu=0}^{\infty} c_m^{(\nu,k_0)} b_{m,k_0}(Z_0). \tag{2.64}$$

For very deep lattices, the CM wave functions resemble simple-harmonic-oscillator (SHO) states, and the energy band gap (known classically as the trap oscillation frequency) is approximated by $\sqrt{u_0}E_{2r}/h$. In Chapter V, I will discuss how transitions can be made from one band index to another for Rydberg atoms in a periodically driven optical lattice.

It is sometimes necessary to write the atom's wave function with respect to a specified well within the periodic potential. At the bottom of well i, located at $Z_{0,i}$, the wave function
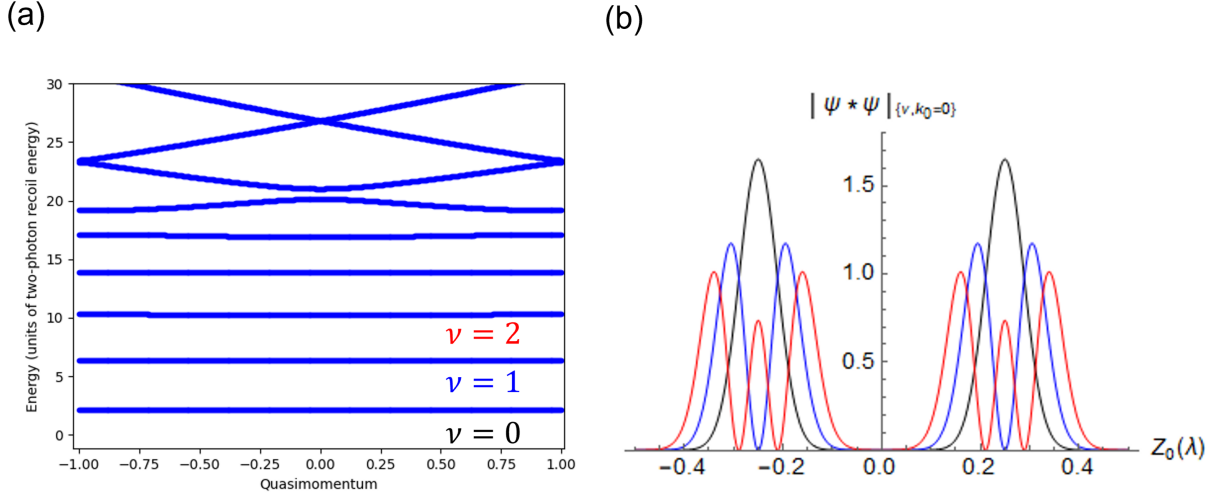
Figure 2.9: Energies (a) and wave functions (b) of first three Bloch bands for $u_0 = 20$.

now is written as a coherent superposition of Bloch functions,

$$\psi_{i,k_0}(Z_0) = \sum_{\nu=0}^{\infty} e^{ik_0 k_L Z_{0,i}} \psi_{\nu,k_0}(Z_0).$$ (2.65)

These functions are known as *Wannier functions* and play a role in experiments where the exact location of the atom within the lattice matters. Note that this is just the Bloch basis with a unitary transformation applied to each eigenstate.

2.4 Photoionization

Eq. 2.53 depends on electric-dipole couplings between the bound atomic states with the FESs of the valence electron. Because the real principal value (p.v.) integral component is taken, only off-resonant couplings are considered. When there is a pole due to a resonant coupling to the FES, the imaginary part of the integral becomes nonzero and an imaginary component of the polarizability arises proportional to the photoionization (PI) cross section σ. In this section, I will derive an expression for the PI cross section of an atomic state in the fine- and hyperfine-structure-free n, l, m_l basis starting from Fermi's golden rule (FGR). I use FGR because the bound atomic state couples to a FES that is part of a continuous distribution of states of similar electric-dipole matrix elements with the bound level.

FGR, in the velocity-gauge, yields a PI rate to the FES $|\epsilon', l', m_l'\rangle$, $\Gamma_{n,l,m_l}^{\epsilon',l',m_l'}(\omega_L)$ given by

$$\Gamma_{n,l,m_l}^{\epsilon',l',m_l'}(\omega_L) = \frac{\pi e^2 \mathcal{E}^2(\mathbf{R}_0)}{2\hbar m_e^2 \omega_L^2} |\langle \epsilon', l', m_l'| e^{i\mathbf{k}_L \cdot \hat{\mathbf{r}}_e}(\hat{\epsilon} \cdot \hat{\mathbf{p}}_e) |n, l, m_l\rangle|^2 \rho(\epsilon'), \tag{2.66}$$

where $\rho(\epsilon')$ is one per unit energy. The energy of the FES is

$$\epsilon' = \frac{2\pi a_0 E_H}{\alpha_{FS}\lambda} + W, \tag{2.67}$$

where, here, α_{FS} is the fine-structure constant, $E_H = 27.2$ eV, λ is the wavelength of the light, and W is the energy of the bound atomic state.

Using the identity $\hat{\mathbf{p}}_e = -i\hbar\vec{\nabla}_e$, where "$e$" means it operates on the valence electron's coordinate $\mathbf{r}_e$ relative to the CM coordinate $\mathbf{R}_0$. Under the E1 approximation, $e^{i\mathbf{k}_L \cdot \hat{\mathbf{r}}_e} \simeq 1$. A generalized expression can now be made for the cross section of PI to $|\epsilon', l', m_l'\rangle$,

$$\sigma_{n,l,m_l}^{\epsilon',l',m_l'}(\omega_L) = \frac{\pi e^2 \hbar^2}{\epsilon_0 m_e^2 \omega_L c} |\langle \epsilon', l', m_l'| \hat{\epsilon} \cdot \vec{\nabla}_e |n, l, m_l\rangle|^2. \tag{2.68}$$

When the laser polarization is $\parallel$ to the quantization axis z_e, only π transitions can be made. The magnetic suborbital quantum number m_l is therefore conserved, and

$$\sigma_{z,n,l,m_l}^{\epsilon',l'} = \frac{3(l_>^2 - m_l^2)}{(2l_> + 1)(2l_> - 1)} \frac{(2l+1)}{l_>} \bar{\sigma}_{n,l}^{\epsilon'l'}, \tag{2.69}$$

where $l_>$ is the larger of l and l'. The polarization-independent cross section is given by,

$$\bar{\sigma}_{n,l}^{\epsilon'l'} = \frac{\pi e^2 \hbar^2}{3\epsilon_0 m_e^2 \omega_L c} \frac{l_>}{(2l+1)} \left| \int_0^\infty u_{\epsilon',l'}(r_e) \left[u_{n,l}'(r_e) \mp \frac{u_{nl}(r_e)}{r_e} l_> \right] dr_e \right|^2, \tag{2.70}$$

where "$-(+)$" is for the case of $l_> = l'(l)$ and $u_{*,l}(r_e) = r_e R_{*,l}(r_e)$. If the polarization is transverse to the atom's quantization axis,

$$\sigma_{x,n,l,m_l}^{\epsilon',l'} = \frac{3(l'(l'+1) + m_l^2)}{2(2l_> + 1)(2l_> - 1)} \frac{(2l+1)}{l_>} \bar{\sigma}_{n,l}^{\epsilon'l'}. \tag{2.71}$$

PI is a useful tool for realizing experiments involving plasmas [111] and cooled and trapped ions [112; 113]. Additionally, it is a mechanism at which astrophysical clouds of charged particles arise [114; 115]. Measurements of PI cross sections traditionally require quantifying the population loss from an atomic ensemble as a function of the light exposure time [116; 117]. These experiments are extremely difficult to conduct, as they require proper

calibration of the total atom number and the laser intensity within the interaction region which often includes many loss factors that cannot be quantified. You certainly cannot stick a beam profiler inside the vacuum chamber at the exact location of the atomic sample! In the next chapter, I will outline an experiment I performed where the PI cross section of the ^{85}Rb $5D_{3/2}$ optical-clock state was obtained at $\lambda = 1064$ nm using the centers and broadening of spectroscopic lines.

Measurement of the Rb $5D_{3/2}$ Polarizability and Photoionization Cross Section in a Deep, 1064-nm Optical Lattice

This chapter is based on Ref. [3].

3.1 Introduction: Measuring 5D Polarizabilities

Understanding how the Rb $5D_j$ levels respond to light is essential for the progress in making a portable optical clock that rivals the current commercially available time standards based on M1 transitions at microwave frequencies. Two counter-propagating optical fields at 778 nm can drive the dipole-forbidden $5S_{1/2} \rightarrow 5D_j$ transitions in the second order. Because the beams are counter-propagating, first-order Doppler shifts can be eliminated if the probed sample is at room temperature. However, as it was demonstrated in [25] for $j = 5/2$, thermal atoms are susceptible to second-order Doppler shifts that hamper the proposed clock accuracy on the order of $\sim 10^{-13}/\sqrt{\tau}$ (τ is the averaging time of the spectral line). Furthermore, the 778 nm interrogation lasers induce AC Stark shifts on the levels that can inhomogeneously broaden obtained spectral lines. Additional optical fields that would tightly confine the probed atoms through the dipole force and cancel the 778-nm AC Stark shift [28] with the appropriate detunings from an atomic resonance could eliminate these two aforementioned uncertainties.

Miniaturized vapor cells engineered for laser cooling are becoming more available [41; 42] for both commercial and academic purposes, making the prospect of the portable clocks developed in [25; 28; 38; 39] with integrated optical dipole traps not too ambitious. The real question that lingers is what trapping wavelength to choose. This is where the the importance of accurately and precisely measured AC polarizabilities for the Rb $5D_j$ states comes into play. In order for a miniaturized optical lattice clock to work properly, a wavelength has

to be chosen such that it provides a polarizability that can cancel out AC Stark shifts at 778 nm, provide tight confinement of the probed atoms, and allow the sample to withstand photoionization long enough to take sufficient measurements. As can be seen in Fig. 2.7, there is a range of estimated (these are not precise calculations) polarizabilities for the $5D$ states both above and below the photoionization (PI) threshold. However, polarizabilities at only a handful of wavelengths have been verified experimentally.

In this experiment, we investigate shifts and lifetimes of the Rb $5D_{3/2}$ state in an ultra-deep ($\sim 10^5 E_r$), 1064-nm optical lattice through resonant absorption spectroscopy of two probing lasers at 795 nm and 762 nm. We choose this lattice wavelength because of its widespread commercial availability and is the high-powered laser we had on hand. Additionally, polarizabilities at other states of Rb, $\alpha_{5S_{1/2}} = 687.3(5)$ [118] and $\alpha_{5P_{1/2}} = -1226(18)$ [108] (in atomic units, i.e., units of $4\pi\epsilon_0 a_0^3$) are known theoretically to a very good uncertainty by way of rigorous Hartree-Fock calculations.

In order to arrive at a measurement of $\alpha_{5D_{3/2}}$ at $\lambda = 1064$ nm, we use the $5P_{1/2} \to 5D_{3/2}$ transition shifts from the optical lattice (field strength of $\mathcal{E}$) measured by a probing 762-nm laser beam,

$$\Delta_{762}^{F'} = -\frac{1}{4}(\alpha_{5D_{3/2}}^S - \alpha_{5P_{1/2}})\mathcal{E}(\mathbf{R}_0)^2, \tag{3.1}$$

where F' denotes the hyperfine state of $5P_{1/2}$. The measurement we make here is purely the scalar polarizability, as we estimate the tensor polarizability to induce splittings of $|m_j|$ that are not observable under the PI broadening of the $5D_{3/2}$ level. While we know $\alpha_{5P_{1/2}}$ to a relative uncertainty of 0.015, $\mathcal{E}(\mathbf{R}_0)^2$ requires knowledge of the atoms' exact location within the lattice field, which is impossible to know directly. In atomic spectroscopy, when there are two unknown measurements, there must be two transitions probed. Thus, we must get $\mathcal{E}(\mathbf{R}_0)^2$ from another shifted transition, the ^{85}Rb D_1 line in this case. And so,

$$\Delta_{795}^{F'} = -\frac{1}{4}(\alpha_{5P_{1/2}} - \alpha_{5S_{1/2}})\mathcal{E}(\mathbf{R}_0)^2. \tag{3.2}$$

Now we take take the ratio of Eq. 3.1 to Eq. 3.2 and arrive at

$$\alpha_{5D_{3/2}}^S = \alpha_{5P_{1/2}} + \frac{d\Delta_{762}^{F'}}{d\Delta_{795}^{F'}}(\alpha_{5P_{1/2}} - \alpha_{5S_{1/2}}). \tag{3.3}$$

Our sample of ^{85}Rb is continuously optically pumped into the $F = 3$ hyperfine ground state with the repumping laser. Thus, there are two excitation pathways to the $5D_{3/2}$ hyperfine states F'' depending on what intermediate state F' is excited. Because of PI, the F'' spectral lines are only resolvable when the optical lattice is at shallow depths, so our measured $\Delta_{762}^{F'}$ is insensitive to F''. Therefore, in this experiment, two polarizability
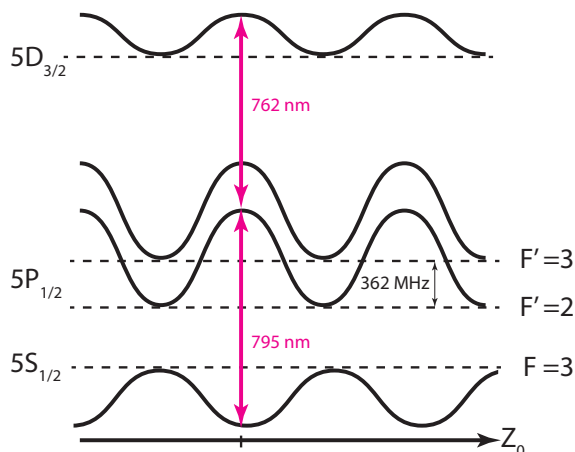
Figure 3.1: Energy levels, transitions, and lattice shifts as a function of CM position Z_0 along propagation axis used for the experiment described in this chapter (not to scale). The $5D_{3/2}$ hyperfine structure is ignored. Dashed lines indicate lattice-free energy levels. The tick mark on the Z_0-axis corresponds to $Z_0 = 0$.

measurements are made, one for each pathway through F'. The final value of $\alpha^S_{5D_{3/2}}$ is a weighted average of both measurements. The field-free and lattice-perturbed energy levels used in this measurement are shown in Fig. 3.1.

3.2 Chamber and In-Vacuum Cavity

Fig. 3.2 shows the experimental setup for laser spectroscopy of ultracold Rb in a deep, 1064-nm optical lattice. The hallmarks of the apparatus used for this experiment are a near concentric in-vacuum cavity with a finesse of 600 at 1064 nm and two detectors: a Si avalanche photodiode and a Rb^+-collecting microchannel plate detector (MCP) which can independently measure populations in $5P_{1/2}$ and $5D_{3/2}$, respectively. Enhancement of the 1064-nm laser field is made possible with the cavity such that lattices with $10^6 E_r$ depths for Rb $5S_{1/2}$ atoms can be achieved. Cavity parameters, as well as specs of the vacuum chamber and ion detection system with the MCP can be found in [43; 119; 120].

In the geometric center of the cavity ($x = 0, y = 0, z = 0$), a MOT of ^{85}Rb or ^{87}Rb atoms can be prepared from three orthogonal arms of retroreflected D_2 cooling lasers and a repumping beam. Because the frequency control of our probing lasers for spectroscopy is designed to access ^{85}Rb transitions, we prepare a MOT of ^{85}Rb in this experiment.

Before the 1064-nm lattice laser is injected into the cavity, it is passed through an acousto-optic modulator (AOM) twice so that the power and frequency of the light sent into the experiment can be controlled via the amplitude (AM) and frequency (FM) modulation of
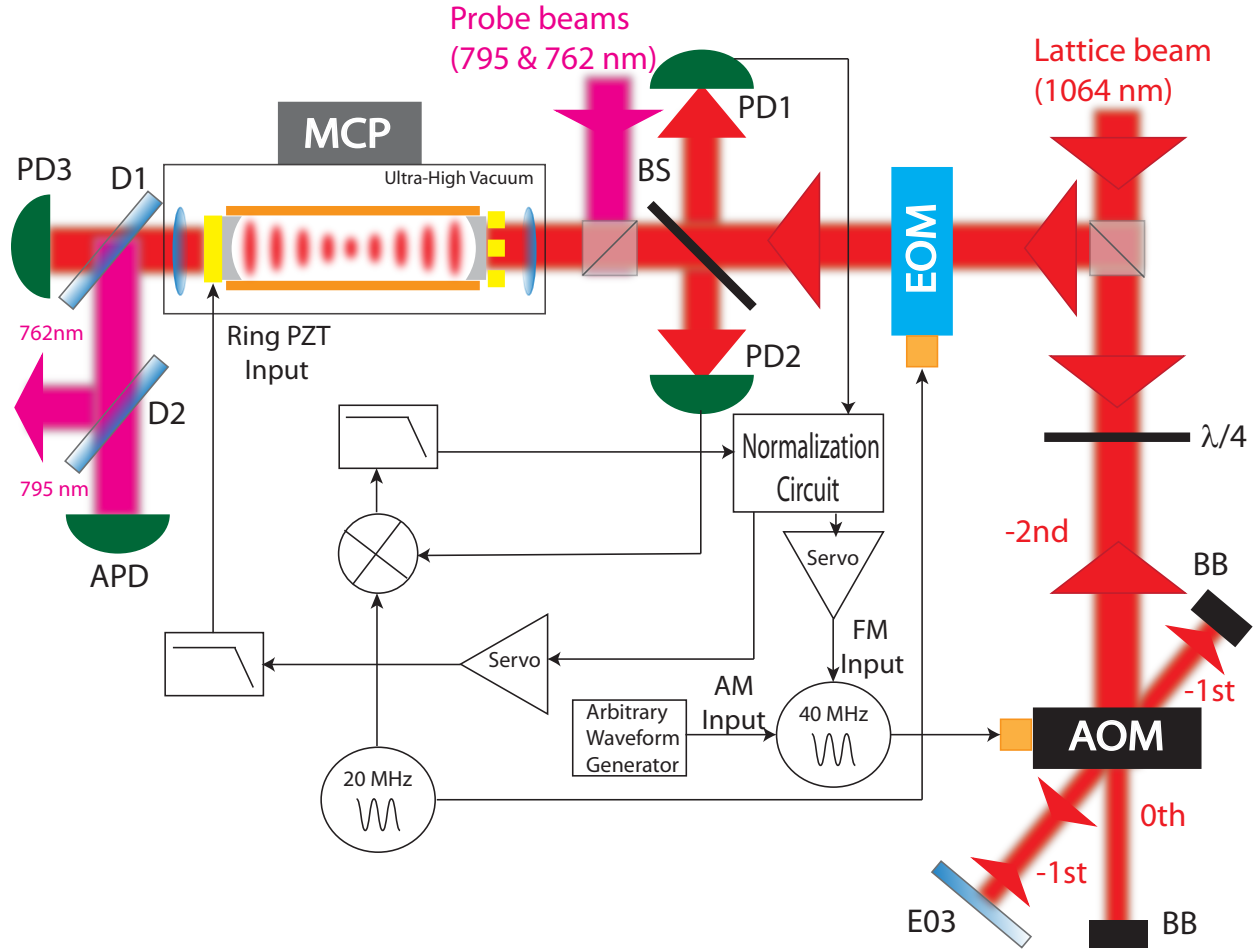
Figure 3.2: Apparatus for the experiment described in this chapter (not drawn to scale). The following acronyms are used: "$\lambda/4$" quarter wave plate, "BB" beam blocker, "AOM" acousto-optic modulator, "EOM" electro-optic modulator, "D1" and "D2" dichroic elements, "BS" beam sampler,"MCP" micro-channel plate detector, "PD1","PD2", and "PD3" germanium photodiodes, "E03" infrared mirror, "APD" avalanche photodiode. Inside the ultra-high vacuum, lenses are placed around the cavity mirrors to enhance input coupling and output collimation. The gold blocks represent the ring and three chip piezos used for control of the cavity length. The orange rods are two of the six total electrodes used for propelling and steering Rb^+ to the MCP, four are not shown. MOT laser beams that cool and trap ^{87}Rb or ^{85}Rb in the center of the cavity are also not shown. Figure adapted from [3].

the 40 MHz AOM driving signal, respectively. The 1064-nm light is then phase modulated with a ~ 20 MHz drive by means of a free-space electro-optic modulator (EOM). A germanium photodiode "PD1" samples the AM-modulated laser light and sends the detected pulse
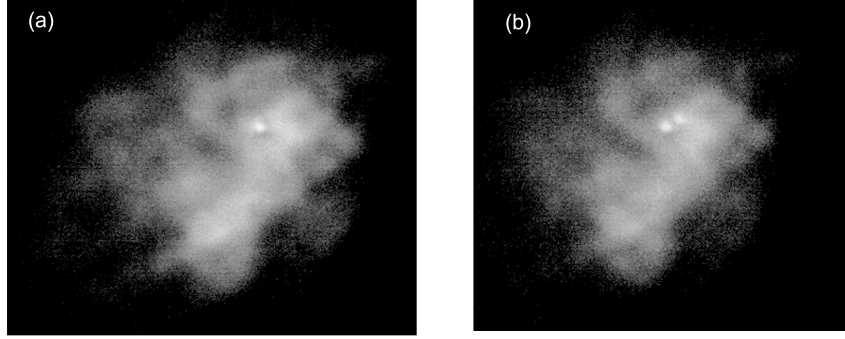
Figure 3.3: Fluorescence images of the MOT in the (x, y)-plane with the cavity tuned to the (a) TEM_{00} mode and (b) TEM_{10} mode.

envelope to the C port of a normalization circuit. A second germanium photodiode "PD2" sends the error signal [121], demodulated by the EOM driver, to the A port. The normalization circuit performs the following operation on voltages C, A, and a fixed parameter B: $V_{out} = AB/C$. Thus, the output error signal that is split off to two servo-amplifiers does not follow the amplitude modulation of the 1064-nm laser. A homebuilt PID circuit is used as the servo for the fast control of the cavity-mode stabilization. Because the laser features no transducer for tuning its frequency to compensate fast jitters hampering the stability of the cavity mode, feedback is provided by FM-modulating the AOM driver. A locking bandwidth of $\sim$ 10 kHz is achieved, which is enough to suppress the fast drifts of the cavity-mode. Low-frequency noise and mechanical vibrations on the laser table that destabilize the circulating 1064-nm mode in the chamber are suppressed by a Toptica PID110 piezo lockbox that controls the ring piezo-electric transducer (PZT) mounted on the output cavity mirror. Three chip piezos are used for applying a constant offset to the length of the cavity.

Once the cavity mode is stabilized, the atoms can be cooled and collected in the optical lattice. During this time, we leave the lattice on simultaneously with the MOT beams. We can choose different transverse electromagnetic modes of the 1064-nm light resonant with cavity. This means the Gaussian profile of the TEM_{00} cavity-mode can be imprinted in the ultracold Rb cloud through transverse compression of the atoms by the dipole force. In Fig. 3.3(a), atoms shaped into the TEM_{00}-mode is shown in a fluorescence image of the MOT in a plane (x, y) transverse to the cavity axis (z). Fig. 3.3(b) shows the case for the TEM_{10} mode. For the experiment described in this chapter, we tune the cavity to be resonant with the TEM_{00} mode.

During the cooling and trapping phase of the experimental cycle, which lasts about 10 ms, the total intensity of the 1064-nm light circulating within the cavity is about 7 GW/m^2 providing a trap depth of about 1 mK for atoms in $\left|5S_{1/2}, F = 3\right\rangle$. These ground state
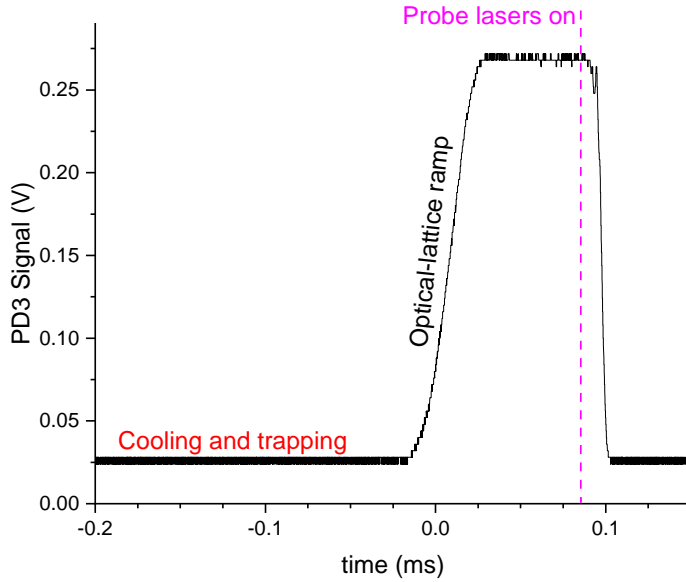
Figure 3.4: Pulse envelope of the 1064-nm laser in one experimental cycle.

atoms will seek regions of high laser intensity due to the large red detuning of the $1064-$nm field from any resonance. In a classical picture, atoms inside these potential wells will roll down and up hills of the same "height," or, more properly, "potential," like a very boring roller coaster. Because there is no light scattering from the FOR optical lattice, one would think they could perpetually continue on this ride. However, there is a strong, viscous force from the 780-nm MOT beams that are now further detuned thanks to the AC Stark shifting by the lattice light. This viscous force is analogous to the kinetic friction between the coaster track and wheels of the train causing the atoms to eventually be too slow to climb up another hill. The overall effect of these separate optical forces is an atom temperature slightly below the Doppler-limit.

Once we have cooled down the atoms to ~ 100 μK in the lattice, the $1064-$nm light within the cavity is smoothly ramped upwards to ~ 70 GW/m^2 via amplitude modulation of the AOM driving signal. At this level, the lattice is now *ultra-deep*, and laser spectroscopy with the probe beams can be performed. The pulse envelope of the lattice intensity in one experimental cycle is detected by PD3 (see Fig. 3.2) and displayed in Fig. 3.4.

3.3 Probe Lasers

As it was explained in the introduction, in order to make a measurement of the scalar polarizability of the Rb $5D_{3/2}$ level in an ultra-deep optical lattice at 1064 nm, we must mea-

sure two frequency shifts: that of the D_1 line and that of the $\left|5P_{1/2}\right\rangle \to \left|5D_{3/2}\right\rangle$ transition. Thus, we require the simultaneous application 795- and 762-nm probe lasers that may be continuously tuned at the order of $\sim$GHz.

A major systematic uncertainty that must be eliminated in the measurement of the $5D_{3/2}$ polarizability at 1064 nm is the linearity of the probe laser frequency scan. In a previous version of this experiment [120], we applied a stack-like voltage sweep to the piezos affixed to the intra-cavity filters of the probe lasers. The following frequency response to the input voltage was highly nonlinear, resulting in an unreliable measurement with a relative uncertainty greater than 0.05. For the measurement described in this chapter, we rectified this problem by using the spectroscopic technique of phase-locked loops (PLLs).

In a PLL, the phase of the probe laser (known as the *slave*) is locked to that of another tunable laser (known as the *master*) which is frequency stabilized to a reliable reference. This reference may be a an ultra-low expansion (ULE) cavity, a frequency comb laser, or an atomic/molecular transition. For this experiment, we choose the lattice-free ^{87}Rb D_1 line ($\left|F=2\right\rangle \to \left|F'=1\right\rangle$) as our reference for the 795-nm PLL and the ^{87}Rb $\left|5P_{1/2}, F'=1\right\rangle \to \left|5D_{3/2}, F''=2\right\rangle$ transition for the 762-nm PLL. When the slave laser's phase is in an unlocked state, its frequency difference between that of the master forms a beat signal that can be mixed and with another RF signal derived from a synthesizer. After filtering, a sharp, step-like error signal is generated with an inflection point at the frequency difference that matches the RF frequency. A high-bandwidth ~ 10 MHz servo amplifier uses this error signal to control the current of the slave laser. Thus, when the slave laser is phase-locked, we can scan the its offset from the master frequency with perfect linearity by changing the frequency of the RF synthesizer (which has a reliable and stable absolute frequency at the order of $\sim$kHz).

Fig. 3.5 depicts the optical layout for the probe lasers used in this experiment and the masters to which they are phase locked. The currents and PZTs of the master lasers (MOGlabs CEL) are resonantly stabilized to the ^{87}Rb $\left|5S_{1/2}, F=2\right\rangle \to \left|5P_{1/2}, F'=1\right\rangle$ and $\left|5P_{1/2}, F'=1\right\rangle \to \left|5D_{3/2}, F''=2\right\rangle$ transitions by means of saturated-absorption and electromagnetically-induced-transparency (EIT) spectroscopy, respectively. We use solenoids wrapped around the atomic vapor cells in order to Zeeman modulate the hyperfine transitions at 250 kHz. This modulation is performed in order to generate error signals for peak-locking the master lasers. Signal generators at 250 kHz along with the phase detectors and servo amplifiers for current and PZT control are all commercially provided in the drivers for MOGlabs CELs. Once we have the master light frequency stabilized down to linewidths of $\sim$100 kHz, we can combine them with the probe (slave) laser beams and detect the beat frequencies using high-bandwidth, "fast" photodiodes (FPD). We pick off some light from our probe lasers
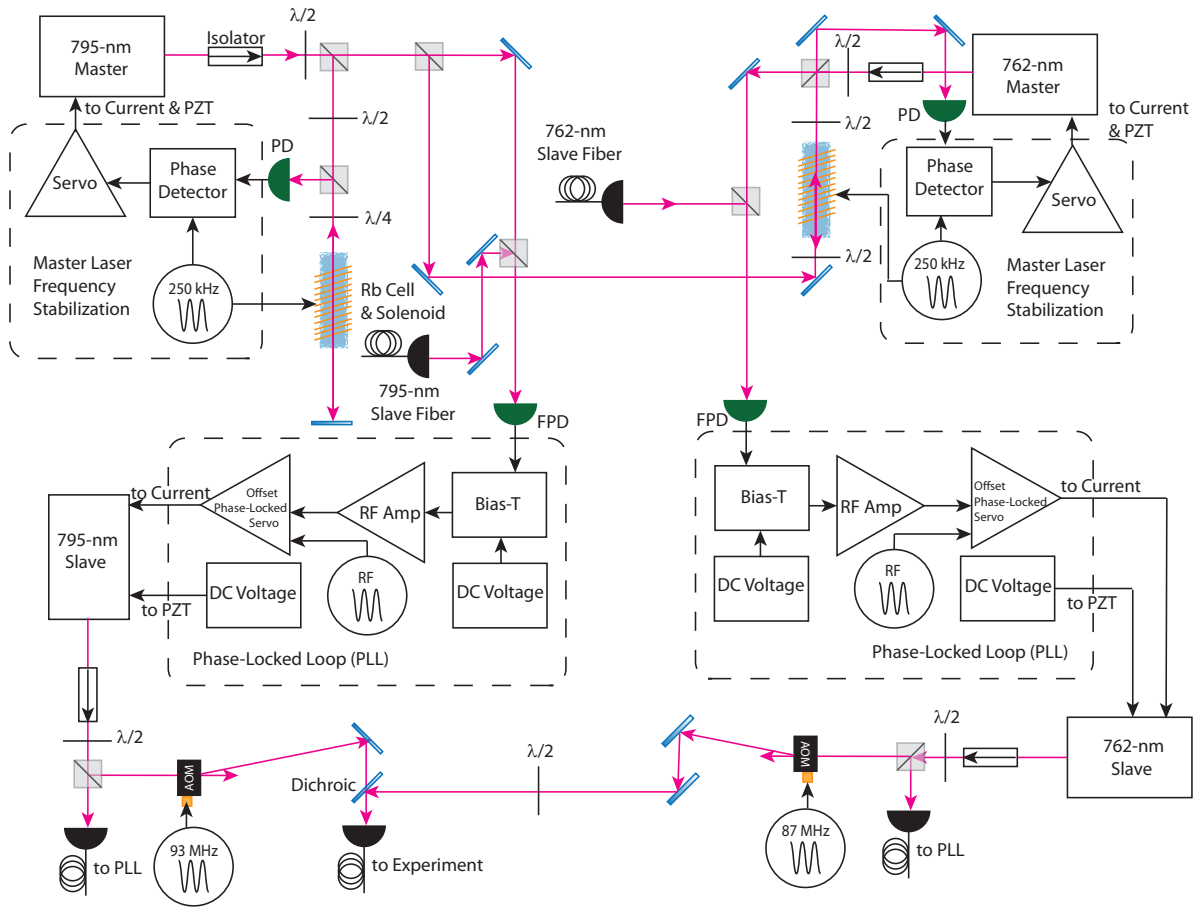
Figure 3.5: Optical layout for frequency and pulse control of the probe lasers (denoted here as "slave" lasers) used in the experiment. Here "FPD" stands for "fast photodiode." Figure adapted from [3].

(AOSense-IF-ECDL-*) and fiber-couple it to be combined with the master laser beams. As the beatnotes from both PLLs are detected and amplified, they are sent to Vescent D2-135 offset phase-locked servo (OPLS) amplifiers which serve both as RF phase detectors and high-bandwidth PID circuits that control the probe lasers' currents. A polarity switch on the OPLS determines whether the RF providing the frequency offset to the probe laser is added to or subtracted from the master laser frequency. For the 795-nm probe laser, we add the RF frequency to that of the master. For the 762-nm probe, we subtract it. When the probe lasers are phase-locked to the master lasers at a given RF offset frequency, they do not deviate from this frequency difference by more than 1 Hz, evidenced by the beatnote between the two 795-nm lasers shown in Fig. 3.6. Consequently, we can scan our probe lasers at frequency resolutions better than ∼100 kHz.
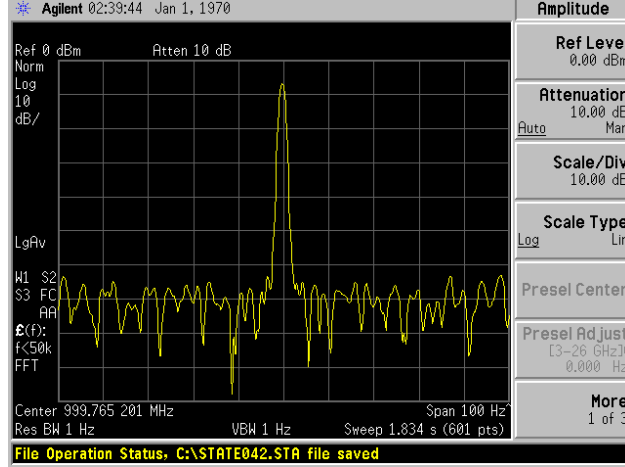
Figure 3.6: Beat signal (logarithmic) of 795-nm master and probe lasers phase-locked in the frequency domain. The linewidth is below the resolution bandwidth (1 Hz) of the spectrum analyzer used here.

In addition to having the ability to linearly scan the frequencies of our probe lasers with resolutions below ~ 1 MHz, we can also pulse them down to 500-ns durations. This is done through amplitude modulation of the RF signals controlling the AOMs that the probe beams are sent through. The pulsed probe beams are combined with the same linear polarization on a dichroic mirror and fiber-coupled to the experiment in order to be coaligned with the 1064-nm laser that is sent to the in-vacuum cavity.

3.4 Absorption Spectroscopy of the ^{85}Rb D_1 Line in the MOT

In this section, we observe only the absorption of the 795-nm probe beam by the ^{85}Rb MOT with the lattice light on and off as a diagnostic for the frequency control of this laser. We use the APD for this measurement of absorption. For this test, the probe laser intensity at the position of the atoms is set such that there is no power broadening and that the absorption line resembles a Lorentzian with a linewidth limited by the lifetime τ of the $5P_{1/2}$ state, $1/\tau = 2\pi \times 6$ MHz when the lattice light is off.

In Fig. 3.7, we demonstrate absorption of the 795-nm probe laser by the ultracold ^{85}Rb with the lattice-light turned off during the interrogation time. The frequency axis depicts the frequency difference between the probe and master laser, which is locked to the ^{87}Rb $|F = 2\rangle \to |F' = 1\rangle$ D_1 transition. We define the offset frequency of 1.446 GHz as ν_1, which corresponds to the $\left|5S_{1/2}, F = 3\right\rangle \to \left|5P_{1/2}, F' = 2\right\rangle$ transition and note that the $F' = 3$ line is 362 MHz away, as expected. The change in transmitted power as a function offset frequency is due to the probe laser's response in power as a function of changing current.
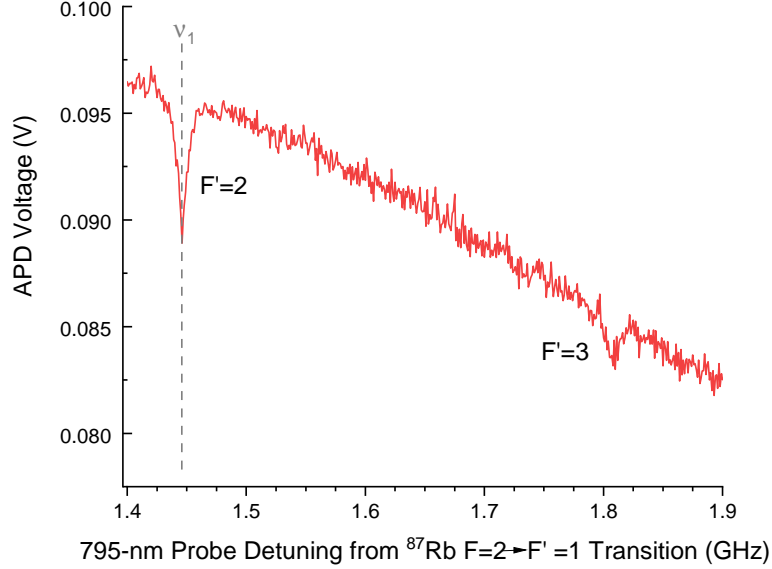
Figure 3.7: Avalanche photodiode (APD) detection of 795-nm laser through the MOT with the 1064-nm optical lattice switched off during the probe pulse. Both hyperfine F' absorption peaks are shown for the $5P_{1/2}$ state.

This feed-forward effect makes a negligible difference in determining the $F = 3 \rightarrow F' = 2$ line center.

In Fig. 3.8(a), we zoom in on the $F' = 2$ hyperfine peak free of the optical lattice field. For Figs. 3.8(b)-(d), we turn on the lattice at three different intra-cavity, standing-wave intensities of 1064-nm lattice field, I_{1064}^{SW}. Ground state atoms trapped near the global potential minimum of the lattice are localized near the maximum intensity of the optical field at $(X_0 = 0, Y_0 = 0, Z_0 = 0)$, where the $\left|5S_{1/2}, F = 3\right\rangle \rightarrow \left|5P_{1/2}, F' = 2\right\rangle$ transition receives the greatest AC Stark shift. These atoms are responsible for the inflection-point-like spectral features in Figs. 3.8(b)-(d), marked by the gray dashed lines. The reason that the blue-shifted spectral feature has this sharp drop-off near the bottom of the deepest lattice well is because, during a frequency scan, the probe laser goes out of resonance right after it accesses the D_1 transition for the most tightly confined atoms. AC Stark shifts of this transition $\Delta_{795}^{F'=2}$ are denoted for these atoms in Figs. 3.8(b)-(d).

Now that we have demonstrated control of the 795-nm probe laser frequency, we can conduct spectroscopy of the $\left|5P_{1/2}\right\rangle \rightarrow \left|5D_{3/2}\right\rangle$ transition by counting the ions resulting from the decay of atoms in the $5D_{3/2}$ state. This spectroscopic measurement requires the application of the 762-nm probe laser.
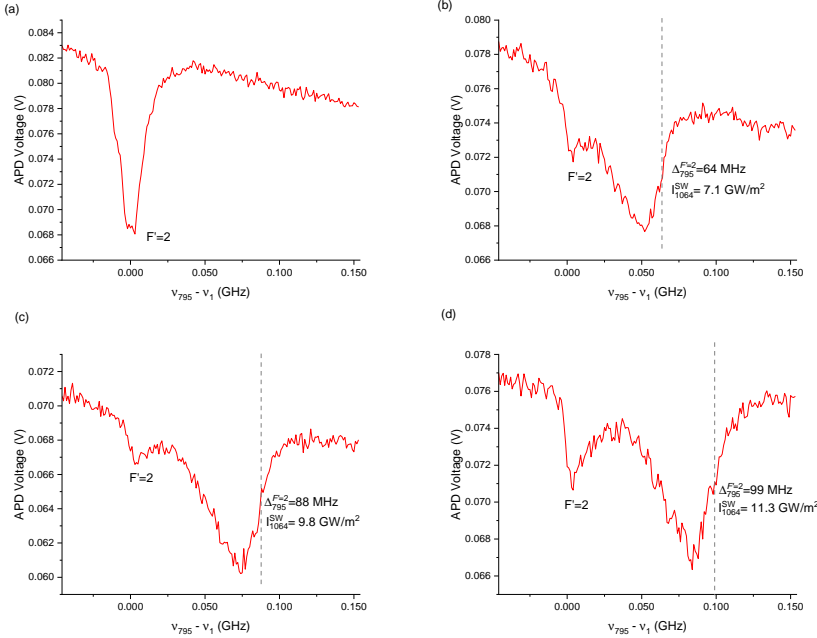
Figure 3.8: Spectroscopy of AC Stark shifts on the D_1 transition ($F = 3 \rightarrow F' = 2$) by the optical lattice for various depths. The dashed lines correspond to the shifts Δ^2_{795} on the atoms experiencing the deepest trapping potential within the intensity gradient of the lattice. For each case, we also give the maximum standing wave intensity I^{SW}_{1064} provided by the lattice.

3.5 Penning-Ionization Spectroscopy of ^{85}Rb $5P_{1/2} \rightarrow 5D_{3/2}$ Transition

Before observing the AC Stark shifts on the $\left|5P_{1/2}\right\rangle \rightarrow \left|5D_{3/2}\right\rangle$ transition, we wish to observe the 762-nm, probe-laser frequency offsets from the 762-nm master that correspond to the lattice-free hyperfine lines. In order to measure the population in $\left|5D_{3/2}\right\rangle$, we must collect ions that form upon excitation into this state. While the optical lattice strongly photoionizes atoms in $\left|5D_{3/2}\right\rangle$, it also shifts the transition frequency, which is something we do not want in this diagnostic of the 762-nm probe frequency control. Another form of achieving ^{85}Rb$^+$, decayed from an excitation into $\left|5D_{3/2}\right\rangle$, is a density-dependent interaction known as Penning ionization.

In Penning ionization, an atom in excited state $|A\rangle$ collides with another atom with internal state $|B\rangle$. If the ionization energy of the atom in $|B\rangle$ is less than the transition energy between state $|A\rangle$ and the ground state, the atom in state $|B\rangle$ is ionized (FES $|\epsilon\rangle$)and the atom in $|A\rangle$ is transferred to the ground state $|G\rangle$. For our case, $|A\rangle = \left|5P_{1/2}\right\rangle$

and $|B\rangle = \left|5D_{3/2}\right\rangle$. Thus, the following interaction takes place [122; 123; 124]

$$^{85}\text{Rb}(5D_{3/2}) +^{85} \text{Rb}(5P_{1/2}) \rightarrow^{85} \text{Rb}^+ + e^- +^{85} \text{Rb}(5S_{1/2}). \tag{3.4}$$
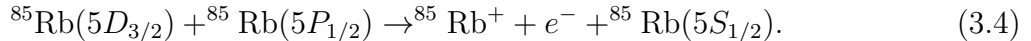
The rate of Penning ionization for atoms in state $\left|5D_{3/2}\right\rangle$ is given through Fermi's golden rule in the context of a direct dipole-dipole interaction coupling $\left|5P_{1/2}\right\rangle$ to $\left|5S_{1/2}\right\rangle$ and $\left|5D_{3/2}\right\rangle$ to $\left|\epsilon'\right\rangle$ or an electron exchange between the two colliding atoms. The rate is numerically calculated and found experimentally to be

$$\Gamma_{Penning} = 3.5 \times 10^{-14}\text{s}^{-1}\text{m}^3/R^3, \tag{3.5}$$

where R is the average atomic spacing for all three spatial dimensions [122; 123; 124]. It is evident that a larger atomic density yields better state readout. Therefore, we must enhance the density of the MOT through compression by the optical lattice during the cooling and trapping portion of the experimental cycle. Lattice depths during this stage are kept around 1 mK. We then pulse the lattice completely off when the 795-nm and 762-nm probe beams are sent through the compressed cloud.

Fig. 3.9, we simultaneously shine the 795-nm and 762-nm probe light on the cigar-shaped cloud compressed by the lattice. The 795-nm light is detuned -36 MHz from the $\left|5S_{1/2}, F = 3\right\rangle \rightarrow \left|5P_{1/2}, F' = 2\right\rangle$ transition, while the 762-nm laser is scanned, in steps of 500 kHz, from -300.0 MHz to -429.5 MHz with respect to the ^{87}Rb $\left|5P_{1/2}, F' = 1\right\rangle \rightarrow \left|5D_{3/2}, F'' = 2\right\rangle$ transition. Penning ions are collected with on the MCP and counted with an SR400 Photon Counter. The detuning where the ^{85}Rb $\left|5P_{1/2}, F' = 2\right\rangle \rightarrow \left|5D_{3/2}, F'' = 3\right\rangle$ transition occurs, with the lower transition laser on resonance, is -357.0 MHz. From this point onward in this chapter, we denote this frequency as ν_2.

The linewidths appear to be on the order of 2-3 MHz, a few factors larger than the natural linewidth of the $5D_{3/2}$ level. We attribute the broadening to excess optical power from the probe lasers and the background magnetic field of the MOT. However, this broadening is negligible for measurements of the AC scalar polarizability and PI cross section in a 1064-nm optical lattice because the PI will broaden the lines to hundreds of MHz.

3.6 Rb $5D_{3/2}$ Polarizability Measurement at $\lambda = 1064$ nm

Demonstrable frequency control of both probe lasers and the lattice-free reference frequencies ν_1 and ν_2 have been established. In order to perform two-step resonance spectroscopy on the atoms trapped in the optical lattice, we simultaneously scan both probe lasers while reading out the number of $5D_{3/2}$ photoions collected by the MCP. The 795-nm probe laser
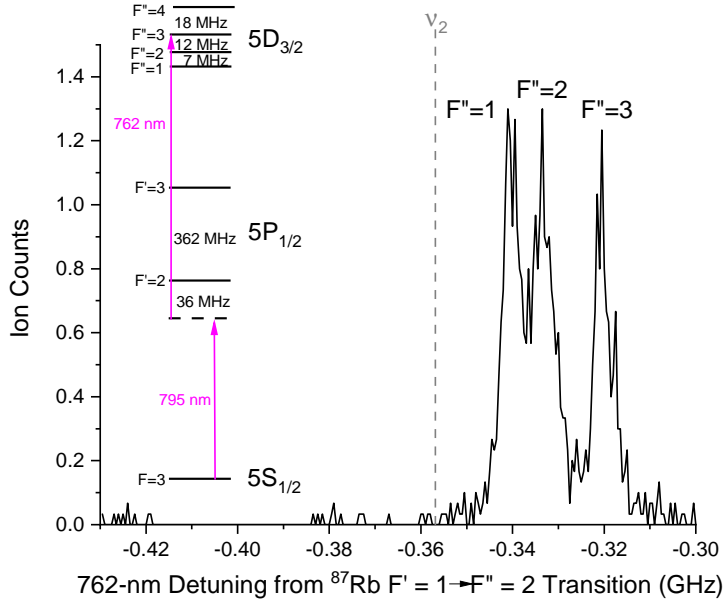
Figure 3.9: Penning-ionization spectroscopy of the ^{85}Rb $|5P_{1/2}, F' = 2 > \rightarrow |5D_{3/2}, F'' >$ transition. The lower-transition laser is -36 MHz detuned from the $|F = 3 > \rightarrow |F' = 2 >$ transition (ν_1). The dashed gray line corresponds to ν_2, the $|5P_{1/2} >, F' = 2 > \rightarrow |5D_{3/2}, F'' = 3 >$ transition when the 795-nm probe frequency is equal to ν_1.

is scanned, in steps of 30 MHz, from -0.036 GHz to 1.344 GHz with respect to ν_1. At each frequency setting ν_{795}, the 762-nm probe laser is scanned from 0.057 GHz to -0.843 GHz with respect to ν_2 in steps of 4 MHz. For every scan, ion counts are averaged over 30 experimental cycles.

Two spectroscopic cone-shaped signal regions on the (ν_1, ν_2)-planes are obtained from the aforementioned scans, each corresponding to an excitation pathway to the $5D_{3/2}$ state through the F' hyperfine sublevel of $5P_{1/2}$. The reason they are cone shaped is that the PI rate, proportional to the intensity of the lattice field at the position of the atoms, becomes the dominant broadening mechanism in the spectroscopic lines. Hence, at larger blue detunings from ν_1, we probe atoms in deeper lattice potentials, the $|5P_{1/2}\rangle \rightarrow |5D_{3/2}\rangle$ spectral line red shifts, and a Lorentzian lineshape is observed with a width mainly dominated by PI broadening, much fatter than those corresponding to the atoms probed in regions of low lattice intensity. These spectroscopic features are exhibited in Fig. 3.10(a). Fig. 3.10(b) shows the analogous numerical simulation. This figure is taken from [3].

A drop in signal strength is noticeable in the middle of the cones, as seen in Fig. 3.10(a). This behavior is a most likely an effect of weak Frank-Condon overlap between CM wave
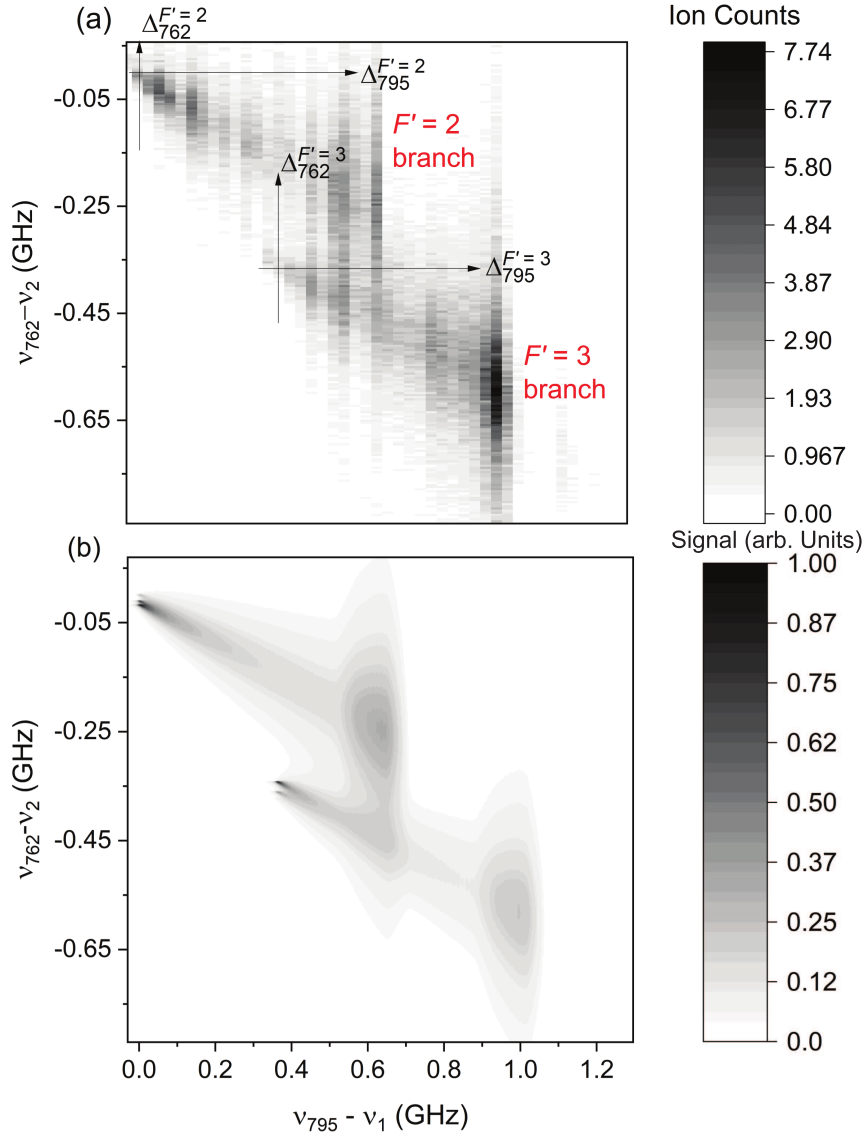
Figure 3.10: In (a), we exhibit the experimental two-step resonance spectroscopy performed by counting photoions generated upon population of $|5D_{3/2}\rangle$. The slopes of each F' cone are used to arrive at a dynamic scalar polarizability measurement for $|5D_{3/2}\rangle$ at $\lambda = 1064$ nm. In (b), we numerically simulate our data using the parameters $\alpha^S_{5D_{3/2}} = -524, \alpha^T_{5D_{3/2}} = 0$, and PI cross section $\sigma = 40$ Mb.

functions of weakly-bound Bloch bands. A semiclassical explanation, where the CM motion is treated classically, has yet to be investigated, but could be modelled with the following numerical methods involving the rapid switching of internal states and their lattice potentials in future endeavours [125; 126].

Lorentzian line centers and widths of the 762-nm probe scans are obtained as fitting
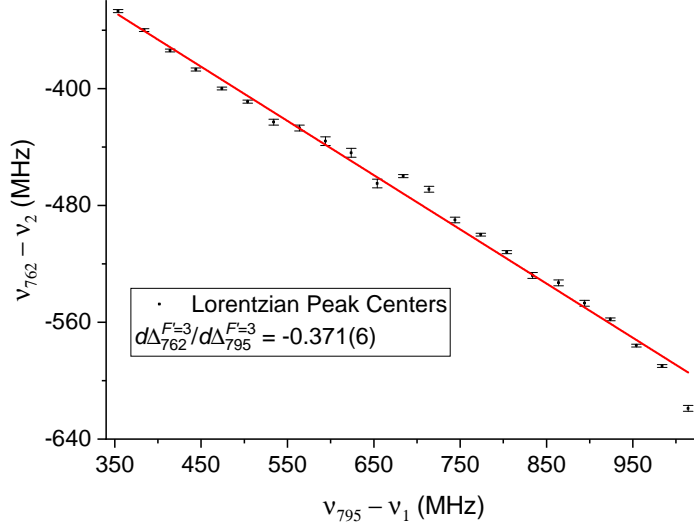
Figure 3.11: Figure taken from [3]. Here we show the linear trend of each Lorentzian line centers for each 762-nm probe spectrum belonging to the $F' = 3$ excitation branch as the lower-transition probe detuning from the lattice free resonance is varied. The slope of this trend is a parameter used to get an AC polarizability measurement of the $5D_{3/2}$ state at $\lambda = 1064$ nm. Vertical error bars correspond to the statistical uncertainties in the fitted line centers.

parameters to data for each 795-nm probe detuning from ν_1. This fitting procedure is performed for each F' cone. Because there is a negligible uncertainty in the systematic effect of laser frequency linearity, the reported uncertainties in our line centers are purely statistical. Fig. 3.11 exhibits the linear trend in fitted line centers $\Delta_{762}^{F'=3}$ as the 795-nm probe laser is tuned, i.e., $\Delta_{795}^{F'=3}$ is changed. A linear fit yields the slope $d\Delta_{762}^{F'=3}/d\Delta_{795}^{F'=3} = -0.371(6)$. Once this slope is included in Eq. 3.3 along with the existing theoretical polarizability estimates at 1064 nm for $5S_{1/2}$ ($\alpha_{5S_{1/2}} = 687.3(5)$) and $5P_{1/2}$ ($\alpha_{5P_{1/2}} = -1226(18)$), we arrive at a $5D_{3/2}$ scalar polarizability of -516(22) for the $F' = 3$ cone. The uncertainty in this value is propagated from the statistical uncertainty in $d\Delta_{762}^{F'=3}/d\Delta_{795}^{F'=3} = -0.371(6)$ and the theoretical uncertainties in $\alpha_{5S_{1/2}}$ and $\alpha_{5P_{1/2}}$. Similarly, we obtain $\alpha_{5D_{3/2}}^{S} = -537(27)$ for $F' = 2$. A weighted average and uncertainty is taken between the two measurements. Our final measurement of the $5D_{3/2}$ scalar polarizability at $\lambda = 1064$ nm is $-524(17)$.

We have made numerical estimates of both the scalar and tensor polarizabilities for $5D_{3/2}$ at $\lambda = 1064$ nm from existing calculations of Rb valence electron energies [127], using matrix elements derived from [128; 129], and from matrix elements and valence electron energies provided by additional sources [130; 131] when transitions to higher $(n \geq 9)P_j$ and $(n \geq 8)F_j$ Rydberg states needed to be taken into account. Matrix elements between the $5D_{3/2}$ state

and FESs are estimated for a set of FES energies spaced at $h \times 40$ GHz within the range of $\epsilon' = 0$ and $\epsilon' \simeq 20$ eV. These calculations set up the integrand of a principal value integral with a pole at $\epsilon' = 0.17$ eV numerically calculated to contribute 19 and -3 to the scalar and tensor polarizabilities, respectively. Contributions from the polarizability of the inner ion core are included from estimates obtained in [28]. Our final estimates are $\alpha^S_{5D_{3/2}} = -511$ and $\alpha^T_{5D_{3/2}} = 13$. From the simulation in Fig. 3.10(b), we estimate that the presence of this tensor polarizability would result in a systematic shift of < 10 in the scalar polarizability, below our measurement's uncertainty of 17. Therefore, in this case, it is not possible to make a tensor polarizability measurement in the presence of a significant PI cross section, as the broadening will mask the $|m_j|$ splittings brought on by the tensor polarizability.

3.7 Photoionization Cross Section

Not only is this experiment intended to investigate the differential light shifts a 1064-nm laser field would place on the $5D_{3/2}$ state, but it also measures the likelihood of the atoms photoionizing at this wavelength. At low values of $|\Delta^{F'}_{795}|$ and $|\Delta^{F'}_{762}|$, atoms are located in regions of the lattice where the 1064-nm intensity is the lowest, spectral broadening from PI is at the same, if not lower, magnitude as other sources: Zeeman broadening from the always-on MOT magnetic field, Doppler broadening, Penning ionization, and 1064-nm power fluctuations. When $5S_{1/2}$ atoms located on the lowest Bloch band are probed, the 762-nm spectrum undergoes PI broadening that supersedes the aforementioned effects. These atoms see the peak intensity of ~ 70 GW/m^2 and are excited to $5P_{1/2}$ when $\Delta^{F'}_{795}$ is at a maximum. In this intensity regime, the measured Lorentzian linewidth $\Gamma/2\pi$ in the 762-nm probe spectrum is thus predominantly derived from the PI-induced decay rate, Γ_{PI},

$$\Gamma_{PI} = \frac{\sigma I}{\hbar \omega_L}, \tag{3.6}$$

where I is the 1064-nm intensity and ω_L is its angular frequency.

Measurements of Γ and I are collected for both excitation pathways through F' and all D_1 AC-Stark shifts from which a detectable spectral line is observed. We are able to make a measurement of the lattice laser's intensity at a given D_1 detuning $\Delta^{F'}_{795}$ using Eq. 3.2, from which we also propagate a 6 MHz uncertainty in $\Delta^{F'}_{795}$ as a conservative estimate. Γ is obtained from Lorentzian linewidths fitted to our spectral data of collected Rb$^+$ counts versus $\nu_{762} - \nu_2$. For every I and Γ measured, we take the ratio $\tilde{\sigma} = \hbar \omega_L \Gamma / I$. Fig. 3.12(a) exhibits the trend of $\tilde{\sigma}$ as I is increased. At CM positions of very large I, from which the exemplary 762-nm probe spectrum used for finding fitting parameters Γ and $\Delta^{F'}_{762}$ in
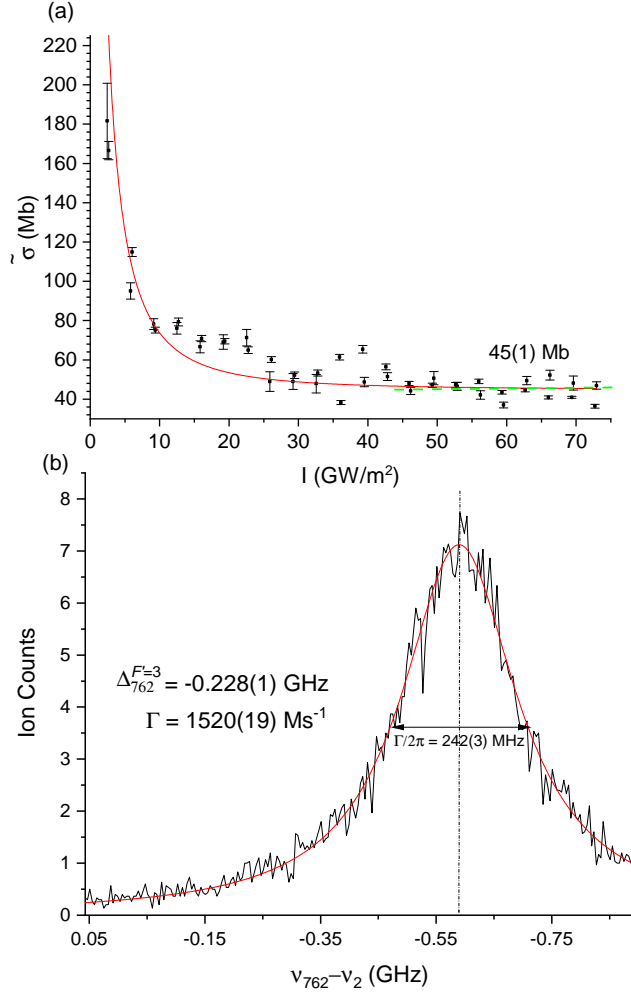
Figure 3.12: Figures taken from [3]. In (a) we show the values of $\tilde{\sigma}$ we obtain for each measured I, along with the fitted function (solid red) from which σ may be derived. The green dashed line represents the arithmetic average in $\tilde{\sigma}$ for all points corresponding to an $I \geq 45$ GW/m^2. Vertical error bars represent propagated uncertainties in $\tilde{\sigma}$, derived from the natural linewidth of the D_1 line and the statistical uncertainty in measured Γ. In (b), we show a typical Lorentzian 762-nm probe spectrum at the given $\Delta_{795}^{F'} = 0.984$ GHz, along with fitting parameters $\Delta_{762}^{F'}$ and Γ we get from the line center and width, respectively.

Fig. 3.12(b) is taken, $\tilde{\sigma} \to \sigma$ and $\Gamma \to \Gamma_{PI}$. The uncertainty in the center and linewidth of Fig. 3.12(b) takes into account the absence of data to the red of the line center, where the PLL starts to come out of lock.

The points in Fig. 3.12(a) follow the given trend:

$$\tilde{\sigma} = \sqrt{\sigma^2 + \gamma^2/I^2}, \tag{3.7}$$

59

where γ corresponds to the other broadening effects previously listed. Using this fit function, we obtain $\sigma = 45(1)$ Mb. An alternative derivation of σ by taking the arithmetic mean of all $\tilde{\sigma}$ above $I = 45$ GW/m^2 also yields $\sigma = 45(1)$ Mb. When the same two fitting procedures are used on simulated 2D spectral maps like the one in Fig. 3.10(b) with σ as an input, we find that these methods yield an overestimate of 1 Mb. Therefore, we arrive at a final $5D_{3/2}$ PI cross section of 44(1) Mb. This value deviates from an estimated fine-structure-removed cross section of 32.4 Mb, calculated from Rydberg-electron model potentials provided by [131]. Effects of atomic polarization, fine-structure, and the robustness of the model potentials at $5D$ are all explanations from this discrepancy that has yet to be determined.

3.8   Conclusion

In summary, we have made measurements of the $5D_{3/2}$ scalar polarizability $\alpha^S_{5D_{3/2}}$ and PI cross section σ at $\lambda = 1064$ nm. We obtain $\alpha^S_{5D_{3/2}} = -524(17)$ (atomic units, i.e., $4\pi\epsilon_0 a_0^3$) and $\sigma = 44(1)$ Mb. Our experimental scalar polarizability matches our estimates within our uncertainty; however, the PI cross section faces a discrepancy with our estimates and a less precise measurement obtained for $5D_{5/2}$ [117] using a trap-loss method. Effects of fine structure on the PI cross section have yet to be determined. Empirically determined shifts and decay-rates for the Rb $5D_j$ states at other optical wavelengths above, below, and at the PI threshold are future experimental directions. Such shifts could be beneficial in eliminating AC Stark shifts and motional decoherence, as well as providing optical trapping in miniaturized rubidium optical frequency standards [25; 28; 38; 39].

CHAPTER IV

Theory of Rydberg Atoms

In the last chapter, I used an ultra-deep optical lattice to make simultaneous polarizability and photoionization measurements on the Rb $\left|5D_{3/2}\right\rangle$ state, potentially useful for commercially available portable rubidium clocks. Measurements were done at the common lasing wavelength of $\lambda = 1064$ nm. With that application of optical lattices for fundamental physics having been explored, I now will move on to the other applications involving circular-state Rydberg atoms.

The secondary goal of this thesis is to exploit how Rydberg atoms behave in optical fields in order to coherently control the parity and shape of the electronic wave function towards circularization. Very large Rydberg atoms in the circular state are useful for precision spectroscopy and single-photon detection experiments that have been proposed in the fundamental physics community. Atomic and molecular states with atoms at very large n principal quantum numbers near the ionization threshold are known as *Rydberg states*. The weakly bound valence electron is therefore free to orbit the inner ion core at distances on the order of hundreds of nm to μm. As a result, there is considerable scaling with n for their physical properties, such as lifetimes, dipole moments, polarizabilities, etc. When atoms in Rydberg states are laser cooled to a few millionths of a degree above absolute zero, they become popular systems for exploring quantum information processing [132; 133] and quantum simulation [134; 102; 135; 136], in addition to the high-precision spectroscopy applications discussed in this thesis [26; 137; 138; 64]. Furthermore, there has been recent fervor in using hot Rydberg atoms at $\sim$300 K in a vapor cell for applications from single-photon generation [139] to electrometry [140; 141; 142; 143]. Here, I give a theoretical presentation of Rydberg atom scaling laws and behavior in external static and RF electromagnetic fields. In the following chapter, I will describe how they respond to optical fields, which is the theoretical basis for the final chapters in this thesis.

4.1 Scaling Laws

The sub-μm size of the wave function for a weakly-bound valence electron grants predictable physical behavior of Rydberg atoms that depends on the nearly-ionized electron's n-state. We refer to these dependencies as *scaling laws.* Scaling laws are a direct result of the exaggerated extent at which the valence electron's wave function vanishes, which, in the quantum regime, is quantified by the expectation value of the electron's radial coordinate relative to the nucleus $\langle \hat{r}_e \rangle$. In the first section, we will review the solution of Schrödinger equation for hydrogen and obtain the expectation value for $\langle \hat{r}_e \rangle$ as a function of n. Subsequently, we will summarize several scaling laws that have a dependence on $\langle \hat{r}_e \rangle$.

4.1.1 Schrödinger Equation

Hydrogen is a unique atom in the sense that one may obtain an exact, analytical formula for its wave function and eigenenrgies. Its simplistic structure consisting of a single electron and proton is so appealing that if the AMO community had the technological prowess to laser cool and optically trap hydrogen, it would be the species of study in a great chunk of the current Rydberg-atom literature. However, its small mass and deeply bound ground state make it difficult to manipulate with laser light; thus, alkalies (Rb, Cs, Na, etc.) and alkaline-earth metals (Sr, Yb, Ca, etc.) are used in its place. Because these atoms feature only one or two valence electrons surrounding an inner ion core, they are systems that closely resemble hydrogen whenever in a Rydberg state. Alkaline and alkaline-earth Rydberg atoms are therefore hydrogen-like with small empirical corrections to their energy level structures known as *quantum defects.* They are a result of the valence electron undergoing shielding of the nuclear charge by electrons of the inner ion core and the polarization of these inner electrons by the outer electron [60; 138; 64]. Hydrogen's electron, on the other hand, undergoes no shielding of the nuclear proton and experiences a Coulomb interaction given by,

$$U_C(\hat{r}_e) = -\frac{e^2}{4\pi\epsilon_0} \frac{1}{\hat{r}_e}. \tag{4.1}$$

Here, as a reminder $\hat{r}_e$ is the operator corresponding to the radial position of the electron with respect to the proton position (the atom's center of mass (CM)). Here $e = 1.602176634 \times 10^{-19}$ C (exact) is the fundamental charge and $\epsilon_0 = 8.8541878128(13) \times 10^{-12}$ F/m is the vacuum permittivity.

I place this potential in the Schrödinger equation for the hydrogen electron[1],

$$\frac{-\hbar^2}{2m_e}\nabla_e^2\psi_e(r_e) - \frac{e^2}{4\pi\epsilon_0}\frac{1}{r_e}\psi_e(r_e) = W\psi_e(r_e), \tag{4.2}$$

where $\hbar = 1.054571817... \times 10^{-34}$ J·s (exact) is the reduced Planck's constant, $m_e = 9.1093837015(28) \times 10^{-31}$ kg is the electron mass, and W is the total energy of the electron. The separation of variables method is used to solve this partial differential equation, where $\psi_e = R(r_e)\Theta(\theta_e)\Phi(\phi_e)$, and so I get

$$\frac{-\hbar^2}{2m_e}\left[\frac{1}{R}\frac{d}{dr_e}\left(r_e^2\frac{dR}{dr_e}\right) + \frac{1/\Theta}{r_e^2\sin\theta_e}\frac{d}{d\theta_e}\left(\sin\theta_e\frac{d\Theta}{d\theta_e}\right) + \frac{1/\Phi}{r_e^2\sin^2\theta_e}\frac{d^2\Phi}{d\phi_e^2}\right] - \frac{e^2}{4\pi\epsilon_0}\frac{1}{r_e} - W = 0.$$

The expression $(1/\Phi)\frac{d^2\Phi}{d\phi_e^2}$ is a constant equal to $-m_l^2$, where m_l is an integer. Thus, $\Phi = e^{im_l\phi_e}$. Then, I obtain

$$\frac{1/\Theta}{\sin\theta_e}\frac{d}{d\theta_e}\left(\sin\theta_e\frac{d\Theta}{d\theta_e}\right) - \frac{m_l^2}{\sin^2\theta_e},$$

which is equal to $-l(l+1)$, where l is a non-negative integer and m_l must range from $-l$ to l for a solution of the equation to exist. The solution to

$$\frac{1}{\sin\theta_e}\frac{d}{d\theta_e}\left(\sin\theta_e\frac{d\Theta}{d\theta_e}\right) + \left[l(l+1) - \frac{m_l^2}{\sin^2\theta_e}\right]\Theta = 0,$$

the general Legendre equation for variable $x = \cos\theta_e$, is $P_l^{m_l}(\cos\theta_e)$, the associated Legendre functions. Including the normalization along the solid angle from 0 to 4π, I have

$$\Theta(\theta_e) = \sqrt{[(2l+1)(l-m_l)!]/[4\pi(l+m_l)!]}P_l^{m_l}(\theta_e).$$

Together, with Φ, the angular part of the hydrogen electronic wave function is given by the spherical harmonics $Y_l^{m_l}(\theta_e, \phi_e)$. It should be noted that here I am neglecting effects of the electron's spin on its orbital angular momentum, which mixes states with different m_l quantum numbers and gives rise to quantum numbers $j = |l+s|, ..., |l-s|$ and $m_j = -j, ..., j$. The angular part of the Schrödinger equation is insensitive to interactions with other electrons in non-hydrogenic atoms, resulting in no change in the angular wave function for the valence electron.

---

[1]Note that I am assuming an infinitely massive proton; otherwise, I would replace m_e with μ, the reduced mass of the atom.

The radial part of Eq. 4.2 becomes

$$\frac{d}{dr_e}\left(r_e^2\frac{dR}{dr_e}\right) - \frac{l(l+1)}{r_e^2}R + \frac{m_e e^2}{2\pi\epsilon_0\hbar^2 r_e}R + \frac{2m_e W}{\hbar^2}R = 0.$$

The normalized solution for $R(r_e)$ is described in [65] and given by

$$R(r_e) = \sqrt{\left(\frac{2}{na_0}\right)^3 \frac{(n-l-1)!}{2n(n+1)!}} e^{-r_e/na_0}\left(\frac{2r_e}{na_0}\right)^l L_{n-l-1}^{2l+1}(2r_e/na_0), \tag{4.3}$$

where

$$L_{n-l-1}^{2l+1}(2r_e/na_0) = (-1)^{2l+1}\left(\frac{na_0}{2}\right)^{2l+1}\frac{d^{2l+1}}{dr_e^{2l+1}}\left[\frac{e^{2r_e/na_0}}{(n+l)!}\frac{d^{n+l}}{dr_e^{n+l}}\left(e^{-2r_e/na_0}r_e^{n+l}\right)\right] \tag{4.4}$$

is an associated Lagrange function. Here, l must be non-negative and has a maximum value of $n-1$, and the eigenenergies for hydrogen are defined by

$$W_{nl} = -\frac{hcR_H}{n^2}, \tag{4.5}$$

where $R_H = m_p R_\infty/(m_p + m_e)$ and $m_p = 1.67262192369(51) \times 10^{-27}$ kg is the proton mass.

For the alkali Rb, the atom used in this thesis, the quantum defects arise from the following modification:

$$\frac{d}{dr_e}\left(r_e^2\frac{dR}{dr_e}\right) - \frac{l(l+1)}{r_e^2}R + \frac{Zm_e e^2}{2\pi\epsilon_0\hbar^2 r_e}R - \sum_{i=1}^{Z-1}\frac{m_e e^2 R}{4\pi\epsilon_0\hbar^2|\mathbf{r}_e - \mathbf{r}_i|} + \frac{2m_e W}{\hbar^2}R = 0, \tag{4.6}$$

for a neutral atom with atomic number Z and core electrons at position $\mathbf{r}_i$. For Rydberg states, a sufficient approximation of the core penetration and polarization effect was presented in [131] and is given by (in atomic units of Hartree's $E_H = 27.211386$ eV).

$$U_l(\hat{r}_e) = -[1 + (Z-1)e^{-a_1\hat{r}_e} - \hat{r}_e(a_3 + a_4\hat{r}_e)e^{-a_2\hat{r}_e}]/\hat{r}_e - \frac{\alpha_d}{2\hat{r}_e^4}[1 - e^{-(\hat{r}_e/r_c)^6}], \tag{4.7}$$

where a_{1-6} are l-dependent constants, α_d is the dipolar core polarizability, and r_c is a radial scaling factor unique to the alkali. Constants a_{1-6} and r_c can be found in [131], while updated measurements of the dipolar polarizabilities using $nD_{5/2}, nF, nG, nH$, and nI states are found in [144; 138], .

One must also include the spin-orbit interaction for a fine-structure state of quantum

number j, given by

$$U_{LS}(\hat{r}_e) = \frac{[j(j+1) - l(l+1) - s(s+1)]}{4m_e^2 c^2 \hat{r}_e} \frac{\partial U_l(\hat{r}_e)}{\partial \hat{r}_e}. \tag{4.8}$$

For alkali metals, the total energies W_{nlj} are not exactly $\propto n^{-2}$, but instead $(n^*)^{-2}$, where $n^* = n - \delta_{lj}(n)$ is the effective principal quantum number and $\delta_{lj}(n)$ is the quantum defect, following the Rydberg-Ritz formula

$$\delta_{lj}(n) = \delta_{0,lj} + \delta_{2,lj}/(n - \delta_{0,lj})^2 + ..., \tag{4.9}$$

where $\delta_{0,lj}$ and $\delta_{2,lj}$ are spectroscopically measured constants [10; 145; 144; 138; 64].

Including Eq. 4.7 and Eq. 4.8 in place of the Coulomb interactions of Eq. 4.6 and modifying W to include the effective principal quantum numbers and mass corrections specific to the alkali, the radial wave function can be obtained through the Numerov method [60], a numerical integration technique that uses n- and l-dependent inner and outer cutoffs of the wave function along with the appropriate sloping of the function's final lobe in order to obtain a solution that vanishes as $r_e \to \infty$.. While the resulting $\langle \hat{r}_e \rangle$ is $\sim (n^*)^2$ instead of n^2 for an alkali, for high-n Rydberg atoms, the scaling laws for the hydrogen atom may be used. To show the effects of the quantum defects on alkali Rydberg wave functions with an example, I plot the radial functions $|r_e R(r_e)|^2$ of $|46S_{1/2}\rangle$ for rubidium and hydrogen in Fig. 4.1.

4.1.2 Summary of Laws

4.1.2.1 Electric-Dipole Moment

In the previous section, a derivation of the scaling law for the hydrogen was provided. When an electric field is applied to the atom, weak admixture with other stationary states of opposite parity occurs in first-order nondegenerate perturbation theory. The perturbed wave function then has a net electric-dipole moment characterized by $-e(r_e)_{nl}^{n'l'}$, where $(r_e)_{nl}^{n'l'}$ is known as the *matrix element* between eigenstates $|nlm_l\rangle$ and $|n'l'm_l'\rangle$. For nearby Rydberg states, the matrix element is approximately the expectation value of $\hat{r}_e$ and therefore scales as n^2.

The dipole moment between a Rydberg state and a low-lying bound state has a less intuitive scaling law. Here, the low-lying-state wave function is approximately a Dirac delta function on the length scales of the Rydberg electron distribution. Therefore, when calculating $(r_e)_{nl}^{n'l'}$, the integral ends up being proportional to the Rydberg radial wave function which has a normalization constant $\propto n^{-3/2}$. Thus, $(r_e)_{nl}^{n'l'} \sim n^{-3/2}$ for low n'.
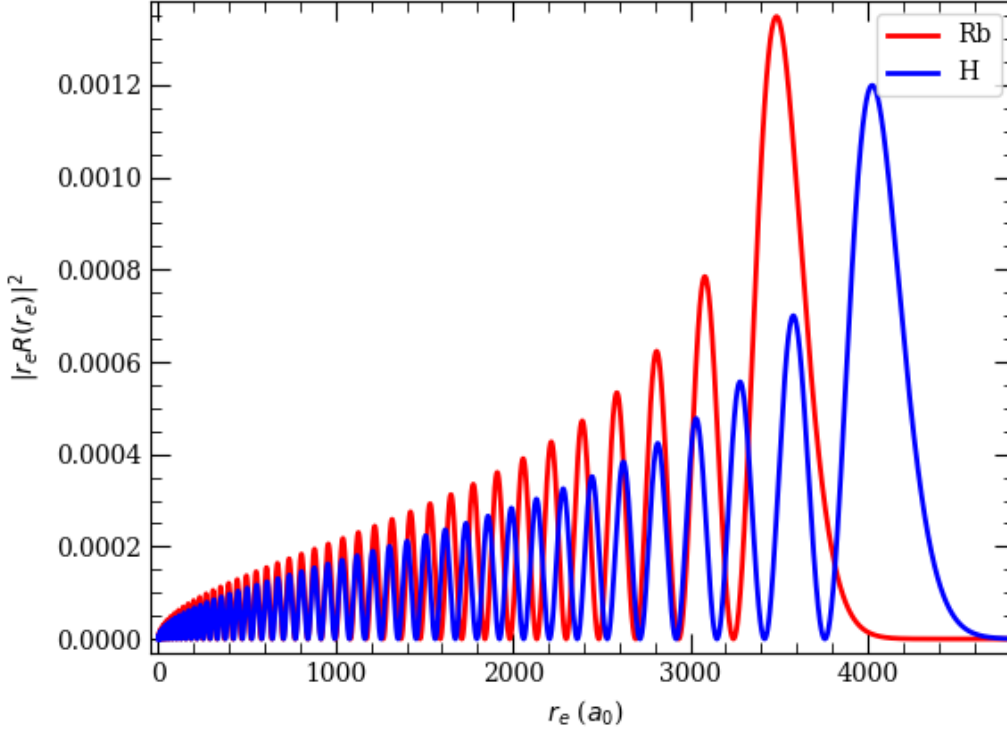
Figure 4.1: Effects of quantum defects on $|r_e R(r_e)|^2$ for Rb in $\left|46S_{1/2}\right\rangle$.

4.1.2.2 Kepler Frequency

One can think of the Kepler frequency $\omega_K/(2\pi)$ classically as the rate at which the Rydberg electron makes one complete revolution about the inner ion core. Quantum mechanically, however, it is the quotient of the energy splitting between two adjacent Rydberg states and h. For Rydberg levels very near the ionization threshold, adjacent states approach degeneracy as n^{-3} and the Kepler frequency vanishes as such. The following simple argument for a Rydberg states of hydrogen with principal quantum number n and $n + \Delta n$ with $\Delta n << n$ supports this scaling law.

$$\omega_K/2\pi = \Delta W/h = -cR_H[(n+\Delta n)^{-2} - n^{-2}] = \frac{2cR_H n\Delta n}{n^2(n+\Delta n)^2} \sim n^{-3}. \qquad (4.10)$$

When $\Delta n \to n$, such as the case with energy splittings between low-lying states and Rydberg states, no scaling law exists.

4.1.2.3 Lifetime

Rydberg atoms in a system with a background of room temperature T experience radiative decay from two main mechanisms: spontaneous emission and stimulated emission from blackbody photons. The decay rates from a Rydberg state to a final state from both mechanisms are added together where the stimulated decay from blackbody radiation is weighted by the thermal photon number at the background temperature of the system T. The decay brought on by stimulated transitions from blackbody photons can be reduced by lowering the background temperature of the system that is radiating the photons to temperatures at the order of ~1-10 K.

The resulting sum ends up being proportional to the cube of the energy splitting between the two levels and the square of the dipole moment associated with the transition. For Rydberg states with low-l quantum numbers, the most significant decay channels are the ones to low-n states due to the cubic dependence of the energy splittings. As mentioned in the previous section, this splitting is roughly constant for all-n. Thus, the lifetime scales as $[(d_e)_{nl}^{n'l'}]^{-2} \sim (n^{-3/2})^{-2} = n^3$. In the case of Rydberg atoms with high orbital-angular-momenta, as is such for a CS, selection rules restrict radiative decay to adjacent Rydberg states with $l\pm1$. Therefore, the lifetime scaling law depends on the Rydberg electron's Kepler frequency. And so, the lifetime scales as $(\omega_K/2\pi)^{-3}[(d_e)_{nl}^{n'l'}]^{-2} \sim n^9/n^4 = n^5$. Consequently, the longest lived Rydberg states are CSs in a cryogenic background that shields blackbody radiation [46; 102; 26; 133]; one can even further extend CS lifetimes via the Purcell effect, where the density of photons resonant for an electric dipole transition is reduced by means of manipulating the volume of the system [146].

4.1.2.4 Polarizability

For a nondegenerate system of Rydberg states, as can be found with those of lower-l quantum numbers, one will find a the state's binding energy exhibit a quadratic dependence on an applied DC electric field. Through second-order perturbation theory, a state- and field-dependent parameter known as the polarizability can be calculated. This parameter is roughly proportional to the square of dipole moments between adjacent states and the inverse of the Kepler frequency. Thus,

$$[(d_e)_{nlm_l}^{n'l'm_l'}]^2/\hbar\omega_K \sim (n^2)^2/n^{-3} = n^7. \tag{4.11}$$

However, as the electric field strength intensifies, nondegenerate perturbation theory becomes invalid and Schrödinger equation must be solved exactly, as will be described in the next section.

4.1.2.5 Two-Body Interactions

Here I detail the scaling laws associated with electric-multipole interactions between two Rydberg atoms labeled A and B with CM positions $\mathbf{R}_{0A}$ and $\mathbf{R}_{0B}$ respectively. Depending on the magnitude of parameter $\mathbf{R} = \mathbf{R}_{0A} - \mathbf{R}_{0B}$, the charged particles that comprise one atom can induce level shifts in the internal Rydberg state on the other and vice versa.

The complete interaction potential between the two atoms is approximated to a maximal-order interaction q_{max} by [147]

$$\hat{U}_{int} = \frac{e^2}{4\pi\epsilon_0} \sum_{q=2}^{q_{max}} R^{-(q+1)} \sum_{L_A=1, L_B=q-1}^{q_{max}-1} \sum_{M=-L_<}^{L_<} f_{ABM} \hat{Q}_A \hat{Q}_B, \qquad (4.12)$$

where

$$f_{ABM} = \frac{(-1)^{L_B}(L_A + L_B)!}{\sqrt{(L_A + M)!(L_A - M)!(L_B + M)!(L_B - M)!}} \qquad (4.13)$$

$$\hat{Q}_{A/B} = \sqrt{\frac{4\pi}{2L_{A/B}+1}} \hat{r}_{eA/B}^{L_{A/B}} Y_{L_{A/B}}^{\pm M}(\hat{\theta}_{eA/B}, \hat{\phi}_{eA/B}), \qquad (4.14)$$

where in operator $\hat{Q}_{A/B}$, the "$+$" is for atom A and the "$-$" is for B.

The leading-order interaction is a dipole-dipole interaction, where the dipole moment of one atom induces a dipole moment in the second atom, which provides a potential that compels the second dipole moment to align parallel to the first. Mathematically, this is where $q = 1$, $L_A = 1$, and $L_B = 1$, so

$$\hat{U}_{int} \simeq \hat{U}_{dd} = -\frac{e^2}{3\epsilon_0 R^3} \hat{r}_{eA} \hat{r}_{eB} \left[Y_1^{-1}(\hat{\theta}_{eA}, \hat{\phi}_{eA}) Y_1^1(\hat{\theta}_{eB}, \hat{\phi}_{eB}) + Y_1^1(\hat{\theta}_{eA}, \hat{\phi}_{eA}) Y_1^{-1}(\hat{\theta}_{eB}, \hat{\phi}_{eB}) \right.$$

$$\left. + 2Y_1^0(\hat{\theta}_{eA}, \hat{\phi}_{eA}) Y_1^0(\hat{\theta}_{eB}, \hat{\phi}_{eB}) \right]. \quad (4.15)$$

Here, the quantization axis is defined as being parallel to $\mathbf{R}$, the internuclear separation vector. Note that this operator only couples adjacent angular momentum states of opposite parity for the Rydberg electron and follows the usual electric-dipole selection rules for the internal states' magnetic sublevels. In a system consisting of a mixture of two adjacent

angular momentum states of opposite parity engendered by an external electromagnetic field making the two states nearly degenerate, the first-order, adiabatic potential on diagonalized state $|k\rangle$ is

$$\Delta W_{ad}^{(k)}(R) \simeq C_3^{(k)}/R^3, \tag{4.16}$$

where $C_3^{(k)} \sim n^2 n^2 = n^4$ due to the two dipole moments in $\hat{U}_{dd}$.

In a system where there is no external field and the ensemble consists of a single internal state or states that do not couple via $\hat{U}_{dd}$, the level must be solved up to the second order, so the adiabatic state $|k\rangle = |n_A l_A j_A m_{jA}\rangle |n_B l_B j_B m_{jB}\rangle$ undergoes a shift

$$\Delta W_{ad}^{(k)}(R) \simeq \sum_{n'_A l'_A j'_A m'_{jA}} \sum_{n'_B l'_B j'_B m'_{jB}} \frac{\langle k| \hat{U}_{dd}(R) |n'_A l'_A j'_A m'_{jA}\rangle |n'_B l'_B j'_B m'_{jB}\rangle}{W_A + W_B - W'_A - W'_B}$$
$$\times \langle n'_A l'_A j'_A m'_{jA}| \langle n'_B l'_B j'_B m'_{jB}| \hat{U}_{dd}(R) |k\rangle = C_6^{(k)}/R^6, \quad (4.17)$$

where the $C_6^{(k)}$ coefficient is known as the *van der Waals* coefficient and describes level shifts brought on by the temporary electric-dipole moments between the two atoms.

Upon inspection of Eq. 4.17, one can see that the scaling law here also depends on the Kepler frequency:

$$C_6^{(k)} \sim n^4 n^4 / n^{-3} = n^{11}. \tag{4.18}$$

Higher-order multipole interactions become observable at very small internuclear distances and can support bound states corresponding to molecular bonds between the two atoms. These μm-long molecules are known as *macrodimers* and have been experimentally observed and imaged in [148; 99]. For the experimental work in this thesis, Rydberg ensembles are dilute enough to make even the leading-order, dipole-dipole interaction barely observable. This is discussed in Chapter VII.

4.2 Electric Fields

A Rydberg electron placed in a static electric field with potential $\phi(\mathbf{R}_0 + \hat{\mathbf{r}}_e)$ experiences the following DC-Stark interaction

$$\hat{U}_S(\mathbf{R}_0, \hat{\mathbf{r}}_e) = -e\phi(\mathbf{R}_0 + \hat{\mathbf{r}}_e). \tag{4.19}$$

The field of strength E_0 can be spatially dependent within the atomic sample, as is seen in ion microscopy apparatuses [149; 112], but the scope of this thesis is only concerned with homogeneous fields, where $\phi(\hat{\mathbf{r}}_e) = E_0(\hat{\epsilon} \cdot \hat{\mathbf{r}}_e)$ and $\hat{\epsilon}$ is the polarization of the field.

4.2.1 Quadratic Stark Effect

For alkali atoms in low-l angular momentum states, the interaction strength of the field typically does not dominate the splittings induced by the quantum defect and fine structure. Therefore, the problem can be solved using non-degenerate perturbation theory to the second order, and the state $|n, l, j, m_j\rangle$ does not mix. Because the second order is taken, the overall Rydberg-level shift depends quadratically on the electric-field strength E_0:

$$\Delta W_{n,l,j,m_j} = -e^2 \sum_{n'l'j'm_j'} \frac{|\langle nljm_j| (\hat{\epsilon} \cdot \hat{\mathbf{r}}_e) |n'l'j'm_j'\rangle|^2 E_0^2}{W_{nljm_j} - W_{n'l'j'm_j'}}, \tag{4.20}$$

which can be simplified to

$$\Delta W_{n,l,j,m_j} = -\frac{1}{2}\alpha_{nljm_j} E_0^2, \tag{4.21}$$

where α_{nljm_j} is the DC polarizability. Fig. 4.2 shows the trend in rubidium polarizabilities as n is varied for $|nS_{1/2}\rangle$ and $|nP_j\rangle$, the Rydberg states relevant to the experimental work in this thesis.

4.2.2 Parabolic Wave Functions and Linear Stark Effect

For Rydberg states that are degenerate without the application of any external forces, such as the high-l (usually $l \geq 3$) hydrogenic states all sharing the same principal quantum number n, where quantum defects, spin-orbit, and hyperfine-coupling effects are experimentally unobservable, the DC electric field induces electric-dipole shifts proportional to E_0: $eE_0 \langle n, l' = l \pm 1, m_l' = m_l, m_s, m_I| \hat{z}_e |n, l, m_l, m_s, m_I\rangle$. Here we choose the polarization of $\mathbf{E}$ to serve as the quantization axis. Because these dipole-interactions are stronger than the Coulomb interactions that the Rydberg electron sees in the hydrogenic manifold, the eigenbasis for this system no longer consists of an l quantum number.

New quantum numbers n_1 and n_2 must be introduced, which arise from the Schrōdinger equation under the following change of coordinates

$$\xi = r_e + z_e = r_e(1 + \cos\theta_e), \tag{4.22}$$

$$\eta = r_e - z_e = r_e(1 - \cos\theta_e), \tag{4.23}$$

$$\nabla^2 = \frac{4}{\xi + \eta} \frac{\partial}{\partial \xi}\left(\xi \frac{\partial}{\partial \xi}\right) + \frac{4}{\xi + \eta} \frac{\partial}{\partial \eta}\left(\eta \frac{\partial}{\partial \eta}\right) + \frac{1}{\xi\eta}\left(\frac{\partial^2}{\partial \phi_e^2}\right). \tag{4.24}$$

Spatially, each value of ξ and η defines a unique paraboloid about the z_e-axis. Values of ξ define surfaces opening downwards (below (x, y)-plane) at angles proportional to ξ, while η defines paraboloids that open upwards (above (x, y)-plane). I derive the Schrōdinger equation
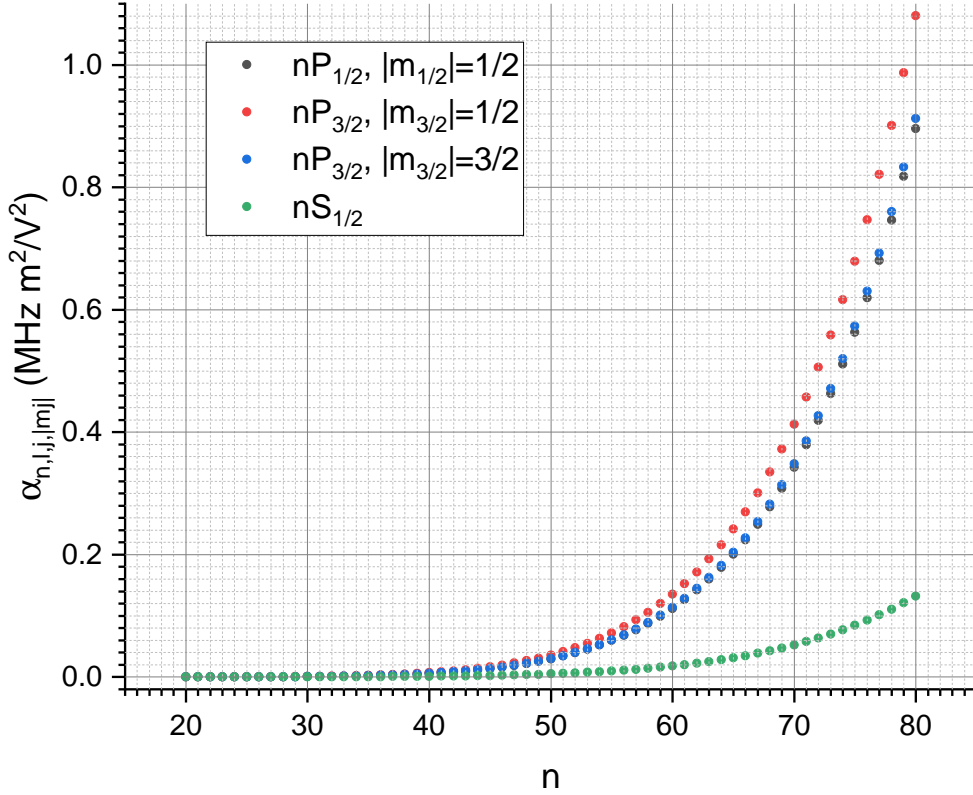
Figure 4.2: DC polarizabilities for Rb-$\left|nS_{1/2}\right\rangle$ and -$\left|nP_j, |m_j|\right\rangle$ Rydberg states as a function of n for $n = 20$-80.

under this transformation that includes the DC-Stark potential $eE_0(\xi - \eta)/2$, following the reasoning of [60; 65],

$$\frac{-\hbar^2}{2m_e}\left[\frac{4}{\xi + \eta}\frac{\partial}{\partial\xi}\left(\xi\frac{\partial\psi_e}{\partial\xi}\right) + \frac{4}{\xi + \eta}\frac{\partial}{\partial\eta}\left(\eta\frac{\partial\psi_e}{\partial\eta}\right) + \frac{1}{\xi\eta}\left(\frac{\partial^2\psi_e}{\partial\phi_e^2}\right)\right] - \frac{e^2}{2\pi\epsilon_0}\frac{\psi}{\xi + \eta} + eE_0(\xi-\eta)\psi_e/2 = W\psi_e.$$
(4.25)

As was done in [60; 65], this equation can be solved using the separation of variables method, where

$$\psi_e = u_1(\xi)u_2(\eta)e^{im_l\phi_e},$$
(4.26)

and, consequently, I get the two ordinary differential equations, written temporarily in atomic

units ($\hbar^2/m_e = 1, e = 1, 4\pi\epsilon_0 = 1$):

$$\frac{d}{d\xi}\left(\xi\frac{du_1}{d\xi}\right) - \frac{m_l^2 u_1}{\xi} + Z_1 u_1 - E_0\xi^2 u_1/4 = -W\xi u_1/2 \tag{4.27}$$

$$\frac{d}{d\eta}\left(\eta\frac{du_2}{d\eta}\right) - \frac{m_l^2 u_2}{\eta} + Z_2 u_2 + E_0\eta^2 u_2/4 = -W\eta u_2/2, \tag{4.28}$$

Z_1, Z_2 are the fractional charges along ξ and η, respectively, that both make up the net charge of the nucleus (or inner-ion core for a nonhydrogenic atom). They are related to quantum numbers n, n_1, n_2, m_l by [60; 65]

$$Z_1 = \frac{1}{n}\left(n_1 + \frac{|m_l|+1}{2}\right) \tag{4.29}$$

$$Z_2 = \frac{1}{n}\left(n_2 + \frac{|m_l|+1}{2}\right), \tag{4.30}$$

where $n = n_1 + n_2 + |m_l| + 1$. The modulus brackets are in compliance with the azimuthally symmetric geometry of the coordinates ξ and η, as well as the electric field pointing only along z_e. In the absence of the electric fields $E_0 = 0$, for the hydrogenic manifold, the energy eigenvalues $W_{n,n_1,n_2,|m_l|}$ from these equations are (back to SI units)

$$W_{n,n_1,n_2,|m_l|} = -\frac{hcR_\infty}{n^2}\left(\frac{m_+}{m_+ + m_e}\right) \tag{4.31}$$

meaning the degeneracy is still not lifted. The eigenfunctions to u_1 and u_2 are termed as the *parabolic wave functions* and have the structure

$$u_1(\xi) \propto \xi^{n_1+|m_l|/2}e^{-\xi/2n} \tag{4.32}$$

$$u_2(\eta) \propto \eta^{n_2+|m_l|/2} e^{-\eta/2n}. \tag{4.33}$$

Using these solutions, I can use the methods of first-order perturbation theory to evaluate the linear Stark shifts when $E_0 \neq 0$ because now the electric-dipole term has nonzero expectation values for a given basis states. Upon evaluation of $eE_0 \langle n, n_1, n_2, |m_l|| (\xi - \eta) |n, n_1, n_2, |m_l|\rangle$,

$$\Delta W^{(1)}_{n,n_1,n_2,|m_l|} = \frac{3}{2}ea_0 E_0 n(n_1 - n_2), \tag{4.34}$$

where, at fields of $\sim (1/3)n^{-5}$, the Stark-shifted hydrogenic states cross those of the adjacent n-manifold. This is known as the *Iglis-Teller limit* [60]. Now the Stark effect has lifted the degeneracy of the hydrogenic manifold in a manner that scales linearly with E_0. The linear Stark shifts for these states are shown in Fig. 4.3(a).
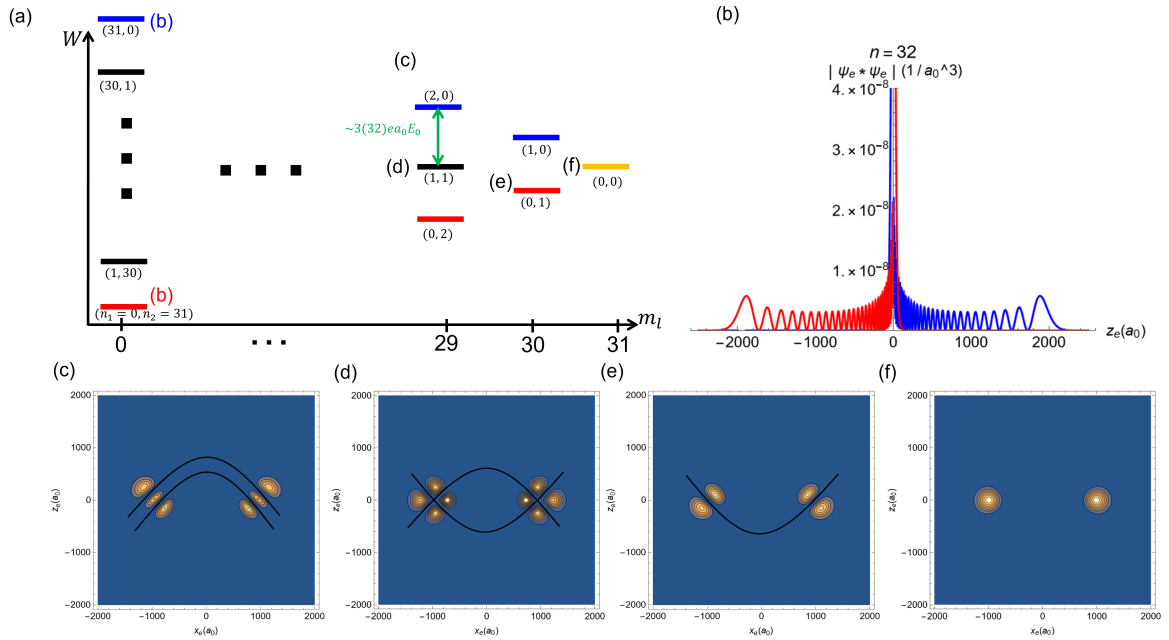
Figure 4.3: (a) Hydrogenic states, each representing a parabolic wave function belonging to $n = 32$ as m_l is varied under the presence of an electric field E_0 pointed along the quantization axis (along positive z_e). The red and blue states of a given m_l are indicated by the colors. The circular state energy level is colored gold. (b) Electron probability density of red and blue states as labeled in (a). The Rydberg electron in the red state spends most of its time along ($z_e < 0$) as expected. (c)-(f) Electron-probability-density contours projected on the $y_e = 0$-plane with parabolic nodal traces shown in black for the labeled states in (a).

Each hydrogenic state in the parabolic basis is a coherent superposition of the states in the spherical basis with quantum numbers n, l, m_l. In the parabolic basis, the quantum numbers have a more intuitive physical interpretation compared to l, and the wave functions are easier to sketch. The parabolic basis provides azimuthally symmetric wave functions for all states, allowing the functions to have the same projection along any plane that includes the z_e-axis.

For the $|m_l| = 0$ states, the Rydberg-electron density is aligned almost entirely along the z_e-axis, as shown in Fig. 4.3(b), while the $|m_l| = n - 1$ states completely avoid alignment along the z_e-axis, but, rather along the (x_e, y_e)-plane. The n_1 and n_2 quantum numbers determine how many downward- and upward-facing parabolas trace out nodes in the electron probability density. These parabolas are overlapped with the Rydberg-electron probability

73

densities $|\psi_e|^2$ projected on the $y_e = 0$-plane in Figs. 4.3(c)-(f). For the circular-state in Fig. 4.3(f), there is no node carved out by a parabola, consistent with $n_1 = n_2 = 0$.

4.2.2.1   The Circular State (CS)

CS atoms are eigenstates of the Hamiltonian in both the spherical (n, l, m_l) and parabolic (n, n_1, n_2, m_l) basis. In the spherical basis, they have maximum l and $|m_l|$ quantum numbers, granting them the strongest magnetic dipole moments of all states within n. For every n manifold with a given electron spin state $|m_s\rangle$, there are exactly two CSs: $|n, l = n - 1, m_l = -n + 1\rangle |m_s\rangle$ and $|n, n - 1, n - 1\rangle |m_s\rangle$. Because l is maximized for CSs, the overlap of the Rydberg-electron probability distribution with the inner ion core of the atom is minimized as the wave function scales as r_e^l. In this section, I will describe the properties of the CS, such as its lifetime, behavior in electric fields, and conventional methods of their preparation.

Lifetimes

I have already shown that high-l Rydberg states have lifetimes that scale with n as n^5. These lifetimes are a reciprocal sum of all possible decay rates to adjacent dipole-allowed states that have more negative energy eigenvalues Such rates describe sponataneous emission transitions driven by the vacuum state $|0\rangle_{\mathbf{k}, \hat{\epsilon}}$ of the electromagnetic field with polarization state $\hat{\epsilon}$ and wavenumber k and thus is weighted by the density ρ_{vac} of all $\mathbf{k}, \hat{\epsilon}$ that can drive the transition. For the CS the only possible dipole-allowed transition in spontaneous emission is the $|n, n - 1, n - 1\rangle \to |n - 1, n - 2, n - 2\rangle$ transition, meaning that the lifetime by spontaneous emission alone is the longest of all states within the n manifold.

The spontaneous emission rate brought on by the $|n, n - 1, n - 1\rangle \to |n - 1, n - 2, n - 2\rangle$ transition can be suppressed by manipulating ρ_{vac}. If the atom in a CS is placed in a 3D cavity of volume v that is resonant at the transition frequency $\omega_0/2\pi$ with FWHM width $\Delta\omega_0/2\pi$, the density of states is perturbed to $\rho_{cav} = 2\pi/(v\Delta\omega_0)$ [146]. Thus the cavity dimensions and mirror reflectivity can yield a quality factor $Q = \omega_0/\Delta\omega_0$ low enough to suppress the density of states at this frequency and, therefore, the decay rate. This is known as the *Purcell effect*.

As previously stated, incoherent blackbody radiation can also induce decay in Rydberg states through stimulated absorption and emission into other states with more negative or more positive energy eigenvalues. The blackbody decay rates for these transitions follow the same structure as the spontaneous emission rate, only that rate is further weighted by the Bose-Einsten distribution function at temperature T, which yields the spectral intensity at frequency $\omega_0/(2\pi)$. This intensity reduces as $T \to 0$. Thus, the environments of CSs, such as the cavities and vacuum chambers, must be cryogenically cooled in order to further

the extend the lifetimes through the suppression of blackbody radiation. CSs in cryogenic cavities engineered to inhibit spontaneous and blackbody decay reportedly can have lifetimes at the order of ~ 10 s. Under such an extended lifetime, if mm-wave spectroscopy probes a Rydberg transition connected to the CS, a Fourier-limited linewidth smaller than ~ 1 Hz can, in principle, be achieved, allowing high-precision measurements of fundamental constants like R_∞ [26].

Electric-Fields

CSs have no permanent dipole moments under the application of $\mathbf{E}$; this is intuitively described by the azimuthally symmetric electron distribution around the positively-charged core. Thus, all possible dipole moments cancel. Quantitatively, the first-order Stark effect is nonexistent for $n_1 = n_2 = 0$, so

$$\frac{3}{2}nea_0 E_0(0 - 0) = 0. \tag{4.35}$$

That is not to say CS Rydberg atoms with n ($|nC\rangle$) are impervious to electric fields. They still have a nonzero DC polarizability given, in the parabolic basis, by [60]

$$\alpha_{nC} = \frac{1}{2}\pi\epsilon_0 a_0^3 n^4[17n^2 - 3(n_1 - n_2)^2 - 9m_l^2 + 19] = \pi\epsilon_0 a_0^3 n^4(4n + 5)(n + 1). \tag{4.36}$$

The second-order Stark effect in the parabolic basis arises from the even-parity couplings to other hydrogenic states afforded by the $\xi^2 - \eta^2$ spatial dependence.

Initialization

To date, CSs cannot be prepared through one- to three-step laser excitation schemes through electric-dipole transitions with the ground state. Laser excitations through this method typically transfer $\hbar$ of spin angular momentum to the atom, where CSs would require $\simeq (n-1)\hbar$. The standard two methods of initializing a sample of CSs are the crossed-fields (ExB) and adiabatic-rapid-passage (ARP) methods.

I will start with explaining the ARP method, as it was the first scheme used to create a sample of CSs in [45]. The technique first requires conventional laser excitation to a low-l, m_l Rydberg state of hydrogen or an alkali that has small quantum defect (nD_j or nF_j states). Excitation is performed in the presence of an electric field $\mathbf{E}$ oriented along the z-axis which generates the Stark splittings of the hydrogenic manifold shown in Fig. 4.3(a). By properly polarizing the Rydberg-excitation laser, either the red (bottom-rung) or blue (top-rung) states in Fig. 4.3(a) for a given $|m_l|$ can be prepared from the low-n launch state.

Microwave radiation that is σ^+ polarized can sequentially couple the red or blue states

of low m_l to $m_l = n - 1$ and vice versa for couplings to the other CS at $m_l = -(n - 1)$. The radiation must be at a frequency $(\omega_\mu/2\pi)$ resonant with the linear and quadratic Stark shifts that the electric field $\mathbf{E} = E_0\hat{k}$ induces on the transition frequencies from the m_l to $m_l + 1$ red or blue states for the states of positive m_l:

$$\omega_\mu = \frac{3}{2}nea_0E_0/\hbar + \frac{3}{4\hbar}\pi\epsilon_0 a_0^3 n^4 \left[(n - m_l - 2)^2 - (n - m_l - 1)^2 + 6m_l + 3\right]E_0^2, \qquad (4.37)$$

so, at a glance, the second-order Stark shift implies that every m_l state requires an independent frequency ω_μ to efficiently be promoted to $m_l + 1$ and, consequently, calls for $\sim n$ independent microwave fields. It turns out that the ARP method grants the convenience of only requiring one microwave field with a variable frequency ω_μ or with a fixed frequency and variable electric field E_0 for Stark tuning the transitions. Note that without the quadratic Stark effect, the possibility of initializing CSs with microwave fields would not be realizable at all because the system would then resemble a simple-harmonic oscillator system that disallows complete population transfer to any of the red or blue states of a given m_l. The microwave couplings under discussion here are denoted in Fig. 4.4 by the solid gray arrows driving transitions among the red states of different m_l quantum numbers.

Once the red or blue Rydberg state $|n, n_1, n_2, m_l\rangle$ is prepared, ω_μ or E_0 is slowly ramped from a larger initial value to a smaller one such that the resonance condition is met for all states through the sweep. Quantum mechanically, the microwave field is creating dressed Rydberg states and the atom remains in a single adiabatic state $|j\rangle$ throughout the sweep, provided it is slow enough. The adiabatic state $|j\rangle$ traverses $n - m_l - 1$ avoided crossings with other adiabatic states $|j'\rangle$ and makes a diabatic transition to those states if the adiabaticity condition is violated. That condition for a single avoided crossing is

$$|\Omega_{N,N-1}|^2 >> \frac{8}{\pi}\dot{\delta}_{N,N-1}, \qquad (4.38)$$

where $\Omega_{N,N-1}$ is the resonant Rabi frequency that couples the diabatic states with N and $N - 1$ excitations of the free microwave field and $\delta_{N,N-1}$ is the angular frequency separating $|n, n_1, n_2, m_l\rangle |N\rangle$ and $|n, n_1', n_2', m_l + 1\rangle |N - 1\rangle$. A chirp of the microwave frequency or a ramp of the electric field is what provides the time dependence on this energy spacing. In some cases, the microwave-field intensity is also pulsed with a slowly varying envelope [75].

Obviously, when the strength of $\Omega_{N,N-1}$ is enhanced, faster sweeps can be prepared and the accuracy of the adiabaticity condition given above breaks down as multiple diabatic states are excited at a given time. When this happens, consecutive, two-level avoided crossings in the energy structures of the adiabatic eigenstates, as found in [45], lose their visibility as
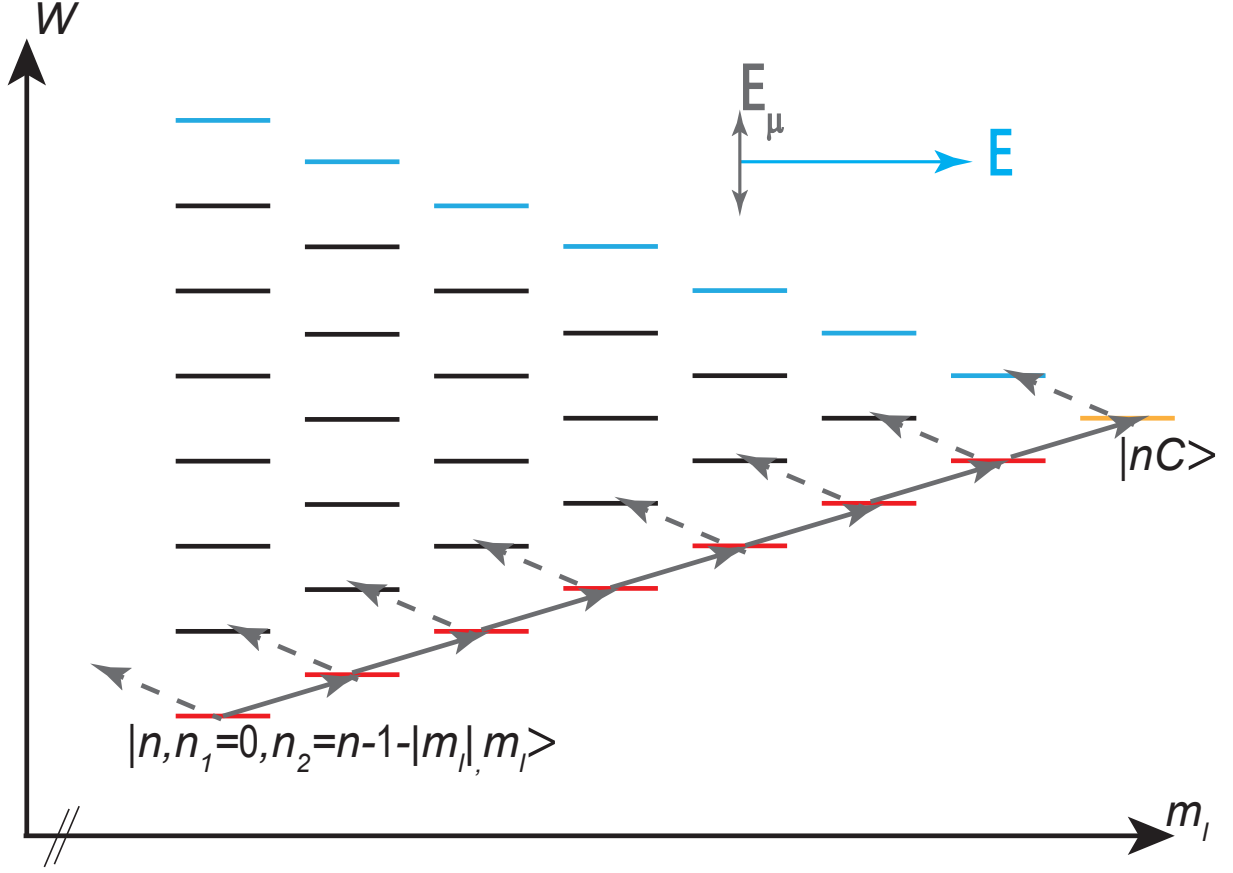
Figure 4.4: Microwave ARP couplings indicated by solid gray arrows coupling each red state $|n, n_1 = 0, n_2 = n - 1 - |m_l|, m_l\rangle$ to the circular state $|nC\rangle$. While the linearly-polarized microwave field $\mathbf{E}_\mu$ orthogonal to $\mathbf{E} = E_0\hat{k}$ provides the desired couplings from m_l to m_l+1, "leakage" transitions can occur that reduce m_l as shown by the dashed gray arrows.

the adiabatic energy spacing sufficiently isolates the dressed states as in [75; 9]. In this regime of the microwave field strength, the purity of the field's circular polarization becomes more crucial. If the microwave field is at such a strength while having a σ^- polarization component, as would happen with a linearly polarized field, unwanted *leakage transitions* would be driven, represented by the dashed arrows in Fig. 4.4 for the linearly polarized microwave field $\mathbf{E}_\mu$ depicted. To combat this, a static magnetic field $\mathbf{B}$ parallel to $\mathbf{E}$ tunes these leakage transitions out of resonance by means of the Zeeman effect. This addition to the ARP method was first realized in [75] for ^{85}Rb atoms using superconducting magnets with strengths of 18 G.

For low-n Rydberg atoms, the microwaves can be radiated into the vacuum chamber with a external antenna and efficient circular polarizer under the application of a strong enough electric fields that induces Stark splittings at the ~ 10 GHz level. The reason that this works only for low-n Rydberg atoms is that the Inglis-Teller limit would not be met under these field strengths. When high-n CSs are desirable, in-vacuum RF antennas and electrodes are often needed, as long external wavelengths would not make it through the chamber's apertures. So in order to make nearly perfect σ^+-polarized RF fields, typically orthogonal sets of RF and ultra-high-vacuum (UHV) compatible capacitor plates are constructed to be pumped down and baked out in the chamber. Then the applied RF needs to be equally split with a phase difference of $\pi/2$ and sent to the capacitors. Adding RF to the chamber then adds the risk of ground loops and unwanted capacitive couplings to other electric-field circuits within the chamber, which often requires breaking vacuum and redesigning the experiment; to put it short, initializing CSs with microwaves is no easy task!

Another method for producing CSs was proposed by considering the classical trajectory of the Rydberg electron in crossed electric $\mathbf{E}$ and magnetic fields $\mathbf{B}$ [71]. In the ExB method, the blue or red state of the $m_l = 0$ hydrogenic manifold is excited from the launch state in a regime where the Stark interaction from the $\mathbf{E}$-field polarized along the z-axis is significantly stronger that the Zeeman effect from $\mathbf{B}$ polarized along the x-axis. The classical trajectory for an atom in this regime is given by case (i) in Fig. 4.5, which resembles an ellipse of eccentricity $\varepsilon \simeq 1$. The Runge-Lenz vector $\mathbf{A}$ (do not confuse this with the vector potential) quantifies the ellipticity of the orbit and points along the semimajor axis of the elliptical orbit in the plane of motion. The red or blue state of $m_l = 0$ corresponds to this trajectory (remember, these states have their electron density completely aligned along the z-axis) and has a Runge-Lenz-vector expectation value of $\simeq n-1$ in atomic units, also equal to $|n_1 - n_2|$ for these outer-two states. The approximation sign corresponds to the fact that there is a small Zeeman interaction reducing ε.

When the Stark effect vanishes due to the absence of an electric field, the Zeeman interaction still remains and induces perfect cyclotron-like motion of the bound electron, depicted by case (iii) in Fig. 4.5. The circularity of this orbit is quantified by its angular momentum vector $\mathbf{L}$ which is parallel to $\mathbf{B}$. The CS corresponds to this trajectory, where $\mathbf{L} = n - 1$ atomic units and $\varepsilon = 0$.

In the intermediate regime (case (ii) in Fig. 4.5) denoted by case (ii) in Fig. 4.5 the eccentricity and circularity are on-par with each other and the energy needed for electron to "hop" onto a different trajectory around the inner-core is

$$\hbar\sqrt{(3nea_0E_0/\hbar)^2 + (eB_0/2m_e)^2}(n-1)[\varepsilon + \sqrt{1-\varepsilon^2}], \tag{4.39}$$

where $\varepsilon = \frac{3nea_0 E_0/\hbar}{\sqrt{(3nea_0 E_0/\hbar)^2 + (eB_0/2m_e)^2}}$. This is exactly the energy splitting between the adiabatic states of the hydrogenic manifold (ignoring the quadratic Stark effect) under these fields.

As mentioned before, we first excite Rydberg atoms in $m_l = 0$ red or blue states where the Stark interaction is much stronger than the Zeeman effect (case (i) in Fig. 4.5. Then the electric field is adiabatically ramped to zero where the magnetic field now defines the quantization axis and the red or blue $m_l = 0$ state is now the CS. The adiabaticity condition for this method, derived in [71], is

$$\frac{d}{dt}\arctan\left(6na_0 m_e E_0/\hbar B_0\right) << \sqrt{(3nea_0 E_0/\hbar)^2 + (eB_0/2m_e)^2}. \qquad (4.40)$$

This method describes a direct adiabatic evolution from the $m_l = 0$ state to the CS, no intermediate states are involved. The best way to interpret this method is through the following classical reasoning. A highly elliptical orbit of the electron around the nucleus is slowly distorted to a circular orbit without the electron hopping onto another orbital trajectory. Analogously, it would be like slowly forcing the Earth's orbit around the Sun to be circular without it being kicked onto Venus' or Mars' orbits.

The ExB method was first applied to an experiment in [72]. In order for this method to work, the fields must have nearly perfect orthogonality, and the electric field noise must be suppressed at its zero level lest the atoms are transferred back into noncircular states. Also, the quantization axis is defined by a magnetic field and not an electric field at the end of the process. Any sort of experiment that would require spectroscopy with another noncircular state, as in [26], would demand an electric field parallel to **B** in order to define and stabilize the hydrogenic states. Thus, an electric field has to then diabatically be switched on that is parallel to **B** and a diabaticity condition must be followed, as in [72]. As you can see, the ExB method is just as complicated as the ARP method even though no microwave fields are involved! Furthermore, both the ARP and ExB methods typically fail at $n > 60$ due to the heightened sensitivity to spurious electric-field fluctuations, and modifications are necessary [74] to initialize high-n CSs.

4.2.3 Electric-Field Ionization

Here I consider a regime where the applied electric field **E** significantly distorts the Coulomb potential binding the Rydberg electron. In a classical argument for an electron of low orbital angular momentum (OAM) and no OAM projection along the field and quantization axis, the electric field $\mathbf{E} = E_{FI}\hat{k}$ induces a saddle point in the Coulomb potential $-1/|z_e|$ atomic units located at $z_e = -1/\sqrt{E_{FI}}$ (here **E** is in atomic units of E_H/ea_0). An electron classically trapped in this potential that has a total energy of $W = -2\sqrt{E_{FI}}$ atomic

79
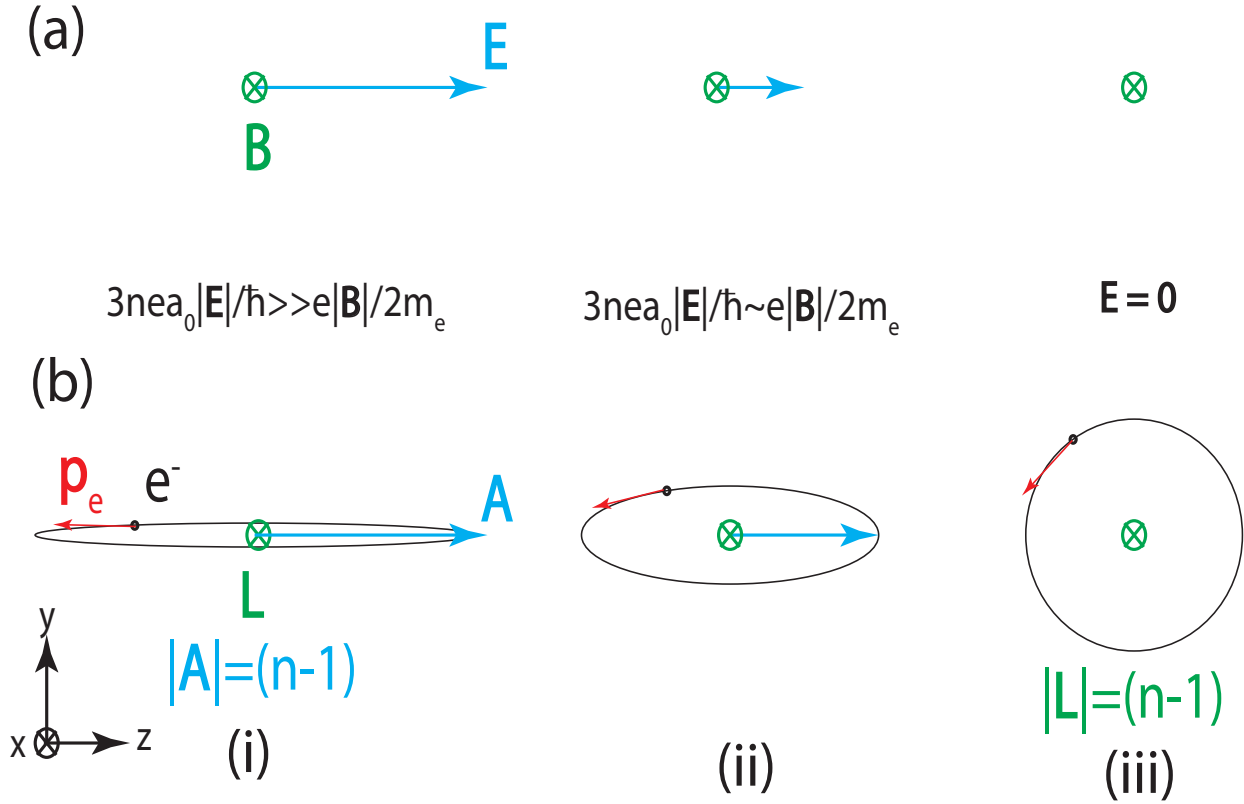
Figure 4.5: Each case of (i)-(iii) represents a regime of relative interaction-strengths by the crossed electric **E** and magnetic **B** fields. (a) Vector representations with linear Stark and Zeeman strengths as **E** is varied from each case. (b) Depiction of classical Rydberg electron trajectory under these fields in the given regimes with the tangential momentum $\mathbf{p}_e$, angular momentum **L**, Runge-Lenz vector **A** shown. The magnitudes of the Runge-Lenz and angular momentum vectors are at their maxima ($n-1$ atomic units) in cases (i) and (iii) respectively. In case (ii), their magnitudes are comparable.

units can now escape. In Fig. 4.6, I depict these distortions and saddle points. Clearly if the electron spends more time along $z_e < 0$, it will more easily escape. And so, the field required to ionize the atom under this classical reasoning is, in SI units,

$$E_{FI} = \frac{W^2}{4}\left(\frac{E_H}{ea_0}\right) = \frac{1}{16n^4}\left(\frac{E_H}{ea_0}\right). \tag{4.41}$$

Because the bound electron behaves like a quantum wave, this limit breaks down in
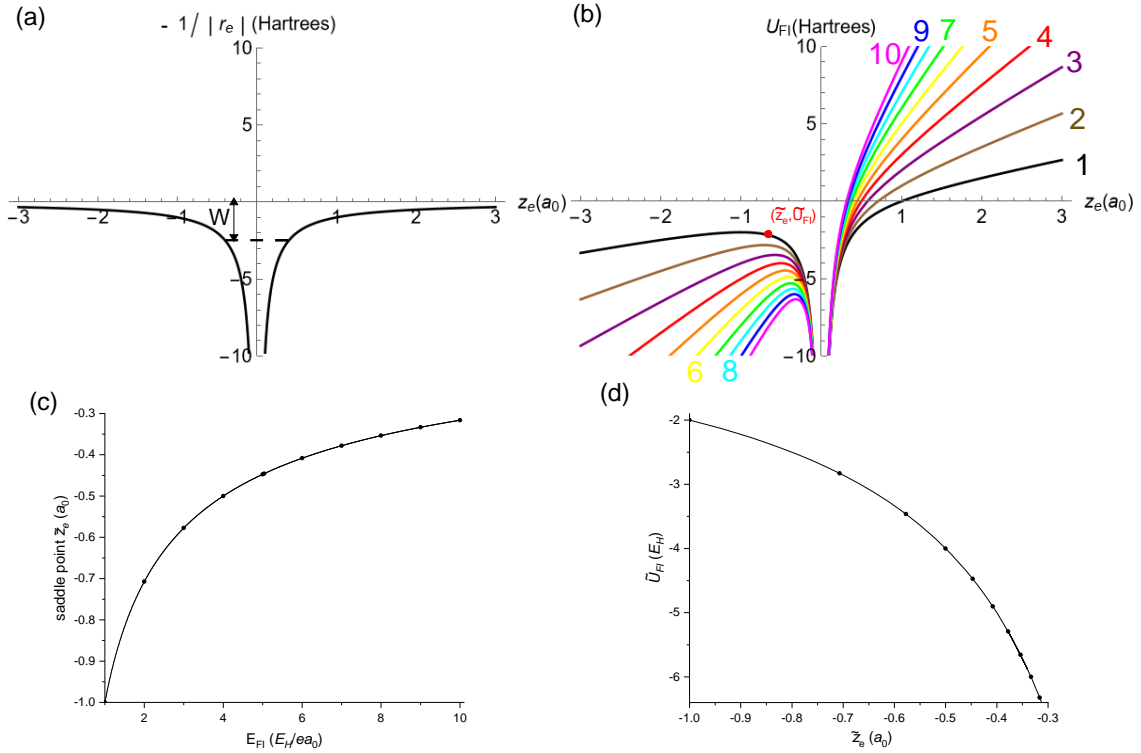
Figure 4.6: (a) Coulomb potential between electron and inner ion core of an arbitrary atomic state with binding energy W. No electric field is applied. (b) Electric field E_{FI} perturbations of Coulomb potential, resulting in net potential energy U_{FI} with indicated field values in atomic units $(E_H/(ea_0))$. The field points along positive z_e. (c) Saddle-point (red point in (a)) position $\tilde{z}_e$ as a function of applied field E_{FI}. (d) Saddle-point potential energy $\tilde{U}_{FI}$ as a function of $\tilde{z}_e$.

various cases but is overall a good approximation. For one, the classical model neglects quantum tunneling of electrons with energies just below $-2\sqrt{E_{FI}}$. I also assumed that the Rydberg electron is localized along the z-axis, which is only true for the $m_l = 0$ hydrogenic states which undergo no centrifugal effects. Thus, the more perpendicular the electron's orbital is from z_e, the larger E_{FI} is required. Also, the further the electron is from the $z_e < 0$ region, as is the case for the blue states, the greater the ionizing field required, $E_{FI} = E_H/(4n^4 ea_0)$ [60; 150]. The red states of the $m_l = 0$ manifold most closely follow the

classical ionization limit $W^2/4$, which is, including the linear Stark shift, in SI units,

$$E_{FI} = \frac{1}{9n^4}\left(\frac{E_H}{ea_0}\right). \tag{4.42}$$

4.2.3.1 Adiabatic Field Ionization

So far I have described the field ionization effects of high-l hydrogenic states, but the experiments discussed in this thesis involve field-ionization of nS and nP Rydberg states of rubidium, which are not degenerate with the hydrogenic manifold thanks to the considerable quantum defects discussed earlier in this chapter [70]. Furthermore, E_{FI} takes the form of a time-dependent pulse with a slew rate slower than the ratio of the square of quantum-defect coupling strength to the differential dipole moments between the hydrogenic and low-l states [151]. For instance, E_{FI} in my experiments is enveloped by a 1 μs-long exponential rise function that quickly drops to zero after it reaches its plateau. Therefore, I will now discuss how these states undergo adiabatic field ionization.

As the electric field is adiabatically ramped up with an exponential-rise dependence, the $(n+3)S$ and $(n+3)P$ Rydberg states reach the Inglis-Teller limit of the electric field ($\delta_{lj}/3n^5$ atomic units) where they merge with the n hydrogenic manifold. Instead of their energy-levels crossing with those of the hydrogenic states, the quantum defect couplings allow them to adiabatically follow into the middle of the hydrogenic manifold. When the electric field reaches the classical ionization limit, the adiabatic state is degenerate and couples with a low-n_1, state from a higher n-manifold that field ionizes at this field, effecting ionization [60]. The field required to ionize the $(n+3)S$ and $(n+3)P$ Rydberg states [60] is, for Rb, approximated in SI units as

$$E_{FI} \simeq \frac{E_H}{16ea_0}(n-1/2)^{-4} \tag{4.43}$$

$$E_{FI} \simeq \frac{E_H}{16ea_0}(n+1/2+1/n)^{-4}, \tag{4.44}$$

respectively. Hydrogenic manifolds with which these low-l states of Rb merge are shown in Fig. 4.7. This slow rise in E_{FI} is beneficial in that different Rydberg states will then ionize at different times, which can therefore allow destructive atomic-state readout using an MCP and particle counter with gated time delays. How this method is used in my Rydberg-atom experiments is explained in Chapter VI.
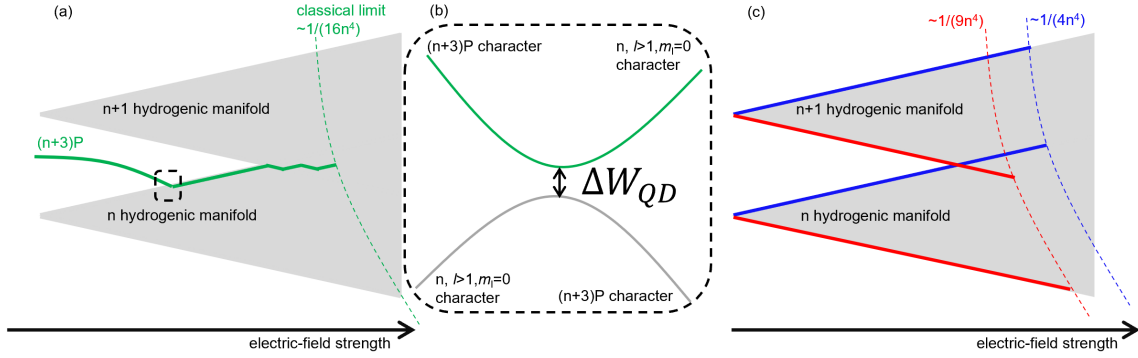
Figure 4.7: In (a), the $(n+3)P$ state with $m_l = 0$ becomes degenerate with hydrogenic states at the Inglis-Teller limit. The quantum defect mixes $(n+3)P$ with other states of high-l character, where it ionizes at the classical limit, depicted by the green, dashed curve. In (b), the inset is zoomed in, showing the avoided crossing with a gap ΔW_{QD} $\delta_{l=1,j}$. In (c), the field-ionization limit is shown for red and blue states of a fixed $m_l > 3$, where the quantum defect provides negligible mixing of states. (Disclaimer: All figures not drawn to scale.)

4.3   Magnetic Fields

I will now consider the paramagnetic behavior of Rydberg states in homogeneous magnetic fields $\mathbf{B} = B_0 \hat{\epsilon}$, where $\hat{\epsilon}$ is the polarization vector of $\mathbf{B}$. Weak Zeeman shifts are chosen to be discussed more thoroughly because all experiments, both demonstrated and proposed, consist of Rydberg atoms in magnetic fields at the mG-to-G levels. In this regime of magnetic field-strengths, especially for $B_0 << 1$ G, the Zeeman splittings of $|n, l, j, m_j\rangle$ are on the order of the Rydberg fine- or hyperfine-couplings for $nS_{1/2}$ and nP_j.

For the range, $n = 40 - 50$ in Rb, magnetic fields below 1 G are strong enough to induce hyperfine-state mixing and decoupling for the $nS_{1/2}$ and $nP_{1/2}$ states. After hyperfine decoupling, F, m_F are no longer "good" quantum numbers and the $|F, m_F\rangle$ states reorder into $|j, m_j\rangle |I, m_I\rangle$ states for a given atomic nuclear spin I. Before this reordering, the Zeeman effect originates from the $\frac{e}{m_e} \mathbf{A}(\hat{\mathbf{r}}_e) \cdot \hat{\mathbf{p}}_e$ interaction, where

$$\mathbf{A} = \frac{1}{2} B_0 \left(- r_{e\perp}^{(2)} \hat{\epsilon}_\perp^{(1)} + r_{e\perp}^{(1)} \hat{\epsilon}_\perp^{(2)} \right), \tag{4.45}$$

is the vector potential with orthogonal polarization vectors $\hat{\epsilon}_\perp^{(1)}$ and $\hat{\epsilon}_\perp^{(2)}$ perpendicular to $\hat{\epsilon}$ and generalized Rydberg-electron coordinates $r_{e\perp}^{(1)}$ and $r_{e\perp}^{(2)}$. The magnetic-dipole potential

is then

$$\hat{U}_Z = \frac{eB_0}{2m_e}\left(-\hat{r}_{e\perp}^{(2)}\hat{p}_{e\perp}^{(1)} + \hat{r}_{e\perp}^{(1)}\hat{p}_{e\perp}^{(2)}\right) = \frac{eB_0}{2m_e}g_F(\hat{\epsilon}\cdot\hat{\mathbf{F}}), \tag{4.46}$$

where $\hat{\mathbf{F}}$ is the total angular-momentum operator of the Rydberg electron after diagonalizing its Hamiltonian under the hyperfine-interaction and g_F is the gyromagnetic factor. Note that $F = |I + j|, .., |I - j|$, so for $I = 5/2$, characteristic of ^{85}Rb, $F = 2$ or 3 with $\left|nS_{1/2}\right\rangle$ and $\left|nP_{1/2}\right\rangle$ Rydberg states. The physics behind the energy separation between $F = 2$ and 3 will be discussed in Chapter VII.

For Rydberg states in $\left|nS_{1/2}, F = 2\right\rangle$ and $F = 3$, g_F is

$$g_{F=2} = g_j\frac{F(F+1) - I(I+1) + j(j+1)}{2F(F+1)} = 2\frac{2(3) - 5(7)/4 + 3/4}{2(2)(3)} = -1/3 \tag{4.47}$$

$$g_{F=3} = 1/3, \tag{4.48}$$

respectively, and, for $nP_{1/2}$ states, $g_{F'} = -1/9$ and $1/9$ for $F' = 2$ and $F' = 3$, respectively.

The magnetic field $\mathbf{B} = B_0\hat{\epsilon}$ is taken to be along the z-axis, or quantization axis. Then, the diagonal Zeeman shifts ΔW_Z of the Hamiltonian for $|F, m_F\rangle$ states become

$$\Delta W_Z = \mu_B g_F m_F B_0, \tag{4.49}$$

where the off-diagonal couplings between $|F, m_F\rangle$ and $|F \pm 1, m_F\rangle$ are determined by first expanding $|F, m_F\rangle$ states into the $|j, m_j\rangle |I, m_I\rangle$ basis using Clebsch-Gordan coefficients $\langle F, m_F|j, m_j\rangle |I, m_I\rangle$, and writing $\hat{U}_Z$ in terms of operators $\hat{I}_z$ and $\hat{J}_z$. This ends up only depending on the $\hat{J}_z$ operator because $g_I = 0$ for ^{85}Rb. Therefore,

$$\hat{U}_Z = \frac{\mu_B}{\hbar}g_j\hat{J}_z B_0, \tag{4.50}$$

so, the off-diagonal elements become

$$\langle F \pm 1, m_F|\hat{U}_Z|F, m_F\rangle = \frac{\mu_B}{\hbar}g_j B_0 \sum_{m_j, m_I} m_j \langle F, m_F|j, m_j\rangle |I, m_I\rangle \langle F \pm 1, m_F|j, m_j\rangle |I, m_I\rangle, \tag{4.51}$$

where all m_I and m_j must satisfy $m_I + m_j = m_F$ in each term. When these elements become stronger than the hyperfine splitting, the reordering of $|F, m_F\rangle$ states into those of the m_I, m_j basis begins. At field strengths beyond this, the Zeeman shifts are

$$\Delta W_Z = \frac{\mu_B}{\hbar}(g_I m_I + g_j m_j)B_0, \tag{4.52}$$

where, for ^{85}Rb, $g_I = 0$. Thus, all $|I, m_I\rangle$ level shifts are the same for a given m_j, as shown
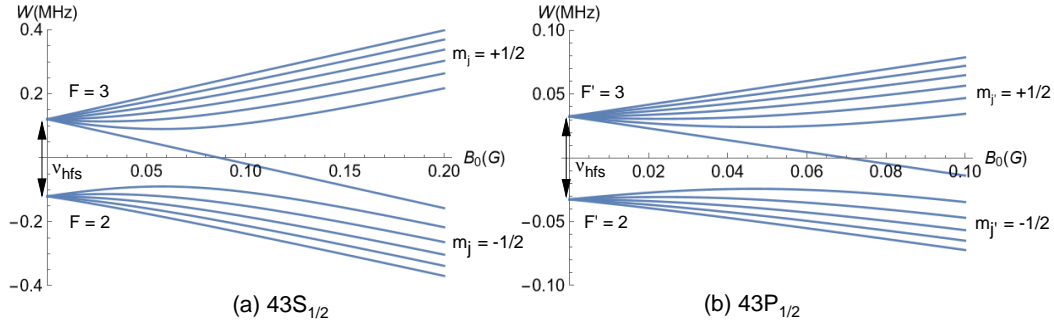
Figure 4.8: Zeeman shifts for (a) $\left|43S_{1/2}, F, m_F\right\rangle$ and (b) $\left|43P_{1/2}, F', m_{F'}\right\rangle$ states of ^{85}Rb. The hyperfine splittings for both states are shown, as well as the reordering of the magnetic substates from the F, m_F-basis to the m_I, m_j basis as B_0 increases. In both cases, **B** points along the quantization axis.
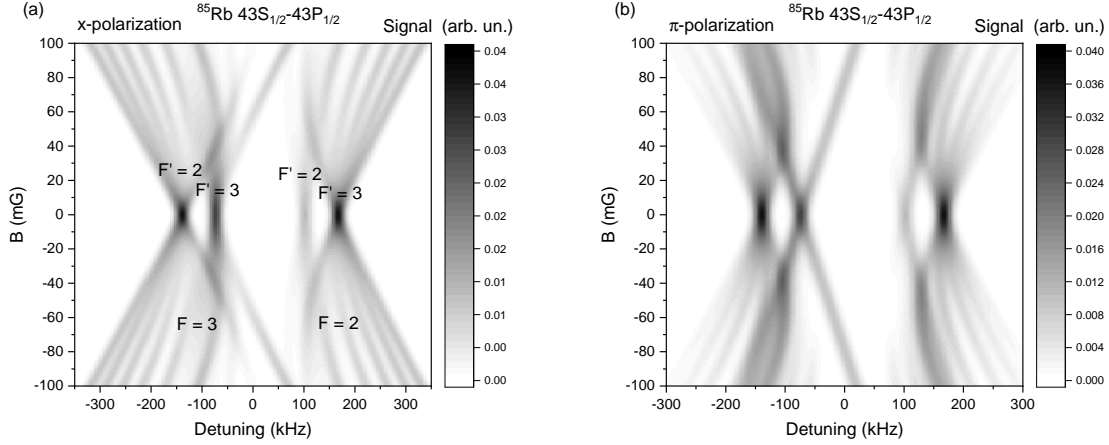
Figure 4.9: Calculated spectra of the $\left|43S_{1/2}, F, m_F\right\rangle \rightarrow \left|43P_{1/2}, F', m_{F'}\right\rangle$ transition for separate polarization cases of the electric-dipole coupling field: (a) x-polarized and (b) π-polarized. For the magnetic fields applied below 100 mG, reordering of the $\left|43P_{1/2}, F', m'_F\right\rangle$ states occur within this range.

in Fig. 4.8.

Experimentally, these level shifts can be detected by probing electric-dipole transitions between two different Rydberg states of different l and j quantum numbers. Cases in which the hyperfine structure of both states is comparable to the Zeeman shifts provide a nontrivial spectrum that is dependent on the coupling field's polarization with respect to $\hat{\epsilon}$. Specifically, the transition $\left|43S_{1/2}, F, m_F\right\rangle \rightarrow \left|43P_{1/2}, F', m_{F'}\right\rangle$ is depicted in Fig. 4.9 for π- and x-polarized electric-dipole coupling fields.
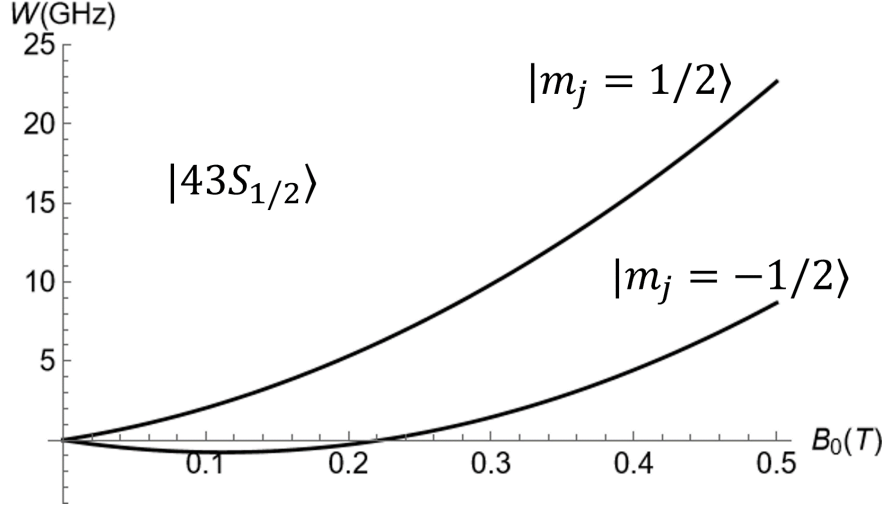
Figure 4.10: Level shifts of $\left|43S_{1/2}, m_I, m_j\right\rangle$, where m_I is fixed and B_0 is increased well above 1 kG. Here, the quadratic behavior at large B_0 is due to diamagnetic effects.

4.3.1 Diamagnetism of Rydberg States

At even stronger fields reaching 1 T, the $\hat{A}^2$ term of the Hamiltonian, describing diamagnetic effects, becomes significant. The diamagnetic interaction is, for $\hat{\epsilon} = \hat{k}$

$$U_D(\hat{\mathbf{r}}_e) = \frac{e^2}{2m_e} A^2(\hat{\mathbf{r}}_e) = \frac{e^2 B_0^2}{8m_e}(\hat{r}_e^2 - \hat{z}_e^2), \tag{4.53}$$

where, for $\left|43S_{1/2}\right\rangle$ in the m_I, m_j basis, $\langle\hat{r}_e^2\rangle - \langle\hat{z}_e^2\rangle = 4.212 \times 10^6 a_0^2$. Thus, because this potential depends on the Rydberg wave function overlap with the vector potential, both m_j states in this case see the same diamagnetic shifts, which are shown for $\left|43S_{1/2}\right\rangle$ in Fig. 4.10.

4.4 Microwave Spectroscopy

Electromagnetic radiation that is either absorbed or emitted by Rydberg atoms ranges from the RF-to-THz spectrum. For instance, Rydberg states at about $n = 50$ will strongly absorb millimeter-wavelength fields. These low-energy transitions are what grant Rydberg states their long lifetimes and narrow energy widths at the order of $2\pi \times 1$ kHz. Therefore, radiated millimeter and microwaves can interact with these states for sub-ms durations τ before the Fourier-limit (FWHM=$0.89/\tau$) reaches the natural linewidths Γ. And so, provided that all systematic perturbations are accounted for, Rydberg energies can be determined through spectroscopy with sub-kHz uncertainties. In order to prevent power-broadening of the spectroscopic transition, the radiated power must often be kept to well below 1 nW depending on the strengths of the first- and multi-order matrix elements of the electric-dipole

86

interaction.

In a two-level Rydberg system, microwave radiation detuned $\delta_\mu = (\omega_\mu - \omega_0)/2\pi$ from the resonance of the transition $\omega_0/2\pi$ with homogeneous coupling strength Ω_0 changes the internal state from $|0\rangle$ to $|1\rangle$ with a probability

$$P_{0\to1} = \frac{\Omega_0^2}{\Omega_0^2 + 4\pi^2\delta_\mu^2} \sin^2\left(\frac{\tau}{2}\sqrt{\Omega_0^2 + 4\pi^2\delta_\mu^2}\right). \tag{4.54}$$

When τ is kept fixed, $P_{0\to1}$ can be rearranged as

$$P_{0\to1} = (\Omega_0^2\tau^2/4)\,\mathrm{sinc}^2\left(\frac{\tau}{2}\sqrt{\Omega_0^2 + 4\pi^2\delta_\mu^2}\right). \tag{4.55}$$

This function is sharply peaked on resonance $\delta_\mu = 0$ with an amplitude determined by the *pulse area* (θ). In general the pulse area is the following quantity,

$$\theta(\tau) = \int_0^\tau \Omega_0(t)dt, \tag{4.56}$$

where $\Omega_0(t)$ has some pule-envelope amplitude-modulating the field. Often times, a square pulse is used where $\Omega_0[\Theta(t) - \Theta(t-\tau)]$ ($\Theta(t)$ is the Heaviside step function). Then $\theta = \Omega_0\tau$. When $\theta = \pi$, population inversion occurs; when $\theta = 2\pi$, the system undergoes population inversion before returning to its initial internal state. However, $|0\rangle$ acquires a π phase shift even though no line appears on resonance. Rydberg microwave spectra corresponding to three different pulse areas are depicted in Fig. 4.11(a)-(c).

In Fig. 4.11(d), τ is kept at 50 μs, $\delta_\mu = 0$, but Ω_0 is varied. As a result $P_{0\to1}$ undergoes periodic oscillations known as *Rabi flopping*. By carefully choosing θ, the population and phase of the initialized Rydberg state $|\psi\rangle = c_0(t)\,|0\rangle + c_1(t)\,|1\rangle$ can be manipulated for internal-state interferometry [46], quantum-state engineering [61; 152; 153], and spin manipulations in quantum processors and simulators [133; 135].

Subsequent chapters will show, through experiment and theory, that microwave radiation is not the only way to manipulate internal Rydberg states of alkali metals, and that microwave driving of Rydberg-Rydberg transitions has major drawbacks in terms of site-selective excitation, phase control, and frequency accessibility. A better way to probe alkali Rydberg transitions would be to use laser light that can, in principle, be focused down to the size a single atom and does not follow conventional Δl selection rules. With this proposed method, transitions between a low-l Rydberg state and the CS, separated by a few THz, can be driven in the first order to initialize a sample of atoms in state $|nC\rangle$ for the fundamental
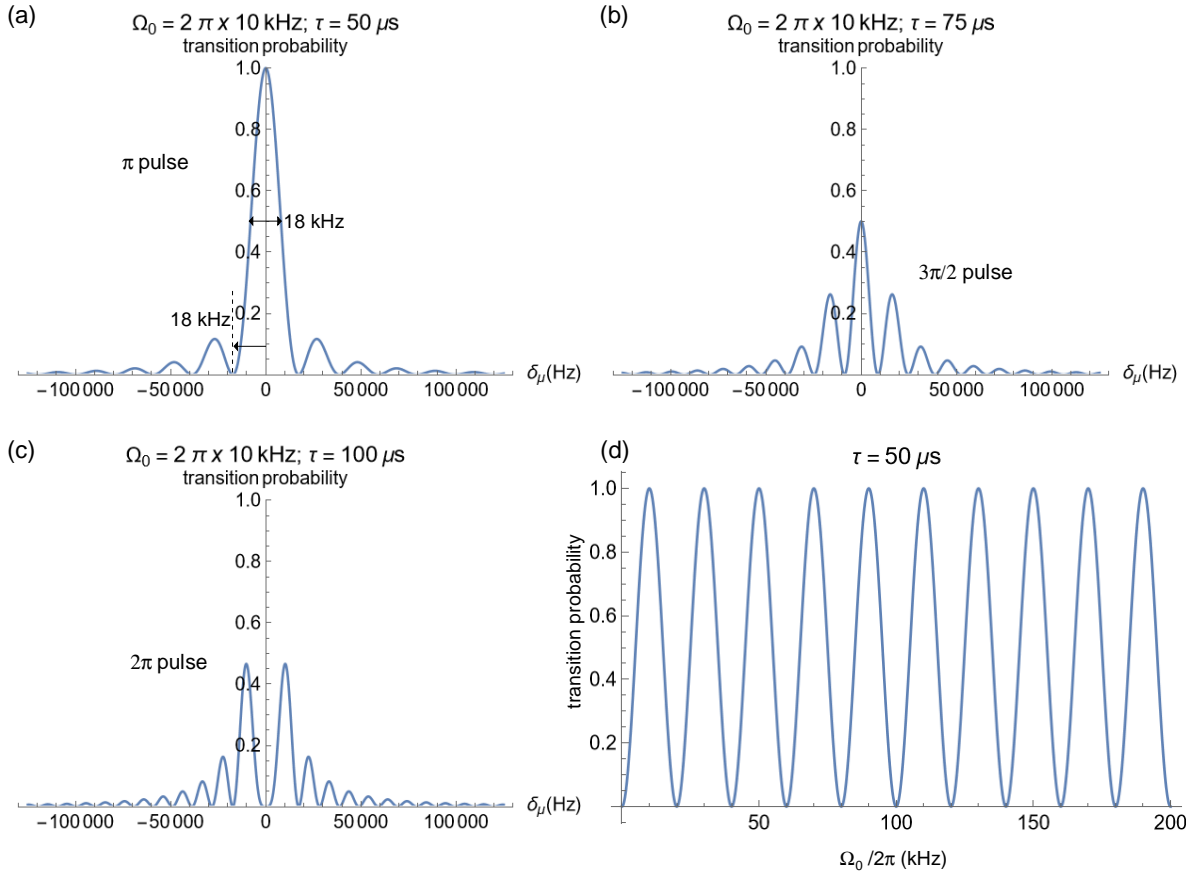
Figure 4.11: Spectroscopy by a microwave source between $|0\rangle$ and $|1\rangle$ Rydberg states with pulse areas: (a) $\theta = \pi$, (b) $3\pi/2$, and (c) 2π. In (d), Rabi flopping is shown at $\tau = 50$ μs and $\delta_\mu = 0$ as Ω_0 is varied.

physics applications initially proposed.

CHAPTER V

Theory of Rydberg Atoms in Light

This chapter is primarily based on Ref. [5].

When a bound atomic electron in the Rydberg state is placed in an electromagnetic field that oscillates at optical frequencies and has a wavelength on the order of the spatial extent of the electron's wave function, unique dynamics arise different from the more commonly observed electric-dipole interactions that deeply-bound atomic states undergo in optical radiation. Electric-dipole interactions between the optical field and the deeply-bound electrons were discussed thoroughly in Chapter II, so I will only briefly discuss them here in the context of Rydberg-atom excitation with lasers and photoionization (PI). For a significant portion of the optical spectrum, Rydberg atoms will mainly experience conservative *ponderomotive forces*, which originate from the valence electron wiggling at the frequency of the applied light field. On the other hand, a conservative electric-multipole force acting on the Rydberg electron is only comparable in strength to the ponderomotive force near very narrow Rydberg-ground resonances (typically < 10 MHz) [86]. For all wavelengths within the optical spectrum, there exist electric-dipole transitions between the Rydberg states and FESs, which leads to PI of the Rydberg atom. All of these effects collectively acting on Rydberg atoms are necessary to understand if deep, time-modulated optical lattices are to be used for preparing a sample of circular states (CSs).

In this chapter, I will describe the classical and quantum origins of the ponderomotive force acting on the Rydberg electron in the first section. Then, I describe PI effects of Rydberg atoms in the following section. For the third section, I will explain ponderomotive shifts and couplings of $nS_{1/2}$ and nP_j Rydberg states in a one-dimensional optical lattice; for Section 5.4, I will explain the effects of lattice-induced fine-structure mixing for nF_j Rydberg states and the PI rates of the mixed states. In Section 5.5, I will discuss hydrogenic-state mixing with $|nF_j\rangle$ in an optical lattice with a depth of $\sim 10^6$ single-photon recoils, as well as the mixed states' lifetimes arising from PI. More for entertainment than pedagogical purposes,

the last section investigates the quantum-electrodynamic description of the ponderomotive interaction with Rydberg electrons for a static and amplitude-modulated optical lattice.

5.1 Ponderomotive Potentials

A classical model of the Rydberg atom with low-velocity center-of-mass (CM) at $\mathbf{R}_0$ and a localized valence-electron at relative position $\mathbf{r}_e$ is presented in Fig. 5.1. The electron experiences an elliptical Keplerian orbit and is free to wobble under any external force with a deviation quantified by vector $\vec{\rho}$. When the external force originates from a monochromatic laser field far-off-resonant (FOR) from any Rydberg-ground transition and the atom, CM motion changes at $\gtrsim 1$ μs timescales, the electron's orbit has a period around ~ 0.1 ns, and the deviation, or quiver motion, has a period matching that of the laser (~ 1 fs). Because these timescales differ so significantly, the Born-Oppenheimer approximation (BOA) can be applied and each vector can be adiabatically separated, i.e., the more slowly varying positions can be treated as constants while the faster is calculated. I will start off this section by deriving the ponderomotive potential energy U_p on the Rydberg electron with a classical model, then use a quantum one.

5.1.1 Classical Model

Under the BOA, $\mathbf{R}_0$ and $\mathbf{r}_e$ remain constant while $\boldsymbol{\rho}$ is rapidly changing under the influence of the laser's electric field at $\mathbf{R}_0 + \mathbf{r}_e$. Neglecting the part of the Lorentz force from the laser's magnetic field, Newton's second law yields, in the direction of the laser's polarization,

$$m_e \ddot{\rho} = -e\mathcal{E}(\mathbf{R}_0 + \mathbf{r}_e) \cos\left[k_L(Z_0 + z_e) - \omega_L t\right], \tag{5.1}$$

so the kinetic momentum $\frac{1}{2m_e}(\mathbf{p}_0 + e\mathbf{A})^2$ is then

$$m_e \dot{\rho} = \frac{e}{\omega_L}\mathcal{E}(\mathbf{R}_0 + \mathbf{r}_e) \sin\left[k_L(Z_0 + z_e) - \omega_L t\right], \tag{5.2}$$

and the kinetic energy, $T(t)$ is the following periodic function,

$$T(t) = \frac{e^2|\mathcal{E}(\mathbf{R}_0 + \mathbf{r}_e)|^2}{2m_e\omega_L^2} \sin^2\left[k_L(Z_0 + z_e) - \omega_L t\right]. \tag{5.3}$$

On average, over many cycles of the optical period, $\langle T \rangle_t$ is

$$\langle T \rangle_t = \frac{e^2|\mathcal{E}(\mathbf{R}_0 + \mathbf{r}_e)|^2}{4m_e\omega_L^2}. \tag{5.4}$$
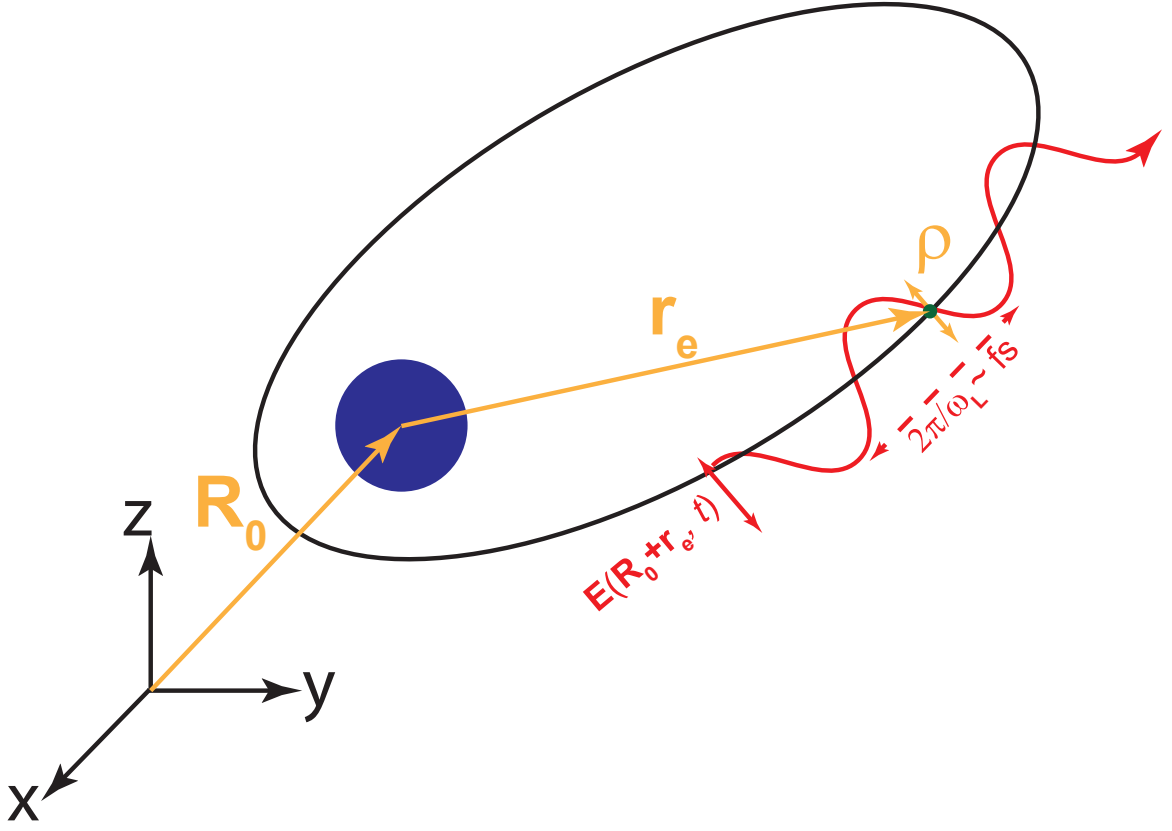
Figure 5.1: Figure adapted from [4]. Relevant position vectors associated with the Rydberg electron (green) in a classical model of the atom: the CM vector $\mathbf{R}_0$ located at the ion-core (blue) position , the relative vector at the position of the Rydberg electron with respect to the CM $\mathbf{r}_e$, and the quiver vector $\boldsymbol{\rho}$ representing deviations from the elliptical orbit. Deviations can arrive from the laser field $\mathbf{E}$ oscillating at frequency $\omega_L/(2\pi)$.

Because the force on the quivering electron is conservative, the kinetic energy acquired on average is equal to the potential energy associated with the ponderomotive force U_p, so

$$U_p = \frac{e^2|\mathcal{E}(\mathbf{R}_0 + \mathbf{r}_e)|^2}{4m_e\omega_L^2}. \tag{5.5}$$

The ponderomotive force is then $\mathbf{F}_p = -\vec{\nabla}U_p = -\frac{1}{4}\alpha_e(\omega_L)\vec{\nabla}|\mathcal{E}(\mathbf{R}_0 + \mathbf{r}_e)|^2$, where $\alpha_e(\omega_L) = -\frac{e^2}{m_e\omega_L^2}$ is the *free-electron polarizability*. It is called so because the electron in this frame is treated like a free particle positioned at $\mathbf{R}_0 + \mathbf{r}_e$.

5.1.2 Quantum Model

Quantum mechanically, the quasi-free electron in the time-frame of vector operator $\hat{\boldsymbol{\rho}}$ has properties of a plane wave that extends through all space with a well-defined canonical momentum $\hat{\mathbf{p}}_0$ conjugate to $\hat{\boldsymbol{\rho}}$. The Hamiltonian operator is

$$\hat{H}_q(t) = \frac{\hat{p}_0^2}{2m_e} + \frac{e}{m_e}[\mathbf{A}(\mathbf{R}_0 + \mathbf{r}_e, t) \cdot \hat{\mathbf{p}}_0] + \frac{e^2}{2m_e}|\mathbf{A}^2(\mathbf{R}_e + \mathbf{r}_e, t)|, \tag{5.6}$$

where $\mathbf{A}(\mathbf{R}_0 + \mathbf{r}_e, t) = \hat{\epsilon}\frac{\mathcal{E}(\mathbf{R}_0 + \mathbf{r}_e)}{\omega_L} \sin[k_L(Z_0 + z_e) - \omega_L t]$, so

$$\hat{H}_q(t) = \frac{\hat{p}_0^2}{2m_e} + \frac{e\mathcal{E}(\mathbf{R}_0 + \mathbf{r}_e)}{m_e\omega_L}(\hat{\epsilon} \cdot \hat{\mathbf{p}}_0)\sin[k_L(Z_0 + z_e) - \omega_L t]$$
$$+ \frac{e^2|\mathcal{E}(\mathbf{R}_0 + \mathbf{r}_e)|^2}{2m_e\omega_L^2}\left[\frac{1}{2} - \frac{1}{2}\cos[2k_L(Z_0 + z_e) - 2\omega_L t]\right], \tag{5.7}$$

Thus, the electron's quiver motion $\vec{\rho}$ yields the following phase-modulated wave function

$$\Psi_q(\vec{\rho}, t) = e^{i\mathbf{p}_0 \cdot \boldsymbol{\rho}/\hbar}e^{-ip_0^2 t/(2\hbar m_e)}e^{-i\frac{e^2|\mathcal{E}(\mathbf{R}_0 + \mathbf{r}_e)|^2}{4m_e\hbar\omega_L^2}}e^{-i\frac{e\mathcal{E}(\mathbf{R}_0 + \mathbf{r}_e)}{m_e\hbar\omega_L^2}(\hat{\epsilon}\cdot\hat{\mathbf{p}}_0)\cos[k_L(Z_0 + z_e) - \omega_L t]}$$
$$\times e^{-i\frac{e^2|\mathcal{E}(\mathbf{R}_0 + \mathbf{r}_e)|^2}{8m_e\hbar\omega_L^3}\sin[2k_L(Z_0 + z_e) - 2\omega_L t]}, \tag{5.8}$$

known as a Volkov state [110] with a time-averaged eigenenergy

$$\frac{p_0^2}{2m_e} + U_p(\mathbf{R}_0 + \mathbf{r}_e). \tag{5.9}$$

The first term is a constant offset for all Rydberg states and can be removed from the eigenenergy. According to the BOA, the term $U_p(\mathbf{R}_0 + \hat{\mathbf{r}}_e)$ now acts as a function of an operator in the relative coordinate's Schrödinger equation,

$$\hat{H}_e = \hat{p}_e^2/(2m_e) + U_C(\hat{\mathbf{r}}_e) + U_{LS}(\hat{\mathbf{r}}_e) + U_p(\mathbf{R}_0 + \hat{\mathbf{r}}_e) + \frac{e\mathcal{E}(\mathbf{R}_0 + \hat{\mathbf{r}}_e)}{m_e\omega_L}\sin[k_L(Z_0 + \hat{z}_e) - \omega_L t](\hat{\epsilon} \cdot \hat{\mathbf{p}}_e), \tag{5.10}$$

where $U_C(\hat{\mathbf{r}}_e)$ arises from the Coulomb interaction between the nucleus and inner-shell electrons and the Rydberg electron and $U_{LS}(\hat{\mathbf{r}}_e)$ accounts for spin-orbit coupling. Electric-dipole interactions that lead to PI, optical-dipole shifts, and Rydberg-ground transitions originate from the final term.
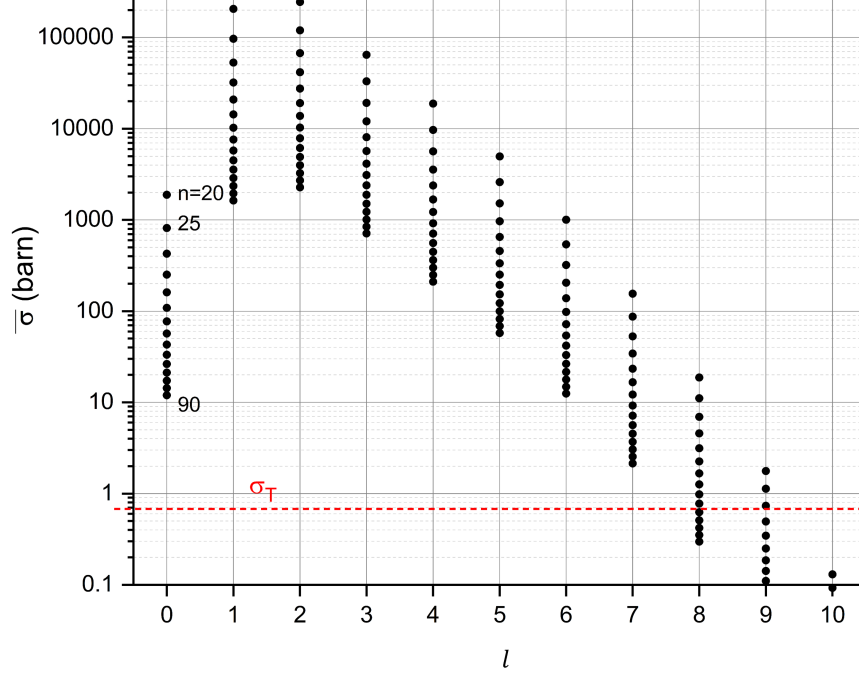
Figure 5.2: Figure taken from [5]. Total shell-averaged photoionization (PI) cross sections for Rb Rydberg states with fine-structure removed and $\lambda = 1064$ nm calculated for every five n and increasing l. The Thomson-scattering cross section $\sigma_T = 0.665$ b (explained in the penultimate section of Chapter V) is denoted by the red, dashed line.

5.2 Photoionization of Rydberg Atoms

When the laser frequency is FOR (typically > 10 MHz) from any $|n, l, j, m_j\rangle$ Rydberg-bound-state electric-dipole transitions, conservative light forces from the final term in Eq. 5.10 are neglected, and the real part of the state polarizability is just $\alpha_e(\omega_L)$. While the real part of the AC polarizability is just $\alpha_e(\omega_L)$, there is also an imaginary part proportional to the the PI cross section σ_{n,l,j,m_j},

$$\sigma_{n,l,j,m_j} = \sum_{l',m_{l'}} (\sigma_{*,n,l,j,m_j-1/2}^{\epsilon',l',m_{l'}} |c_{\uparrow,m_j-1/2}^{j,m_j,s,l}|^2 + \sigma_{*,n,l,j,m_j+1/2}^{\epsilon',l',m_{l'}} |c_{\downarrow,m_j+1/2}^{j,m_j,s,l}|^2), \qquad (5.11)$$

where "$*$" denotes the polarization of the laser field, resulting in Eq. 2.70 for a laser propagating along z and Eq. 2.69 for one along x. The quantities $c_{\uparrow,m_j-1/2}^{j,m_j,s,l}$ and $c_{\downarrow,m_j+1/2}^{j,m_j,s,l}$ are Clebsch-Gordan coefficients. Cross sections $\sigma_{*,n,l,j,m_j\mp1/2}^{\epsilon',l',m_{l'}}$ are proportional to $\bar{\sigma}_{n,l}^{\epsilon',l'}$, which, is the sum over all $l' = l \pm 1$ allowed by electric-dipole selection rules. Quantities $\bar{\sigma}_{n,l}^{\epsilon',l'}$ are presented in Fig. 5.2 for $\lambda = 1064$ nm.

It is noteworthy that I made the electric-dipole (E1) approximation when it is not at

all true that $\langle r_e \rangle << \lambda$ for Rydberg states. Against all intuition, the E1 approximation is indeed valid for transitions between orbitals (free or bound) of the Rydberg electron when studying electric-multipole interactions between the optical radiation and atoms. In order to believe this with a classical example, consider the case of a free electron making a parabolic orbit around a heavy ion. As it turns the corner at the closest distance from the ion's CM, optical Bremsstrahlung radiation is most likely to be emitted from the particle at a rate proportional to the square of its Coulomb acceleration [68], which is maximum at this turning point. This change in energy of the electron is enough for it to transition into a bound orbital: recombination of the ion-electron pair into a bound Rydberg state occurs. Recombination is the opposite effect of PI, so it can be concluded that the process occurs where $\mathbf{r}_e \to 0$ and where the E1 approximation ($r_e << \lambda$) is valid. Experimental verification of the E1 approximation's reliability in studying Rydberg PI was provided in [154]. For high-l atomic states that do not orbit close to the ion core, like the CS, PI cross sections drop towards the Thomson scattering cross section and are immeasurable even with modern experimental equipment.

A quantum explanation for the PI effect occurring near the ion core requires investigating the overlap between Rydberg and FES wave functions, which was theoretically determined to be the strongest when the kinetic energies of the two electronic states were minimal and the Coulomb acceleration was maximal [155; 156]. Similar reasoning also explains *propensity rules* , where electric-dipole matrix elements are stronger for $\Delta l = +1$ than -1 transitions [156].

In this section, I will show how much higher-order multipoles contribute to $\mathbf{A} \cdot \mathbf{p}_e$ matrix elements in the context of bound-free transitions with Rydberg $|nF\rangle$ states neglecting spin-orbit coupling. Using the n, l, m_l basis for a fixed spin state of the electron, the matrix element coupling $|nF\rangle$ and the FES $|\epsilon', l', m_{l'}\rangle$ is, including all multipole orders for a π-

polarized laser field in the paraxial approximation

$$\langle \epsilon', l', m_{l'}| U_{AF}(\mathbf{R}_0 + \hat{\mathbf{r}}_e, t) |n, l = 3, m_l\rangle e^{i\omega_{n,l}^{\epsilon'l'}t} = -i\frac{e\hbar\mathcal{E}(\mathbf{R}_0)}{m_e\omega_L}$$

$$\times \langle \epsilon', l', m_{l'}| \sin[k_L(X_0 + \hat{x}_e) - \omega_L t]\frac{\partial}{\partial z_e} |n, l = 3, m_l\rangle e^{i\omega_{n,l}^{\epsilon'l'}t}$$

$$\simeq \frac{-e\hbar\mathcal{E}(\mathbf{R}_0)}{2m_e\omega_L}e^{ik_L X_0} \langle \epsilon', l', m_{l'}| e^{ik_L \hat{r}_e \sin\hat{\theta}_e \cos\hat{\phi}_e}\frac{\partial}{\partial z_e} |n, l = 3, m_l\rangle$$

$$= -i^{m_{l'} - m_l}\frac{e\hbar\mathcal{E}(\mathbf{R}_0)}{2m_e\omega_L}e^{ik_L X_0} \int d^3\mathbf{r}_e \psi_{\epsilon',l',m_{l'}}^* J_{m_{l'} - m_l}(k_L r_e \sin\theta_e)e^{-i(m_{l'} - m_l)\phi_e}\frac{\partial \psi_{n,l,m_l}}{\partial z_e}$$

$$= -i^{m_{l'} - m_l}\frac{e\hbar\mathcal{E}(\mathbf{R}_0)}{4m_e\omega_L}e^{ik_L X_0}\sqrt{\frac{2l'+1}{2l+1}\frac{(l'-m_{l'})!}{(l'+m_{l'})!}\frac{(l-m_l)!}{(l+m_l)!}}$$

$$\times \left\{ \left[\int_0^\infty u_{n',l'}(r_e)[u'_{n,l}(r_e) - \frac{u_{n,l}(r_e)}{r_e}(l+1)]\left[\int_0^\pi J_{m_{l'} - m_l}(k_L r_e \sin\theta_e)P_{l'}^{m_{l'}}(\cos\theta_e)P_{l+1}^{m_l}(\cos\theta_e)\right.\right.$$

$$\times (l - m_l + 1)\sin\theta_e d\theta_e\right]dr_e + \int_0^\infty u_{n',l'}(r_e)[u'_{n,l}(r_e) + \frac{u_{n,l}(r_e)}{r_e}l]\left[\int_0^\pi J_{m_{l'} - m_l}(k_L r_e \sin\theta_e)P_{\ell'}^{m_{l'}}(\cos\theta_e)\right.$$

$$\left.\left.\times P_{l-1}^{m_l}(\cos\theta_e)(l + m_l)\ \sin\theta_e\ d\theta_e\right]dr_e\right\}, \quad (5.12)$$

where it is assumed that $\omega_L = \omega_{n,l}^{\epsilon',l'}$.

Under the E1 approximation $k_L r_e \to 0$, the matrix element becomes proportional to $\delta_{m_{l'}}^{m_l}$, and the integrals of the associated Legendre functions allow only $l' = l \pm 1$. For $\omega_L = 2\pi c/(532 \text{ nm})$, I present calculations of $\sigma_{z,n,l,m_\ell}^{\epsilon',l',m_l'}$, where $n = 15$ and $\epsilon' = 0.083E_H$. Similar calculations in the context of $|nD_j\rangle$ PI are provided in [157; 154] Calculations of the cross section are presented in Fig. 5.3(a) for ranges of $l' : [0, 14]$ and $m_l' : [-l', l']$. The relation between the matrix element and the cross sections are

$$\sigma_{z,n=15,l=3,m_\ell}^{\epsilon'=0.083E_H, l', m_l'} = \frac{\pi e^2\hbar^2}{\epsilon_0 m_e^2\omega_L c}|\langle \epsilon' = 0.083E_H, l', m_l'| U_{AF}(\mathbf{R}_0 + \hat{\mathbf{r}}_e) |n = 15, l = 3, m_l\rangle|^2. \quad (5.13)$$

As can be seen in the figure, at $\lambda = 532$ nm the cross sections proportional to dipole-forbidden matrix elements are a factor of 10^5 smaller than the $|15, l = 3, m_l = 0\rangle \to |0.083E_H, l' = 4, m_l' = 0 >$ cross sections favored by propensity rules. The leading dipole-forbidden transitions are $|15, l = 3, m_l = 0\rangle \to |0.083E_H, l' = 5, m_l' = \pm 1\rangle$, which have $\sigma = 0.18$ b (1 b$= 10^{-28}$ m^2). Thus, the classical and quantum arguments of the E1 approximation's validity for Rydberg-atom absorption and emission of radiation in the optical spectrum agree well.
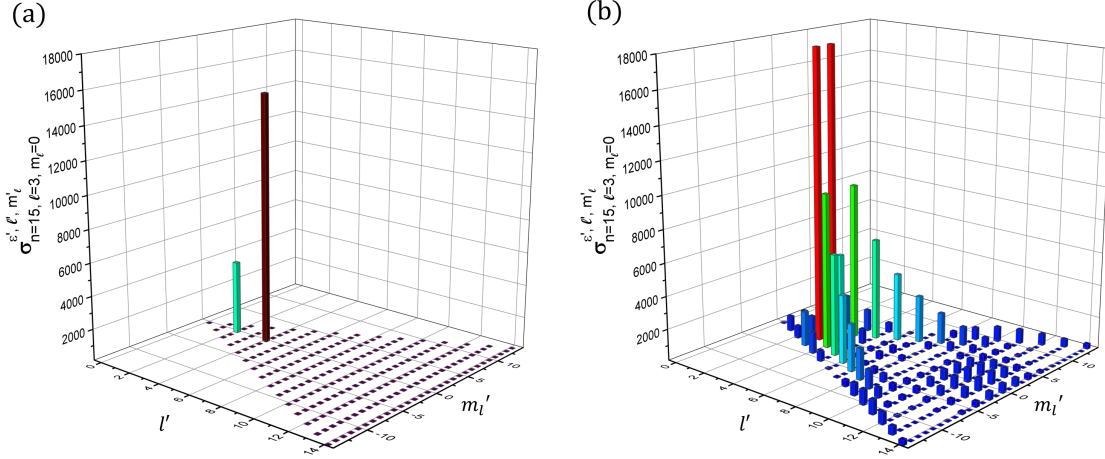
Figure 5.3: Figure taken from [5]. $|15F\rangle$ PI cross sections for $|15, l = 3, m_l = 0 >\to$ $|0.083E_H, l', m_l' >$ ionization channels with $\lambda = 532$ nm and $\kappa = 1$ in (a). The E1 approximation is adhered to, even though the optical wavelength varies within the Rydberg wave function. If atom's inner ion core sees a significant spatial variation of the ionizing radiation, which is what happens when the wavelength is artificially reduced by a factor of $\kappa = 1000$ and spatially resembles an X-ray, the E1 approximation fails. This failure is shown in (b), where dipole-forbidden transitions contribute most to the overall $|15F_j >$ PI cross section.

Artificial enhancement of the dipole-forbidden cross sections are possible by increasing k_L by a numerical factor $\kappa = 1000$ without reducing the $1/\omega_L$ prefactor. It is not possible in any experimental setting to make X-ray wavelengths with optical frequencies. Dipole-forbidden ionization channels that are permitted by X-rays always have their excitation rates reduced by κ [155]. In Fig. 5.3(b), I present the now more visible dipole-forbidden cross sections with an artificial wavelength of 0.532 nm (ω_L and ϵ' remain the same). Here, the E1 approximation is demonstrably invalid, as the previously favored transition of $|15, l = 3, m_l = 0\rangle \to$ $|0.083E_H, l' = 4, m_l' = 0\rangle$ now contributes a cross-section contribution of 5451 b while the dipole-forbidden channels $|15, l = 3, m_l = 0\rangle \to |0.083E_H, l' = 3, m_l' = \pm1\rangle$ provide the primary contributions of 17850 b each.

By choosing a both a dipole-allowed $|15, l = 3, m_l = 0\rangle \to |0.083E_H, l' = 4, m_l' = 0\rangle$ and -forbidden transition $|15, l = 3, m_l = 0\rangle \to |0.083E_H, l' = 3, m_l' = 1\rangle$, radial range of the $U_A F$ is presented for both respective channels in Fig. 5.4(a) and (b). This demonstration is done by varying the upper constraints r_{max} in the radial integrals of Eq. 5.12. Fig. 5.4(a) shows that σ begins to oscillate around the converging value of $\sigma_0 = 15220$ b below 100 a_0, lower than the distance from the nucleus to the final slope of the radial wave function (~ 400 a_0). In fact, by

96
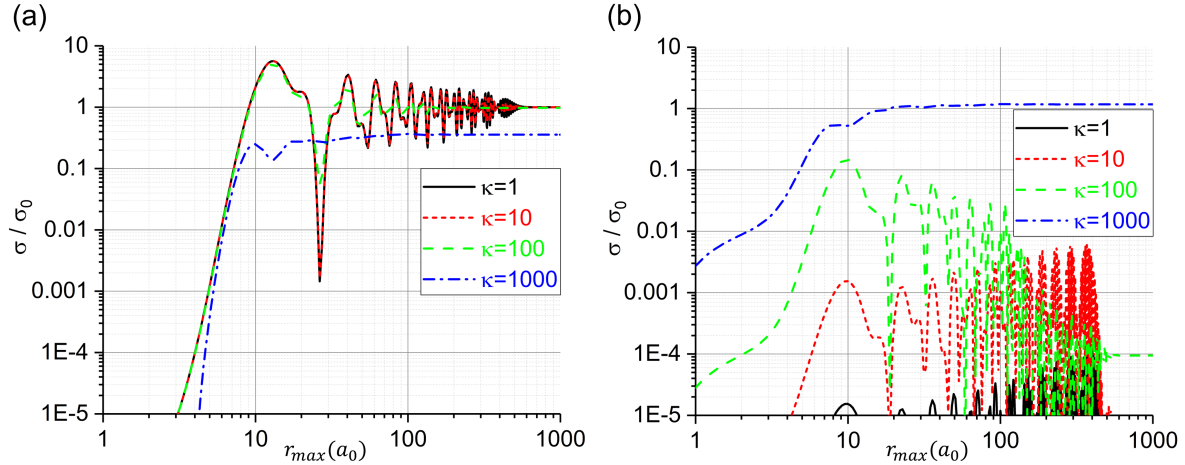
Figure 5.4: Figure taken from [5]. Calculation of σ with the indicated κ for the $|15, l = 3, m_l = 0 > \rightarrow |0.083E_H, l' = 4, m'_l = 0 >$ channel ($\lambda = 532$ nm and $\sigma_0 = 15220$ b) in (a). For (b), the same is done for the $|15, l = 3, m_l = 0 > \rightarrow |0.083E_H, l' = 3, m'_l = 1 >$ PI channel ($\lambda = 532$ nm and $\sigma_0 = 17850$ b). The purpose of this calculation is to investigate the radial range of light-matter electric-multipole interactions. Because the converging results of the PI cross sections do not change for up to $\kappa = 100$, it is concluded that the range is less than $50a_0$.

increasing κ even to 100, there is no change in the converging value of σ_0, suggesting that the atom-field interaction extends to a distance of $50a_0$ from the CM position for $\lambda = 532$ nm. As κ is increased to 1000, there is an evident drop in σ_0 for the dipole-allowed transition while the converging value of the dipole-forbidden cross section shown in Fig. 5.4(b) rises from $<< 1$ b to $\sigma_0 = 17850$ b, which suggests that the potential provided by the artificial X-ray varies substantially within the range of the atom-field interaction. The range of electric-multipole atom-field interactions for Rydberg atoms were similarly discussed in [157; 154; 156; 158].

While electric-multipole interactions with the laser are short-range effects most evident in regions where the Coulomb interactions are the greatest, ponderomotive interactions are mostly visible in regions where the acceleration of the bound-electron is at a minimum and is primarily quivering at the frequency of the field. Both effects will be discussed in the following sections for a standing-wave laser field that provides an optical lattice having a propagation direction serve as the quantization axis. Each section will discuss effects on the Rydberg atom's CM, internal state, and PI-induced decay rate. The laser field will be presented as an ideal standing wave with intensity

$$I(\mathbf{R}_0 + \mathbf{r}_e) = c\epsilon_0\mathcal{E}_0(\mathbf{R}_0 + \mathbf{r}_e)^2(1 + \cos[2k_L(Z_0 + z_e)]). \tag{5.14}$$

If the standing wave does not have a transverse intensity profile that varies significantly within the Rydberg-electron wave function, $\mathcal{E}_0(\mathbf{R}_0 + \mathbf{r}_e)^2 \simeq \mathcal{E}_0(\mathbf{R}_0)^2$, which can also be safely made under the paraxial approximation.

5.3 $nS_{1/2}$ and nP_j Alkali Rydberg Atoms in an Optical Lattice

This section concerns effects of $nS_{1/2}$ and nP_j Rydberg atoms placed inside a one-dimensional optical lattice of wavelength $\lambda = 1064$ nm and intensity given by Eq. 5.14. In particular, the first sub-section deals with shifts in the internal-state energies and the couplings between two orthogonal Rydberg states. The second sub-section discusses the classical forces on the CM vector but does not review Bloch's theorem for atoms in optical lattices, as it was already covered in Chapter II. The third sub-section derives expressions for $\Gamma_{PI,n,l,j,|m_j|}$ for all possible nS and nP Rydberg states, which arises from photoionization (PI).

5.3.1 Internal-State Effects

Considering that the lattice waist is much larger than the Rydberg-atom diameter, I discuss effects on the Rydberg electron's internal state from the ponderomotive potential operator

$$
\begin{aligned}
U_p(\mathbf{R}_0 + \hat{\mathbf{r}}_e) &= -\frac{1}{2}\alpha_e(\omega_L)\mathcal{E}(\mathbf{R}_0)^2(\hat{\mathbb{1}} + \cos\left[2k_L(Z_0 + \hat{z}_e)\right]) \\
&= U_0 f(\mathbf{R}_0)[\hat{\mathbb{1}} + \cos\left(2k_L Z_0\right)\cos\left(2k_L\hat{z}_e\right) - \sin\left(2k_L Z_0\right)\sin\left(2k_L\hat{z}_e\right)] \\
&= U_0 f(\mathbf{R}_0)[\hat{\mathbb{1}} + \sum_{p=0}^{\infty}(-1)^p[\cos\left(2k_L Z_0\right)(2k_L)^{2p}\hat{z}_e^{2p}/(2p)! - \sin\left(2k_L Z_0\right)(2k_L)^{2p+1}\hat{z}_e^{2p+1}/(2p+1)!]],
\end{aligned}
$$

(5.15)

where $f(\mathbf{R}_0)$ is the normalized transverse profile of the lattice and the $\cos\left(2k_L\hat{z}_e\right)$ operator can couple an electronic state with itself or another state with an even change in the l quantum number with m_j and m_l being conserved (e.g., couplings between $|nS_{1/2}\rangle$ and $|n'S_{1/2}\rangle$ or $|nS_{1/2}\rangle$ and $|nD_j\rangle$). Alternatively, $\sin\left(2k_L\hat{z}_e\right)$ can only couple Rydberg states of the same m_j and m_l with odd changes in l (e.g., couplings between $|nS_{1/2}\rangle$ and $|nP_j\rangle$ or $|nS_{1/2}\rangle$ and $|nH_j\rangle$).

For an atom located near the center of the lattice's transverse Gaussian profile, $f(\mathbf{R}_0) \simeq 1$ and the shift on Rydberg state $|n, l, j, m_j\rangle$ with energy $W_{n,l,j}$ can be calculated with first-order nondegenerate perturbation theory. The energy shift can be calculated in this way

because the off-diagonal couplings between orthogonal Rydberg states are usually (at least for $n < 60$) much weaker than the quantum-defect or fine-structure shifts when $l = 0$ or 1, even when U_0 is at a depth of 10^5 single-photon recoils. Therefore,

$$\Delta W_{n,l,j,|m_j|}(Z_0) = U_0 + U_0 \sum_{p=0}^{\infty} (-1)^p (2k_L)^{2p} \frac{\langle n, l, j, |m_j|| \, \hat{z}_e^{2p} \, |n, l, j, |m_j|\rangle}{(2p)!} \cos{(2k_L Z_0)}$$

$$= U_0[1 + \kappa_{n,l,j,|m_j|} \cos{(2k_L Z_0)}]. \quad (5.16)$$

The diagonal matrix element $\kappa_{n,l,j,|m_j|} = \langle n, l, j, |m_j|| \cos{(2k_L \hat{z}_e)} |n, l, j, |m_j|\rangle$ depends entirely, on the spatial variation of the lattice wells within the Rydberg-electron wave function. For low-n wave functions that have their final radial lobes at distances from the nucleus that are much smaller than the lattice constant $\lambda/2$, $\kappa_{n,l,j,|m_j|} \to 1$. When the wave function extends over a certain integer number of lattice constants, $\kappa_{n,l,j,|m_j|}$ can calculate to be zero; these Rydberg states are referred to as *tune-out states*. In Rb, $65S_{1/2}$ and $74S_{1/2}$ are tune-out states for $\lambda = 1064$ nm [44], where the shift on the internal state no longer has a dependence on the lattice-propagation direction. Calculations of $\kappa_{nS_{1/2}}$ for $nS_{1/2}$ states of Rb are presented in Fig. 5.5(a). As can be seen, for S-states between the two tune out levels at $n = 65$ and 74, internal-state Rydberg atom energies will undergo red shifts in regions of standing-wave intensity maxima. Beyond this, the high- and low- field seeking behavior oscillates with n, which affirms that the wave function shape with respect to the laser wavelength is necessary for determining Rydberg-atom light shifts, something that is not taken into account for with deeply bound atomic states. In Fig. 5.5(b), the differences in $\kappa_{n,l,j,|m_j|}$ among $nS_{1/2}$, $(n+1)S_{1/2}$, and $nP_{1/2}$ Rydberg states are presented.

While $nS_{1/2}$ states are spatially isotropic, the electron densities in nP_j Rydberg atoms have different angular dependencies based on on the m_j quantum number. Generally, the larger the $|m_j|$ value, the larger the $\kappa_{n,l,j,|m_j|}$ quantity is. This is a consequence of a weak spatially averaged Rydberg wave function along z where the electron density is aligned perpendicular to the quantization axis. Differences in $\kappa_{nS_{1/2}}$ from $\kappa_{nP_{3/2},|m_j'|}$ are apparent in Fig. 5.5(c). Also, one can note that $|\Delta\kappa|$ for $nP_{3/2}$ is typically much larger than that of $nP_{1/2}$ no matter what $|m_j|$ is chosen. There are, however, certain transitions, i.e., *magic transitions*, that can be chosen so $|\Delta\kappa| \simeq 0$, evident in both Fig. 5.5(b) and (c). For applications involving Rydberg-Rydberg transitions with a prolonged T_2^* time [26], these systems are ideal because the differential light shifts between the two Rydberg states are minimized [63]. Thus, many coherent Rabi flops can be observed between these two magic states under the implementation of a $1064-$nm optical lattice.

The ponderomotive potential can also induce changes in the Rydberg-electron's momen-

tum. Quantum-mechanically, this means that there are nonzero couplings between two different Rydberg states similar to those that can be found with homogeneous and static electromagnetic fields. The relaxed selection rules of Eq. 5.15 allow any change in orbital angular momentum (OAM) of the Rydberg electron but conserve the OAM's projection along the lattice propagation axis. Proportional to the $\cos(2k_L Z_0)$ term, the electronic coordinate operators $\hat{z}_e$ to even powers $2p$ result in even changes in the OAM quantum number l. To the lowest order in $\hat{z}_e$, Rydberg atoms centered near intensity extrema of the standing-wave field $(\cos(2k_L Z_0) \simeq 1)$ experience diamagnetic-like potentials

$$U_p(\hat{z}_e) \simeq U_0(\hat{\mathbb{1}} - 2k_L^2 \hat{z}_e^2), \tag{5.17}$$

from which an effective, static and homogenous magnetic field pointing along z can be obtained, $B_0 \simeq 4k_L\sqrt{U_0 m_e}/e$. This interaction can couple internal states with the same l but different n, where the electron only sees a change in its radial momentum, as is the case with couplings between $nS_{1/2}$ and $(n+1)S_{1/2}$ atoms, or $\Delta l = \pm 2, 4, 6, ...$ In Fig. 5.5(d), I compute the matrix element $\langle (n+1)S_{1/2} | \cos(2k_L \hat{z}_e) | nS_{1/2} \rangle$ as a function of n, which for Rb consists of a maximum at $n = 58$ when $\lambda = 1064$ nm.

Atoms located near the inflection points of the lattice intensity gradient see nearly linear potentials resembling the DC Stark effect. For this case, $\sin(2k_L Z_0) \simeq 1$ and, to the lowest order in $\hat{z}_e$,

$$U_p \simeq 2U_0 k_L \hat{z}_e \tag{5.18}$$

with an effective electric field parallel to B_0 and magnitude $E_0 \simeq 2k_L U_0/e$. Evidently, this potential couples states with odd changes in l such as the $nS_{1/2}$ and $nP_{1/2}$ Rydberg states. The Rb matrix elements $\langle nP_{1/2} | \sin(2k_L \hat{z}_e) | nS_{1/2} \rangle$ also are shown in Fig. 5.5(d). They have a peak value at $n = 46$.

Population transfer from one internal Rydberg state to another can only occur if the ponderomotive interaction supplies sufficient momentum and energy to the bound electron. For energy conservation, the strength of U_p can exceed the energy splitting between the two states $\hbar\omega_{n,l,j,|m_j|}^{n',l',j',|m_{j'}|} = W_{n',l',j',|m_{j'}|} - W_{n,l,j,|m_j|}$ and mix $|n',l',j',m_{j'}\rangle$ with $|n,l,j,m_j\rangle$, as is discussed in the next two sections with fine-structure and hydrogenic-state mixing. Thus, an atom in $|n,l,j,m_j\rangle$ is adiabatically transferred to $|n',l',j',m_{j'}\rangle$ upon movement along Z_0. Alternatively, energy conservation can be achieved keeping U_p low in strength but yielding oscillatory behavior at the frequency of $\omega_{n,l,j,|m_j|}^{n',l',j',|m_{j'}|}/(2\pi)$ by modulation of the lattice amplitude or phase. As a result, the rotating-part of the harmonic potential allows energy to be conserved and electronic transitions to be driven between $|n',l',j',m_{j'}\rangle$ with $|n,l,j,m_j\rangle$. In the final section of this chapter, I investigate this method of population transfer at the
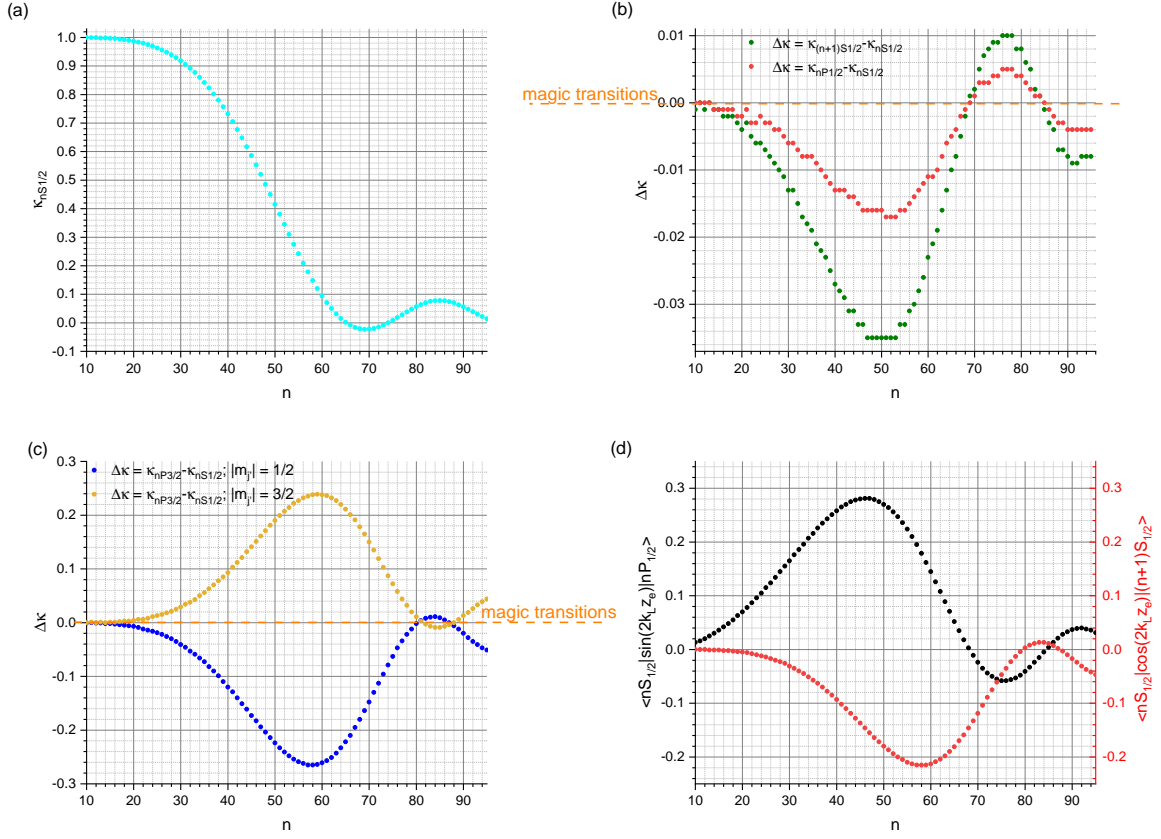
Figure 5.5: The matrix element $\kappa_{nS_{1/2}} = \left\langle nS_{1/2} \right| \cos\left(2k_L \hat{z}_e\right) \left| nS_{1/2} \right\rangle$ is evaluated in (a) for $n = 10 - 95$. Differences from $\kappa_{nS_{1/2}}$ as n changes by 1, as well as differences between $\left| nS_{1/2} \right\rangle$ and $\left| nP_{1/2} \right\rangle$ are displayed in (b). In (c), $\Delta\kappa$ is shown between $\left| nP_{3/2}, |m_{j'}| \right\rangle$ and $\left| nS_{1/2} \right\rangle$ for $|m_{j'}| = 1/2$ and 3/2. Off-diagonal matrix elements of the ponderomotive potential U_p as a function of n are presented in (d).

single-photon limit in order to deliver parallels between it and elastic Thomson and inelastic Compton scattering. Population transfer between Rydberg states with relaxed Δl selection rules are necessary for using optical lattices to initialize a sample of circular states (CSs) from a laser-excitable, low-l sample.

5.3.2 Center-of-Mass Effects

The Force acting on the Rydberg-atom CM for atoms in $nS_{1/2}$ and nP_j is classically determined to be

$$\mathbf{F}_p = -2k_L \hat{Z}_0 \kappa_{n,l,j,|m_j|} \sin\left(2k_L Z_0\right), \tag{5.19}$$

with a maximum near the inflection points of the intensity gradient. Trapped atoms initialized near this region undergo a breathing-like motion at an oscillation frequency of $k_L\sqrt{8U_0/M}$. Near the pondeormotive-potential maxima of the lattice, atoms undergo metastable equilibrium, where non-stationary motion induces skipping over many lattice peaks and troughs. Stable equilibrium that confines atoms to local intensity maxima or minima (depending on n) is only achieved where U_p is at a local minimum.

5.3.3 Photoionization Effects

In the regime where U_p is too low to conserve energy for transitions among $nS_{1/2}$, $nP_{1/2}$, and $nP_{3/2}$, each internal state under the ponderomotive potential remains well-defined in the spherical basis and only is shifted in energy through non-degenerate perturbation theory. That means each state of a given $n, l, j, |m_j|$ has its own photoionization-induced decay rate $\Gamma_{PI,n,l,j,|m_j|}$ as follows,

$$\Gamma_{PI,nS_{1/2}}(Z_0) = \frac{I(Z_0)\bar{\sigma}_{n,l=0}}{\hbar\omega_L} \tag{5.20}$$

$$\Gamma_{PI,nP_{1/2}}(Z_0) = \frac{I(Z_0)\bar{\sigma}_{n,l=1}}{\hbar\omega_L} \tag{5.21}$$

$$\Gamma_{PI,nP_{3/2},|m_j|=1/2}(Z_0) = \frac{I(Z_0)(10\bar{\sigma}_{n,l=1} + 9\bar{\sigma}_{n,l=1}^{\epsilon',l'=2})}{20\hbar\omega_L} \tag{5.22}$$

$$\Gamma_{PI,nP_{3/2},|m_j|=1/2}(Z_0) = \frac{I(Z_0)(21\bar{\sigma}_{n,l=1} + 9\bar{\sigma}_{n,l=1}^{\epsilon',l'=0})}{20\hbar\omega_L}, \tag{5.23}$$

where $I(Z_0) = 2I_0(1 + \cos{(2k_L Z_0)})$, with I_0 being the peak single-beam, running-wave laser intensity. Here,

$$\bar{\sigma}_{n,l} = \sum_{l'} \bar{\sigma}_{n,l}^{\epsilon',l'}, \tag{5.24}$$

where each l' is degenerate when $\epsilon' = W_{n,l,j} + \hbar\omega_L$ is fixed.

Inspection of the $\Gamma_{PI,nP_{3/2},|m_j|}$ rates reveals that a polarized Rydberg sample can lead to a faster ($|m_j| = 3/2$) or slower ($|m_j| = 1/2$) PI rate than that for an average mixture of $|m_j|$ atoms. When averaging over all m_j, $\bar{\Gamma}_{PI,nP_{3/2}} = \Gamma_{PI,nP_{1/2}}$. Also, by observation of Fig. 5.2, Rydberg atoms in $|nS_{1/2}\rangle$ have much lower PI cross sections and rates than those in $|nP_{1/2}\rangle$. This is a result of Cooper minima which arise from destructive relative phases between bound and free radial wave functions under integration for the matrix elements [106].

5.4 nD_j and nF_j Alkali Rydberg Atoms in an Optical Lattice: Fine-Structure Mixing

Alkali Rydberg atoms with internal states of $|nS_{1/2}\rangle$ and $|nP_j, m_j\rangle$ have sizeable quantum defects, and the j splitting in P-state fine structure is sizeable enough that a lattice of 10^5 photon recoils does not mix adjacent states for $n < 60$. However, this parameter regime fails for higher OAM states that have lower quantum defects and spin-orbit coupling strengths. When the fine-structure splittings of a given $|n, l, j, m_j\rangle$ state become twice the lattice depth, nondegenerate perturbation theory cannot be used to calculate the eigenvalues and eigenenergies of the system. States of the same $n, l,$ and $|m_j|$ but different j quantum numbers can be coupled in the off-diagonals of the Rydberg-electron Hamiltonian. This condition is met for $|(n > 30)D_j\rangle$ and all $|nF_j\rangle$ Rb Rydberg states when $U_0 \simeq 10^5 E_r$. The $\Delta l = 0$ coupling matrix element that resides in the off-diagonals and is multiplied by a factor of $U_0 \cos(2k_L Z_0)$ is given by

$$\langle n, l, j \pm 1, m_j | \cos(2k_L \hat{z}_e) | n, l, j, m_j \rangle = \sum_{p=0}^{\infty} \frac{(-1)^p (2k_L)^{2p}}{(2p)!}$$
$$\times \left(c_{\uparrow, m_j-1/2}^{j\pm 1, m_j} c_{\uparrow, m_j-1/2}^{j, m_j} \langle n, l, m_j - 1/2 | \hat{z}_e^{2p} | n, l, m_j - 1/2 \rangle \right.$$
$$\left. + c_{\downarrow, m_j+1/2}^{j\pm 1, m_j} c_{\downarrow, m_j+1/2}^{j, m_j} \langle n, l, m_j + 1/2 | \hat{z}_e^{2p} | n, l, m_j + 1/2 \rangle \right). \quad (5.25)$$

These couplings are nonzero because $\langle n, l, m_j - 1/2 | \hat{z}_e^{2p} | n, l, m_j - 1/2 \rangle$ $\neq \langle n, l, m_j + 1/2 | \hat{z}_e^{2p} | n, l, m_j + 1/2 \rangle$, which combats the orthogonality of the two fine-structure states.

In Fig. 5.6, Eq. 5.25 is evaluated for $|nD_j, |m_j|\rangle$ states in (a) and $|nF_j, |m_j|\rangle$ in (b). One thing that is consistent in both calculations is that the couplings generally get stronger as n is increased. This observation is most likely an effect of the pronounced anisotropy of the wave functions with respect to the lattice periodicity as the atom gets larger.

Couplings between $|n, l, j, m_j\rangle$ and $|n, l, j \pm 1, m_j\rangle$ may have the strength to induce adiabatic population transfer between the two states. For instance, the splitting between $|50F_{5/2}\rangle$ and $|50F_{7/2}\rangle$ for Rb is $\Delta W_{LS} = h \times 1.27$ MHz, according to Fig. 5.6(c), which lists the Rb fine-structure splittings as a function of n for D- and F-states. If $U_0 = h \times 10$ MHz, the off-diagonal couplings between j and $j \pm 1$ have maximum values greater than $\Delta W_{LS}/2$. The Hamiltonian for $n = 50$ in this case is
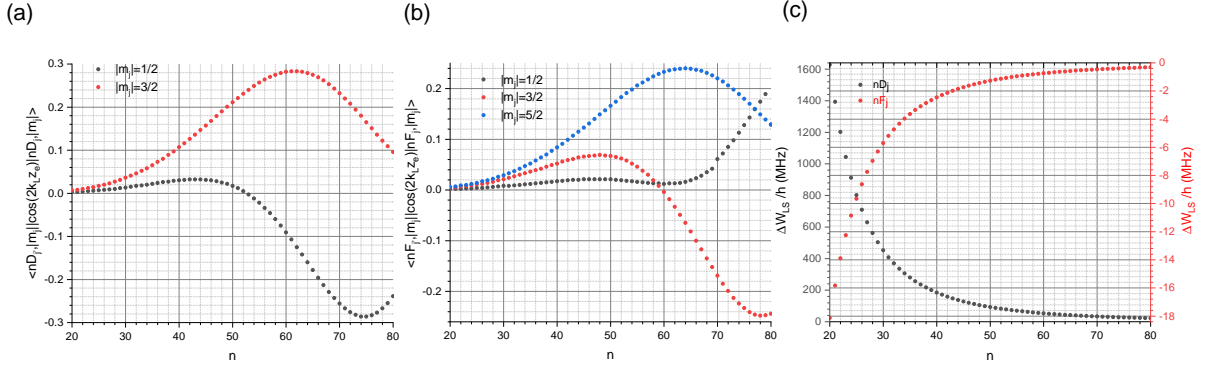
Figure 5.6: In (a), coupling strengths between two different fine-structure states of a given $|m_j|$ by the z-propagating lattice are presented for $|nD_j\rangle$. In (b), fine-structure couplings are presented for $|nF_j\rangle$. Fine structure splittings, primarily from LS-couplings, are presented for $|nD_j\rangle$ and $|nF_j\rangle$ in (c).

where each element of the matrix is in units of $h\times$ MHz. No longer are the $|n,l,j,|m_j|\rangle$ basis states for this Hamiltonian; the eigenvalues unique quantum numbers $k=|m_j|$ corresponding to the adiabatic potentials take on the following Z_0-dependent form (assuming $j=|l-s|$ here),

$$\left|\psi_{k=|m_j|}(Z_0)\right\rangle = c_{n,l,j,k}(Z_0)\left|n,l,j,|m_j|\right\rangle + c_{n,l,j+1,k}(Z_0)\left|n,l,j+1,|m_j|\right\rangle, \tag{5.26}$$

where $c_{n,l,j,k}$ and $c_{n,l,j+1,k}$ depend on the following parameters: the matrix elements in Fig. 5.6(b), U_0, K_L, and ΔW_{LS}. Eigenenergies are plotted in Figs. 5.7(a)-(c) in a system that lacks any stray or external, DC electric field $\mathbf{E}$. These shifts on $W_{50F_{5/2}}$ and $W_{50F_{7/2}} = W_{50F_{5/2}} + \Delta W_{LS}$ are denoted by ΔW_k and presented in units of GHz.

Fig. 5.7(a) displays the PI rates Γ_k for each k state in units of s^{-1}. Expressions for these rates are the following:

$$\Gamma_k(Z_0) = \frac{I(Z_0)\sigma_k(Z_0)}{\hbar\omega_L}, \tag{5.27}$$

104

where

$$\sigma_k(Z_0) = \frac{\pi e^2 \hbar^2}{\epsilon_0 m_e^2 \omega_L c} \sum_{l',m_{l'},m_s} \left| \sum_{j,m_l,m_s} M_{n,l,m_l,m_s}^{\epsilon',l',m_{l'},m_s} c_{n,l,j,k}(Z_0) \langle j, m_j | m_l m_s \rangle \right|^2$$

and

$$M_{n,l,m_l,m_s}^{\epsilon',l',m_{l'},m_s} = \langle \epsilon', l', m_{l'}, m_s | i\hat{p}_{x,e} | n, l, m_l, m_s \rangle \delta_{l',l\pm1} \delta_{m_{l'},m_l\pm1}. \tag{5.28}$$

in SI units. Near the $\lambda = 1064$-nm lattice-intensity minima there are naturally no photoions generated. At the inflection points, avoided crossings are noticeable mainly for $|m_j| = 5/2$ which consists of the strongest off-diagonal coupling of $(h \times 1.66 \text{ MHz})\cos{(2k_L Z_0)}$. Here, $|c_{n,l,j,k}(Z_0)| - |c_{n,l,j+1,k}(Z_0)|$ is at a minimum and the two unperturbed, fine-structure states are maximally mixed. Thus, σ_k does not have the form of $\sigma_{x,n,l,j,|m_j|}$ or $\sigma_{x,n,l,j+1,|m_j|}$ but a coherent mixture of PI cross-sections. When $Z_0 = 0$, the $|m_j|$ levels are comfortably nondegenerate that $|\psi_k(0)\rangle \to |n, l, j, |m_j|\rangle$, so $\sigma_k(0) \simeq \sigma_{x,n,l,j,|m_j|}$. In the previous section, I demonstrated that the larger the $|m_j|$, the larger the PI cross section for a given l and j. It then is agreeable that the $|50F_{5/2}, |m_j| = 5/2\rangle$ and $|50F_{7/2}, |m_j| = 7/2\rangle$ have the most substantial PI rates near 22 ks^{-1}.

Adiabatic population transfer from $|50F_{5/2}\rangle$ to $|50F_{7/2}\rangle$ is apparent in Figs. 5.7(b) and (c) ((c) is a close-up of (b) for $|m_j| = 5/2$), where the expectation value of operator $\hat{j} = 2.5 |50F_{5/2}\rangle \langle 50F_{5/2}| + 3.5 |50F_{7/2}\rangle \langle 50F_{7/2}|$ is evaluated for each k at a given Z_0. These are the colored dots labeled $\langle j \rangle$. Nearly perfect adiabatic transfer is possible as the atom slowly moves from an intensity minimum to maximum in the case of $|m_j| = 5/2$. Mild population transfer is also observable for $|m_j| = 3/2$, but the $|m_j| = 1/2$ states seem to mostly retain their j-quantum numbers without appreciable fine-structure transitions.

In Fig. 5.7(d), a field of $E_z = 0.1$ V/cm is applied along the direction of the lattice propagation axis. At 10 V/m and $|n = 50, l = 3\rangle$ in Rb, the DC Stark couplings among l, m_l and $l \pm 1, m_l$ have strengths of $\sim h \times 25$ MHz, superseding spin-orbit coupling. Therefore, it is appropriate to work in the $|m_l, m_s\rangle$ basis when calculating the effects of the optical lattice. Before the lattice perturbation is applied to the system, the second-order DC Stark effect splits the F-state into seven sublevels: $|m_l = 0\rangle, ||m_l| = 1, \downarrow\rangle, ||m_l| = 1, \uparrow\rangle, ||m_l| = 2, \downarrow\rangle,$ $||m_l| = 2, \uparrow\rangle, ||m_l| = 3, \downarrow\rangle,$ and $||m_l| = 3, \uparrow\rangle$. States of different $|m_l|$ are split according to the differences in the DC polarizability at $n = 50, l = 3$ while states of different m_s of a given $|m_l|$ (except $m_l = 0$) are split by 1.27 MHz from the fine-structure. Note that the $m_l = 0$ state does not split due to a lack of spin-orbit coupling. Because $||m_l|, \uparrow\rangle$ cannot couple to $||m_l|, \downarrow\rangle$ through $U_p(\hat{z}_e)$, the light-shifts on the internal electronic states can be computed through first-order nondegenerate perturbation theory in the n, l, m_l, m_s basis.
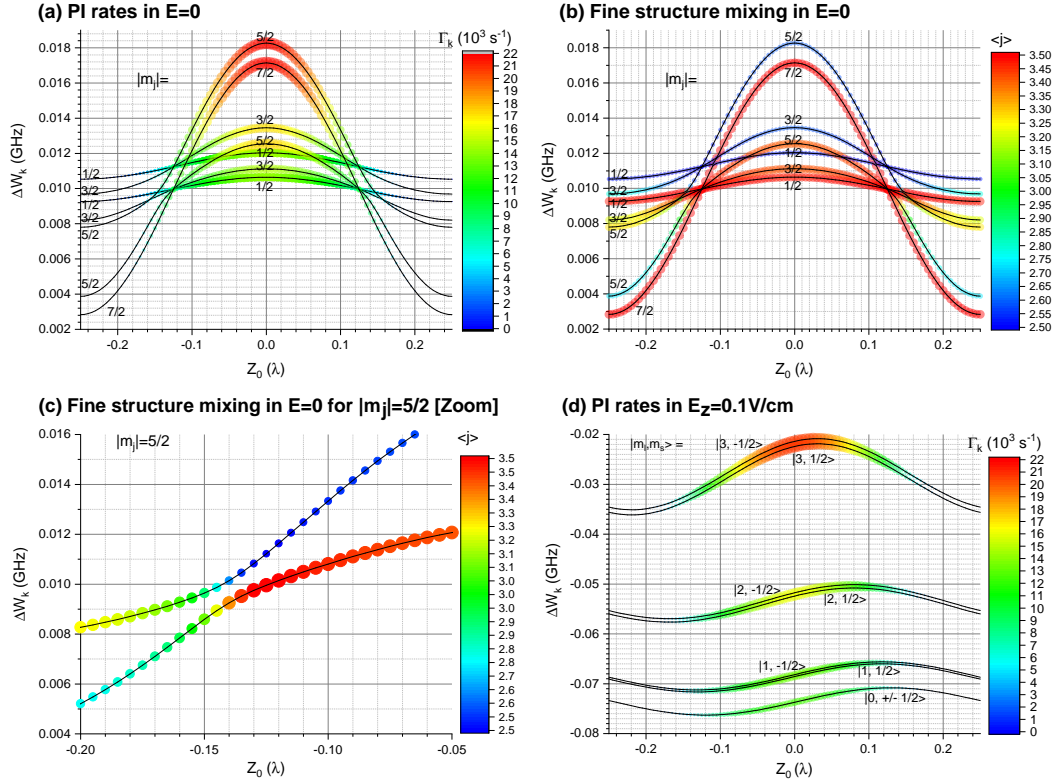
Figure 5.7: Figure taken from [5]. (a) and (b): Rb $|50F_j>$ states in an optical lattice with $\lambda = 1064$ nm and depth $U_0 = h \times 10$ MHz$= 2410E_{2r}$. Light shifts of the adiabatic states $|\psi_k(Z_0)>$ are plotted as a function of longitudinal CM positions. In (a), the dot colors and sizes represent the PI rates; in (b), dot colors and sizes represent the value $\langle j \rangle$ (see text for details). (c) A close-up view of the avoided crossing near the lattice inflection point for $|m_j| = 5/2$. (d) Calculated light-shifts for the same lattice conditions when a longitudinal electric field of strength 0.1 V/cm is applied. The sizes and colors of the dots indicate PI rate.

As indicated in Fig. 5.7(d), the $|m_l| = 3$ states experience the strongest modulation along Z_0 due to a smaller overlap of the Rydberg wave function and ponderomotive potential. On the other hand, $|m_l = 0\rangle$ sees the most overlap as electron orbits primarily along the lattice propagation axis. The results of these adiabatic lattice potentials imply that the application of a longitudinal DC electric field can inhibit adiabatic fine-structure transitions of the lattice and stabilize the purity of the Rydberg state in the spherical basis. Therefore, the PI rate is $\sigma_{x,n,l,|m_l|}I(Z_0)/(\hbar\omega_L)$ with a fixed cross-section along Z_0. This is all true provided that it does not have the strength mix the $|nF\rangle$ states with $|nD\rangle$ and $|nG\rangle$. Another noteworthy feature of this system is the longitudinal shift in the lattice wells with respect to the 1064-nm intensity minima, leading to future investigations of CM dynamics with a slowly-varying electric field.

5.5 Hydrogenic Rydberg States in an Optical Lattice: l-Mixing with nF_j States

I now consider the case where $U_0/h = 1.5$ GHz with $\lambda = 1064$ nm and $|50F\rangle$ Rb Rydberg atoms. This condition is achievable with two counter-propagating laser beams with waists of $w_0 = 20$ μm and powers of 200 W. The quantum defects at this n are $\delta_{50F_{5/2}} = 0.016485(1)$ and $\delta_{50F_{7/2}} = 0.0165093(7)$ [145]. The energy spacing from $|nF\rangle$ to $|nG\rangle$ is then 658 MHz [64], and the lattice now has the strength to mix $|nF\rangle$ with states belonging to the hydrogenic manifold that are all degenerate with each other.

The ponderomotive potential expressed in Eq. 5.15 induces mixing among $|n, l, j, m_j\rangle$ and $|n', l', j', |m_j|\rangle$ with any Δl and Δj allowed. Population transfer from $l = 3$ all the way to $l = 49$ is then permitted as the atom moves adiabatically along Z_0. Eigenstates for this system are indexed by quantum number k, where, in general,

$$|\psi_k(Z_0)\rangle = \sum_{n,l,j} c_{n,l,j,|m_j|}(Z_0) |n, l, j, |m_j|\rangle . \tag{5.29}$$

In the example presented here, there is no sum over n, as it is fixed at 50, but 94 eigenstates arise ($k \in [0, 93]$), where $k = 0$ mostly consists of $50F$-character with $m_s = -1/2$ and $k = 93$ is the adiabatic state closest to the ionization threshold when $Z_0 = 0$.

Because PI rates generally decrease with l for $l > 2$, low k states that consist mainly of $|50F\rangle$ must have the fastest PI rates. PI rates in this example take the following form

$$\sigma_k(Z_0) = \frac{\pi e^2 \hbar^2}{\epsilon_0 m_e^2 \omega_L c} \sum_{l',m_{l'},m_s} \left| \sum_{l,j,m_l,m_s} M_{n=50,l,m_l,m_s}^{\epsilon',l',m_{l'},m_s} c_{n=50,l,j,m_j}(Z_0) \langle j, m_j | m_l m_s \rangle \right|^2 .$$

In Fig. 5.8, I present the absolute energies for each $|\psi_k(Z_0)\rangle$ as a function of Z_0 in units of cm^{-1} (multiply by $100c$ to convert to Hz). As seen in the figure, $k = 0$ and $k = 1$ have maximum PI rates of 1.6 Ms^{-1}; for comparison, the natural lifetimes of Rb $|50F\rangle$ with a 300 K environment is on the order of 10^4 s^{-1} [3].

As mentioned in previous sections, atoms with Z_0 near the inflection points have internal eigenstates that resemble the parabolic wave functions of a fixed $|m_l|$ due to the Stark-like interaction with an effective DC electric field of $E_0 \simeq 2k_L U_0/e$ [159]. When $Z_0 = 0$, $|\psi_k(Z_0 = 0)\rangle$ resembles hydrogenic states mixed by a diamagnetic-like interaction with effective field $B_0 \simeq 4k_L\sqrt{U_0 m_e}/e$ [159]. An interesting energy-level structure arises in this region. For $k = 3$ to $k = 65$, the Rydberg electron's eigenenergy has a sub-wavelength modulation along Z_0. Its corresponding wave funciton resembles those of a vibrator state, but when $k > 65$, the modulation drops below the nm-level and electronic wave functions

resemble rotor states [160; 161; 162; 163]. Within this manifold of rotors and vibrators lies wave functions with $l = 49$ character, which have very little electronic overalap with the atom's inner ion core. Thus, when the atom moves to the appropriate Z_0, a slow envelope of the optical lattice light may invert the entire population from $l = 3$ to $l = 49$ with the $|m_j|$ quantum number remaining conserved.

Near the intensity maximum of $Z_0 = 0$, the $k = 0$ and $k = 1$ states photoionize 10 times faster than any other lattice-mixed eigenstate. Figs. 5.8(b) and (c) show that the Stark-like eigenstates close to the inflection points photoionize more strongly than the roto-vibrational states near the bottoms of the lattice wells. In fact Fig. 5.8(c), the drop off in Γ_k from the Stark-like to diamagnetic-like regime is apparent, i.e., the rates go from $\Gamma_k \sim 130$ ks^{-1} to 70 ks^{-1}. This drop mirrors the jump from low-l hydrogenic-state character near the inflection points to high-l character at the intensity maxima. Also, it can be concluded by observing the PI rates that the rotor states consist of the most high-l character near $l = 49$.

In Fig. 5.8(d), a closer look at the subwavelength modulation of the force acting on the CM along Z_0 is shown. Splittings arising from the spin-orbit coupling between two configurations of the electron's intrinsic angular momentum further indicate that the l has a lattice-induced dependence on Z_0, for the energy gaps within every two levels are not fixed in this direction. The potential energy structures for the CM here unravel a novel innovation for vector atom interferometry of Rydberg atoms. In spinor atom interferometry, the atom's CM showcases its wavelike properties through its diffraction and phase-sensitive interference all the while undergoing changes in the internal state (as opposed to scalar atom interferometry where the electronic state remains fixed). An incident matter wave $\psi_0(\mathbf{R}_0)$ on this potential would undergo diffraction at an angle 50 times greater than what would be provided by an optical lattice because the lattice constant here is $\simeq 10$ nm [164]. Gravitational waves and dark-matter forces, for instance, may impart a more clearly visible phase shift on the diffracted matter-wave orders the more they are separated [164; 165]. Also, the rich internal-state structure and adiabatic state transfer along Z_0 of the atomic matter waves would provide parallels with the interferometry of solid nanoparticles [166].

While the ponderomotive interaction has thus far been discussed in the context of coherent laser fields forming an optical lattice, it would be beneficial to explain this force at the single-photon level using Fock states of the incident optical fields. With this description, the effect of internal-state population transfer of the bound electron can be derived from a system involving multiple optical wavelengths.
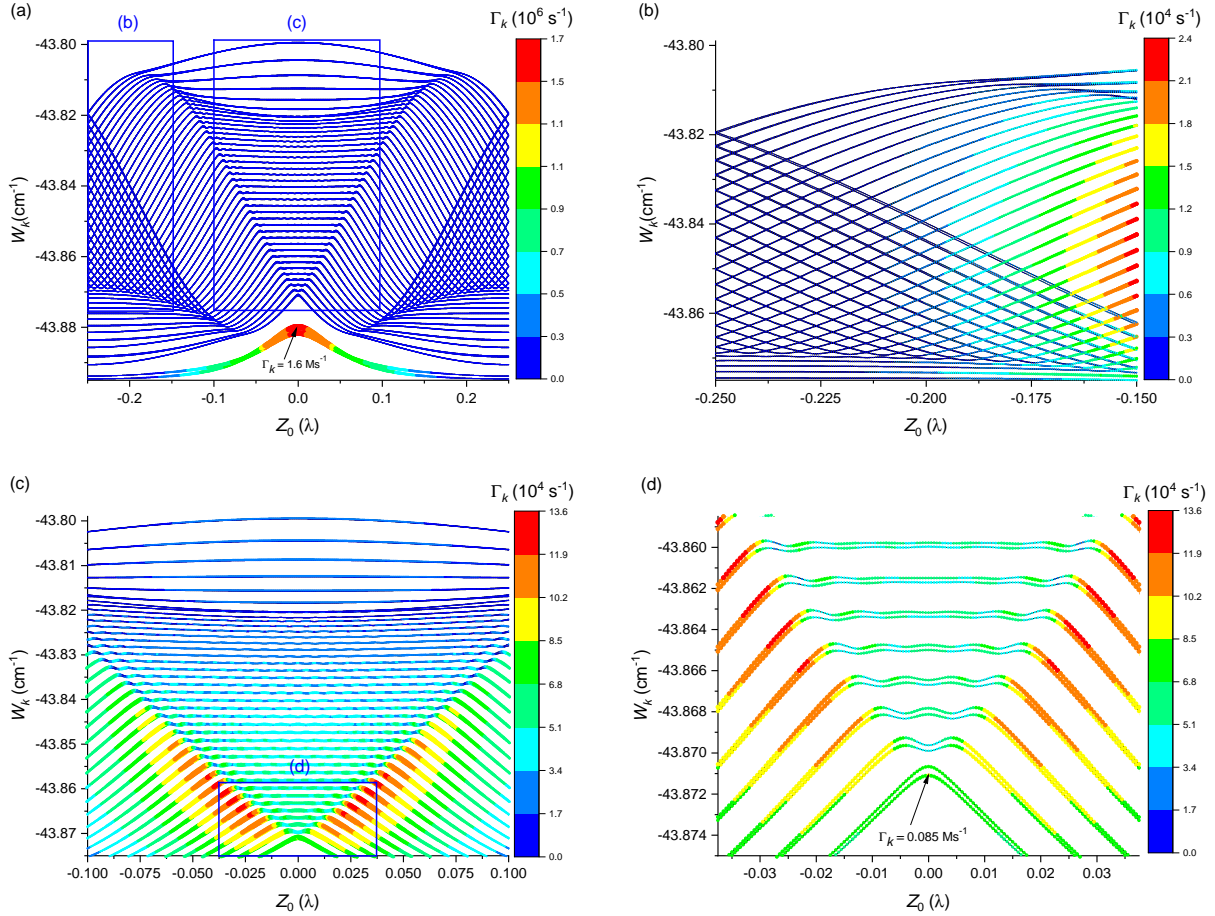
Figure 5.8: Figure taken from [5]. Adiabatic eigenenergies as a function of CM position Z_0 for $n = 50$ and $m_j = 1/2$, $\lambda = 1064$ nm, and lattice depth $2U_0 = h \times 3$ GHz $= 1.48 \times 10^6 \, E_r$. Subfigures (b) and (c) are closeups of the boxed regions in (a). A closeup of the boxed region in (c) is presented in (d), where the spin-orbit-induced splittings are observable. Dot colors correspond to a bin of PI rates $\Gamma_k(Z_0)$, indicated by the color scales provided. Dot diameters are proportional to $\Gamma_k(Z_0)$. I enhance the diameters in (b) by a factor of 50 with respect to those in (a) and by a factor of 10 in (c) and (d).

5.6 Quantum-Electrodynamic Description of the Ponderomotive Interaction

In a fully quantum description of the ponderomotive force, where the electromagnetic field is quantized along with the electron's coordinates, the effect of a single quantum of the electromagnetic field with polarization state α and wave number k resembles a scattering interaction when incident on the electron. The electron can exist in quantum state $|g\rangle$ or

109

$|e\rangle$, while the electromagnetic field of mode $\mathbf{k}, \alpha$ exists as an arbitrary Fock state $|N\rangle_{\mathbf{k},\alpha}$ with field energy $(N + 1/2)\hbar\omega_{\mathbf{k}}$. The vector-potential operator has the form

$$\hat{\mathbf{A}}(\hat{\mathbf{r}}, t) = \sum_{\mathbf{k},\alpha} \sqrt{\frac{\hbar}{2\omega_{\mathbf{k}}V}} \hat{a}_{\mathbf{k},\alpha} e^{i(\mathbf{k}\cdot\hat{\mathbf{r}} - \omega_{\mathbf{k}}t)} \hat{\epsilon}_\alpha + \text{h.c.}, \tag{5.30}$$

where V is the volume of the system that manipulates the density of states in mode $\mathbf{k}, \alpha$ and $\hat{a}_{\mathbf{k},\alpha}$ is the mode's annihilation operator. Note that $\hat{\mathbf{r}}$ is the vector operator corresponding to the electron's coordinate with respect to the lab frame.

The minimum coupling Hamiltonian consists of the term proportional to electromagnetic field intensity, which is where the ponderomotive term originates. Using the quantized radiation field, the ponderomotive potential operator is then,

$$\sum_{\mathbf{k},\mathbf{k}',\alpha,\alpha'} \frac{e^2\hbar}{4m_eV} \left[\frac{\hat{a}_{\mathbf{k},\alpha}\hat{a}_{\mathbf{k}',\alpha'}}{\sqrt{\omega_{\mathbf{k}}\omega_{\mathbf{k}'}}} e^{i[(\mathbf{k}+\mathbf{k}')\cdot\hat{\mathbf{r}} - (\omega_{\mathbf{k}}+\omega_{\mathbf{k}'})t]} \hat{\epsilon}_\alpha \cdot \hat{\epsilon}_{\alpha'} + \frac{\hat{a}^\dagger_{\mathbf{k},\alpha}\hat{a}^\dagger_{\mathbf{k}',\alpha'}}{\sqrt{\omega_{\mathbf{k}}\omega_{\mathbf{k}'}}} e^{i[-(\mathbf{k}+\mathbf{k}')\cdot\hat{\mathbf{r}} + (\omega_{\mathbf{k}}+\omega_{\mathbf{k}'})t]} \hat{\epsilon}_\alpha \cdot \hat{\epsilon}_{\alpha'} \right.$$
$$\left. + \frac{\hat{a}^\dagger_{\mathbf{k},\alpha}\hat{a}_{\mathbf{k}',\alpha'}}{\sqrt{\omega_{\mathbf{k}}\omega_{\mathbf{k}'}}} e^{i[(\mathbf{k}'-\mathbf{k})\cdot\hat{\mathbf{r}} + (\omega_{\mathbf{k}}-\omega_{\mathbf{k}'})t]} \hat{\epsilon}_\alpha \cdot \hat{\epsilon}_{\alpha'} + \frac{\hat{a}_{\mathbf{k},\alpha}\hat{a}^\dagger_{\mathbf{k}',\alpha'}}{\sqrt{\omega_{\mathbf{k}}\omega_{\mathbf{k}'}}} e^{i[(\mathbf{k}-\mathbf{k}')\cdot\hat{\mathbf{r}} + (\omega_{\mathbf{k}'}-\omega_{\mathbf{k}})t]} \hat{\epsilon}_\alpha \cdot \hat{\epsilon}_{\alpha'} \right], \tag{5.31}$$

where the creation and annihilation operators act on the electromagnetic field and the terms in the potential's phase act on $|g\rangle$ and $|e\rangle$. Considering only one incident mode of the radiation field $\mathbf{k}, \alpha$ and one scattered field $\mathbf{k}', \alpha'$ out of the sum in Eq. 5.31 with initial $|N\rangle_{\mathbf{k},\alpha} |M\rangle_{\mathbf{k}',\alpha'}$ and final $|N'\rangle_{\mathbf{k},\alpha} |M'\rangle_{\mathbf{k}',\alpha'}$ states of the radiation field, elastic scattering occurs when $\omega_{\mathbf{k}} = \omega_{\mathbf{k}'} = \omega$ and only the last two terms of Eq. 5.31 are nonvanishing. Here, $|e\rangle = |g\rangle$ and two possible transitions occur

$$\langle g| \langle N+1|_{\mathbf{k},\alpha} \langle M-1|_{\mathbf{k}',\alpha'} \hat{U}_p |N\rangle_{\mathbf{k},\alpha} |M\rangle_{\mathbf{k}',\alpha'} |g\rangle = \frac{e^2\hbar\sqrt{(N+1)M}}{4m_eV\omega} \hat{\epsilon}_\alpha \cdot \hat{\epsilon}_{\alpha'} \langle e^{i(\mathbf{k}'-\mathbf{k})\cdot(\mathbf{R}_0+\hat{\mathbf{r}}_e)} \rangle$$

$$\tag{5.32}$$

$$\langle g| \langle N-1|_{\mathbf{k},\alpha} \langle M+1|_{\mathbf{k}',\alpha'} \hat{U}_p |N\rangle_{\mathbf{k},\alpha} |M\rangle_{\mathbf{k}',\alpha'} |g\rangle = \frac{e^2\hbar\sqrt{N(M+1)}}{4m_eV\omega} \hat{\epsilon}_\alpha \cdot \hat{\epsilon}_{\alpha'} \langle e^{i(\mathbf{k}-\mathbf{k}')\cdot(\mathbf{R}_0+\hat{\mathbf{r}}_e)} \rangle$$

$$\tag{5.33}$$

5.6.1 Thomson Scattering

The ponderomotive interaction is the mechanism behind elastic Thomson scattering when there is a single photon in a given mode $\mathbf{k}, \alpha$ within the volume v incident on the bound electron in state $|g\rangle$. If the volume is a symmetric box, then initial states $|1\rangle_{\mathbf{k},\alpha} |0\rangle_{\mathbf{k}',\alpha'}$ and $|0\rangle_{\mathbf{k},\alpha} |1\rangle_{\mathbf{k}',\alpha'}$ are equally likely and both transitions in Eq. 5.33 have the same amplitudes for

all scattered states $\mathbf{k}'$. In this discussion, I will assume that the valence electron is nearly detached from the ionic core and its wave function resembles the free-particle plane wave. Fermi's golden rule yields the rate of Thomson scattering Γ_T within solid angle $d\Omega$

$$d\Gamma_T = \frac{2\pi}{\hbar} \left| \frac{e^2 \hbar}{2 m_e v \omega} \hat{\epsilon}_\alpha \cdot \hat{\epsilon}_{\alpha'} \right|^2 \rho_{vac, \omega_{\mathbf{k}'} = \omega_{\mathbf{k}}} = \frac{2\pi}{\hbar} \left| \frac{e^2 \hbar}{2 m_e v \omega} \hat{\epsilon}_\alpha \cdot \hat{\epsilon}_{\alpha'} \right|^2 \frac{v \omega^2 d\Omega}{8 \pi^3 c^3 \hbar}, \tag{5.34}$$

and, dividing by photon flux c/v for the single-photon state,

$$\frac{d\sigma_T}{d\Omega} = \frac{e^4}{16 \pi^2 m_e^2 c^4} |\hat{\epsilon}_\alpha \cdot \hat{\epsilon}_{\alpha'}|^2. \tag{5.35}$$

Integration of the polarization couplings over the solid angle Ω results in the Thomson scattering cross section of $\simeq 0.665$ barns. For Rydberg atoms in the presence of a single-quantum of optical radiation in a free-space vacuum, Thomson scattering is the lowest-order effect acting on the valence electron.

5.6.2 Cavity-Generated Optical Lattices: Elastic Scattering

Now, I will detail the elastic scattering of a quantized radiation field with a bound Rydberg electron in state $|g\rangle = |n, l, j, m_j\rangle$ in a volume bound by an extremely-high-Q optical resonator of volume V that allows two counter-propagating modes of the same frequency ω and polarization but opposite propagation directions $\mathbf{k}$ and $-\mathbf{k}$. Thus, the quantized radiation field is in state $|N\rangle_{\mathbf{k},\alpha} |N\rangle_{-\mathbf{k},\alpha}$ and the following energy shift $\Delta W_{n,l,j,m_j}$ is obtained when summing over all possible transitions of the field for the case $|e\rangle = |g\rangle$,

$$\Delta W_{n,l,j,m_j} = \frac{e^2}{4 m_e \omega^2} \frac{2 \hbar \omega}{v} \langle g| N + \sqrt{N(N+1)} \cos\left[2\mathbf{k} \cdot (\mathbf{R}_0 + \hat{\mathbf{r}}_e)\right] |g\rangle, \tag{5.36}$$

which agrees with the result obtained using a classical radiation field. The two possible transitions of the radiation field that were added were the scattering of a photon of mode $\mathbf{k}$ into $-\mathbf{k}$ and the opposite event.

5.6.3 Cavity-Generated Optical Lattices: Inelastic Scattering

The cavity can also trap optical modes that are an integer number m of $\Delta\omega_{FSR}/(2\pi) = c\epsilon_0^{1/2}/(2\epsilon^{1/2} v^{1/3})$ away from ω where ϵ is the permittivity of the cavity medium and v is the cavity volume. Consider the case where there are four modes $(\mathbf{k}, -\mathbf{k}, \mathbf{k}', -\mathbf{k}')$ trapped with two unique frequencies $(\omega_{\mathbf{k}} = \omega, \omega_{\mathbf{k}'} = \omega + m\Delta\omega_{FSR})$, where $m\Delta\omega_{FSR} = \omega_0$, the angular frequency spacing between $|g\rangle = |n, l, j, m_j\rangle$ and $|e\rangle = |n', l', j', m_{j'}\rangle$. Tuning of ω_0, $\epsilon^{1/2}$,

or $V^{1/3}$ can meet the resonance condition for a transition from $|g\rangle$ to $|e\rangle$. All modes are assumed to exist in the same polarization state $\alpha = 1$.

Initially, the quantized radiation field is in state $|N\rangle_{\mathbf{k}} |N\rangle_{-\mathbf{k}} |M\rangle_{\mathbf{k}'} |M\rangle_{-\mathbf{k}'}$. For electronic transition $|g\rangle \rightarrow |e\rangle$, the following changes in the radiation field are possible

$$|N\rangle_{\mathbf{k}} |N\rangle_{-\mathbf{k}} |M\rangle_{\mathbf{k}'} |M\rangle_{-\mathbf{k}'} \rightarrow |N+1\rangle_{\mathbf{k}} |N\rangle_{-\mathbf{k}} |M\rangle_{\mathbf{k}'} |M-1\rangle_{-\mathbf{k}'} \tag{5.37}$$

$$|N\rangle_{\mathbf{k}} |N\rangle_{-\mathbf{k}} |M\rangle_{\mathbf{k}'} |M\rangle_{-\mathbf{k}'} \rightarrow |N\rangle_{\mathbf{k}} |N+1\rangle_{-\mathbf{k}} |M-1\rangle_{\mathbf{k}'} |M\rangle_{-\mathbf{k}'} . \tag{5.38}$$

When evaluating the matrix element $\langle e = n', l', j', m_{j'}| \hat{U}_p |g = n, l, j, m_j\rangle$, the sum over these Fock-state transitions is taken. The result is

$$\frac{e^2 \hbar}{4 m_e \omega v} \langle n', l', j', m_{j'}| \sqrt{M(N+1)} e^{i(\mathbf{k}'+\mathbf{k})\cdot(\mathbf{R}_0 + \hat{\mathbf{r}}_e)} |n, l, j, m_j\rangle$$

$$+ \frac{e^2 \hbar}{4 m_e \omega v} \langle n', l', j', m_{j'}| \sqrt{M(N+1)} e^{-i(\mathbf{k}'+\mathbf{k})\cdot(\mathbf{R}_0 + \hat{\mathbf{r}}_e)} |n, l, j, m_j\rangle$$

$$= \frac{e^2 \hbar \sqrt{M(N+1)}}{2 m_e \omega v} \langle n', l', j', m_{j'}| \cos\left[(\mathbf{k}'+\mathbf{k})\cdot(\mathbf{R}_0 + \hat{\mathbf{r}}_e)\right] |n, l, j, m_j\rangle$$

$$= \frac{e^2 \hbar \sqrt{M(N+1)}}{2 m_e \omega v} \langle n', l', j', m_{j'}| \cos\left[(\mathbf{k}'+\mathbf{k})\cdot\mathbf{R}_0\right] \cos\left[(\mathbf{k}'+\mathbf{k})\cdot\hat{\mathbf{r}}_e\right]$$

$$- \sin\left[(\mathbf{k}'+\mathbf{k})\cdot\mathbf{R}_0\right] \sin\left[(\mathbf{k}'+\mathbf{k})\cdot\hat{\mathbf{r}}_e\right] |n, l, j, m_j\rangle . \tag{5.39}$$

I have, up until now, left the Rydberg atom's CM coordinate as a classical parameter. When this coordinate is quantized $\mathbf{R}_0 \rightarrow \hat{\mathbf{R}}_0$ and the particle behavior of the inner ion core takes on wavelike properties defined by quantum state $|\nu\rangle_i$, where $i = g, e$. In this system of a bichromatic optical lattice, the ν characterizes a Bloch band belonging to a specific internal state of the Rydberg electron. For a sufficiently deep optical lattice, the energy spacing of $\Delta\nu = 1$ is proportional to the classical trap oscillation frequency of the CM. However, the anharmonicity of the sinusoidal potential induces deviations in this energy spacing.

The operators $\cos\left[(\mathbf{k}+\mathbf{k}')\cdot\hat{\mathbf{R}}_0\right]$ and $\sin\left[(\mathbf{k}'+\mathbf{k})\cdot\hat{\mathbf{R}}_0\right]$ govern how the transition $|\nu\rangle_g \rightarrow |\nu'\rangle_e$ proceeds, where the former and latter induces $\nu' - \nu = 2q$ and $2q + 1$ changes respectively for $q = 0, \pm 1, 2, ...$. Thus, according to the calculated matrix element, for even-integer changes in the orbital-angular-momentum (OAM) quantum number of the internal state, where the parity of the Rydberg-electron wave funciton remains the same from the transition, the motional quantum number must also undergo an even integer change. Its spectrum representing the probability of $|g\rangle \rightarrow |e\rangle$ as a function of $m\Delta\omega_{FSR}$ would feature a central peak near ω_0, as well as sidebands located near even-integer multiples of the classical trap oscillation frequency. Alternatively, odd-parity transitions from $|g\rangle$ to $|e\rangle$ yield spectra with

no feature near ω_0 and sidebands located near odd-integer multiples of the oscillation frequency. Sample spectra of even- and odd-parity transitions are featured in Fig. 5.9(a) and (b) for the even- and odd-parity cases, respectively. Experimentally, the even-parity case has previously been observed in [62; 63; 85] while the odd-parity had not up until this work.
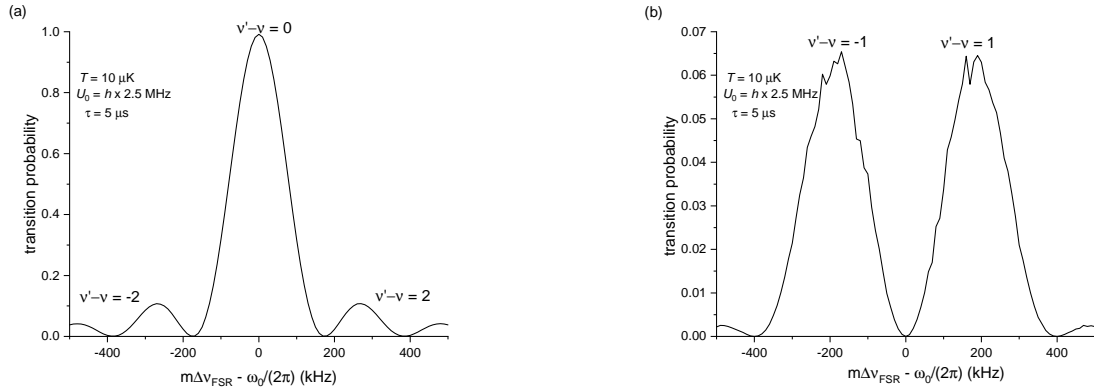
Figure 5.9: Spectrum of ponderomotive transition within optical cavity for $|g\rangle \rightarrow |e\rangle$ when $|g\rangle$ and $|e\rangle$ have the same (a) and opposite (b) parities. These transitions are experimentally realizable by amplitude modulation of the lattice. Half lattice depth $U_0 = h \times 2.5$ MHz, temperature $T = 10$ μK, interaction time $\tau = 5$ μs.

I have just described an alternate method of driving Rydberg-Rydberg transitions that doesn't require enhancing U_0 to a level comparable to the Kepler frequency. Very shallow lattice fields can in principle conserve energy for population transfer from one Rydberg state to another, provided that there are multiple optical modes with a beat frequency on the order of the transition frequency. Instead of the elastic Thomson scattering taking place in this case, the exchange of $|g\rangle$ to $|e\rangle$ and $\mathbf{k}, \alpha$ to $\mathbf{k}', \alpha'$ parallels Compton scattering in the limit of very few photons, as depicted in the seagull graph of Fig. 5.10. Note that this interaction occurs in first-order perturbation theory.

The lattice system presented in this sub-section represents one that is amplitude modulated. In actuality there is one extra set of counter-propagating modes allowed with frequencies at $\omega - m\Delta\omega_{FSR}$ that lead to similar matrix elements to the ones calculated. It is noteworthy that amplitude modulation of the optical lattice inhibits the drive of odd-parity transitions near ω_0; i.e., the modulation frequency must be detuned by an odd-integer of the trap oscillation frequency. For this prohibited ponderomotive transition to occur, the
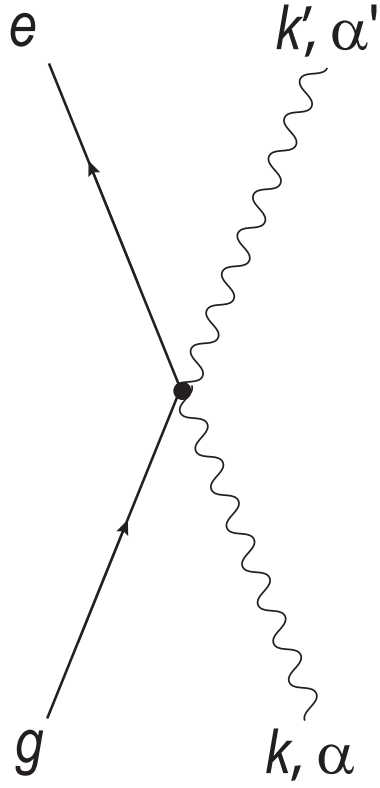
Figure 5.10: Seagull graph depicting low energy Compton scattering that induces both changes in the quantum states of the Rydberg electron and radiation field.

matrix element must include an additional term proportional to $\sin\left[(\mathbf{k}+\mathbf{k}')\cdot(\hat{\mathbf{R}}_0+\hat{\mathbf{r}}_e)\right]$, which is possible if $\mathbf{k}'$ is unmatched with $-\mathbf{k}'$. Under this condition, phase, not amplitude, modulation of the optical lattice occurs, but a high-Q optical cavity would prevent such a mismatch, as that would mean a considerable amount of light in mode $\mathbf{k}',\alpha'$ is escaping. Phase modulation of the optical lattice (a.k.a. "shaking"), which would allow both even- and odd-parity transitions to be made at the Fourier-limit, would need to be performed in free space.

5.7 Conclusion

At this point of the discussion, I have provided a thorough description of Rydberg atoms in electromagnetic fields and described how optical radiation can exchange energy with the Rydberg electron through the ponderomotive interaction. This effect can either be elastic, where the electron remains in the same quantum state $|g\rangle$, or inelastic, where both the optical field and Rydberg electron experience a change in field energy. In the latter case, the Rydberg electron moves from one quantum state $|g\rangle$ to another $|e\rangle$, as the exaggerated size of the wave function with respect to the optical wavelength conserves angular momentum with relaxed selection rules. Consequently, there exists a way to optically manipulate the internal state of the Rydberg atom completely through the ponderomotive ($e^2 \hat{A}^2/(2m_e)$) force, free from the use of any RF or microwave radiation. As a result, highly anisotropic Rydberg states like the circular state, beneficial for applications in fundamental physics, can now be initialized at the high spatial resolution of a laser field focused down to the size of a single Rydberg atom.

CHAPTER VI

Apparatus for Rydberg-Atom Experiments

Key properties of alkali-Rydberg-atom interactions with static and dynamic electromagnetic fields and themselves have previously been outlined in the last two chapters. In short, one should understand from the information provided that the valence electron's elongated wave functions at the order of $\sim \mu$m enhance their sensitivity to electromagnetic fields from the DC to optical range of the spectrum, including the thermal radiation emitted by surrounding bodies at room temperature. Therefore, a proper apparatus different from the one described in Chapter III must be constructed in order that high-resolution spectroscopy and quantum control of the Rydberg states may be performed near the level of the natural linewidth $\sim$kHz for low-l states. This system must incorporate methods of laser cooling and trapping, high-resolution Rydberg state excitation/detection, blackbody shielding, stray-electromagnetic-field suppression, and mm-wave spectroscopy in one setup. Much of the work in [6] concerned the construction and design of this setup and can be read about. In this chapter, I will briefly describe the basic elements of the experimental setup and spend more time explaining the technical modifications that were made since [6].

In Section 1, the basic components of the chamber are described, as well as the methods needed for achieving ultra-high vacuum (UHV). In Section 2, techniques for achieving a sample of rubidium on the order of the Doppler temperature are described. In Section 3, the tunable diode laser system needed for exciting Rydberg states from ^{85}Rb is explained. Section 4 provides information regarding the adiabatic electric-field ionization needed to discern the population within a specified state. The hallmarks of Rydberg-Rydberg spectroscopy using radiated microwaves as a diagnostic tool are explained in Section 5. Section 6 details how the stray DC electric and magnetic fields can be suppressed in order to minimize shifts and broadening in the Rydberg states' energy levels.

6.1 Vacuum Chamber

The vacuum chamber, of which the construction was thoroughly described in [6], consists of an in-vacuum Rb reservoir heated by means of a dimmer supplying high current through heat tape wrapped around the reservoir and surrounding flanges. When heated $\sim 10°$C above room temperature, the Rb vapor pressure becomes workable for sufficient loading into a cold-atom sample. The heated alkali vapor from this reservoir, consisting of a natural mix of Rb isotopes, passes through an opened valve and is mechanically diverted downwards to a borosilicate vapor cell with the help of an L-shaped aluminum piece. At the foot of this piece, a ~ 5 mm diameter hole is drilled to allow access of the atoms upwards to the *science chamber*, provided that a gate valve separating the two chambers is opened. Unique to this experiment, a liquid-helium cryostat is in thermal contact with two copper buckets located within the science chamber. The cylindrical cryostat has an inner- outer-layer, but much of the work in [6] and this dissertation only uses the inner layer. Also, due to the recent shortage and expense of liquid helium, I have thus far only cooled the in-vacuum buckets to 77 K with liquid nitrogen, reserving the helium use for circular-state spectroscopy at the $\sim$Hz-linewidth level. In addition shielding a considerable amount of blackbody radiation to prolong Rydberg lifetimes, the secondary effect of the cryostat is to keep the background pressure of the science chamber in the range of 1-5$\times 10^{-9}$ Torr.

Achieving such pressures for UHV requires the use of several sophisticated pumps. In-vacuum components must first be rinsed with distilled water, then scrubbed with Micro-90, followed by sonication in a water bath. Glass pieces need to be wiped with methanol or acetone. Once everything is properly configured inside the chamber, it is sealed with the appropriate gaskets and bolts tightened to their maximum torque. The following vacuum pumps are attached: a rotary-vane roughing pump sealed to the outlet of a turbomolecular pump and an ion pump (20 L/s). The roughing pump, which consists of a rotor transferring the background gases of the chamber interior to the exterior, drops the chamber pressure from 760 Torr to 10^{-3} Torr while the turbomolecular pump relies on collisions between a rotating blade ($\sim$75 krpm) and an atmospheric molecule to force the fluid out of the chamber. Turbomolecular pumps can yield pressures down to $\sim 10^{-8}$ Torr, the sweet spot for atom trapping, but an unfortunate effect known as *outgassing* elevates this figure. Adsorbed gases on the materials inside the chamber are slowly released into the chamber atmosphere from this effect. Materials like solder and rubber outgas excessively and prohibit the creation of an UHV. For all of the adsorbed molecules to be outgassed and pumped out of the chamber when the interior components are at room temperature, turbomolecular pumping for a duration of several months is required. Speeding up this outgassing and pumping requires heating the

entire chamber above $\sim 100°$C for two weeks. When heating, the components are wrapped in heat tape and aluminum foil in a procedure known as a *bake-out*. After the bake-out, the ion pumps can be activated to drop the chamber to a pressure of $\sim 10^{-9}$ Torr. Ion pumps consist of free-electrons in a Penning-trap array ionizing the remaining background gases so that they can strike a titanium cathode. Sputtered titanium coats the surface of the pump and can then react with the other remaining background gases in the chamber to form inert compounds. With the help of the ion pump, background pressures at the level of $\sim 10^{-9}$ Torr permit a Rb MOT to be generated with lifetimes longer than about 1 s, of which only 15.2 ms are used in my experiments, due to the short duration of the experimental cycle.

6.2   Laser Cooling

Laser cooling is performed on the ^{85}Rb D_2 line using a homebuilt, 780-nm external-cavity diode laser (ECDL). The laser's current and piezo are both stabilized on a saturated-absorption (SA) peak detuned -92 MHz from the $\left|5S_{1/2}, F = 3\right\rangle \rightarrow \left|5P_{3/2}, F' = 4\right\rangle$ cycling transition. This SA spectrum is provided in Fig. 6.1 and is used as the error signal input to two homebuilt servo-amplifiers. The power output of this ECDL is no greater than 30 mW, which is insufficient for providing radiation pressure, so the laser is first sent through a tapered amplifier (TA) that enhances the laser power to 2 W before it is split up into two beams (which are further split for laser cooling): one for the 2D$^+$ MOT and one for polarization-gradient (PG) cooling. In both the lower primary-MOT and upper science chamber, a second ECDL tuned to the $F = 2 \rightarrow F' = 3$ hyperfine transition of the D_2 line is used as a repumper that is coaligned with the cooling beams; for this laser, the intensity is no greater than 10 mW/cm^2.

6.2.1   2D$^+$ MOT

As seen in Fig. 6.2, the atoms are initially cooled in the lower primary MOT chamber. The racetrack coils surrounding the vapor cell, shown in Fig. 6.3, form a two-dimensional quadrupole field $\mathbf{B}_q$ over the (y, z)-plane and a nullified magnetic field in the x-direction. Four counter-propagating beams with an elliptical profile of semi-minor and -major axes of 0.5 cm and 2 cm respectively are used to generate a MOT in two dimensions. On average, the beams have total powers of 27 mW each. These beams are always on and are split up after being sent through an AOM that upshifts the laser frequency by 82 MHz, making the MOT detuning from resonance $\simeq -10$ MHz. A cold atomic beam collimated by the radiation pressure imposed by the cooling laser is thus generated in the lower chamber. With the aid of a tertiary beam pair forcing the atoms upwards through the hole of the diverter piece
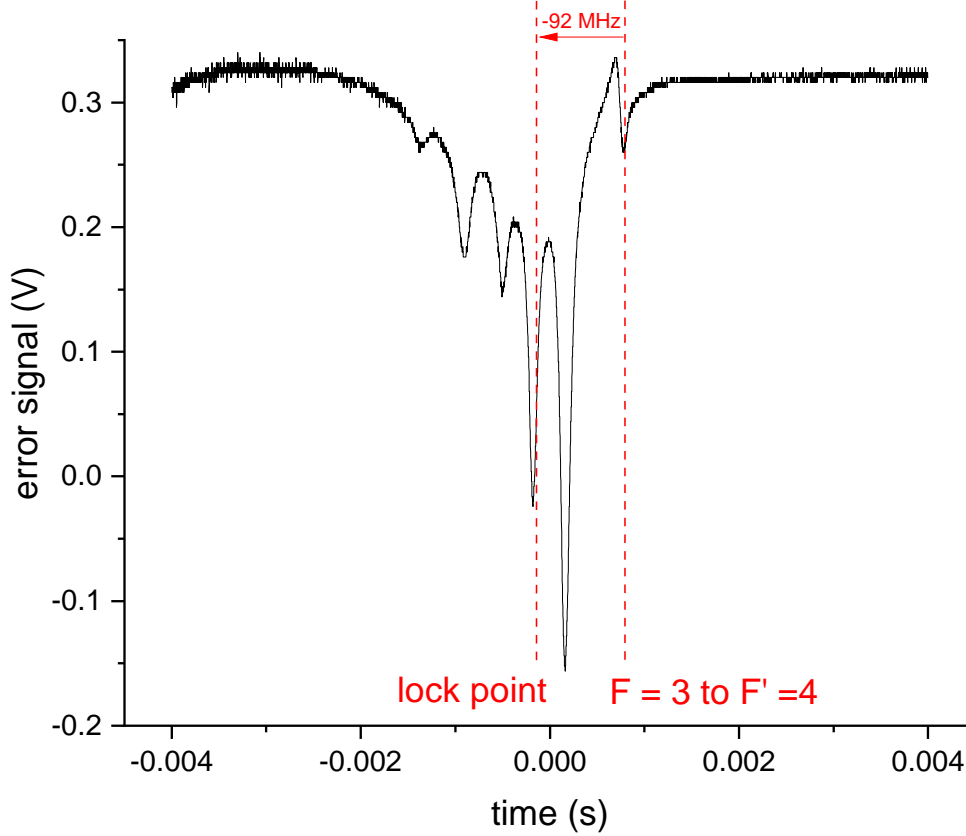
Figure 6.1: Oscilloscope representation of the SA spectrum (^{85}Rb $|F = 3\rangle \rightarrow |F'\rangle$) of the ECDL used for laser cooling in this apparatus. The laser is "locked" to the side of the $F' = 2$ and $F' = 4$ crossover resonance.

into the science chamber, an appreciable sample of ^{85}Rb is available for further cooling to sub-Doppler temperatures. I refer to this configuration described as a 2D$^+$ MOT, where the "+" indicates the inclusion of a pair of slightly misaligned beams pushing the atoms upwards [167]. When the ambient lights of the lab are off, a little pink cloud of fluorescing ^{85}Rb is visible in this lower chamber with the aid of a cell-phone camera, as seen in Fig. 6.3.

6.2.2   PG Cooling

The second set of beams split from those of the 2D$^+$ MOT is upshifted in frequency by 68 MHz (overall -24 MHz detuning) with a separate AOM driver, which pulses them on for a duration of 14.2 ms. I circularly polarize these beams as well in order to achieve PG cooling in the corkscrew configuration, described in Chapter II. Each beam has a Gaussian
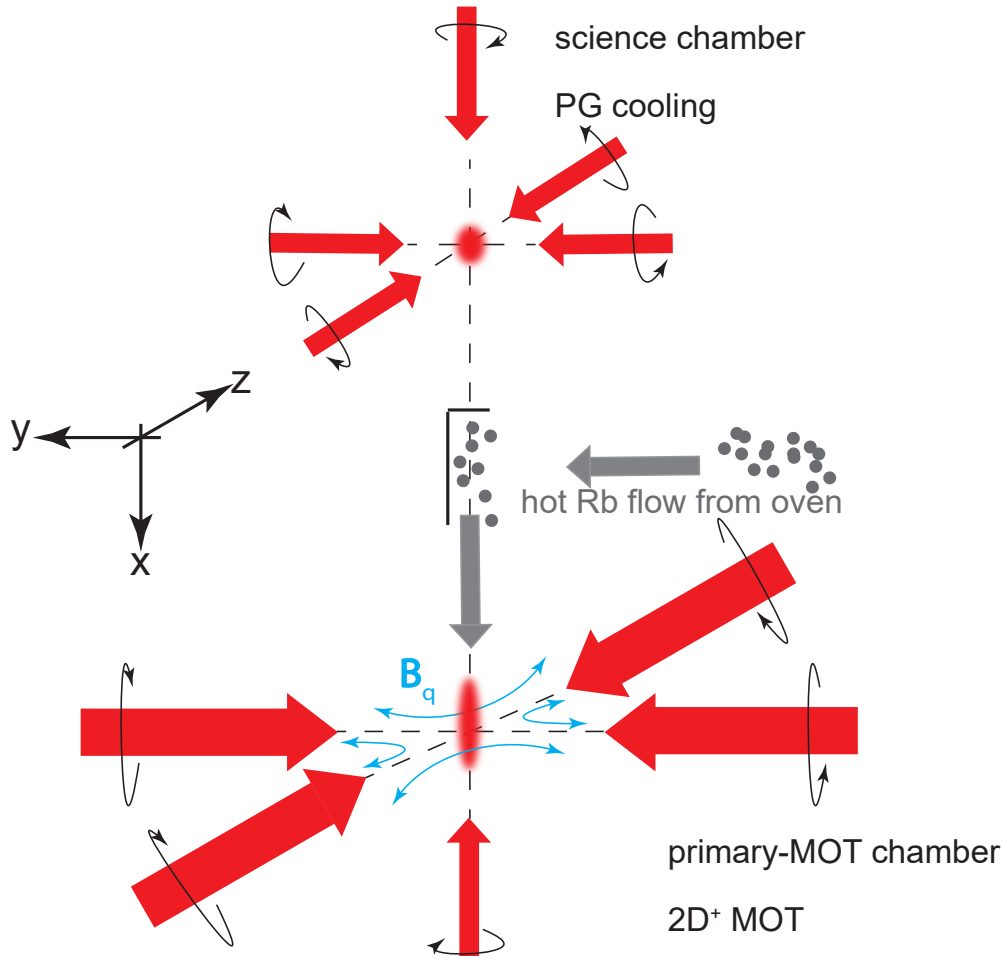
Figure 6.2: Simplified sketch of apparatus showing the complete trajectory of Rb from the oven to the experiemnt and the laser-cooling methods. The x-direction aligns with gravity. Note that the L-shaped diverter plate has a hole in its foot to allow passage of the cold beam up into into the science chamber. Orientation of each beam's circular polarization with respect to the dotted axes is shown by the black arrows.

waist of about 3 mm and an overall optical power of 19 mW. Noteworthy of this apparatus is that the vertical beams of the PG cooling along the x-direction also push the cold beam of ^{85}Rb, generated in the primary-MOT chamber, towards the science chamber. In many other double-stage, cold-atom setups, the laser beams doing the pushing are separately aligned from the PG-cooling beams, blue-detuned from the cycling transition, and transversely diverging; here I have a counter-propagating pair of red-detuned beams (slightly misaligned) guiding the atoms upwards against gravity while cooling them near the geometric center of the science chamber in accordance with the other four PG-cooling beams. Optical molasses,

120
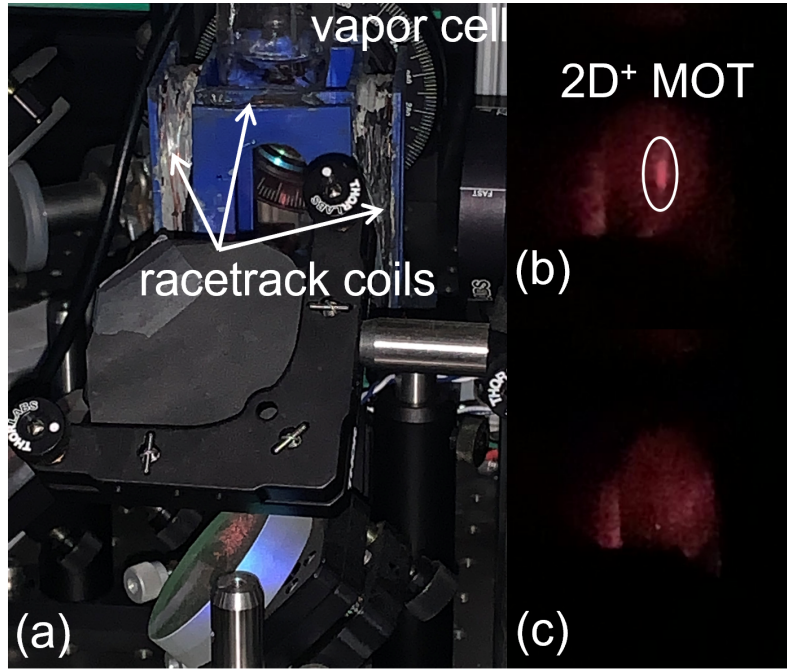
Figure 6.3: In (a) an image of the primary-MOT chamber is shown, which consists of a vapor cell with enameled-copper racetrack coils generating the transverse field gradient. The $2D^+$ MOT can be faintly seen here. Image (b) shows a better view of the fluorescing cold beam generated by the $2D^+$ MOT, which vanishes in (c) when $\mathbf{B}_q = 0$.

formed by the PG cooling, does not require a magnetic quadrupole field $\mathbf{B}_q$; thus, the atoms are not trapped, but cooled to sub-Doppler temperatures. As evidence of the ^{85}Rb-molasses' cold temperature, the atoms persist in the science chamber on the order of ~ 3 s after blocking the cooling light of the $2D^+$ MOT. You cannot see the optical molasses in the chamber by eye, as the atomic density is too low, but a high-quality CCD camera (Cooke Corporation Pixelfly) can image it (see Fig. 6.4). Once a sample of ultracold ^{85}Rb is prepared in its ground-state, the valence electron can subsequently be promoted to a Rydberg state through laser excitation.

6.3 Rydberg-State Excitation

Light originating from a separate, low-power ($\sim 50\mu$W) ECDL at 780 nm is used in combination with a higher-power (~ 40 mW) commercial ECDL (Toptica TA-SHG 110) at 480 nm
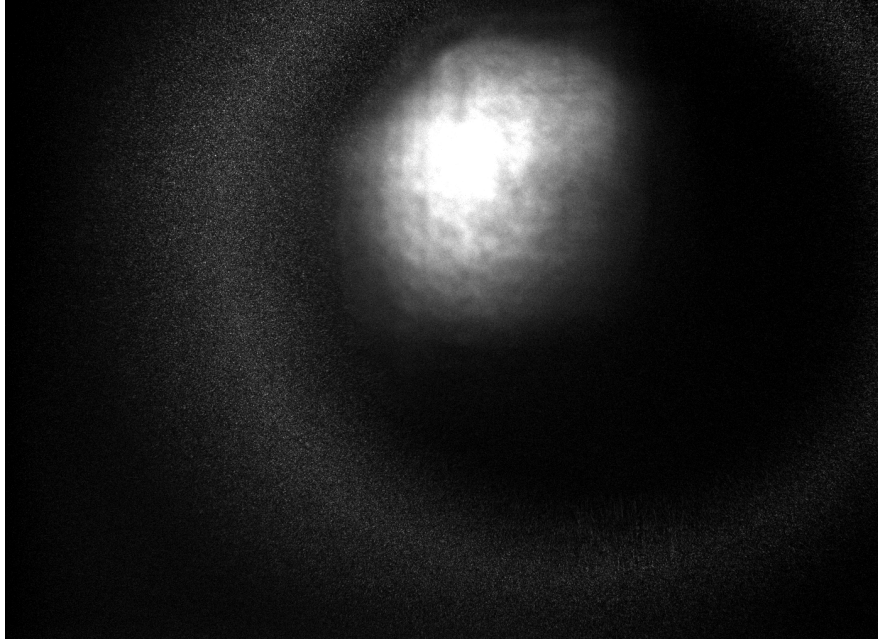
Figure 6.4: CCD image of optical molasses generated in the science chamber through PG cooling.

to promote the ultracold, ground-state ^{85}Rb atoms to $\left|nS_{1/2}\right\rangle$ Rydberg states, essential for the experiments performed in Chapters VII and VIII. The transition $\left|5S_{1/2}\right\rangle \rightarrow \left|nS_{1/2}\right\rangle$ is treated like a single-field coupling even though I use two lasers. A reason for this is that the lower-transition beam is detuned $\delta_L/2\pi = +100\text{-}140$ MHz from the cycling transition, which greatly reduces the maximum scattering rate of $\Gamma/2 \simeq 19$ Ms^{-1}, as well as the population in the intermediate state. When the 480-nm laser has its frequency set so that both beams match the energy spacing between $\left|5S_{1/2}\right\rangle$ and $\left|nS_{1/2}\right\rangle$, the off-resonant, two-photon transition between the two states, derived from second-order perturbation theory [168], is characterized by the peak Rabi frequency, Ω_0,

$$\Omega_0 \simeq \frac{\Omega_1 \Omega_2}{2\delta_L}, \tag{6.1}$$

where Ω_1 is the peak Rabi frequency for the resonant transition $\left|5S_{1/2}, F = 3\right\rangle$ $\rightarrow \left|5P_{3/2}, F' = 4\right\rangle$ and Ω_2 is that for $\left|5P_{3/2}\right\rangle \rightarrow \left|nS_{1/2}\right\rangle$.

Both the current and piezoelectric transducer (PZT) of the homebuilt, 780-nm ECDL are actively compensated to stabilize the emitted laser frequency to either the $F' = 2, 4$ or $F' = 3, 4$ crossover resonances of a saturation spectrum. With the use of two consecutive AOM's each upshifting the 780-nm laser by 100 MHz, the detuning $\delta_L/2\pi$ ends up being either about 100 MHz or 140 MHz from the transition between uppermost hyperfine levels

of $\left|5S_{1/2}\right\rangle$ and $\left|5P_{3/2}\right\rangle$. The latter detuning is used in cases where resonant light scattering needs to be minimized as much as possible, such as experiments involving optical lattices. If too much scattering occurs, the atoms will be heated enough through radiation pressure to escape the lattice wells. In Chapter II, this was not an issue because of the low-intensities of the probe lasers and the strong trapping potential of the optical lattice; thus resonant excitation was allowable for spectroscopy. The peak 780-nm laser power delivered to the atoms is 50 μW at a measured-Gaussian $(1/e^2)$ waist of 31 μm; thus, using the saturation intensity of 3.9 mW/cm^2 [92], the value of $\Omega_1/2\pi$ is 118 MHz. At a detuning of 100 MHz, the photon scattering rate therefore is estimated to be $\Gamma_{sc} \simeq 7$ Ms^{-1} while a $\delta_L/2\pi$ of 140 MHz yields a rate of about 5 Ms^{-1}.

I use a commercial Toptica TA-SHG 110 to generate the 480-nm light needed to excite atoms into $\left|nS_{1/2}\right\rangle$ Rydberg states. The laser consists of a commercial master oscillator power amplifier (MOPA) at 960 nm (Toptica TA 100) with both low ($\sim$ 1 mW) and high ($\sim$ 1 W) power outputs. This high-power output is mode-matched with a commercial ring-cavity (Toptica SHG Pro) that further enhances the circulating field intensity of the 960-nm light. One of the mirrors is affixed to a piezo-actuator that is stabilized to a cavity resonance by means of the Pound-Drever-Hall (PDH) method [121]; a commercial Toptica PID 110 circuit is used to achieve this. Within the ring cavity sits a nonlinear crystal that doubles the 960-nm light. It is critical to maintain this crystal at the temperature $(18 - 32°C)$ which yields the most 480-nm power. Even though the 960-nm power entering the cavity is around 1 W, the naturally poor conversion efficiency of the second-harmonic generation results in only 150-200 mW of blue light emitted from the laser.

The blue light is switched on or off for the experiment with the aid of an AOM that shifts the frequency by 40 MHz. This 40-MHz carrier wave is pulsed using a Mini-Circuits ZASWA-2-50DR+ switch triggered by a TTL pulse synchronized with the experimental clock. Amplification of the switch output is performed with a ZHL-2-8-S RF power amplifier, sending 2 W of RF power to the AOM when the switch is on. An optical fiber delivers the first AOM-diffracted order to the experimental table, where it is expanded in the vertical direction with a cylindrical lens telescope. At most, 38 mW of blue light makes it to the chamber, incident at an angle 60° from the propagation axis of the 780-nm beam. A spherical, achromatic lens focuses this light near the center of the chamber, which is estimated to have an elliptical profile with a minimum semimajor waist of $\sim$ 500 μm and semiminor waist of $\sim$ 10 μm. As a result, the peak blue-beam intensity is estimated to be $\simeq 4.8 \times 10^6$ W/m^2 at the focal-point of the focusing lens. Walking mirrors align the semimajor axis of this blue elliptical beam with the Rayleigh range of the 780-nm excitation laser; as a result, a cigar-shaped cloud of Rydberg atoms is prepared within the optical molasses when the

$\left|5S_{1/2}\right\rangle \to \left|nS_{1/2}\right\rangle$ resonance is met.

Frequency control of the 960-nm MOPA (and therefore 480-nm light) is performed by sending the low-power output through a Fabry-Perot interferometer and monitoring the optical power loss with a photodiode. This photodiode signal is sent through a homebuilt PID-circuit that controls the piezo of the MOPA's master laser. On a cavity resonance, the MOPA frequency is characterized by $mc\epsilon_0^{1/2}/(2\epsilon^{1/2}L)$, where L is the cavity length, ϵ is the cavity medium's permittivity, and m is the mode number. Once the MOPA is in the locked state, its frequency may be tuned by changing ϵ and leaving all other cavity parameters constant (temperature and length are fixed); this sort of laser tuning for spectroscopy was developed by the Raithel Lab in [169]. By implementing a stepper motor to expand or compress the volume, and therefore pressure, of the cavity medium, $\epsilon^{-1/2}$ scales linearly with a digitally-controlled angular turn of the motor's axle. A single digital pulse sent to the stator electromagnets of this synchronous motor is referred to as a *step*. One step translates to a 157.2-kHz change in frequency of the MOPA, as calibrated by the fine structure of the $\left|53D_j\right\rangle$ state in ^{85}Rb. With such frequency control of the 480-nm laser, Rydberg-state linewidths and shifts from external electromagnetic fields may be monitored and quantified.

6.4   Rydberg-State Detection

The apparatus described in this chapter only permits destructive detection of rubidium Rydberg atoms using field ionization, which is described in Chapter IV. A negative high voltage (typically -500 V to -1500 V) is generated from an SRS PS325/2500V-25W power supply and connected to the low-level-voltage input of a DEI PVX-4150 pulse generator; a non-ionizing low-DC (-10 V to 10 V) bias voltage, ϕ_z, is sent to the high-level input. This pulse generator is gated using an inverted TTL that switches the negative high voltage on at low level for a duration of 1 μs. The output pulse is square and therefore gives a flat electric field value throughout its duration, which is problematic when trying to distinguish between two Rydberg states that ionize at two different electric fields. For Rydberg atoms of different internal states to be detected within the same ionization pulse, an adiabatic ramp needs to be applied to the system. Passing the output of the pulse generator through a 51-Ω resistor and 1-nF-capacitance SHV cable gives the pulse an exponential rise up to its maximum value towards the end of the sequence where it suddenly drops down to a low-DC voltage.

Right at the output of the DEI pulse generator, its own noise combined with that of the SRS power supply must be suppressed during the Rydberg-excitation and Rydberg-Rydberg spectroscopy sequences of the experimental cycles in Chapters VII and VIII, lest
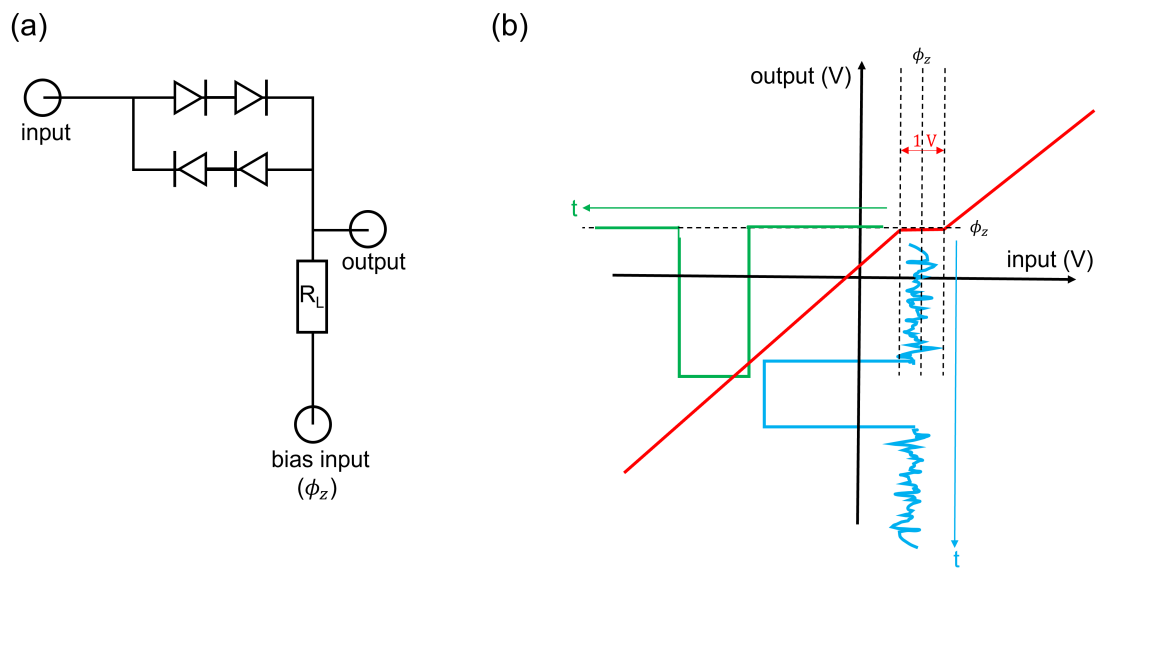
Figure 6.5: In (a) a schematic of the clamp switch circuit is shown. Function of this circuit is shown in (b), where the red curve displays the output voltage as a function of input signal when the device is biased at ϕ_z. Suppression of the background-level noise originating from the high-voltage power source in the input signal (cyan) is evident in the output (green).

the states be broadened and shifted by unwanted DC-Stark effects. In order to preclude this broadening and shifting, a diode-device designed by the Raithel Lab, placed directly at the output of the pulse generator and known as a *clamp switch*, inhibits the electric-field noise generated by the high-voltage power source at times when the ionization pulse is off throughout the experiment. The clamp-switch circuit is roughly sketched out in Fig. 6.5(a) with its functionality graphically described in (b). As can be seen by the graph, the low-DC bias voltage I apply to the system when the pulse is off can only be sent to the experiment and not the noise of the high-voltage or pulse generator provided that such noise is below 1 V.

The ionization field is realized in the science chamber with a pair of parallel, copper plate electrodes. One electrode is in contact with the common ground of the experiment, while the other is in line with the SHV cable delivering the high voltage. After the adiabatic pulse generates $^{85}\text{Rb}^+$ at different fields of the rise for different Rydberg states, the ions will arrive at the particle detector after some time delay that is dependent on the neutral-atom state before ionization. I provide an example of this delay in Fig. 6.6. Ions that were
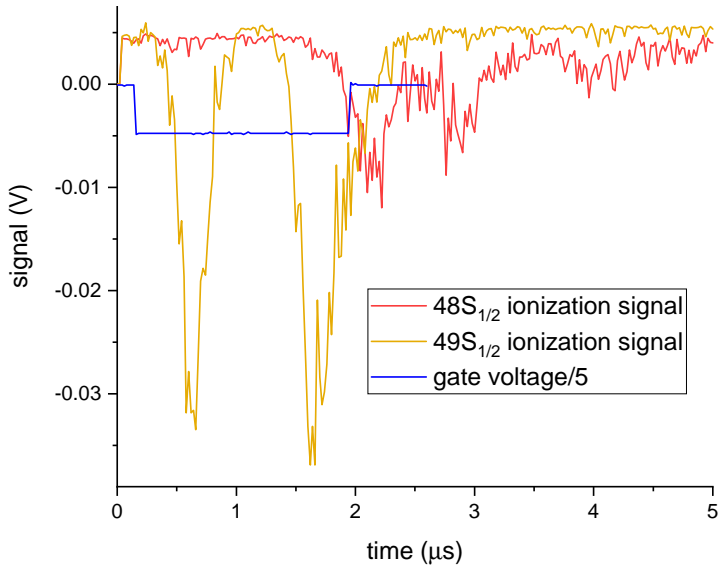
Figure 6.6: Electronic ionization signal from the detector as a function of time delay. Ions created from neutral $49S_{1/2}$ atoms arrive at the particle detector earlier than those of the more tightly bound state $48S_{1/2}$. This arrival time delay is used coordinately with the counting gate to determine the absolute count rate and relative population of $49S_{1/2}$ to $48S_{1/2}$.

previously neutral Rydberg atoms with internal states closer to the ionization threshold will arrive at the detector earlier than those that were in more deeply bound states. Because of this state-dependent time delay, a particle counter (SRS Model SR400) receiving the output voltage of the detector is able to tally the number of ions within a specified gate and therefore can discern the population within that Rydberg state before the ionization. This counter features two such gates, so the population in two separate Rydberg states can be simultaneously recorded. All components of the Rydberg-state-detection system of the science chamber are featured in Fig. 6.7.

The particle detector mentioned consists of chevron microchannel plates (MCP). An incident ion is accelerated through the MCP with the help of three electrodes: a front, middle, and back. The potential difference between consecutive electrodes must be no greater than ~ 1 kV lest damage may occur to the device. In this thesis, the middle is not connected to any voltage and is left as a floating ground that is charged by the potential difference between the front and back electrodes. I ground the back electrode while applying a voltage of -1800 V to the front. As the accelerated ion enters the MCP, secondary emission of electrons occurs from the collision of the ion with the walls of the angled microchannels;
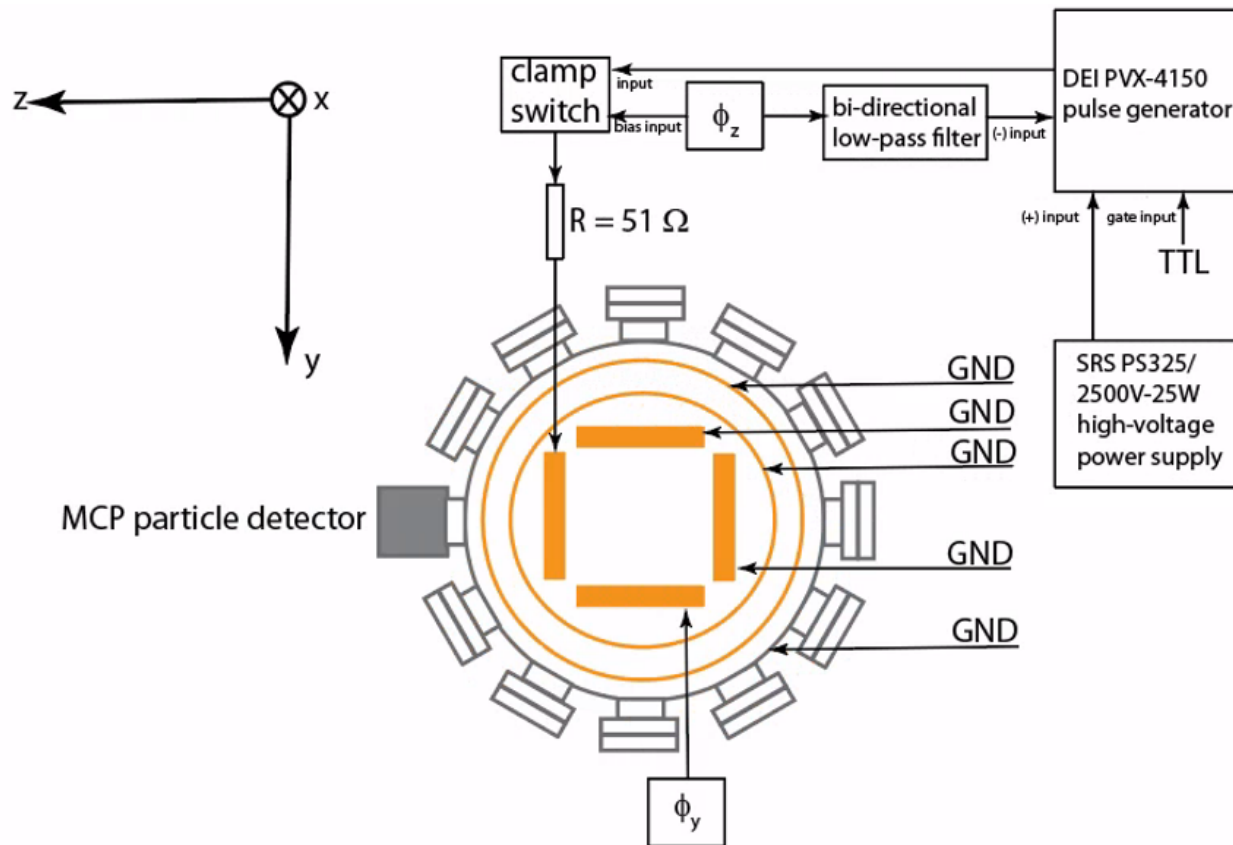
Figure 6.7: Top view of science chamber, internal copper electrodes, cryogenic copper buckets, and its electronic connections are absent. The top and bottom electrodes for the x-direction are not shown, nor are the vacuum pumps/gauges, internal electrode holders, and the grounded shell surrounding the electrodes [6].

the emitted secondary electrons are accelerated towards the grounded back electrode and also strike the walls, emitting more electrons. Consequently, this electron multiplication from the MCP enhances the charge of the incident particle. The cluster of electrons exiting the microchannels strike a phosphor screen that is typically biased at 1 kV with a fourth electrode. Thus, the screen lights up and is visible with a CCD camera. However, the data in my thesis require an electronic pulse corresponding to an incident ion to be counted by the SR400. For this reason, a homebuilt bias-T circuit picks off the fast pulse of the multiplied electrons generated by the ion that an ORTEC Model VT120 amplifies before the SR400. Key features of the MCP are included in Fig. 6.8.
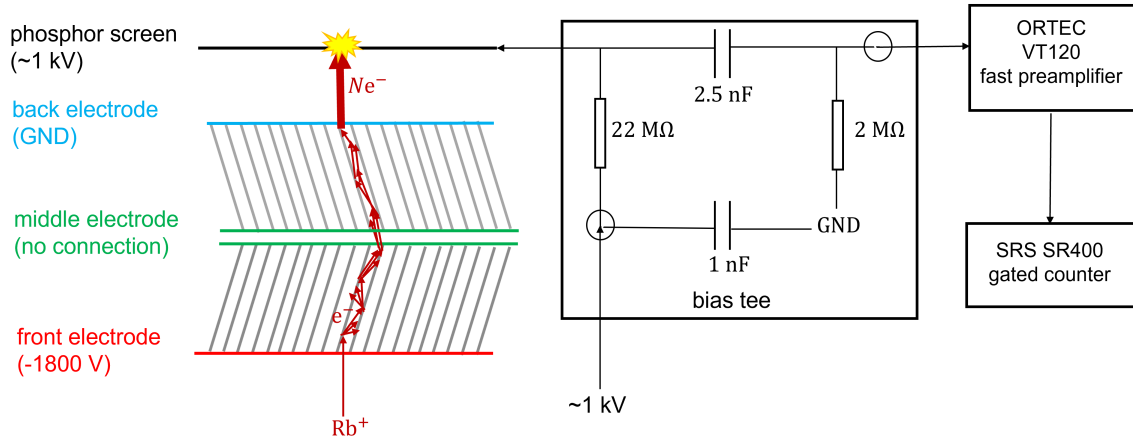
Figure 6.8: Rough schematic of the MCP that converts a signal from a single Rb ion into a bunch of N electrons. Its electronic pulse reaches a particle counter through capacitive coupling in a bias tee.

6.5   Microwave Spectroscopy

As a diagnostic, Rydberg-Rydberg transitions may be driven through conventional $\mathbf{A} \cdot \hat{\mathbf{p}}_e$ microwave couplings. When performing the microwave drives of these transitions, I start with a stable, 10-MHz frequency reference (a portable SRS Model FS725 clock) downconverted from the ^{87}Rb $|F = 1\rangle \rightarrow |F = 2\rangle$ magnetic-dipole transition at 6.8 GHz. This reference phase locks the synthesized frequency (generated from either an HP8673D or Agilent N5183A signal generator) to the clock transition allowing sub-Hz precision and accuracy in the emitted frequency. Coaxial cables are fed into a variety of horn antennas depending on the microwave band used for spectroscopy. For all experiments, radiated microwaves leave the horn antennas polarized along the x-axis and pass through the science chamber windows towards the cold Rydberg sample.

Coherent control of the internal Rydberg states for this apparatus via emitted microwaves is demonstrated in the following diagnostic experiment. Here, the ground state of ^{85}Rb is excited to $|58S_{1/2}\rangle$ where a 10 μs microwave pulse drives the $|58S_{1/2}\rangle \rightarrow |59S_{1/2}\rangle$ transition through an off-resonant, two-photon Raman pulse. Thus, the two-photon Rabi frequency is proportional to the microwave power incident on the atoms. Microwave power transmitted from the HP8673D, P_μ, is proportional to that radiating from the Pasternack PE9852/2F-15 horn antenna, as no intermediate nonlinear devices are included in the lineup. Fig. 6.9 exhibits the Rabi flopping that occurs as the microwave intensity is increased on a logarithmic
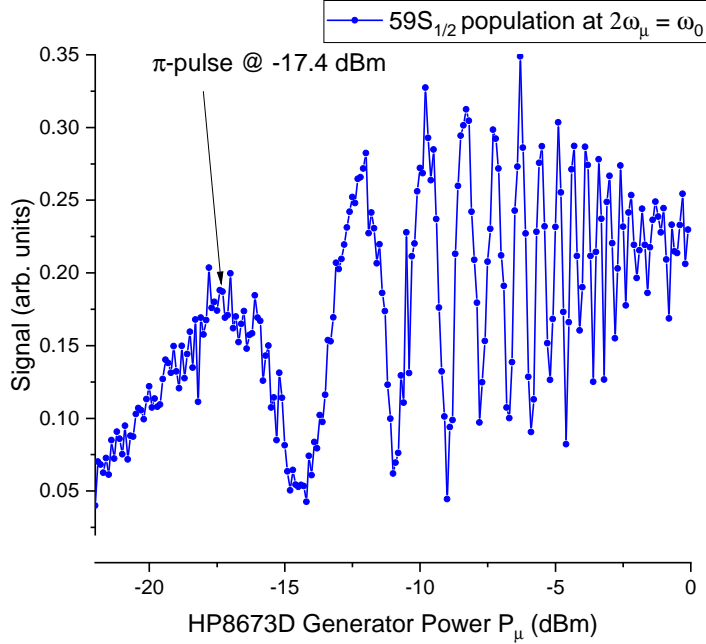
Figure 6.9: Rabi flops for the $\left|58S_{1/2}\right\rangle \to \left|59S_{1/2}\right\rangle$ transition, where the pulse area is scanned by varying P_μ.

scale. For the signal axis, I monitor the proportion of counts collected within the gate overlapping the $59S_{1/2}$ ionization signal to the gate overlapping the signal from both Rydberg states. At a microwave frequency setting ω_μ of $2\omega_\mu/(2\pi) = 38.768524$ GHz, P_μ is scanned up to 1 mW, where the fringe contrast is reduced, indicative of the transition beginning to saturate.

When the upper-state population reaches its first local maximum at $2\omega_\mu = \omega_0$, the pulse area, θ, is π. The microwave-frequency spectrum of this transition has a $\sin x/x$-like shape, where the central peak at $\omega_0/2$ has a Fourier-limited linewidth of $94/2$ kHz and the nearest sidebands are visible, as shown in Fig. 6.10(a) for the $\theta = \pi$ pulse. First-order sidebands of the spectrum reach the strength of the central peak when P_μ is enhanced to yield $\theta = 3\pi/2$ in (b) while in (c) the central peak vanishes as $\theta = 2\pi$. However, at $\omega_\mu = \omega_0/2$, the amplitude of $\left|58S_{1/2}\right\rangle$ acquires a phase shift of π.

It is noted that the observation of a Fourier-limited spectrum for an $\left|nS\right\rangle \to \left|n'S\right\rangle$ transition is possible even in the presence of uncancelled, stray electric and magnetic fields. One reason is the following: similar gyromagnetic ratios, which are l and not n-dependent prevent Zeeman splitting and inhomogeneous line broadening for this transition. Another reason is that the $l = 0$ Rydberg states have the weakest DC polarizabilities within an n manifold, and they do not change considerably as n is changed by one like the case shown in this section $(\Delta\alpha_{n,l,j,|m_j|} < 5$ kHz m^2/V$^2)$. Thus, DC Stark shifts and line broadening due to
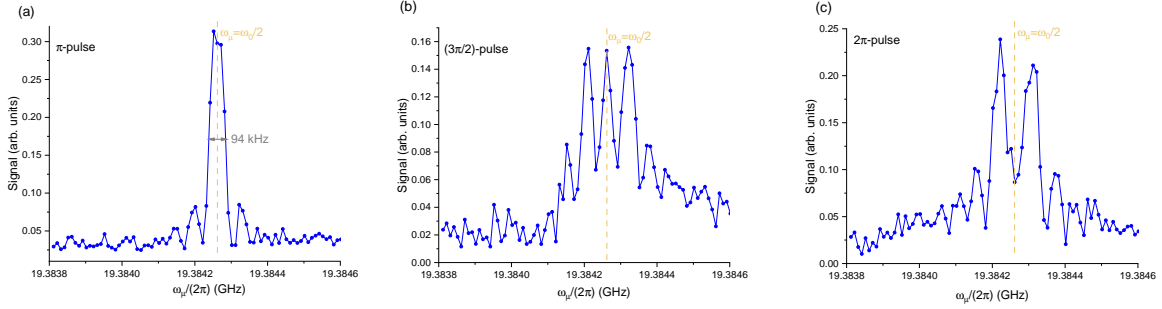
Figure 6.10: Two-photon microwave spectra of the $\left|58S_{1/2}\right\rangle \to \left|59S_{1/2}\right\rangle$ transition.

position-dependent stray fields are minimal in the spectra of Fig. 6.10.

For transitions that induce a nonzero change in orbital angular momentum, such as $\left|nS_{1/2}\right\rangle \to \left|nP_j\right\rangle$, the differences in the respective states' gyromagnetic ratios make the spectral lines susceptible to Δm_j-dependent splittings and inhomogeneities in the magnetic field. Furthermore, the differences in $\alpha_{n,l,j,|m_j|}$ are on the order of ~ 70 kHz m^2/V^2 for $n = 50\text{-}60$ as $|\Delta l| = 1$, so a stray electric field that is position-dependent throughout the sample would shift the spectral line and asymmetrically broaden it. Chapters VII and VIII involve dipole-allowed Rydberg-Rydberg transitions as integral aspects of the experiments, which leads to the requirement of stray electric and magnetic field cancellation in order to achieve the narrowest linewidths.

6.6   DC Electric and Magnetic Field Control

As mentioned in the previous section, the transition $\left|nS_{1/2}\right\rangle \to \left|nP_j\right\rangle$ is susceptible to stray electric and magnetic fields that leak into the chamber. Stray electric fields mainly originate from interactions of the ionized Rb atoms and the internal Cu electrodes but also can arise from electronics and potential differences external to the science chamber. Undesirable, stray magnetic fields will enter the chamber from ferromagnetic materials (e.g., ball drivers, iron stools, and toy demo magnets) lying around in the lab. Described in Ref. [6] and depicted in Fig. 6.11, three pairs of parallel electrodes and external Helmholtz coils are used to generate static potential differences ϕ_i and magnetic fields B_i along the Cartesian axes of the apparatus $i = x, y, z$. The potential differences generate orthogonal homogeneous electric fields parallel to each of the axes that can be controlled to make a field in an arbitrary direction that cancels the stray field. Similarly this procedure can be performed for reducing
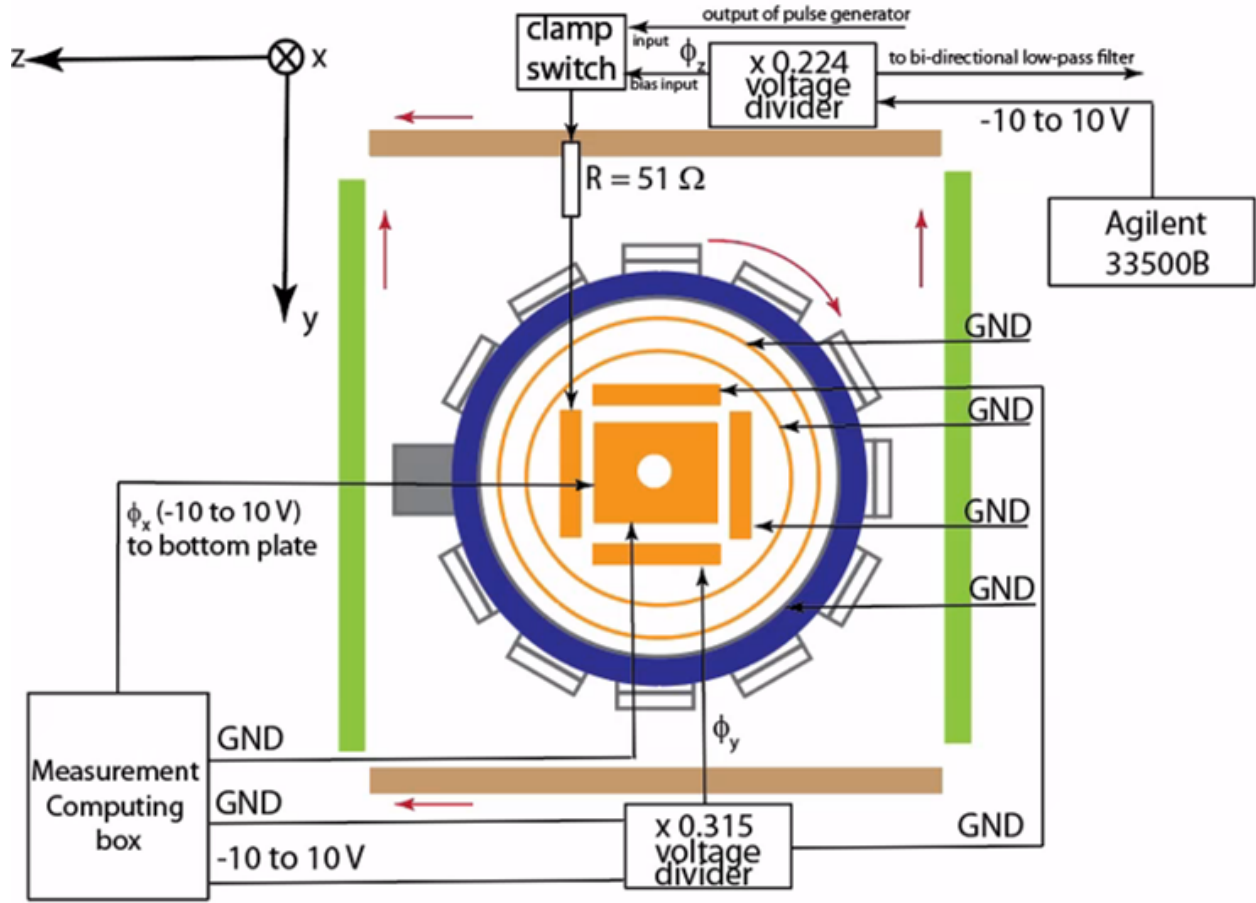
Figure 6.11: Electronics that generate ϕ_i and B_i for $i = x, y, z$ and the connections to the science chamber (top view). The red arrows indicate the directions of the current in the coils that generate the magnetic fields. The bottom Helmholtz coil and Cu electrode in the x-direction is not shown.

the Zeeman effects of the stray B-fields. In this section, I will describe the procedure for using the science chamber's electrodes and Helmholtz coils to reduce linewidths and shifts on $\left|nS_{1/2}\right\rangle \to \left|nP_{1/2}\right\rangle$ transitions brought on by these stray fields.

6.6.1 Stray Electric Fields

Two different power supplies are used to provide the potentials needed for cancelling the stray electric fields. A Measurement Computing USB-3114 digital power source provides two ground (GND) and two static potentials in the range $[-10, 10]$ V to the x- and y-direction electrode pairs. Additionally, an Agilent Model 33500B arbitrary waveform generator allows a quasistatic electric-field to be realized in the z-direction instead of the fields flat with time

that the USB-3114 box can only offer. Because the electrodes have a larger spacing in the x-direction, the electric-field calibration factor is weaker. For this reason, the noise of the Measurement Computing box's needs not be reduced with a voltage divider. On the other hand, the calibration factor is about four times larger in the y-direction, which requires the noise to be reduced by a factor of ~ 3 (3.17 to be exact) with a voltage divider. The divider, however, limits the maximum possible value of $|\phi_y|$ to 3.15 V. In the z-direction, the electrodes have similar calibration factor meaning the potential supplied by the Agilent 33500B must multiplied by 0.224 to minimize the noise; this voltage divider consists of two channels that provide ϕ_x to the bi-directional low-pass filter and high input of the pulse generator used for pulsed field ionization while simultaneously biasing the clamp switch the trims the pulse generator's noise.

The overall noise figures are found in Ref. [6], but there was a recalibration in the factor f_i since then. Calibration factor f_i is defined from the relation, $E_i = (\phi_i - \phi_{i0})/f_i$ where ϕ_{i0} is the potential in the i-direction that yields a minimal DC Stark shift on the Rydberg-Rydberg spectrum. These calibration factors are found in Table 6.2.

Table 6.1:
Calibration factors for converting potential ϕ_i to electric-field E_i using $E_i = (\phi_i - \phi_{i0})/f_i$, where ϕ_{i0} changes on a day-to-day basis.

i	f_i (cm)
x	-19.6(3)
y	-5.63(7)
z	-7.83(9)

The procedure for finding ϕ_{i0}, which changes on a day-to-day basis is detailed in the following. Spectroscopy is first performed on an $\left|nS_{1/2}\right\rangle \rightarrow \left|nP_{1/2}\right\rangle$ transition with microwaves while varying ϕ_i in the i-th direction and keeping the other potentials on the orthogonal electrodes constant at some guess value. Transition-frequency shifts in the i-th direction therefore have the expected parabolic dependence from the DC Stark effect, as shown in Fig. 6.12; the vertex corresponds to the voltage ϕ_{i0} that minimizes the stray-field component in that direction. Subsequently, the potential in the i-th direction is fixed at ϕ_{i0} while the stray-field component along the second axis is minimized. Iterations of this procedure are performed until the most-blue-shifted and narrowest spectral line is achieved. For this setup, one really only has to do this zeroing procedure every few weeks, as the interaction region remains pretty stable as long as the laser alignment is not perturbed. Even when this procedure needs to be performed, field zeros rarely change by more than ~ 5 %.
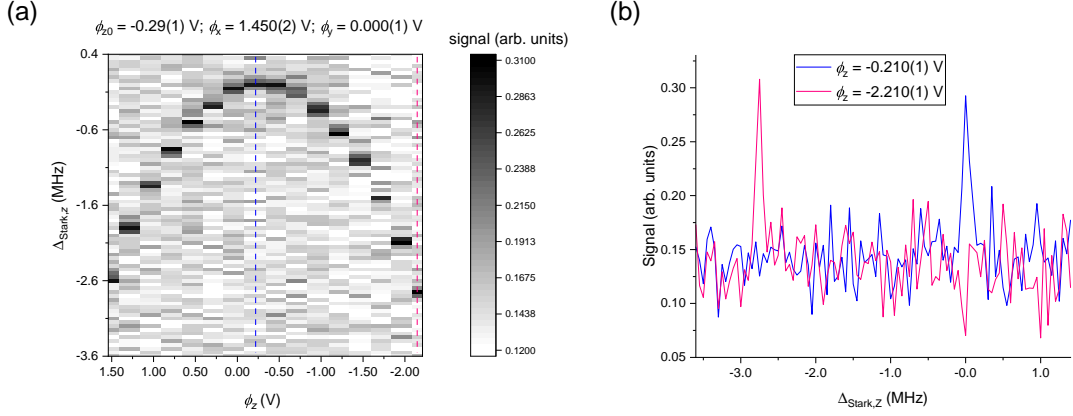
Figure 6.12: Graph (a) displays an example of electric-field zeroing in the $i = z$ direction for $\left|44S_{1/2}\right\rangle \rightarrow \left|44P_{1/2}\right\rangle$. The vertex of the parabola is located where $\phi_z = \phi_{z0}$. Graph (b) shows the differences in spectral lines as ϕ_z is moved from ϕ_{z0}.

6.6.2 Stray Magnetic Fields

The Helmholtz coils that give magnetic fields in arbitrary directions in order to minimize Zeeman effects on the $\left|nS_{1/2}\right\rangle \rightarrow \left|nP_{1/2}\right\rangle$ are in connection with Kepco ATE power supplies. There is one supply per coil pair, providing up to 2 A of DC current (I_i for pair $i = x, y, z$) through the copper wires. The magnetic-field-to-current calibration factors k_i, defined as $B_i = k_i(I_i - I_{i0})$ where I_{i0} is the current yielding the narrowest linewidths, are presented in Table 6.2 [6].

Table 6.2:
Calibration factors for converting current I_i to magnetic-field B_i using $B_i = k_i(I_i - I_{i0})$, where I_{i0} changes on a day-to-day basis [6].

i	k_i (mG/A)
x	325.55(1)
y	353.85(1)
z	162.86(2)

Stray magnetic fields are vectorially subtracted in a similar manner as the electric-fields are. A guess value for the zeroing currents is initially provided in the directions different from i, while I_i is scanned and the spectral lines of the $\left|nS_{1/2}\right\rangle \rightarrow \left|nP_{1/2}\right\rangle$ transitions are collected. I determine I_{i0} to be the current where the Zeeman broadening is the least significant. Then, the next direction is zeroed with iterations repeating until the Zeeman effect is minimized. In this procedure, however, the microwave power is reduced considerably in order to resolve the hyperfine structure of the Rydberg states. Thus, I am looking to achieve the narrowest

peaks corresponding to possible hyperfine transitions $\left|nS_{1/2}, F\right\rangle \to \left|nP_{1/2}, F'\right\rangle$. An example of this magnetic-field zeroing will be provided in the next chapter where Rydberg hyperfine structure is introduced and measured for the $\left|nP_{1/2}\right\rangle$ states.

6.7   Optical Dipole Trap & Lattice

In Chapter VII, I demonstrate the feasibility and underlying physics behind laser-driven Rydberg-Rydberg transitions via the ponderomotive interactions, which is the basis of the ongoing effort in preparing circular Rydberg states for fundamental-physics applications completely with optical fields. Because the strength of the ponderomotive interaction is proportional to the gradient of the laser field's intensity profile, a tightly-focused, optical lattice of high power (~ 1 W per beam) must be overlapped with the ultracold Rydberg sample. A small focal-spot size ($\sim 10~\mu$m) near the interaction region has the additional advantage of manipulating the internal states of alkali Rydberg atoms with a spatial resolution enhanced from that of microwave radiation.

Light for the lattice originates from a Nd:YAG fiber laser that emits up to 10 W of optical power at 1064 nm. I do not care about the absolute optical frequency for the experiment in Chapter VII but about the overall linewidth of the laser, which is favorable (< 100 kHz) in this case. The main beam, shown in Fig. 6.13, is split into two high-power (880-940 mW) beams that are used to form the one-dimensional lattice inside the science chamber. A DC phase shift of $\eta_2 = \pi$ can be applied to one of the beams in order to invert the intensity profile of the lattice; an aspect of this apparatus that was introduced in Refs. [170; 154; 157] for enhancing the trapping efficiency of Rydberg atoms within the lattice wells. Such a phase shift is realized with a Conoptics M350-105-02-RP-C phase-shifter. Potential difference V_π of about 750 V is applied to achieve this translational lattice shift of $\lambda/4$. The two high-power beams, denoted by optical fields $\mathbf{E}_u^{(i)}$ and $\mathbf{E}_u^{(r)}$, are fiber-coupled to the science chamber, where their transverse diameters are enlarged with telescopes that magnify the waists of the fiber modes by a factor of 10. These beams are walked into the chamber and focused down with achromatic lenses to a spot size of $\sim 15~\mu$m, verifiable by the image of the focal spot in Fig. 6.14 captured outside the chamber with a waist measured to be $w_0 = 15.1~\mu$m. The achromatic lenses focusing the high-powered lattice beams sit on translation stages that allow longitudinal overlap of the focusing region with the cigar-shaped sample of Rydberg atoms formed by the interacting region of the 780- and 480-nm excitation lasers.

Noticeable in Fig. 6.13 is a third beam path that is split from $\mathbf{E}_u^{(i)}$. This beam is phase-modulated by means of an iXblue Model NIR-MPZ-LN-20 and is denoted by $\mathbf{E}_m^{(i)}$; ponderomotive transitions among Rydberg states of the same or opposite parity require the presence
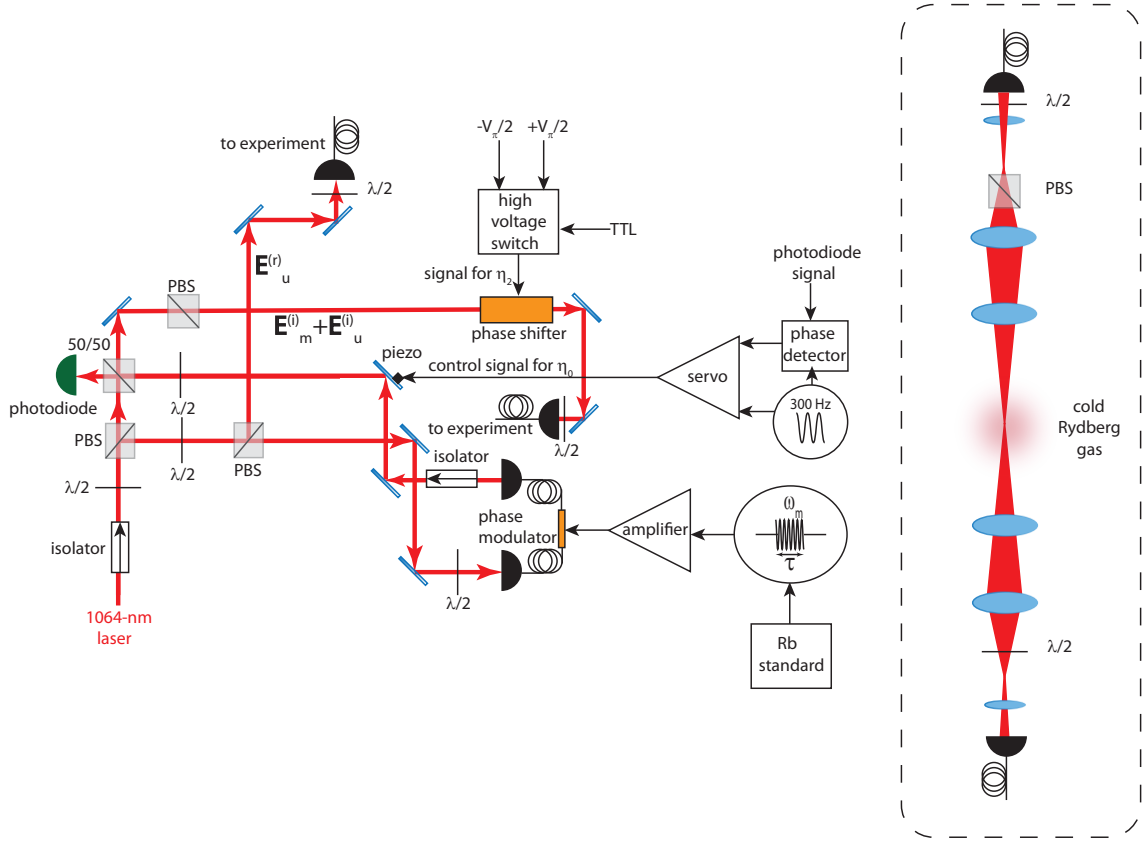
Figure 6.13: Schematic of 1064-nm laser optics used for creating a phase-modulated optical lattice. Abbreviations are the following: "$\lambda/2$"-half wave plate, "PBS"-polarizing beamsplitter, "50/50"-50:50 beamsplitter, "ω_m"-modulation frequency, and "V_π"-modulation depth of phase shifter. Figure adapted from [7].

of this third beam at a fixed global phase difference η_0 with respect to the unmodulated beams. Coherent addition of the unmodulated and modulated incident beams is performed through the readout of of a Mach-Zehnder interferometer that yields fringes as a function of the signal applied to the piezo-actuated mirror in Fig. 6.13. In order that the global phase offset between the unmodulated and modulated beams is eliminated, the signal on the piezo must actively align the mirror so that the photodiode reads destructive interference between the two beams. Reliable stabilization of this mirror requires lock-in detection of the photodiode with a 300 Hz local-oscillator so that a noise-filtered error signal with an inflection point near the photodiode minimum is fed into the TOPTICA PID 110 servo-amplifier. Beam $\mathbf{E}_m^{(i)}$ is coaligned with $\mathbf{E}_u^{(i)}$ and has a peak power of 12 mW. Also, the 780-nm excitation beam is coupled to the same fiber as these incident beams, allowing close alignment to the 1064-nm incident beams save for the chromatic aberration of ~ 2.5 mm generated by the focusing

lens.
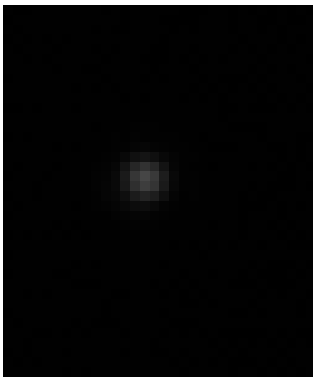
Figure 6.14: Transverse profile of 1064-nm lattice at focal point of the lens.

Before an optical lattice can be made, a single-beam, free-running optical dipole trap formed from optical field $\mathbf{E}_u^{(i)}$ alone needs to be aligned with the atomic sample. Successful overlap of this beam's Rayleigh range with the Rydberg excitation region is the most experimentally challenging procedure in this thesis. After many months of failed attempts at getting the tightest 1064-nm focus at the location of the Rydberg sample, I decided to use the more easily observable AC Stark shifts realized by the off-resonant and co-propagating 780-nm beam to locate the longitudinal position of the 1064-nm focus. The beam is blue-detuned on the order of ~ 100 MHz and thus provides a positive energy shift on the rubidium ground state at its most intense region, and because the electric-dipole and ponderomotive interactions are negligible for the Rydberg state, atoms shifted by the dipole-force of the 780-nm laser are excited to Rydberg state at a red detuning of the 480-nm laser from the field-free resonance. The focusing lens' distance from the Rydberg excitation region, set by the translation stage on which it sits, yields the maximum red shift on the Rydberg line when it is at a position where the 780-nm focus is aligned with the molasses. Knowing that the co–propagating, 1064-nm laser has a focus 2.5 mm away, maximum ponderomotive and optical dipole shifts can be effected on the internal atomic states with a single 1064-nm beam.

In Fig. 6.15, this scheme is put into practice by increasing the 780-nm power and setting the 480-nm frequency to be detuned by about -20 MHz (the 780-nm beam is detuned by $+100$ MHz). Rydberg counts are monitored in real-time by the particle counter while the translation stage moves the focusing lens closer and further from the science chamber's geometric center. When ions are detected, I know that I excited atoms experiencing the 780-nm, AC Stark shifts and that I am in the vicinity of the 780-nm focus of the lens. In order to pinpoint the focus, I gradually move the translation stage in steps of 0.25 mm and scan the 480-nm laser over the Rydberg resonance; the translation-stage setting where the

shift is ~ 90 MHz at -2.75 mm in Fig. 6.15 is the location of the 780-nm focus. Thus, the focusing lens is then moved outwards by 2.5 mm.
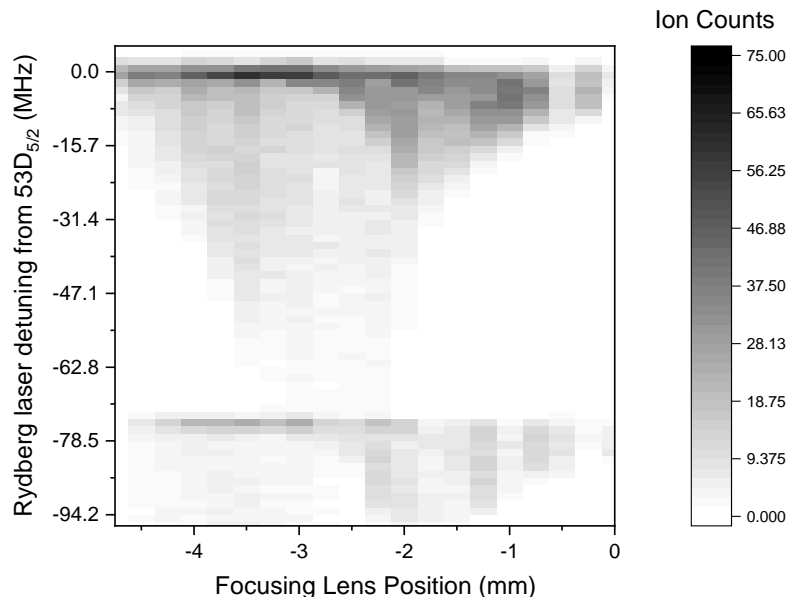
Figure 6.15: AC Stark shifts imposed by 780-nm excitation beam on the $|53D_j\rangle$ states when it is detuned ~ 100 MHz from the $F = 3 \rightarrow F' = 4$ transition. The position of the focusing lens is shown relative to its initial position and is plotted for each Rydberg spectrum (more negative positional values correspond to the lens moving further away from the science chamber center).

When the 780-nm power is lowered, and the detuning is increased to 140 MHz, and the 1064-nm beam is unblocked, the single 1064-nm beam yields the optical-dipole and ponderomotive shifts on the Rydberg state that are observable by the atomic feature blue-detuned from the field-free, $|46S_{1/2}\rangle$ Rydberg resonance, as seen in Fig. 6.16. An optical lattice is formed when the counter-propagating beam is sufficiently coupled into the fiber of the single-beam dipole trap by means of its walking mirrors and focusing lens. Evidence of the enhancement in electric-dipole and ponderomotive light shifts are shown in Fig. 6.16 with the second beam aligned. As explained in Chapter II, the inflection point corresponds to the region where the atoms see the greatest optical intensity in the lattice field.
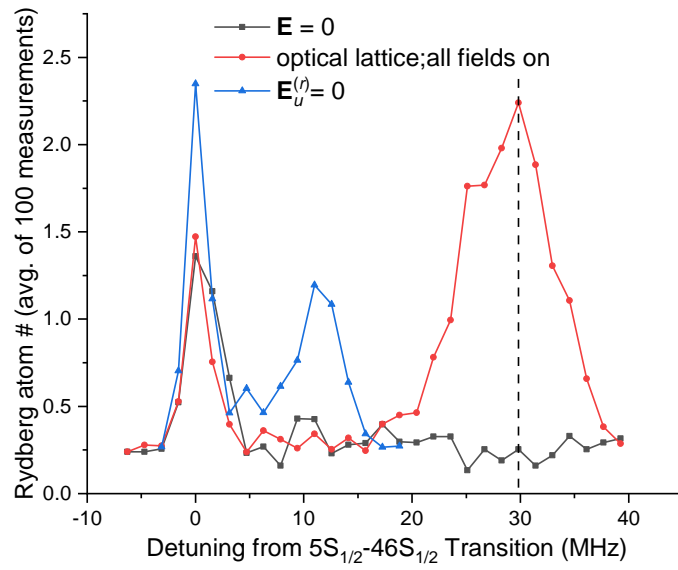
Figure 6.16: Light shifts from the 1064-nm laser on the $\left|5S_{1/2}\right\rangle \to \left|46S_{1/2}\right\rangle$ transition as for the case of no light (gray), the incident field only, i.e., $\mathbf{E}_u^{(r)} = 0$ (blue), and both $\mathbf{E}_u^{(i)}$ and $\mathbf{E}_u^{(r)}$ present (red). The dashed line is where the 480-nm detuning is set during the experiments of Chapter VIII. Figure taken from [7].

CHAPTER VII

Measurement of $nP_{1/2}$ Rydberg Hyperfine Structure in ^{85}Rb

This chapter is based on Ref. [8].

7.1 Introduction

In some cases, the hyperfine sublevels of a Rydberg state can be observed in spectroscopic data when at frequency resolutions near 1 kHz or better. Rydberg $\left|nS_{1/2}\right\rangle$- and $\left|nP_{1/2}\right\rangle$-states of rubidium in particular have hyperfine structure (HFS) that can be measured in mm-wave spectroscopy of the atomic samples. Experiments involving the Rydberg hyperfine levels for these two series of states have the benefit of a larger Hilbert space that includes $\left|F\right\rangle$ basis states, where $F = |j + I|, ..., |j - I|$ and I is the nuclear spin. Therefore, experiments with quantum simulators and processors can involve procedures where the Rydberg $\left|F\right\rangle$ state is manipulated with external mm-waves through magnetic-dipole transitions, similar to those in [105], in place of or in addition to manipulations on the electronic states removed from HFS-coupling. Using such manipulations with a $j = 1/2$ fine-structure state, where all tensor polarizabilities of the Rydberg electron vanish, means that the presence of any off-resonant, stray electric field, static or oscillatory, would not hamper fidelities of the experimental sequences. Precise knowledge of the Rb HFS for all $n > 20$ in $\left|nS_{1/2}\right\rangle$ and $\left|nP_{1/2}\right\rangle$ would be necessary to engage in such experiments.

At the time of this dissertation's completion, the rubidium $nS_{1/2}$ HFS structure has been measured in [171; 10; 6] for ^{85}Rb and in [171; 172; 10; 173] for ^{87}Rb. In [174; 175; 176; 177], measurements were provided for states with $(n \leq 13)P_{1/2}$ states in ^{87}Rb and ^{133}Cs, which both have sizeable hyperfine couplings compared to ^{85}Rb. However, the $nP_{1/2}$ HFS for $n > 13$ states of Rb has only been spectrally observed in [10] with no measurement provided due to the low frequency resolution. Systematic uncertainties for such a measurement originated

from Doppler broadening and limited interactions times related to the effusive beam of Rb used as the Rydberg sample [10]. As described in the previous chapter, our apparatus provides polarization-gradient cooling of the rubidium sample that would prevent these sources of systematic uncertainties for ^{85}Rb; i.e., the interaction time may be extended up to 40 μs and the Doppler broadening would be on the order of $\sim$Hz. Horn antennas located outside the chamber can drive transitions from a fixed hyperfine sublevel ($F = 2$ or 3) of $\left|nS_{1/2}\right\rangle$ to both the hyperfine states ($F' = 2$ or 3) of $\left|nP_{1/2}\right\rangle$ with $n = 42 - 46$. Referencing the mm-wave synthesizer to an atomic standard also allows the spectral resolution to be well below 1 Hz, eliminating any systematic errors in the linearity of the frequency axis. Therefore, with the Rydberg-atom apparatus used for the data collection in this dissertation, a measurement of the HFS coupling constant for $nP_{1/2}$ in ^{85}Rb can be experimentally derived with a reasonable overall uncertainty.

While this measurement does not pertain directly to achieving CS atoms with optical lattices for applications to fundamental physics, it is a yield of electromagnetic field zeroing procedure, which is necessary for the experiments demonstrating ponderomotive transitions in the next chapter and the schemes outlined in the following procedure for initializing a system of CSs. Furthermore, nP_j Rydberg states play roles in the study of ultracold, long-range molecules among Rydberg atoms and ions [178; 179; 112], ground-state atoms [180; 181], and other Rydberg atoms [182; 99; 183]. While millimeter-wave spectroscopy has yet to be performed among the bound molecular states of multiple Rydberg atoms, in principle, including the hyperfine substructure of one of the constituent atom's internal state would be helpful in accurately understanding these spectra. The HFS of $nP_{1/2}$ would also be useful in furthering the understanding of dipole-dipole interactions among Rydberg atoms [184; 185] and Rydberg electrometry [140; 141; 142; 143; 186], the latter of which already is found to have HFS-sensitive effects in Cs [186].

In Section 2, I explain the origins pertaining to the hyperfine-coupling interaction. Section 3 sketches out this measurement's spectroscopy procedure, with results provided in Section 4. An uncertainty analysis covering statistical errors from the fits to spectra, as well as systematics arising from stray magnetic fields and Rydberg density-dependent dipole-dipole interactions, is found in Section 5.

7.2   Theory

Because the orbiting Rydberg electron has a net angular momentum $|\mathbf{J}| = \hbar\sqrt{j(j+1)}$ associated with its motion, the corresponding magnetic moment $\boldsymbol{\mu}_e$ generates a magnetic field that exerts a torque on $\boldsymbol{\mu}_N$, the magnetic moment of the atom's nucleus. For a purely

classical and intuitive example of what is going on here, one should think of the way two bar magnets interact when placed near each other; they will rotate in accordance to the magnetic fields generated. (however, quantum mechanics, which dictates the case described in this chapter, forbids a continuous rotation of the magnetic moment). Potential energy involved with this interaction yields a majority of the level splitting found in the Rydberg level of n, l, j quantum numbers.

For this system, the "good" quantum numbers become those belonging to the set $F = |j + I|, ..., |j - I|$. With $j = 1/2$ and $I = 5/2$ in the case presented here, $F = 2$ or 3, and the hyperfine coupling purely is a result of the magnetic dipole-dipole potential from the two momenta.

When j and I are both ≥ 1, the nucleus' residual electric quadrupole moment [68] can interact with the Rydberg electron through a Coulomb force and break symmetries in the splittings between adjacent F states. The next higher-order, electric-multipole moment, the octupole moment, realizes an effect that is only nonzero for cases where $j \geq 3/2$.

For the $\left| nP_{1/2} \right\rangle$ Rydberg states of ^{85}Rb, the complete interaction, in atomic units, is

$$\hat{H}_{\mathrm{hfs}} = \frac{A_{\mathrm{hfs}}}{[n - \delta_{l,j}(n)]^3} \hat{\mathbf{I}} \cdot \hat{\mathbf{J}}, \tag{7.1}$$

where A_{hfs} is the quantity to be measured. The measurement provided in this work will be in the SI units of GHz. Note that this operator in Eq. 7.1 only acts on the nuclear-spin and electron-angular-momentum parts of the atomic state.

In order to understand what influences the strength of A_{hfs}, one must start by looking at the classical magnetic dipole-dipole interaction treated as a quantum operator in this case, acting on Rydberg state $\left| nP_{1/2} \right\rangle \left| I, m_I \right\rangle$, where $I = 5/2$ and $m_I \in \{-5/2, -3/2, ..., 5/2\}$,

$$\frac{-\mu_0}{4\pi \hat{r}_e^5} [3(\hat{\boldsymbol{\mu}}_N \cdot \hat{\mathbf{r}}_e)(\hat{\boldsymbol{\mu}}_e \cdot \hat{\mathbf{r}}_e) - \hat{r}_e^2 \hat{\boldsymbol{\mu}}_N \cdot \hat{\boldsymbol{\mu}}_e], \tag{7.2}$$

where $\hat{\boldsymbol{\mu}}_N = (\mu_B g_I / \hbar) \hat{\mathbf{I}}$ and $\hat{\boldsymbol{\mu}}_e = -(\mu_B g_J / \hbar) \hat{\mathbf{J}}$. I neglected the term proportional to $\delta(\hat{\mathbf{r}}_e)$ because these are not S-states. The first term in the brackets vanishes due to electric-dipole selection rules, while the second term contributes to the evaluation of A_{hfs}. As a result,

$$\hat{H}_{\mathrm{hfs}} = -\frac{\mu_0 \mu_B^2 g_I g_J}{4\pi\hbar} \left\langle \frac{1}{\hat{r}_e^3} \right\rangle_{n,l,j} \left[\frac{1}{2}(\hat{I}_+ \hat{J}_- + \hat{I}_- \hat{J}_+) + m_I m_j \left| m_I, m_j \right\rangle \left\langle m_I, m_j \right| \right], \tag{7.3}$$

where $\langle \hat{r}_e^{-3} \rangle_{n,l,j} \propto \{1/[n-\delta_{l,j}(n)]^3\}[1-2\delta_2/(n-\delta_0)^3]$ [187]. The latter quantity, which depends on δ_0 and δ_2, induces changes below the uncertainty budget of the experiment described in this chapter.

Using the identity, in atomic units, $\hat{\mathbf{I}} \cdot \hat{\mathbf{J}} = \frac{1}{2}[F(F+1) - I(I+1) - J(J+1)]$, the interval between the $F = 2$ and $F = 3$ states results in a HFS splitting ν_{hfs} depending on $3A_{\text{hfs}}/[n - \delta_{l,j}(n)]^3$.

7.3   Methods

I use the apparatus detailed in Chapter VI for this experiment. The rubidium atoms are laser cooled through PGs before being laser-excited to Rydberg state $\left| nS_{1/2} \right\rangle$ for a duration of 5 μs. For this experiment, where photon scattering from the 780-nm laser is not detrimental to the results, a detuning of $\simeq$ 100 MHz from the D_2 cycling transition suffices. A complete timing diagram of the spectroscopy sequence is shown in Fig. 7.1(a) with a level diagram presented in (b). Here, F and m_F are the quantum numbers associated with the $\left| nS_{1/2} \right\rangle$ Rydberg states while F' and $m_{F'}$ are those belonging to $\left| nP_{1/2} \right\rangle$. Due to the optical polarizations and the close proximity of the laser detuning to the uppermost hyperfine level of the $\left| 5P_{3/2} \right\rangle$ state, a majority of atoms are populated in $F = 3$ versus 2. Therefore, our mm-wave spectroscopy only observes the $nP_{1/2}$ HFS visible on this F line.

Probing the $\left| nS_{1/2}, F = 3 \right\rangle \rightarrow \left| nP_{1/2}, F' \right\rangle$ transitions for $n = $ 42-44 and 46 is done with two different horn antennas that are both polarized parallel to the experiment's x-axis. The mm-waves are first synthesized by the Rb-standard-referenced Agilent MXG Analog Signal Generator (Model N5183A). For the $n = $ 42-44 spectra, the mm-waves are then doubled by a SAGE Model SFA-192KF-S1 frequency multiplier before being radiated by a horn 40 cm from the atoms. With the $\left| 46S_{1/2} \right\rangle \rightarrow \left| 46P_{1/2} \right\rangle$ transition, doubling is not necessary, and the signal generator can be connected directly to a separate horn antenna located 30-cm from the sample. Detecting the Rydberg populations in either internal state requires SSFI with a maximum pulse height of 100-150 V/cm.

7.4   Results

For each spectrum in the $n = $ 42-44 and 46 series, the mm-wave interrogation lasts for a duration of $\tau = 40$ μs, and the mm-wave power is lowered in order that the HFS peaks may be resolved near the Fourier limit of $0.89/\tau = 22$ kHz, which would imply a coupling frequency of 10 kHz and negligible AC Stark shifts from the probing field. Scans of the mm-wave frequency are completed with a $\sim$ 160 kHz range around the "center-of-gravity" transition frequency [10], i.e., the Rydberg transition with HFS removed, in steps of 2 kHz.

Measurements of the HFS in the $n = $ 42-44 and 46 series first require an arithmetic average of eight individual frequency scans. After averaging, a double Lorentzian function is
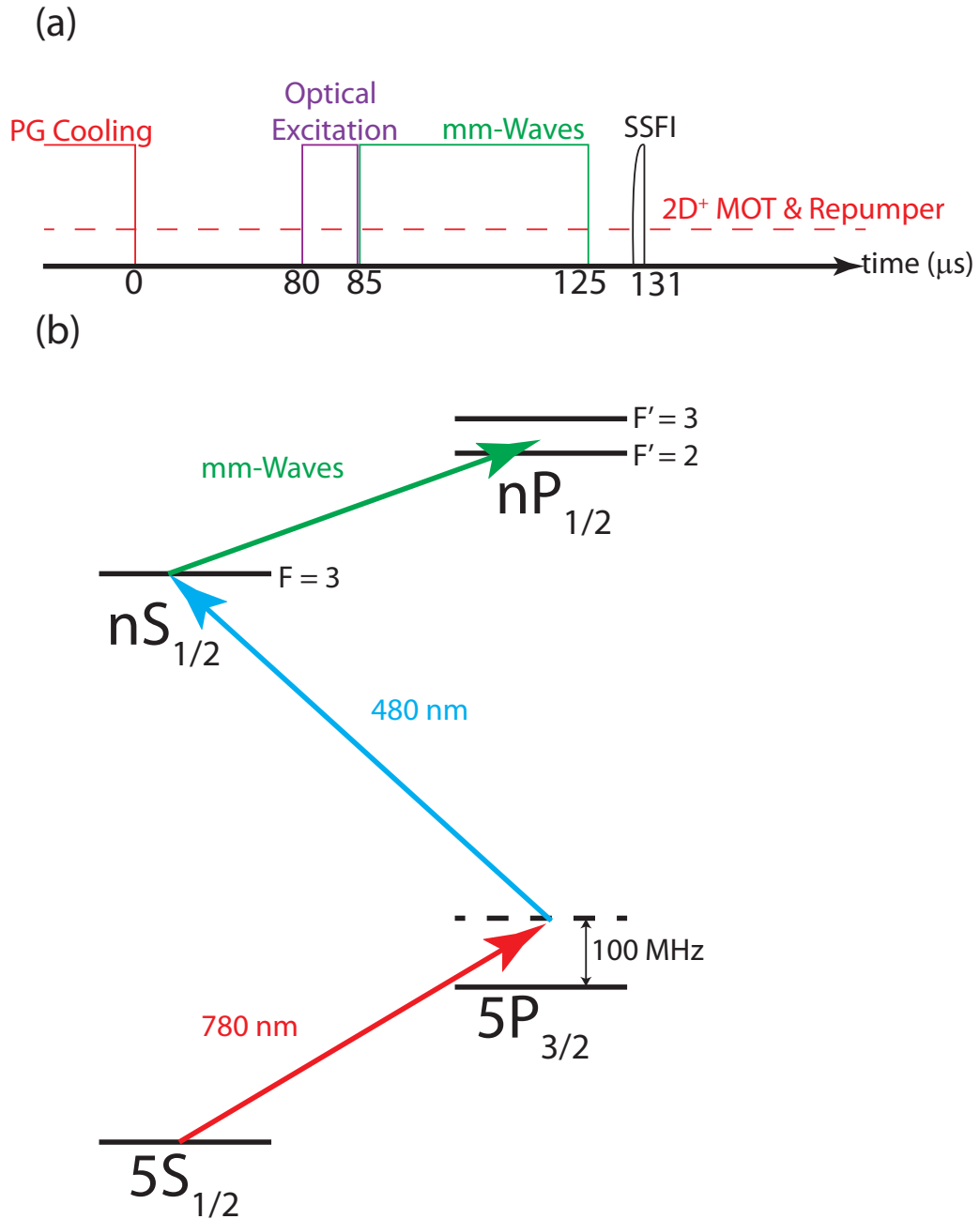
Figure 7.1: Figure taken from [8]. In (a) the timing sequence is provided while (b) exhibits the relevant levels and coupling fields involved with this experiment.

fit to the data, where the differences in the peak centers are used to find ν_{hfs}. The statistical uncertainty associated with this parameter is determined by taking the quadrature sum of
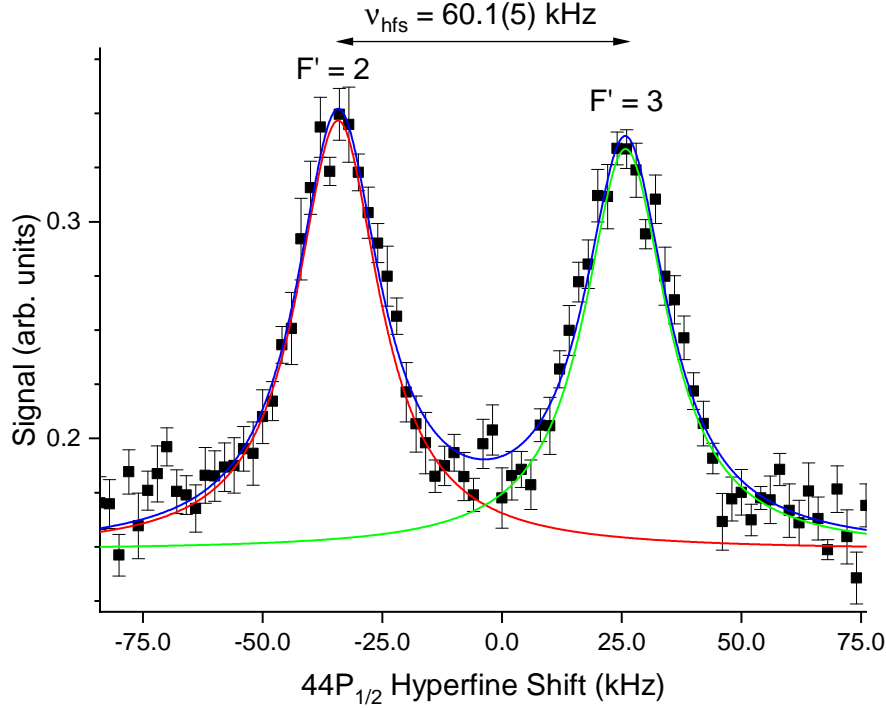
Figure 7.2: Figure taken from [8]. Arithmetic average of eight individual spectroscopic probes of the $\left|44S_{1/2}, F = 3\right\rangle \rightarrow \left|44P_{1/2}, F'\right\rangle$ transitions. The hyperfine splitting ν_{hfs} is derived from the line-center fits of each hyperfine peak. Fourier sidebands around the peaks are barely visible in this spectrum. Error bars indicate the standard error of the mean (SEM) in the spectroscopic signal strength over the set of eight individual scans.

the center-fit uncertainties. In Fig. 7.2, the spectrum for $\left|44S_{1/2}, F = 3\right\rangle \rightarrow \left|44P_{1/2}, F'\right\rangle$ is provided with a derived ν_{hfs} of 60.1(5) kHz.

Eq. 7.1 is used to find A_{hfs} from ν_{hfs} for a given n spectrum. Note that this expression depends on the Rydberg-Ritz equation [60] and the experimentally measured values δ_0, δ_2 for Rb $P_{1/2}$ states. Quantities $\delta_0 = 2.6548849(10)$ and $\delta_2 = 0.2900(6)$ are taken from [10]. Uncertainties pertaining to these quantities are below the overall measurement uncertainty in this study and are therefore ignored. By means of propagating the uncertainty, $\delta A_{\mathrm{hfs}} = A_{\mathrm{hfs}} \delta\nu_{\mathrm{hfs}} / \nu_{\mathrm{hfs}}$. In Table 7.1

7.5   Uncertainty Analysis

The uncertainty originating from the Lorentzian fitting of the averaged scans is 0.007 GHz and is purely statistical. This means if the average were over several thousand more scans,

Table 7.1:
Table adapted from Ref. [8]. List of HFS splittings and A_{hfs}. Eq. 7.1 is used with $\delta_0 = 2.6548849(10)$, $\delta_2 = 0.2900(6)$ [10]. Uncertainties shown are purely statistical. The average in A_{hfs} is weighted.

n	ν_{hfs} (kHz)	A_{hfs} (GHz)
42	72.7(6)	1.476(12)
43	65.3(6)	1.429(13)
44	60.1(5)	1.416(12)
46	54(1)	1.466(27)

Average A_{hfs} (GHz)	1.443
Statistical uncertainty (GHz)	0.007

this value would approach zero. There still exists possible systematic uncertainties originating from deficiencies in our experimental setup, mainly from stray magnetic fields leaking into the chamber and dipole-dipole interactions between two atoms based on the average interatomic distances R.

While background electric fields can distort each hyperfine peak due to inhomogeneous broadening, each line undergoes the same distortion and the resulting HFS splitting is insensitive to this. A lack of a DC tensor polarizability in the $nP_{1/2}$ series permits this insensitivity, as all $|m_F|$ and $|m_{F'}|$ suborbitals undergo the same Stark shifts. Upon inspection of Fig. 7.2, both peaks appear symmetric, implying that the inhomogeneous broadening is negligible. In order to achieve such symmetric lines, the internal electrodes of the science chamber compensate the stray electric fields and reduce them to a value below 50 mV/cm when appropriate potential differences $\phi_{x,0}, \phi_{y,0}$, and $\phi_{z,0}$ are applied to the copper plates. Fig. 7.3(a) shows the behavior of the $\left|44S_{1/2}\right\rangle \to \left|44P_{1/2}\right\rangle$ transition as a function of ϕ_z. Note here the transition is broadened enough that the HFS is not resolvable. As stated in the previous chapter, the vertex of the parabola denotes the location of $\phi_{z,0}$.

In order to show that the HFS is not affected by external electric fields, I lower the power of the incident microwaves to resolve the HFS of $\left|43P_{1/2}\right\rangle$ and scan E_x about the location of $E_x = 0$. As shown in Fig. 7.3(b), ν_{hfs} does not change up to $|E_x| = 50$ mV/cm, although the individual lines tend to asymmetrically broaden in the same manner at this point.

Stray magnetic fields will, however, contribute a systematic uncertainty to the measurement, and need to be reduced down to a total strength below 5 mG. In order to achieve this, the external Helmholtz coils with dimensions detailed in [6] provide a controllable DC magnetic field in all three Cartesian directions. For the y-direction, perpendicular to the mm-wave polarization, the Zeeman effect of the HFS pertaining to $\left|43P_{1/2}\right\rangle$ is calculated in Fig. 7.3(c) and experimentally shown in Fig. 7.3(d). The behavior is not intuitive, for the $F' = 2$ peak broadens more than that of the $F' = 3$ state. This unusual structure
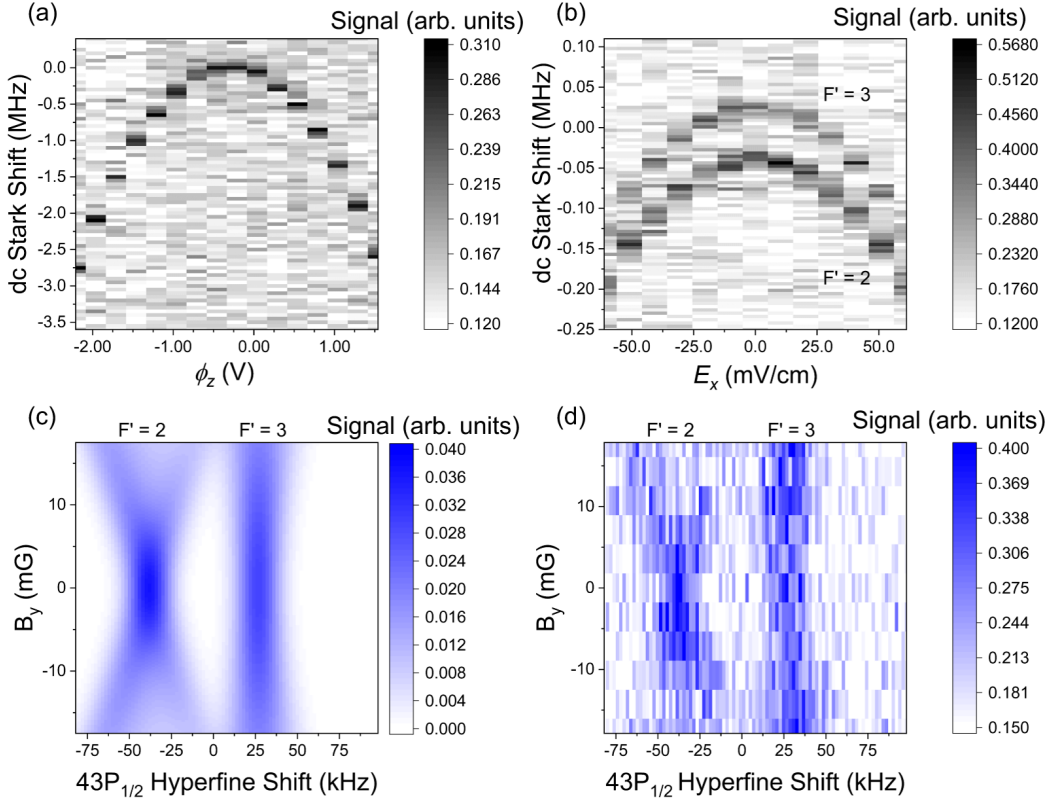
Figure 7.3: Figure taken from [8]. In (a), the spectral line shift of the $\left|44S_{1/2}\right\rangle \to \left|44P_{1/2}\right\rangle$ transition as a result of the second-order Stark effect, is shown as ϕ_z is varied. Here the difference in DC polarizabilities for the two states is $\Delta\alpha = 9.564$ kHz/(V/m)^2. Map (b) shows the insensitivity of the HFS splitting as the electric field in the x-direction, E_x, is varied. This spectrum is of the $\left|43S_{1/2}, F=3\right\rangle \to \left|43P_{1/2}, F'\right\rangle$ transition. A calculation of the Zeeman effect on the $\left|43S_{1/2}, F=3\right\rangle \to \left|43P_{1/2}, F'\right\rangle$ transition is shown for the case of a nonzero magnetic field component B_y perpendicular to the microwave polarization (x direction) is shown in (c). The experimental data corresponding to this calculation is provided in (d).

can mostly be attributed to the reordering of states of m_F and $m_{F'}$ quantum numbers into states with m_j, m_I and $m_{j'}, m_I$ quantum numbers as the field strength is increased. For this measurement, the currents for all three directions are chosen such that the individual HFS peak linewidths are made similar and minimized.

In order to quantify the uncertainty brought on by the stray magnetic fields, I follow an analysis similar to [137], where the ν_{hfs} of $n=43$ is measured for a distribution of set magnetic fields in all directions, independently, within 10 mG from the zero field. The standard error of the mean (SEM) is taken over this set of ν_{hfs}, which results in $\delta\nu_{\mathrm{hfs}} = 0.6$ kHz and
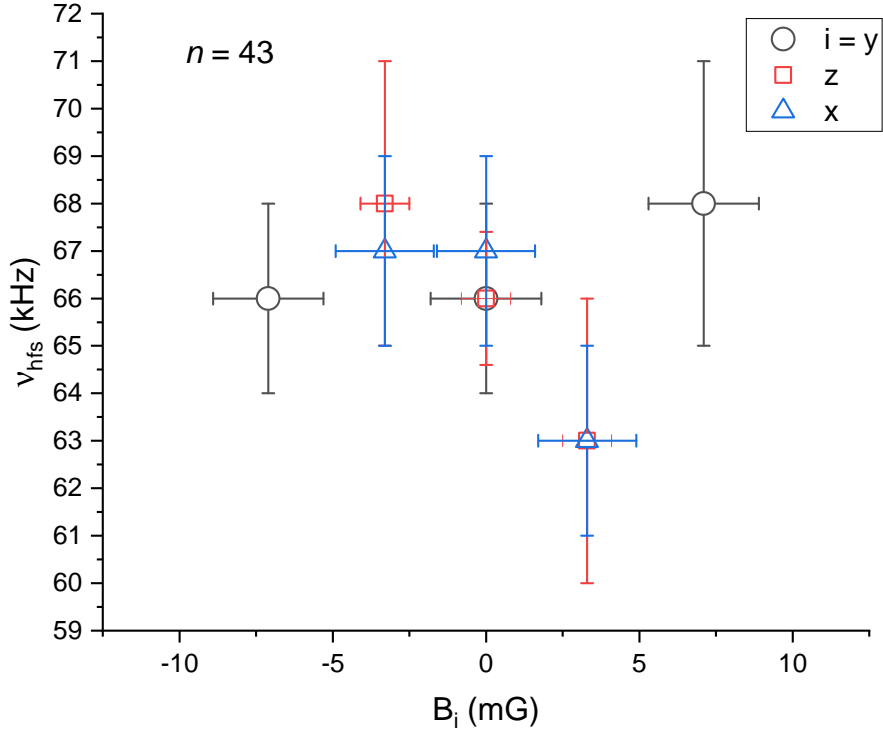
Figure 7.4: Figure taken from [8]. Distribution of the $43P_{1/2}$ HFS ν_{hfs} determined from spectroscopic measurements at independent field B_x, B_y, and B_z settings from their zero-field values. The vertical error bars indicate the spectroscopic measurement uncertainty while the horizontal bars indicate the magnetic field noise originating from the current source.

$\delta A_{\mathrm{hfs}} = 13$ MHz. The distribution of measurements for $n = 43$ are displayed in Fig. 7.4.

Another source of systematic error is the two-body, long-range interaction between Rydberg atoms separated at a distance R, given by a series expansion in Eq. 4.12. In essence, this interaction simply arises from the long-range Coulomb forces that the constituent charged particles experience. The leading nonzero term in this expansion is a dipole-dipole potential, which contributes state-mixing and shifting in the first order when the two atoms involved have electronic states of opposite parities. This first order effect can be approximated as C_3/R^3, where C_3 is a dispersion coefficient that was theoretically calculated to be 1.7 GHz μm^3 in Rb for $n = 43$. Second-order dipole-dipole interactions, known as van der Waals shifts, which occur when atoms of the same parity interact with each other are estimated to yield shifts of 1 mHz, well within the uncertainty budget for this experiment.

Quantifying the systematic uncertainty from the C_3/R^3 shift, experimental knowledge
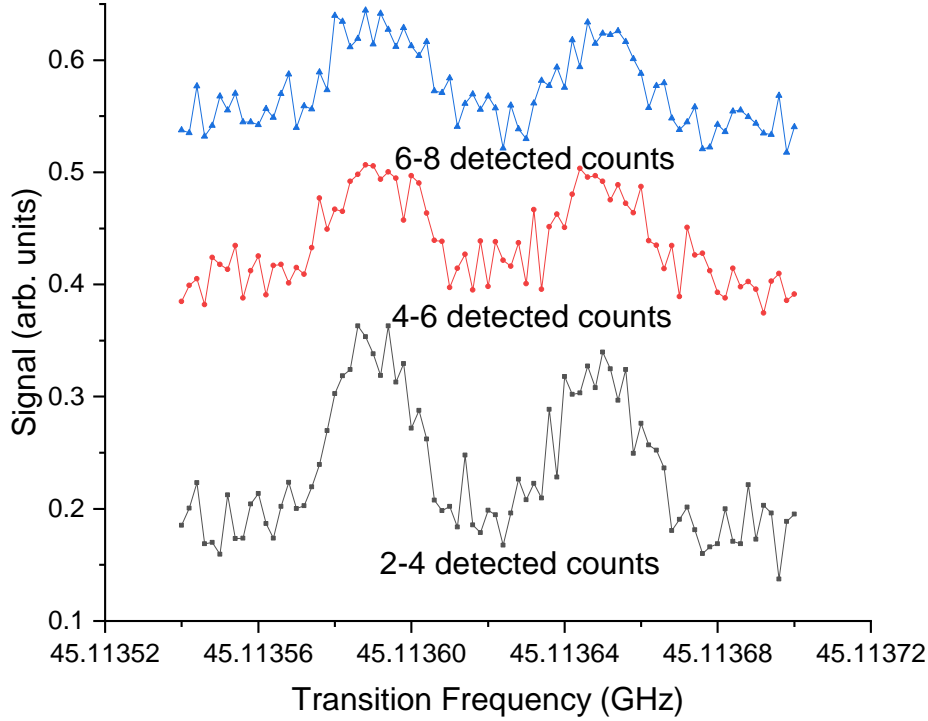
Figure 7.5: Figure taken from [8]. Here the count rate is increased by approximately a factor of four by lengthening the Rydberg excitation pulse. Shifts originating from dipole-dipole interactions can only have a maximum of about 1 kHz.

of R must be obtained. To do this, mm-wave scans were taken of the $\left|44S_{1/2}, F = 3\right\rangle \rightarrow \left|44P_{1/2}, F'\right\rangle$ transition with different Rydberg sample sizes:2-4, 4-6, and 6-8 detected Rydberg counts. An increase in Rydberg counts is achieved by prolonging the interaction times of the Rydberg excitation lasers by 5-10 μs. As the count rate is increasing by a factor of four, the dipole-dipole shifts are expected to increase as such. However, as observed in Fig. 7.5, there are no noticeable shifts in the peaks by greater than 1 kHz, which implies that $R \gtrsim 120$ μm. This 1 kHz uncertainty in ν_{hfs} results in the largest systematic uncertainty contribution of $\delta A_{\text{hfs}} = 27$ MHz.

Adding the three uncertainties in quadrature, the statistical (7 MHz) and two systematic errors from stray magnetic fields (13 MHz) and dipole-dipole interactions (27 MHz), results in a total measurement uncertainty in the ^{85}Rb $nP_{1/2}$ hyperfine coupling constant of 31 MHz. Therefore, the final measurement result is $A_{\text{hfs}} = 1.443(31)$ GHz.

7.6   Conclusion

In summary, the cancelling of stray electromagnetic fields has allowed a precision measurement of the $nP_{1/2}$ hyperfine coupling constant in ^{85}Rb. Possible applications for this measurement include hyperfine Rydberg qubits [105], improved models for Rydberg molecules [178; 179; 112; 180; 181; 182; 99; 183] and Rydberg microwave-field sensors [140; 141; 142; 143; 186].

CHAPTER VIII

Coherent Driving of $nS_{1/2} \to nP_{1/2}$ and $nS_{1/2} \to (n+1)S_{1/2}$ Rydberg Transitions with a Phase-Modulated Optical Lattice

This chapter is based on Ref. [7].

In the previous chapter, I demonstrated how the stray electric and magnetic fields that can shift and asymmetrically broaden the Rydberg levels used for fundamental physics experiments can be minimized, which also led to a precise measurement of the ^{85}Rb hyperfine structure for Rydberg-$nP_{1/2}$ atoms. This chapter discusses the method of exciting Rydberg atoms to nearby states completely with laser fields through the ponderomotive interaction (see Chapter V). As a means to conserve energy throughout the electronic transitions, the laser phase is modulated in time at appropriate frequencies set by an amplified microwave signal fed into an electro-optic fiber phase modulator, as shown in Fig. 6.13. Angular-momentum conservation is provided by the spatial variation of the laser-field's intensity gradient, here in the form of a one-dimensional optical lattice, within the wave function of the Rydberg electron. Note that all-optical probing of Rydberg transitions implies that that the spatial region of excitation can have an upper limit dictated by the Rayleigh range of the lattice and its transverse beam waist, which, through the arguments of classical optics, is smaller by a factor of at-least 10^3 than that which would be provided by microwave radiation.

In the scope of fundamental-physics experiments, where precise knowledge of the Rydberg levels minimally affected by stray perturbations, a small interaction region afforded by the focal region of laser fields is necessary. Any spatial variation of the perturbations, which would be more likely with a larger interaction region, would lead to inhomogeneous broadening of the Rydberg levels and systematic uncertainties in the experiment. Interaction regions significantly smaller than those provided by RF fields aid in the elimination of such broadening. Thus, the CS Rydberg atom experiments discussed in the introduction would

need to be in a sampling region provided by the laser fields that generate them through the ponderomotive effect. Ponderomotive transitions both satisfy the spatial resolution requirements and the large change in orbital-angular-momentum (OAM) required for initializing a sample of CSs in a small region.

Evidence in the ponderomotive transitions of Rydberg atoms using a laser field was first provided in [62; 63]. There, the laser field, with a gradient also formed by a one-dimensional optical lattice, was intensity modulated at q-order subharmonics of the Rydberg transitions. However, the technique of amplitude modulation was prohibitive in terms of selection rules. Only even-parity changes in the atom's internal state were allowed by the angular-momentum structure of the resulting coupling potential. Such transitions were of the $nS_{1/2} \rightarrow n'S_{1/2}$ sort. If one wanted to drive odd-parity transitions, changes in the atom's motional state ν would be necessary via detuning the modulation frequency by odd-integer multiples of the trap oscillation frequency [85]. In most of the likely applications of ponderomotive laser transitions, changes in the atomic motional state ν are not ideal, as the anharmonicity yields asymmetric broadening for every value of $\Delta\nu$, which hampers fidelity and precision in applicable experiments. Also, changes in ν could result in unwanted heating and motional dephasing throughout the desired protocol. Therefore, a method of recoil-free ponderomotive manipulation of a Rydberg atom's internal state is needed. Ponderomotive transitions realized by phase-modulation of the optical lattice afford recoil-free, odd- and even-parity transitions.

There is considerable interest in optical manipulation of Rydberg-Rydberg transitions also in the subfields of quantum information [188; 133] and simulation [134; 102; 135; 136; 189]. In these applications, entrapment of the atoms by conservative optical forces are often an experimental requirement to prolong coherence times throughout the gate sequences. Usually, only a small portion is optically trapped with a significant amount of spectators surrounding them; the trapped atoms, confined in a region governed by the laser focal spot, must be the only ones participating in the gate operations. This calls for a method of changing the Rydberg state entirely with laser fields.

Recently, isolated-core excitations (ICEs) of rare-earth and alkaline-earth Rydberg states, performed by visible-wavelength laser fields, have allowed this sort of high-spatial selectivity in experiments involving the control of Rydberg-Rydberg transitions. In ICEs the laser field changes the internal state of the Rydberg atom's ion core through an $\mathbf{A} \cdot \mathbf{p}_e$ interaction [190; 191; 192; 193; 194; 195; 196]. Not only can ICEs change the internal atomic state based on electric-dipole selection rules, the energy levels can also be shifted through AC Stark shifts, attracting the Rydberg atoms towards the intensity maxima of the laser fields [194; 197; 196]. However, ICEs are only experimentally viable with certain rare-earth and alkaline-earth

atoms, where the inner ion core is able to absorb visible radiation. Alkali atoms have inner ion cores electronically similar to noble gases, which are only sensitive to wavelengths in the deep-UV and X-ray spectral ranges. Furthermore, the dipole-allowed changes in the atom's internal state through ICE usually lead to an autoionizing interaction between the two valence electrons when the Rydberg-state OAM is low, which is sometimes unwanted. Therefore, the method discussed in this chapter, ponderomotive optical manipulation by laser phase-modulation, is a desirable alternative that circumvents these issues.

This chapter is outlined in the following way. In Section 1, theoretical expressions of the ponderomotive light shift and coupling frequencies are presented, as well as a discussion of the numerical simulation used to fit to data. Section 2 outlines the timing sequence of the spectroscopic measurements, as well as the procedure for obtaining the unperturbed reference frequencies ω_0 of the Rydberg transitions involved. Sections 3 and 4 feature the results from ponderomotive spectroscopy of odd-, $46S_{1/2} \rightarrow 46P_{1/2}$, and even-parity, $48S_{1/2} \rightarrow 49S_{1/2}$ transitions, respectively. Section 5 discusses the spectral features of the experimental data.

8.1   Theory

As a review from the concepts in Chapter V, using the same notation for the coordinates of the atomic CM ($\mathbf{R}_0$) and Rydberg electron ($\hat{\mathbf{r}}_e$), the total optical field $\mathbf{E}$ of angular frequency ω_L exerts the following ponderomotive interaction $U_p(\mathbf{R}_0 + \hat{\mathbf{r}}_e, t)$

$$U_p(\mathbf{R}_0 + \hat{\mathbf{r}}_e, t) = -\frac{1}{2}\alpha_e(\omega_L)\langle \mathbf{E}^2(\mathbf{R}_0 + \hat{\mathbf{r}}_e, t)\rangle_{t_q}, \tag{8.1}$$

where the average is taken over the quiver-time $t_q = 2\pi/\omega_L$ of the Rydberg electron in the optical field. The total field $\mathbf{E}$ is the vector sum of $\mathbf{E}_u^{(i)}$, $\mathbf{E}_u^{(r)}$, and $\mathbf{E}_m^{(i)}$, where

$$\begin{aligned}
\mathbf{E}_u^{(i)}(\mathbf{R}_0 + \mathbf{r}_e, t) &= \hat{\epsilon}^{(i)}\mathcal{E}_u^{(i)}(\mathbf{R}_0)\cos\left[k_L(Z_0 + z_e) - \omega_L t + \eta_2(t)\right], \\
\mathbf{E}_u^{(r)}(\mathbf{R}_0 + \mathbf{r}_e, t) &= \hat{\epsilon}^{(r)}\mathcal{E}_u^{(r)}(\mathbf{R}_0)\cos\left[k_L(Z_0 + z_e) + \omega_L t\right], \\
\mathbf{E}_m^{(i)}(\mathbf{R}_0 + \mathbf{r}_e, t) &= \hat{\epsilon}^{(i)}\mathcal{E}_m^{(i)}(\mathbf{R}_0)\cos\left[k_L(Z_0 + z_e) - \omega_L t + \eta_0 + \eta_1\cos\left(\omega_m\Delta s/c - \omega_m t\right) + \eta_2(t)\right].
\end{aligned}$$

Recall from Chapter V that phase η_0 is relative to the unmodulated lattice beams, η_1 is the phase amplitude of the modulation (with angular frequency ω_m), and $\eta_2(t)$ is the phase difference between the counter-propagating lattice beams. Also note that Δs quantifies the modulation signal's path length from the position of the fiber EOM to the location of the Rydberg atoms. It is a global phase-offset that can be ignored in the following equations. The polarization vectors of the incident (i) and return beams (r), $\hat{\epsilon}^{(i)}$ and $\hat{\epsilon}^{(r)}$ are kept linear

and parallel with half wave plates and a polarizing beamsplitter. The shaping and control of each phase and field strengths for every beam are done with standard optics shown in Fig. 6.13.

After averaging over the quiver period, the field intensity scales as

$$\langle \mathbf{E}^2(\mathbf{R}_0 + \hat{\mathbf{r}}_e, t) \rangle_{t_q} = \frac{1}{2}[\mathcal{E}_m^{(i)}]^2 + \frac{1}{2}[\mathcal{E}_u^{(i)}]^2 + \frac{1}{2}[\mathcal{E}_u^{(r)}]^2 + \mathcal{E}_m^{(i)}\mathcal{E}_u^{(i)} \cos[\eta_0 + \eta_1 \cos(\omega_m t)]$$
$$+ \mathcal{E}_m^{(i)}\mathcal{E}_u^{(r)}(\hat{\epsilon}^{(i)} \cdot \hat{\epsilon}^{(r)}) \cos[2k_L(Z_0 + \hat{z}_e) + \eta_0 + \eta_1 \cos(\omega_m t) + \eta_2(t)]$$
$$+ \mathcal{E}_u^{(i)}\mathcal{E}_u^{(r)}(\hat{\epsilon}^{(i)} \cdot \hat{\epsilon}^{(r)}) \cos[2k_L(Z_0 + \hat{z}_e) + \eta_2(t)]. \quad (8.2)$$

Fields $\mathbf{E}_u^{(i)}$ and $\mathbf{E}_u^{(r)}$ contribute a time-independent, conservative potential to the Hamiltonian. Phase $\eta_2(t)$ takes the form of a Heaviside step function with amplitude π for experiments that require inversion of the lattice intensity profile; the inflection point of this step aligns with the start of the phase-modulation sequence $\eta_1 \cos(\omega_m \Delta s/c - \omega_m t)$ of duration τ. We can thus treat this phase as time-independent. The energy shift that the last time-independent term in Eq. 8.2 induces is calculated with first-order perturbation theory, with an expectation value given by

$$\left\langle \frac{-1}{2}\alpha_e(\omega_L)\mathcal{E}_u^{(i)}\mathcal{E}_u^{(r)}(\hat{\epsilon}^{(i)} \cdot \hat{\epsilon}^{(r)}) \cos[2k_L(Z_0 + \hat{z}_e) + \eta_2] \right\rangle = -\frac{1}{2}\alpha_e(\omega_L)\mathcal{E}_u^{(i)}\mathcal{E}_u^{(r)}(\hat{\epsilon}^{(i)} \cdot \hat{\epsilon}^{(r)})$$
$$\times \langle \cos(2k_L\hat{z}_e) \rangle \cos(2k_L Z_0 + \eta_2), \quad (8.3)$$

where $\kappa_{n,l,j} = \langle \cos(2k_L\hat{z}_e) \rangle_{n,l,j}$, particular to a Rydberg state with quantum numbers n, l, and j. The first three terms in Eq. 8.2 induce a ponderomotive offset U_{ofs} that is Rydberg-state and position independent. With the energy shift computed in Eq. 8.3, the conservative, time-independent light shift on the Rydberg atom's internal energy as a function of Z_0 is

$$\Delta W(Z_0) = U_{ofs} + U_0 \cos(2k_L Z_0 + \eta_2), \quad (8.4)$$

where

$$U_0 = -\frac{1}{2}\alpha_e(\omega_L)\mathcal{E}_u^{(i)}\mathcal{E}_u^{(r)}(\hat{\epsilon}^{(i)} \cdot \hat{\epsilon}^{(r)})\langle \cos(2k_L\hat{z}_e) \rangle. \quad (8.5)$$

is the half-modulation lattice depth.

Fields $\mathbf{E}_u^{(m)}$ and $\mathbf{E}_u^{(r)}$ contribute two time-dependent terms from Eq. 8.2:

$$\mathcal{E}_m^{(i)}\mathcal{E}_u^{(i)} \cos[\eta_0 + \eta_1 \cos(\omega_m t)],$$
$$\mathcal{E}_m^{(i)}\mathcal{E}_u^{(r)}(\hat{\epsilon}^{(i)} \cdot \hat{\epsilon}^{(r)}) \cos[2k_L(Z_0 + \hat{z}_e) + \eta_0 + \eta_1 + \eta_1 \cos(\omega_m t) + \eta_2].$$

While the top expression can conserve energy in a ponderomotive transition from one Rydberg state to another, there is no $\hat{z}_e$ operator that is able to compensate the change in angular momentum. Thus, the top expression has no net effect on the Rydberg atom. The bottom expression, which has a sinusoidal dependence on $\hat{z}_e$ and also varies with time at the order of the Kepler frequency, allows a coupling between two different internal states of the Rydberg atom. From here onward, one can assume that the Mach-Zehnder interferometer of Fig. 6.13 is locked to the peak of a fringe, ensuring that $\eta_0 = 0$. Using the Jacobi-Anger expansion [198], the ponderomotive potential brought on by the interference of the incident modulated and reflected unmodulated beams can then be written as a Z_0-dependent atom-field coupling of Rydberg states $|0\rangle$ and $|1\rangle$, $\hat{U}_{AF}(Z_0, t)$:

$$
\begin{aligned}
\hat{U}_{AF}(Z_0, t) = &-\frac{1}{2}\alpha_e \mathcal{E}_m^{(i)} \mathcal{E}_u^{(r)} (\hat{\epsilon}^{(i)} \cdot \hat{\epsilon}^{(r)}) \cos\left(2k_L Z_0 + \eta_2(t)\right) \Bigg\{ \langle 1| \cos\left(2k_L \hat{z}_e\right) |0\rangle \\
&\times \left[J_0(\eta_1) + 2\sum_{\text{even } q>0} J_q(\eta_1) \cos\left(q\omega_m t\right)\right] + \langle 1| \sin\left(2k_L \hat{z}_e\right)|0\rangle \left[2\sum_{\text{odd } q} J_q(\eta_1) \sin\left(q\omega_m t\right)\right] \Bigg\} \\
&\times (|1\rangle\langle 0| + |0\rangle\langle 1|). \quad (8.6)
\end{aligned}
$$

Under the rotating-wave approximation (RWA), U_{AF} is simplified as

$$
\hat{U}_{AF}(Z_0, t) = \frac{\hbar}{2}\Omega_{q,0}|\cos\left(2k_L Z_0\right)|e^{i(\xi - q\omega_m t)}|1\rangle\langle 0| + \text{h.c.}, \quad (8.7)
$$

with a q-order maximum Rabi frequency given by

$$
\Omega_{q,0} = -\frac{\alpha_e(\omega_L)}{\hbar}\mathcal{E}_m^{(i)}\mathcal{E}_u^{(r)}(\hat{\epsilon}^{(i)} \cdot \hat{\epsilon}^{(r)}) \langle 1| \sin\left(2k_L \hat{z}_e\right)|0\rangle J_q(\eta_1), \quad (8.8)
$$

for odd-parity transitions and

$$
\Omega_{q,0} = -\frac{\alpha_e(\omega_L)}{\hbar}\mathcal{E}_m^{(i)}\mathcal{E}_u^{(r)}(\hat{\epsilon}^{(i)} \cdot \hat{\epsilon}^{(r)}) \langle 1| \cos\left(2k_L \hat{z}_e\right)|0\rangle J_q(\eta_1), \quad (8.9)
$$

for transitions that maintain parity. The position-dependent phase factor ξ has a staircase-like behavior, as shown in Fig. 8.1. Phase ξ changes in increments of π at every lattice well, making the time-independent prefactor of the coupling $\hat{U}_{AF}$ completely real. Note that if $\eta_2 = \pi$, the entire staircase structure of ξ shifts upwards by π. An atom barely trapped within a lattice well (trajectory 1 in Fig. 8.1(c)) sees a net phase $\Delta\xi$ shift of $\pm 2\pi$ throughout its trajectory over the interaction time τ because its oscillation amplitude Z_1 spills beyond the inflection points of a local intensity minimum. A deeply trapped atom (trajectory 2 in Fig. 8.1(c)) has an oscillation amplitude Z_1 that remains within 0.125λ of an antinode

and will see no phase shift throughout its trajectory over the interaction time. A benefit of both behaviors for trapped atoms is the removal of laser-based Doppler effects that would normally be around in ICE transitions and conventional laser spectroscopy. This Doppler-free feature also remains by the ponderomotive interaction if the laser beam is free-running, something that is not possible through the $\mathbf{A} \cdot \hat{\mathbf{p}}_e$ interaction. Atoms untrapped by the lattice (trajectory 3 in Fig. 8.1) and skipping over many wells undergo a series of π phase shifts. Effectively, the fast-moving atoms see a phase dependence linear with their position that contributes broad, optical Doppler shifts to the transition. These Doppler shifts will be discussed further in Section 5.

A considerable advantage of the ponderomotive drive is the independence that the matrix elements $\langle 1 | \cos (2k_L \hat{z}_e) | 0 \rangle$ and $\langle 1 | \cos (2k_L \hat{z}_e) | 0 \rangle$ have from the magnitude of order q. The coupling remains in the first order as q is increased to arbitrary values. This aspect contrasts with conventional $\mathbf{A} \cdot \hat{\mathbf{p}}_e$ drives in q-order perturbation theory, where the coupling strength rapidly drops by the excessive energy detunings from intermediate states. For instance, driving a 10-th-order Rydberg-Rydberg transition with microwave radiation at a frequency 1/10-th of the transition is not possible with commercially available power amplifiers that do not violate FCC regulations. Energy denominators in the 10-th-order coupling potential are to blame for this. On the other hand, the first-order behavior of the ponderomotive drive means the Rydberg-Rydberg transition can be driven at the same microwave modulation frequency as the previous case with reasonable powers sent into the phase-modulator to attain the global maximum of J_q. One would only need to moderately increase the laser power to compensate the mild drop-off in matrix elements and global maximum of J_q. With Rydberg-atoms, this is important because massive increases in laser-power greatly enhance the photoionization rate. Most phase modulators commercially available today limit $q \simeq 10$, based on RF damage thresholds and phase sensitivities. At this case of $q \simeq 10$, the above equations imply that Rydberg states with the same parity separated by sub-THz energies (~ 100 GHz) could be driven with only a more-commonly available microwave source at 10 GHz.

Experimental evidence of ponderomotive transitions is presented through phase-modulation spectroscopy of both even- and odd-parity transitions; a sufficient numerical model to compare with data is thus necessary. Our model is semiclassical with the Rydberg CM being treated as a classical particle subject to Newton's equations of motion and the electron as a two-level ($|0\rangle$ and $|1\rangle$) quantum wave function undergoing position-dependent state changes by $\hat{U}_{AF}(Z_0)$. A Maxwell-Boltzmann distribution is used to initialize the CM position and velocity within the lattice for a given trajectory. An average over 1000 trajectories is used for each simulated spectrum. After initialization for a given trajectory, $\Delta W(Z_0)$ provides a
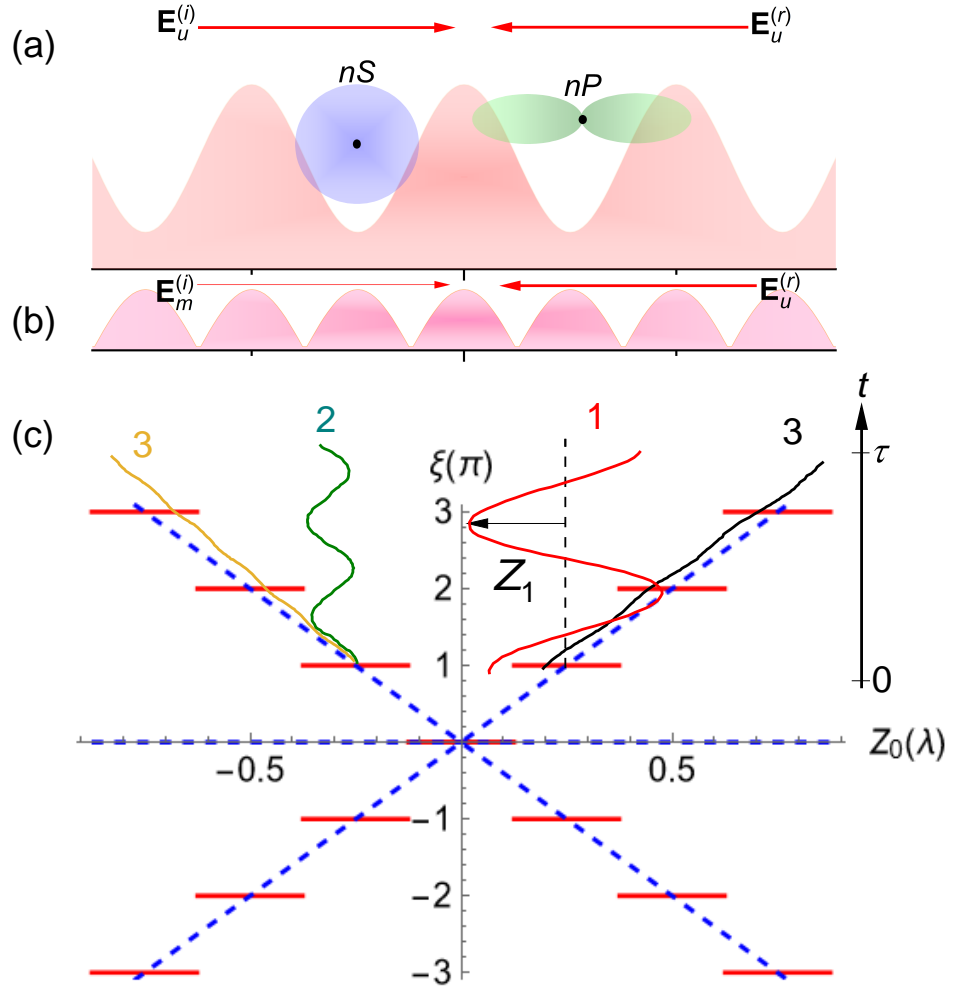
Figure 8.1: Figure taken from [7]. Figure (a) shows potential $U_0 \cos(2k_L Z_0 + \eta_2) + U_{ofs}$ generated by the time-independent part of the lattice intensity gradient. The size of the lattice wells are shown relative to the electron wave functions of the Rydberg states involved. Figure (b) shows the magnitude of the coupling potential $\hat{U}_{AF}$ at a given instant in time. This harmonic potential is generated by fields $\mathbf{E}_m^{(i)}$ and $\mathbf{E}_u^{(r)}$. In (c), the ξ phase function of the coupling is a staircase structure that changes depending on the atomic trajectories ((1,2) for trapped, 3 for untrapped). It differs from the three simultaneous and linear phases that a higher-order Raman transition would provide, indicated by the dashed blue lines. All figures are shown along the Z_0-axis.

sinusoidal, semiclassical classical force on the CM of the Rydberg atom. By "semiclassical force," we mean that the populations of $|0\rangle$ and $|1\rangle$ weigh the state-dependent force from the
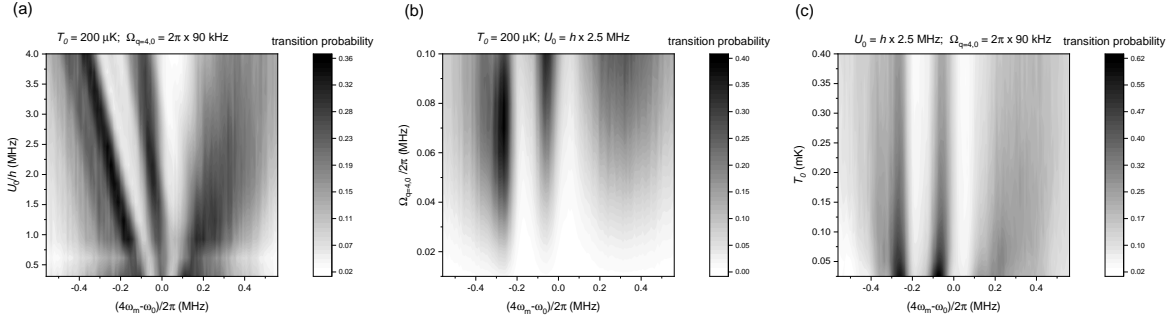
Figure 8.2: Figure taken from [7]. Numerical simulations of $\left|48S_{1/2}\right\rangle \rightarrow \left|49S_{1/2}\right\rangle$ spectra as (a) U_0, (b) $\Omega_{q=4,0}$, and T_0 are varied.

lattice at every integration timestep throughout the simulation. Within the duration τ of the lattice phase-modulation, the simulation integrates Newton's equations using timesteps no greater than 10 ns. At every timestep, the arrived value of Z_0 is used to find the instantaneous Rabi frequency, detuning from resonance, and populations in $|0\rangle$ and $|1\rangle$. These populations arise from the familiar two-level Rabi problem calculated in Chapter II, ignoring decay.

The separation of the sidebands from the Doppler-free peak is dependent on the depth parameter U_0, as will be explained in Section 5. As shown in Fig. 8.2(a), when U_0 is increased with the peak Rabi frequency Ω_0 and initial temperature T_0 remaining constant, they shift away from the central, Doppler-free peak. An appropriate spacing from the Doppler-free peaks that matches experimental spectra is used to estimate U_0 in the experiment, more reliable than using optical power measurements and transverse beam profiling. As shown in Fig. 8.2(b), changing the Rabi frequency modifies the signal strengths of the Doppler-shifted peaks relative to each other and relative to the Doppler free peak. Fitting the correct signal-strength ratios among the three peaks to the data allows an estimate of $\Omega_{q,0}$. Variations in initial temperatures of the sample T_0 are reflected in the linewidths and overall peak heights, with hotter atoms compromising the visibility in the spectra. One can also make out a steep, linear shift of the Doppler-free peak towards the field-free resonance as T_0 is enhanced, as seen in Fig. 8.2(c).
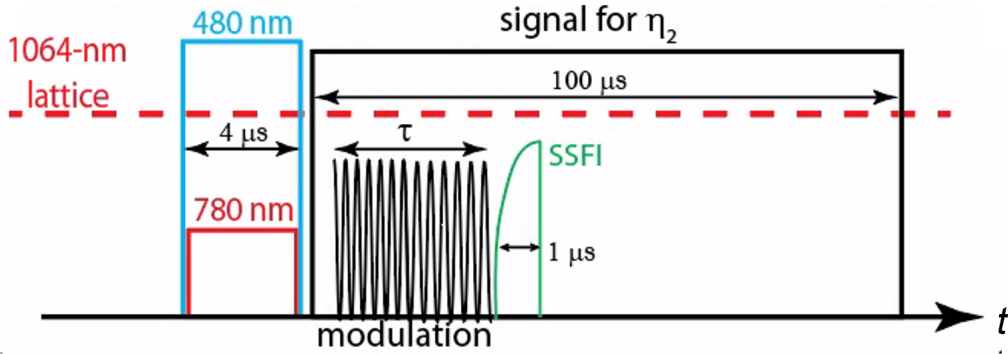
Figure 8.3: Timing sequence of the experiment. Figure adapted from [7].

8.2 Methods

After the laser-cooling light in the science chamber is switched off, the Rydberg-excitaion lasers are simultaneously switched on for a duration of 4 μs. In this experiment, the intermediate-state detuning of the 780-nm beam is set to approximately 140 MHz. However, there is still noticeable heating from the scattering of D_2 light during the excitation, as the experimental spectra were estimated to have a sample with $T_0 \sim 200$ μK. The blue, 480-nm laser is tuned to the resonance of atoms near the intensity maxima of the optical lattice, along the dashed line of Fig. 6.16. The optional phase shift $\eta_2 = \pi$ can be applied to the DC phase shifter before the pulsing of modulation signal $\eta_1 \cos(\omega_m t)$ into the fiber EOM. This inverts the intensity gradient, allowing the low-field-seeking Rydberg atoms to be initialized in harmonic-like lattice well near the nodes of the lattice. Immediately after the phase-modulation is applied, the state-selective field ionization (SSFI) (explained in great depth in Chapter VI) tallies the final internal-state populations ($|0\rangle$ or $|1\rangle$). Throughout the entire spectroscopy sequence, the unmodulated beams of the 1064-nm lattice stays on at a constant power level, unless beam $\mathbf{E}_u^{(r)}$ is extinguished during the experiment. A complete timing sequence is shown in Fig. 8.3.

Transition frequencies ω_0 between states $|0\rangle$ and $|1\rangle$, unperturbed by light shifts from the optical lattice, need to be measured in order to correctly quantify the effects of Doppler shifting and state-dependent ponderomotive forces on the spectra when the 1064-nm laser shines on the atoms. In order to do this, microwave radiation from a horn antenna can be used to probe the two transitions studied ($\left|46S_{1/2}\right\rangle \rightarrow \left|46P_{1/2}\right\rangle$ and $\left|48S_{1/2}\right\rangle \rightarrow \left|49S_{1/2}\right\rangle$) when no lattice light is entering the chamber. The atom-field interaction time with the microwave radiation here $\tau = 6$ μs is much shorter than that in the previous chapter, so the
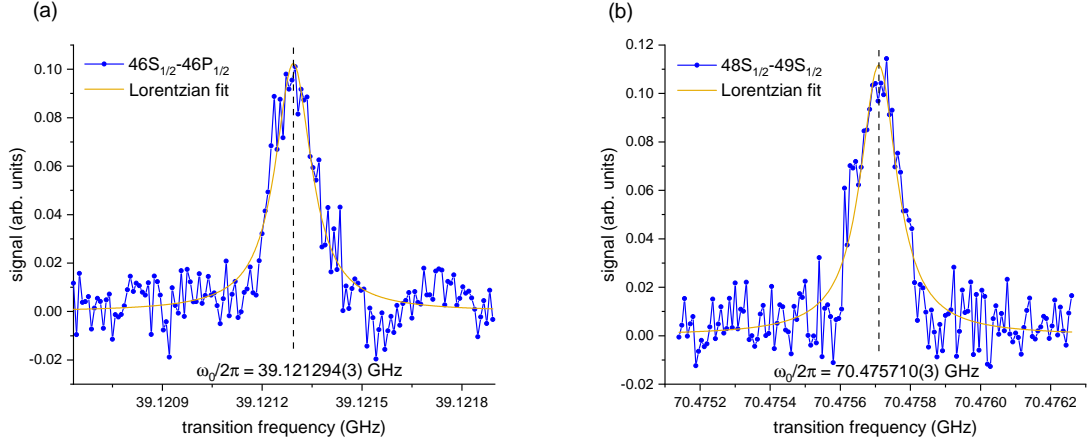
Figure 8.4: Figure taken from [7]. Microwave spectra driven by radiation from an antenna with the lattice light completely off for (a) $46S_{1/2} \to 46P_{1/2}$ and (b) $48S_{1/2} \to 49S_{1/2}$. Pulse duration is $\tau = 6$ μs.

HFS of $46P_{1/2}$ cannot be observed. We use this interaction time because it is on the order of τ for the ponderomotive driving by the modulated lattice. We deliberately chose this length of an interaction time in order to broaden the transition and ignore mixing of the $46P_{1/2}$ hyperfine states by the ponderomotive interaction. Also, atoms probed for too long have greater propensities to transversely fly out of the lattice and degrade the acquired signals.

Fig. 8.4 shows the conventional microwave spectra of the odd- and even-parity transitions driven by microwave radiation. Lorentzian fits are used to find the line centers and measurements of ω_0 for each transition. Note again that no optical lattice light is on throughout these diagnostic measurements.

8.3 Spectroscopy of $nS_{1/2} \to nP_{1/2}$ Rydberg Transitions

An odd-parity drive of $\left|46S_{1/2}\right\rangle \to \left|46P_{1/2}\right\rangle$ is performed. Rydberg atoms undergoing the ponderomotive-optical-lattice shifts are initialized in the $\left|0\right\rangle = \left|46S_{1/2}\right\rangle$ state. The modulated beam, $\mathbf{E}_m^{(i)}$, pulsed on for $\tau = 6$ μs, is scanned in modulation frequency ω_m, from $\omega_m/(2\pi) = 13.040211$ GHz to 13.040633 GHz in frequency steps of 3 kHz. A first-order drive using the $q = 3$ modulation harmonic, with $\eta_1 = 1.3(3)\pi$ allows the probing of $\left|0\right\rangle \to \left|1\right\rangle = \left|46P_{1/2}\right\rangle$, a transition determined in the previous Section to be spaced at $\omega_0/(2\pi) = 39.121294$ GHz without any perturbations. Fig. 8.5, shows evidence of this $q = 3$ drive when the optional η_2 phase shift is not applied; i.e., the lattice is not inverted.

159
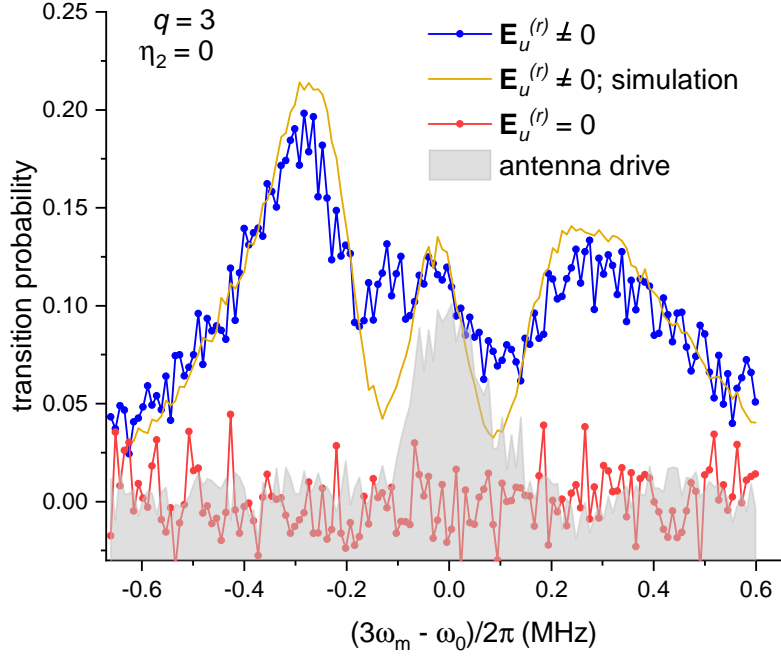
Figure 8.5: Figure taken from [7]. The blue points show the relative population in $|1\rangle = |46P_{1/2}\rangle$ with respect to $|0\rangle = |46S_{1/2}\rangle$ as $3\omega_m$ is scanned over ω_0 in steps of 9 kHz. These data represent an average over 10 individual scans, each with 400 measurements. The gold line is the corresponding simulation fit to the data. The "transition probability" is the absolute ratio of ions in the $|1\rangle$ gate to the $|0\rangle$ gate minus the arithmetic average of the same ratio for all pink data points. The pink points are the population in $|1\rangle$ when $\mathbf{E}_u^{(r)} = 0$, proving that an intensity gradient is necessary to drive the transition and conserve angular momentum. The shaded spectrum is the same antenna drive as in Fig. 8.4(a). Pulse duration is $\tau = 6$ μs for all spectra.

Three peaks appear, the two sidebands correspond to spectroscopic signals from the untrapped atoms moving along trajectory 3 in Fig. 8.1(c) and trapped atoms of trajectory 1 making changes in their motional quantum number ν by ± 2. The sidebands are shifted from the central, Doppler-free peak on the order of $2k_L\langle V_0\rangle$ or $2\omega_1$, where $\langle V_0\rangle$ is the average CM velocity of the Rydberg atom. Here, the central peak is red-shifted from ω_0 because most atoms spend the duration of their trajectory near the lattice antinodes [199] and the $|46P_{1/2}\rangle$ state experiences a shallower lattice potential than that for $|46S_{1/2}\rangle$. The stronger signal in the red-shifted side peak relative to the blue is also related to the nonmagic condition of $|0\rangle$ and $|1\rangle$ at $\lambda = 1064$ nm. From the simulation, it is estimated that $U_0 \sim h \times 2.5$ MHz and $\Omega_{3,0} \sim 2\pi \times 70$ kHz with $T_0 \sim 200$ μK. Evidence that the angular momentum must

160

be conserved to make the transition by means of the lattice intensity gradient is shown by extinguishing $\mathbf{E}_u^{(r)}$, where it is evident in Fig. 8.5 that this inhibits any population transfer into $|1\rangle$ (pink data).

Overlap of the three peaks is a result of inhomogeneous broadening of the Doppler-free peak by the nonmagic condition. In a different experimental setting, this condition can be made magic by choice of lattice wavelength, Rydberg states, and alignment angles. For this experiment, because the lattice mode differs from that of a near-concentric cavity, optical aberrations arising from misalignments and unwanted diffraction from the metallic vacuum chamber accentuate the existing differential light shift by inducing asymmetric broadening in the line. Other means of broadening, e.g., the $46P_{1/2}$ HFS, Zeeman splitting from stray magnetic fields, and dipole-dipole shifts, in addition to the aberrations are not included in the simulation and contribute a slight mismatch in the lineshape. However, the measured linewidth of the central, Doppler-free peak is ~ 200 kHz, at the same order of magnitude as the Fourier limit. ICE transitions, which are used to optically manipulate certain alkaline-earth atoms cannot reach spectral widths at this narrow of level.

When $\eta_2 = \pi$, the intensity maxima of the lattice become minima. This shift in phase occurs slightly before the rise time of the modulation signal $\eta_1 \cos(\omega_m t)$ but after the optical excitation. Rydberg atoms are collected near the intensity minima, implying that a greater portion of all atoms will be trapped and the Doppler-free peak will be blue-shifted from ω_0 [199]. This method of trapping Rydberg atoms was first demonstrated in [170]. In Fig. 8.6, the Doppler-free peak is shown to outmatch the shifted sidebands in signal strength. Also, there is a clear blue-shifting in signal as expected, which proves that a majority of atoms are in a trap of stable equilibrium. However, the central peak is broader and slightly weaker ($\sim$ 1-2%) than the simulation with the sidebands stronger than what was numerically calculated.

The mismatch between the experimental and theoretical curves may have to do with how sudden, or diabatic, the inverting phase shift of $\eta_2 = \pi$ is. A slow, dragging of the lattice along the propagation axis provides some heating to the coldest atoms trapped within the lattice well. As described in Section 1, increases in temperature degrade the signal strength. Also, some atoms may even be heated out of the lattice well, causing them to join the atoms with trajectory 3 in Fig. 8.1 and partially add to the signals of the sidebands.

8.4   Spectroscopy of $nS_{1/2} \rightarrow (n+1)S_{1/2}$ Rydberg Transitions

For an even-parity drive of $|0\rangle = \left|48S_{1/2}\right\rangle$ to $|1\rangle = \left|49S_{1/2}\right\rangle$, where $\omega_0 = 2\pi \times 70.475710$ GHz, the $q = 4$ harmonic of a 17 GHz modulation frequency needs to be used, as the bandwidth of the fiber phase modulator only reaches about 30 GHz. Furthermore, microwave equip-
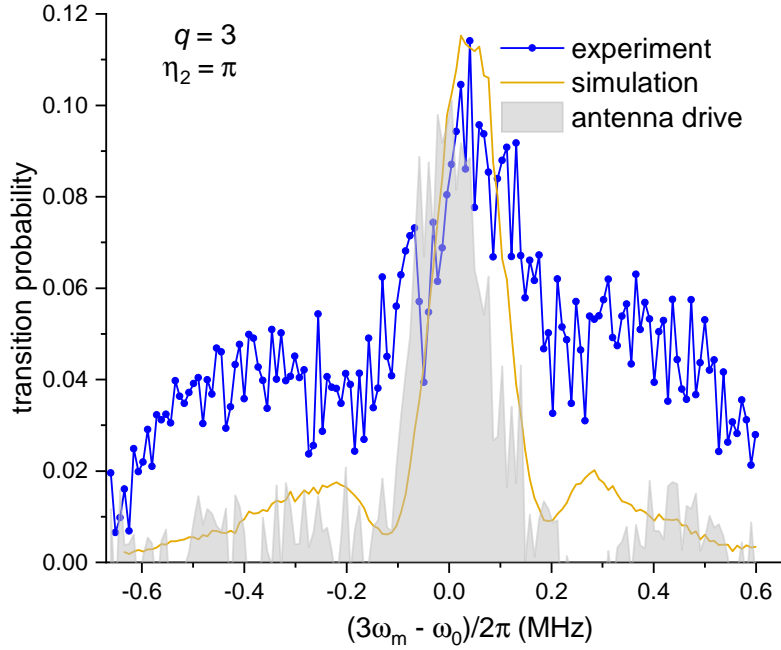
Figure 8.6: Figure taken from [7]. Here the same transition is driven as in Fig. 8.5 but the lattice is shifted by $\eta_2 = \pi$ before the modulation pulse.

ment at 17 GHz is far more commercially available than that at 70 GHz, implying that this high-order drive is necessary. Amplitude η_1 must be increased to $1.7(4) \times \pi$, and the pulse duration is increased to $\tau = 12\ \mu$s in hopes of achieving a narrower linewidth of the Doppler-free peak. Fig. 8.7 shows a lattice-phase-modulation spectrum of the $|0\rangle \rightarrow |1\rangle$ transition (where $\langle 0| \hat{\Pi} |0\rangle = \langle 1| \hat{\Pi} |1\rangle$ here with $\hat{\Pi}$ being the parity operator). Because $\eta_2 = 0$ at all times, atoms are initialized in $|0\rangle$ near the local maxima of the standing-wave pattern in concordance with the 1 MHz linewidth of the 480-nm laser, just as they were prepared in Fig. 8.5.

The Doppler-free line in Fig. 8.7, red-shifted from ω_0, has a Lorentzian structure that is fit with the dashed, green curve. An estimated linewidth of 96 kHz is obtained, also on the order of the Fourier limit ($0.89/\tau = 74$ kHz). The numerical simulation fits the data with a $U_0 = h \times 2.5$ MHz and $\Omega_{4,0} = 2\pi \times 90$ kHz.

Up until this point, I have made the assumption that the systems in this and the previous Section consisted of two levels, $|0\rangle$ and $|1\rangle$, separated by energy $\hbar\omega_0$ and driven in the first order by laser phase modulation at the q-harmonic of frequency ω_m. While the pulse duration τ is much less than the 300-K-blackbody-limited lifetime of 70 μs, preventing significant decay channels to other states during the drive, one cannot consider this system two level
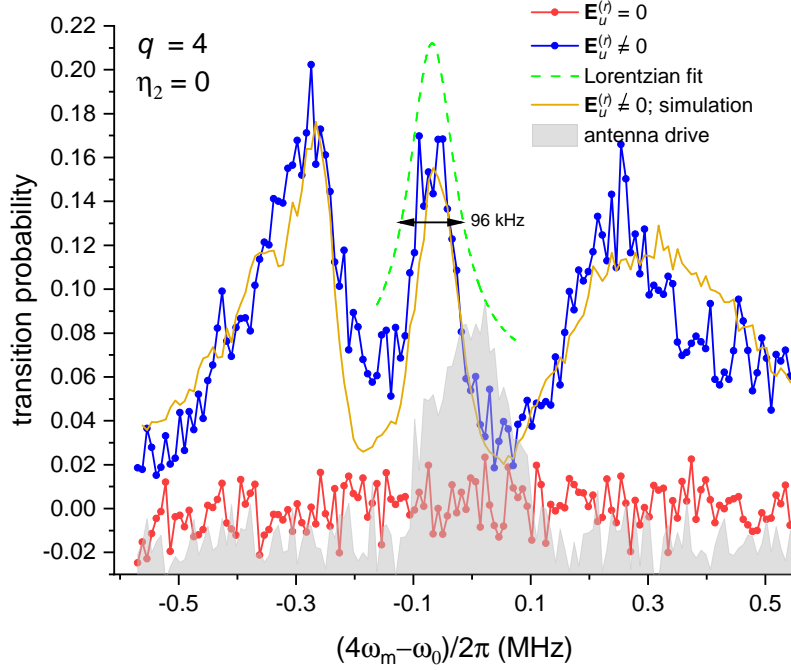
Figure 8.7: Figure taken from [7]. In this even-parity drive, $|0\rangle = \left|48S_{1/2}\right\rangle$ and $|1\rangle = \left|49S_{1/2}\right\rangle$. Here, $q\omega_m$ is stepped by $2\pi \times 8$ kHz over $\omega_0 = 2\pi \times 70.475710$ GHz. Blue data are averages of 10 single ω_m scans each featuring 400 measurements. The green, dashed line is a Lorentzian fit of the central, Doppler- and recoil-free peak with a FWHM of 96 kHz. The gold curve is the numerical simulation scaled by $1/2$ to agree with our experimental efficiency in state selectivity. Pink data points are averaged over 6 single ω_m scans of 400 measurements and correspond to the same drive with $\mathbf{E}_u^{(r)}$ blocked. The shaded spectrum is that originating from a two-photon antenna drive with all 1064-nm light off. Optical pulse duration is $\tau = 12$ μs; antenna-drive duration is $\tau = 6$ μs.

if some other harmonic, q' drives another transition from $|0\rangle$ to $|2\rangle$, separated by an energy $\hbar\omega_0' \sim q'\omega_m$. By the nature of phase modulation at large η_1, several other harmonics $q' \neq q$ appear in the Hamiltonian, which can drive other transitions if the aforementioned resonance condition is met.

How well the resonance condition is met is what needs to be determined by considering the overlap of spectral lines. If there is significant overlap of both the $|0\rangle \rightarrow |1\rangle$ and $|0\rangle \rightarrow |2\rangle$ transitions, interference of the probability amplitudes would influence the observed spectra. Parameter $|\delta| = |(q - q')\omega_m + (\omega_0' - \omega_0)|$ quantifies the separation of the two atomic states ponderomotive dressed-atom picture. Note that in this experiment, $|q\omega_m - \omega_0| \rightarrow 0$, making $|\delta| \simeq |\omega_0' - q'\omega_m|$. For a coupling strength $\Omega_{q',0}$ on the order of 1 MHz, which is a slight

overestimate for what has been observed in this chapter, the power-broadened width is $\Gamma = \Omega_{q',0}$ and $\Gamma^2/(4\delta^2) < 0.01$ in order there is not an overlap of both peaks that exceeds 1 % in transition probability. The condition for neglecting interference is $|q'\omega_m - \omega_0'| > 2\pi \times 5$ MHz.

In the odd-parity case, $\omega_m \sim 13$ GHz and $|0\rangle = |46S_{1/2}\rangle$, so the lowest value of $|q'\omega_m - \omega_0'|$ is $2\pi \times 159$ MHz, satisfying the condition. This additional coupling occurs when $q' = 9$ and ω_0' corresponding to the $|46S_{1/2}\rangle \rightarrow |47P_{1/2}\rangle$ transition. For the even-parity case, where $\omega_m \sim 17$ GHz and $|0\rangle = |48S_{1/2}\rangle$, the lowest $|q'\omega_m - \omega_0'|$ is $2\pi \times 170$ MHz, with $q' = 17$ and ω_0' for the $|48S_{1/2}\rangle \rightarrow |51D_{3/2}\rangle$ transition. Note that the maximum q feasible by electro-optic modulators available today is around 10 based on the crystal phase sensitivity and RF damage thresholds. In conclusion, assuming that $|0\rangle$ and $|1\rangle$ are the two relevant states is correct.

8.5 Discussion of Spectral Features

I will now present a discussion on the CM dynamics behind each spectral line obtained in the experiment. Each discussion will explain the shifts and broadening mechanisms behind each line using a classical model of the Rydberg's CM coordinate with parallels to a fully-quantized model introduced as needed.

8.5.1 Doppler-Free Features from Barely Trapped Atoms

Highly energetic atoms that oscillate in a lattice well with turning points very close to the local potential maxima at $Z_0 : 0, \pm\lambda/2, \lambda, 3\lambda/2, ...$, but nonetheless are still trapped, are some of the Rydbergs initialized for the spectra in Figs. 8.5 and 8.7. Even though the 480-nm laser has a center frequency parked near the shifts brought on by atoms located exactly at the intensity antinodes, which are therefore not trapped and skipping over many wells, its nonzero linewidth also excites these barely trapped atoms slightly offset from positions $Z_0 : 0, \pm\lambda/2, \lambda, 3\lambda/2, ...$ In Fig. 8.1(c), such a trajectory is labeled as trajectory 1.

In order to get a closer look at this sort of trapped trajectory, a simulation of its evolution in the noninverted ($\eta_2 = 0$) optical lattice for drive Fig. 8.5 is shown in Fig. 8.8. A Runge-Kutta algorithm is used to perform the simulation for an atom with a randomly chosen initial position and velocity. What's notable in these trajectories is that their oscillation frequency is slower than that of a deeply trapped atom (see trajectory 2 of Fig. 8.1(c)). The reason for this is that the large amplitude Z_1 of these oscillations, which turn near the intensity antinodes, cause the harmonic approximation of the trap-oscillation frequencies ω_1 to fail and actually be smaller than what is estimated. Amplitude Z_1 stretches beyond 0.125λ from the intensity nodes, meaning that it sees three different values of ξ throughout its evolution
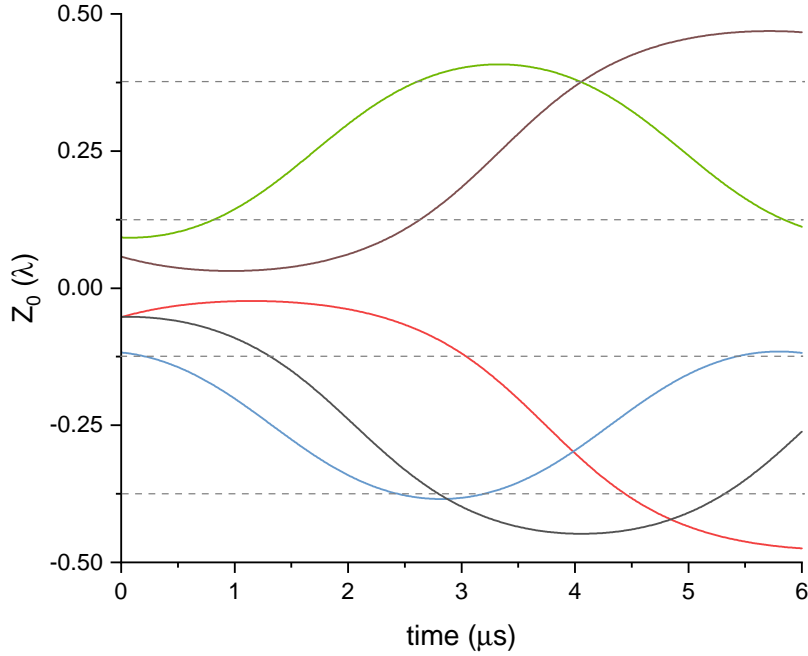
Figure 8.8: Random trajectories of trapped atoms in an optical lattice with large amplitudes Z_1. Here $\eta_2 = 0$, and the dashed lines correspond to boundaries where ξ changes by π.

in the trap. However, the atom spends most of its time in the vicinity of the turning points throughout the spectroscopic duration. A phase difference of 2π exists between the two turning points, meaning that the atom sees the same coupling value $\hat{U}_{AF}$ throughout the interaction time, which removes Doppler broadening and shifting from the central peaks of Figs. 8.5 and 8.7.

Here, I will justify why the barely trapped atom spends most of its time near the turning points. To do this, it's best to consider a fully quantized model of the atom's CM coordinate. For simplicity, a lattice with a full depth of $20E_{2r}$ is observed, where Bloch bands $\nu = 4$ and 5 correspond to the last two motional states for trapped atoms, as seen in Fig. 8.9. Atoms with these energy eigenstates correspond to the classical trajectories discussed above (although the lattices used in the experiment are about $\sim 10^3 E_{2r}$ in depth and ν is much larger). When observing the CM distribution for an atom in $\nu = 5$ with quasimomentum parameter $k_0 = 0$, one can see that atoms of this high energy are mostly concentrated near the intensity antinodes. Thus, it can be concluded that the larger the amplitude of the classical oscillation is conducive to a larger ponderomotive light shift on the internal-state energy of the atom.

165
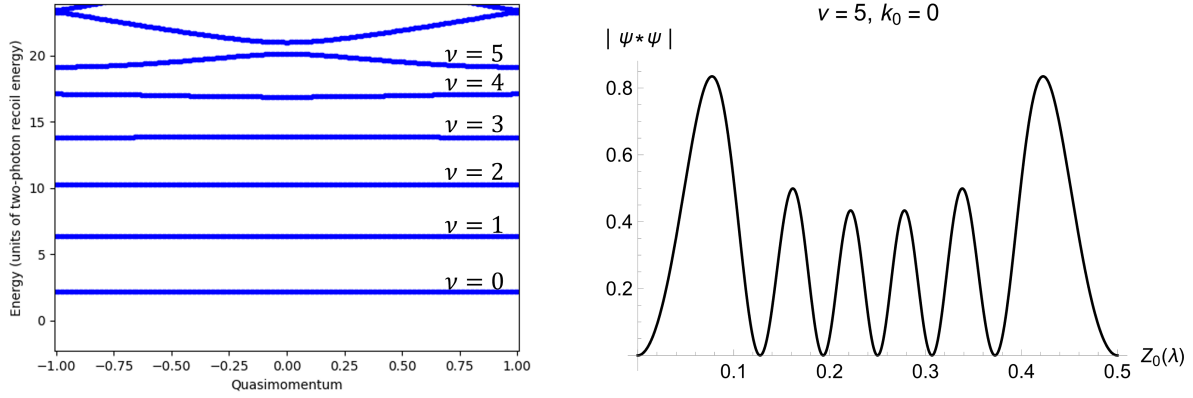
Figure 8.9: On the left, the band structure for an unflipped ($\eta_2 = 0$) lattice is shown with $2U_0 = 20E_{2r}$. CM probability distribution of an atom with quasimomentum of zero and $\nu = 5$ for the same lattice shown on the right.

Because $|1\rangle$ sees a shallower lattice depth than $|0\rangle$ in all experimental cases and the internal energy shifts of the atoms are near a maximum for the trajectories discussed, the effect on the transition frequency between the two quantum states is a red-shift from ω_0. These red-shifts are apparent in Figs. 8.5 and 8.7. Additionally, the unwanted effects of inhomogeneous broadening due to mode impurities of the lattice are evident and cause deviations from the numerical spectra, which are based on an ideal standing-wave with a TEM$_{00}$ transverse mode. These impurities are reflected in the experimental spectra because there is a differential light shift between $|1\rangle$ and $|0\rangle$.

These barely trapped trajectories also contribute to signal in the sidebands. As seen in the coupling potential with trapped trajectory $Z_0(t) = Z_1 \cos(\omega_1 t)$,

$$\hat{U}_{AF}(t) = \frac{\hbar\Omega_{q,0}}{2} \cos(2k_L Z_1 \cos(\omega_1 t)) e^{-iq\omega_m t} |1\rangle \langle 0| + \text{h.c.}, \tag{8.10}$$

which, due to the Jacobi-Anger expansion, leads to three independent drives,

$$\hat{U}_{AF}(t) \simeq \frac{\hbar\Omega_{q,0}}{2} J_0(2k_L Z_1) e^{-iq\omega_m t} |1\rangle \langle 0| - \frac{\hbar\Omega_{q,0}}{2} J_2(2k_L Z_1) e^{-i(q\omega_m - 2\omega_1)t} |1\rangle \langle 0|$$
$$- \frac{\hbar\Omega_{q,0}}{2} J_2(2k_L Z_1) e^{-i(q\omega_m + 2\omega_1)t} |1\rangle \langle 0| + \text{h.c..} \tag{8.11}$$

The term with phase $q\omega_m - 2\omega_1$ contributes to the blue-shifted peaks of Figs. 8.5 and 8.7, while $q\omega_m + 2\omega_1$ contributes to the red-shifted sideband. The red-shifted sideband is stronger

because the $2\hbar\omega_1$ energy-shift on the atomic state tunes the negative light shift on the transition frequency closer to resonance. As found in a fully quantum description of the CM coordinate, these sidebands in the coupling potential are responsible for inducing changes in the motional quantum number ν by ± 2.

8.5.2 Doppler-Free Features from Deeply Trapped Atoms

In Fig. 8.6, η_2 is shifted by π just before the modulation is applied to the lattice. This means that atoms excited by the 480-nm laser near the intensity antinodes are suddenly initialized near the nodes. Therefore, the trapped trajectories resemble trajectory 2 in Fig. 8.1(c). Most atoms prepared in $|0\rangle$ lie on a low Bloch band near $\nu = 0$ and have classical CM oscillations with amplitudes $Z_1 < 0.125\lambda$. Because of this, the atoms see a fixed phase ξ throughout their evolution in the trap and have Doppler-shifts depending on their momentum completely removed in central peak of the spectrum. Furthermore, the low motional states ν they occupy feature appreciable CM distributions near the intensity nodes, meaning the smallest possible light shift from the lattice is applied to the internal-state energies of $|0\rangle$ and $|1\rangle$.

With the same simulation, random, trapped trajectories are plotted in Fig. 8.10. The same lattice parameters are used as inputs as those in Fig. 8.8 with the only difference being that the shift $\eta_2 = \pi$ is applied, inverting the lattice intensity profile before the atom's evolution in the trap. Oscillations here occur at a faster frequency with a period around ~ 5 μs, meaning that they converge towards the harmonic approximation $\propto \sqrt{U_0}$. For these low-energy oscillations, the atom spends more time near the region of stable equilibrium and primarily sees the minimal light shifts in its internal energy that the intensity antinode provides.

As the ponderomotive light shift brought on by the intensity antinode is the smallest in this case of deeply trapped atoms, the minimum light shift for $|1\rangle$ is actually larger than that for $|0\rangle$. Consequently, the effect on the Doppler-free transition is a blue-shift from ω_0.

Because Z_1 is smaller for trajectory 2 than 1, the motional shifts in ν are less significant, causing a reduction in signal for the side peaks. Also, upon inspection of the experimental spectrum obtained in Fig. 8.6, an observable increase in signal strength in the blue sideband with respect to the red peak is a result of the positive increase in the transition frequency induced by the differential light shifts. Thus, an effect opposite to that found in Fig. 8.5 is shown as expected.
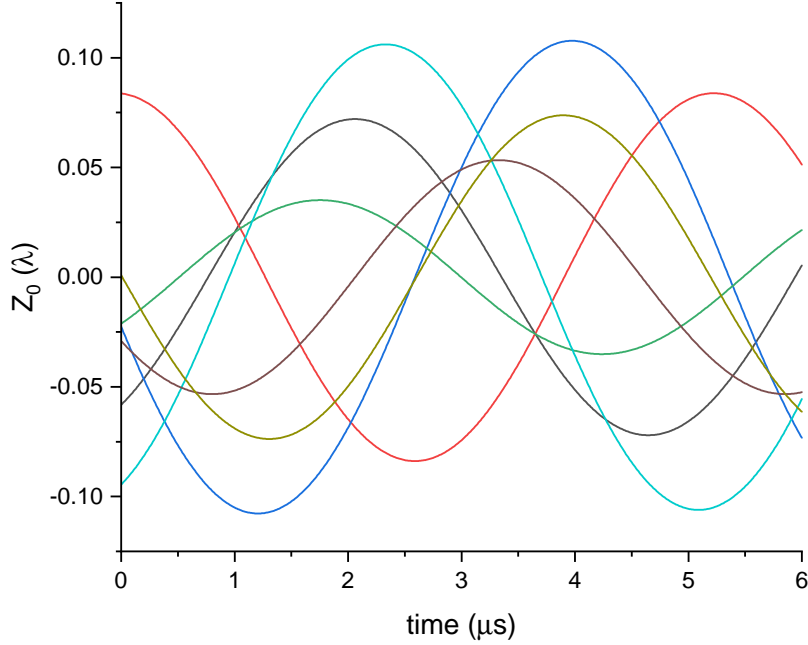
Figure 8.10: Random trajectories of trapped atoms in an optical lattice with small ampli-
tudes $Z_1 < 0.125\lambda$. Here the intensity profile is flipped ($\eta_2 = \pi$), and the phase
ξ remains fixed.

8.5.3   Spectral Features from Untrapped Trajectories

Now I will discuss the spectra for untrapped atoms with trajectory 3 in Fig. 8.1(c) and how
they undergo optical Doppler shifts through the ponderomotive coupling $\hat{U}_{AF}$. Many often
confuse the Doppler-shifts from ponderomotive optical transitions with those from Raman
transitions. The main difference in these totally different forms of spectroscopic driving stems
from their quantum-mechanical origins. Even though they are responsible for population
transfer between E1-violating states, Raman transitions are still based on the potentials of
induced electric-dipole moments in the electronic wave function in higher-order perturbation
theory. On the other hand, ponderomotive transitions promote population transfer between
E1-violating states in first-order perturbation theory entirely by the inelastic scattering of a
photon off an electron.

In general, two laser fields with wave vectors $\mathbf{k}_L$ and $\mathbf{k}'_L$ at angular frequencies ω_L and ω'_L
can drive transitions between Rydberg states $|0\rangle$ and $|1\rangle$ of the same parity with separation
$q(\omega'_L - \omega_L)$, where q is a nonzero integer and $2q$ is the order of the transition in pertur-
bation theory. When $q > 1$, laser intensities need to be greatly enhanced to compensate

168

the reduction in atom-field coupling strengths. Position-dependent phases accumulated by subsequent absorption and emission can be $\pm q(k'_L + k_L)Z_0$ or $q(k'_L - k_L)Z_0$ which occur at all Z_0. These phases are responsible for Doppler effects because Z_0 is really a time-dependent quantity that is tied to V_{0z}.

Two-photon, Doppler-free spectroscopy is a specific case of a Raman transition. With two-photon, Doppler-free Raman transitions involving two counter-propagating laser fields of angular frequency ω_L (at half of ω_0) and of wave vectors $k_L \hat{k}$ and $-k_L \hat{k}$, at all positions along Z_0 excitation to $|1\rangle$ from $|0\rangle$ can involve subsequent, stimulated absorptions of fields $k_L \hat{k}$ and $-k_L \hat{k}$. This is the Doppler-free case, as the laser field imparts no net CM-position-dependent phase during the coupling of $|0\rangle$ and $|1\rangle$, $(k_L - k_L)Z_0 \simeq 0$. The phase here is zero for all Z_0 and is represented by the dashed, blue line in Fig. 8.1(c). Additionally, the electronic transition can conserve energy by absorbing light from the same fields ($k_L \hat{k}$ or $-k_L \hat{k}$) at any point along Z_0. Resultant continuous and position-dependent phases are $2k_L Z_0$ and $-2k_L Z_0$ and are represented by the upward- and downward-sloping blue, dashed lines in Fig. 8.1(c). These phase shifts are responsible for Doppler-effects in this sort of spectroscopy, which contribute to a fat, Gaussian background added to the Doppler-free, Lorentzian peak [67].

Ponderomotive transitions have very different phase behavior in their atom field coupling expression. In all cases, the first-order interaction imparts a phase $\xi(Z_0)$ that has the staircase behavior shown in Fig. 8.1(c). As long as an atom has an oscillatory behavior that stays between two adjacent local maxima of the lattice intensity gradient, the transition will be removed from the Doppler effect. Because of this, no velocity-dependent shifting or broadening shows up in the central spectral features near ω_0. The sidebands, however, do have a dependence on V_{0z}; they appear shifted away from ω_0 because they partially correspond to untrapped atoms getting a sequence of π phase shifts as they move along Z_0. Effectively, the sort of atom is moving much faster than the trapped one and sees an energy chirp $\hbar \dot{\xi} = \hbar(d\xi/dZ_0)\langle V_{0z} \rangle$, where $d\xi/dZ_0 \sim \pm 2k_L$ and $\langle V_{0z} \rangle$ is the time-averaged velocity of the atom along Z_0. Therefore, the Doppler energy shift for these untrapped, fast-moving atoms is coincidentally similar to those of atoms undergoing two-photon Raman transitions involving counter-propagating fields. For this experiment, the Doppler-shifted peaks with broadening dependent on the velocity distribution of the atoms, lie on top of the signals at $\pm 2\omega_1$ corresponding to motional changes of ± 2. Both signals make up the red- and blue-shifted sidebands in all spectra. It is important remember, however, that the two effects are independent and do not interfere spectroscopically.

8.6   Conclusion

The leading benefit of this form of laser manipulation of Rydberg-Rydberg transitions is the insensitivity to Δl. With phase modulation of the optical lattice, the ponderomotive force can induce internal-state transitions of the Rydberg atom for *any* value of Δl without making changes in the motional quantum number ν. There are several reasons why changing ν is problematic. Firstly, these $\Delta \nu$ transitions are broadband because they require detunings from ω_0 at the classical trap oscillation frequency (CTOF). For CM, matter waves with high ν quantum numbers, this detuning deviates greatly from the CTOF based on the anharmonicity of the potential. Therefore, the transition is inhomogeneously broadened by the distribution of ν in the sample. Furthermore, these $\Delta \nu$ transitions can sometimes overlap the broad Doppler-shifted peaks at $\pm 2k_L \langle V_0 \rangle$ based on the experimental conditions of the system. Both mechanisms ruin the fidelity in experiments in high-precision spectroscopy [26], quantum control [61], and quantum information [133]. Previous demonstrations of ponderomotive transitions using amplitude-modulated lattices in [62; 63] were limited to the even-parity case because of their resulting coupling potentials $\hat{U}_{AF}$ arising from the beam geometry of two counter-propagating modulated lasers. Because this method of phase modulation was proven to work well with low l Rydberg atoms, I will now propose methods in the subsequent chapter implementing this technique in the initialization of high-l, CS Rydberg atoms ($\Delta l > 20$) completely with laser fields.

CHAPTER IX

All-Optical Circularization of Rydberg Atoms in Novel Lattice Traps

This chapter is based on Ref. [9].

At this point, internal-state transitions of alkali Rydberg atoms using the ponderomotive interaction have been discussed theoretically and demonstrated experimentally with phase- and intensity-modulation of an optical-field gradient [62; 7]. The method of creating a beat frequency between the incident and scattered field of the ponderomotive drive, as well as the structure of the intensity gradient used, allows freedom in the type of Δl, $\Delta \nu$, and Δm_l selection rules provided by the light shining on the Rydberg atoms. For the proposed techniques of ponderomotive laser manipulation in this chapter, it is desired that $\Delta l = \Delta m_l \rightarrow n - 1$ and $\Delta \nu = 0$. Such large changes in quantum numbers are required for initializing a system of circular-state (CS) Rydberg atoms for applications in fundamental physics.

As described in chapter IV, lasers are unable to prepare a sample of CSs through the $\mathbf{A} \cdot \hat{\mathbf{p}}_e$ interaction. Instead, electromagnetic couplings in the RF/microwave band must be adiabatically ramped in intensity and frequency over the resonance condition for the hydrogenic states shifted by parallel DC electromagnetic fields that are perpendicular to the RF/microwave polarization. This technique is known as adiabatic rapid passage (ARP) [45; 75]. Alternative techniques use pulse and frequency shaping of the applied RF fields by quantum optimal control (QOC) theory [200; 153], where iterations of varied experimental parameters are performed until the maximum fidelity is reached.

RF and microwave fields are challenging to work with in an experimental setting. They cannot be focused to sizes smaller than the atomic interaction regions implemented. Scattering off metallic experimental equipment distorts the spatial mode of the fields and modifies the waves' polarizations, two effects that can hamper an otherwise well controlled experiment. Furthermore, enhancing the power of the radiating RF field risks the complication

of cross-talk among other electronics in the lab, something that is not a problem when increasing optical power. Replacing the RF/microwave fields with lasers to interact with the atoms would ease up the complexity of the aforementioned circularization procedures. Additionally, the modes provided by the laser fields would allow site-selective excitation of CSs at the spatial size of the atom, which aids in the elimination of inhomogeneous broadening by position-dependent perturbations.

Three novel methods of all-optical circularization through the $\hat{A}^2$ term using dynamic optical traps are introduced in this chapter. In the first method provided in Section 1, two co-propagating Laguerre-Gaussian beams of opposite winding numbers 14 and -14 and a beatnote at 4.2 THz, focused near the diffraction limit, promote $|21F\rangle$ Rydberg atoms of ^{85}Rb to $|32C\rangle$ in a single-shot drive. The experimental requirements for such an experiment are also discussed. For the second method of obtaining $|32C\rangle$ introduced in Section 2, two different optical frequencies at ω_L' and ω_L, where $\omega_L' - \omega_L = 2\pi \times 350$ MHz, both form a standing wave oriented perpendicular to the static electric and magnetic fields (known as *stabilization fields*), $\mathbf{E}_0$ and $\mathbf{B}_0$, which are parallel to each other and lift the degeneracies of the hydrogenic manifold. The procedure of ARP is simulated in this case using light-matter interactions with the optical beat frequency and power adiabatically ramped. In Section 3, a two-dimensional, phase-modulated optical lattice oriented perpendicular to the stabilization fields provides a time-orbiting well for a trapped Rydberg atom that provides the same coupling as a σ^+-polarized RF field in an ARP scheme. Section 4 compares the three different proposed schemes.

9.1 Circularization by Laguerre-Gaussian Laser Fields

Conventional laser beams, which are shaped into Hermite-Gaussian (HG) modes [201], carry an $\hbar$ of angular momentum in a single quantum of energy from the overall field. It is therefore impossible to use a focused laser in the TEM$_{00}$ mode to excite a ground-state atom directly into the circular state (CS) or to excite a low-angular-momentum Rydberg state to the CS with a single light-matter interaction. One needs to ensure that the laser carries angular momenta on the order of $\sim n\hbar$ for the purpose of optically circularizing the atoms. While HG modes lack this amount of angular momentum, lasers in Laguerre-Gaussian (LG) modes propagate like a vortex with an orbital-angular-momentum winding integer of m [202]. This Section describes using two, co-propagating Laguerre-Gaussian beams of opposite winding numbers $|m|$ and $-|m|$ to transfer a low-l Rydberg atom into the CS through an inelastic ponderomotive interaction. When starting the circularization sequence with $|n'F\rangle$ Rydberg states to generate $|nC\rangle$, the winding number of each beam

must have an integer-valued magnitude $(n-4)/2$. Furthermore, these beams must have a beatnote that matches the frequency spacing between $|n'F\rangle$ and $|nC\rangle$.

When the two LG beams of radial index $p = 0$ and winding numbers $-|m|$ (beam 1) and $|m|$ (beam 2) with angular frequencies ω_{L_1} and $\omega_{L_2} = \omega_L + \omega_b$, respectively, are overlapped and co-propagate, they have the following electric-field dependence in the laboratory frame

$$\mathbf{E}(\mathbf{r},t) = \frac{\hat{\epsilon}\mathcal{E}_1 w_{0_1}}{2w_1(z)}\sqrt{\frac{1}{|m|!}}\left[\frac{\sqrt{2}\rho}{w_1(z)}\right]^{|m|}L_0^{|m|}\left[\frac{2\rho^2}{w_1(z)^2}\right]\exp\left[\frac{-\rho^2}{w_1(z)^2}\right]\exp\left[\frac{-ik_{L_1}\rho^2}{2R_1(z)}\right]\exp[i\psi_1(z)]$$

$$\times \exp[i(|m|\phi - k_{L_1}z) + i\omega_{L_1}t] + \frac{\hat{\epsilon}\mathcal{E}_2 w_{0_2}}{2w_2(z)}\sqrt{\frac{1}{|m|!}}\left[\frac{\sqrt{2}\rho}{w_2(z)}\right]^{|m|}L_0^{|m|}\left[\frac{2\rho^2}{w_2(z)^2}\right]$$

$$\times \exp\left[\frac{-\rho^2}{w_2(z)^2}\right]\exp\left[\frac{-ik_{L_2}\rho^2}{2R_2(z)}\right]\exp[i\psi_2(z)]\exp[-i(k_{L_2}z + |m|\phi) + i\omega_{L_2}t] + \text{c.c.}, \quad (9.1)$$

where

$$w_i(z) = w_{0_i}\sqrt{1 + (z/z_{R_i})^2}, \tag{9.2}$$

$$R_i(z) = z + \frac{z_{R_i}^2}{z}, \tag{9.3}$$

$$\psi_i(z) = (|m| + 1)\arctan\left(z/z_{R_i}\right), \tag{9.4}$$

for [1] beams $i = 1$ and 2, and $L_{p=0}^{|m|}$ is the Laguerre polynomial. The beam waist is w_{0_i}, and the Rayleigh length is z_{R_i}. Cylindrical coordinates $\mathbf{r} = (\rho, \phi, z)$ are most appropriate for this sort of beam geometry. An intensity profile along the z-axis is shown in Fig. 9.1(a) using $\lambda_1 = 536$ nm, $\lambda_2 = 532$ nm, and $|m| = 14$.

LG laser fields notably have the $|m|$ dependent phase that changes as the azimuthal angle is varied. When two co-propagating LG modes of opposite winding numbers are overlapped, a rotating-wave, optical lattice is formed along the azimuthal direction. If $\omega_b = 0$, this lattice is truly stationary, but nonzero values of the beat frequency result in a lattice rotation at the rate ω_b. When ω_b is at the rate of the internal-state dynamics of the Rydberg atom, as is the case here for circularization, the CM sees a time-averaged potential that eliminates the modulation of the lattice.

In this method of circularization with LG beams, $\omega_b/(2\pi)$ must be on the order of THz, as will be explained below. Therefore, the time-averaged ponderomotive potential simply causes a repulsive force on the atom away from the walls of the tubular trap effected by the LG intensity profile. Fig. 9.1(b) shows the time-averaged ponderomotive potential on the (x, y)-plane of the laboratory frame using the same optical parameters as in (a). On the

---

[1]Here, ψ_i denotes a Gouy phase factor for beams $i = 1$ and 2, and are not quantum wave functions.
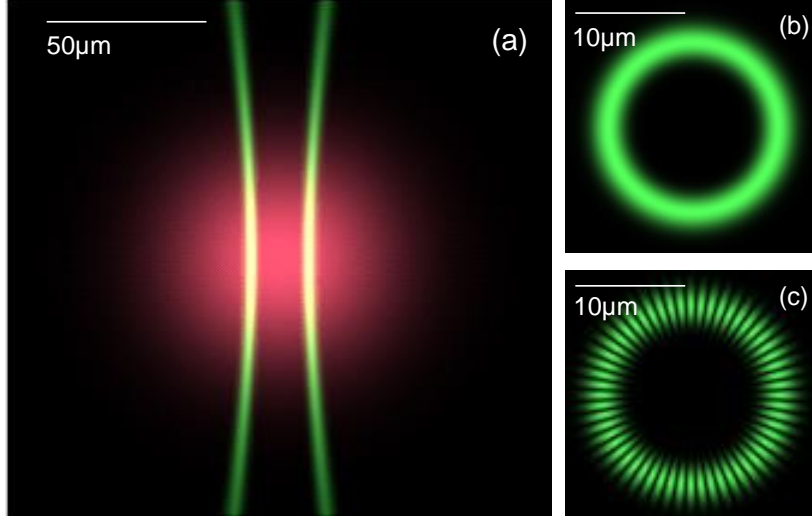
Figure 9.1: Figure taken from [9]. Laguerre-Gaussian trap for Rydberg-atom circularization: (a) view in the (x, z)-plane where beams overlap the laser-cooled cloud, (b) time-average of ponderomotive potential that provides radial trapping, (c) instantaneous, azimuthal lattice potential at time $t = 0$ that circularizes $|21F\rangle$ states.

other hand, the $|n'F\rangle$ Rydberg electron notices the intensity gradient of the azimuthal lattice that is rotating near the frequency separation between $|n'F\rangle$ and $|nC\rangle$. An instantaneous snapshot of this lattice potential, which also couples states $|n'F\rangle$ and $|nC\rangle$, is presented in Fig. 9.1(c).

All effects just discussed and presented below regarding the LG light-matter interactions are afforded by the $\hat{A}^2$ potential of the minimum coupling Hamiltonian. I want to emphasize that my proposed method differs from previous work [203; 204] which investigated the *electric-multipole* interactions of LG lasers and Rydberg states.

9.1.1 Ponderomotive Interactions

The ponderomotive potential, $V_p(\mathbf{R}_0 + \hat{\mathbf{r}}_e)$, that traps the electron towards the center of the radius circumscribed by the overlapped LG beams 1 and 2 is given by

$$V_p(\mathbf{R}_0 + \hat{\mathbf{r}}_e) = \frac{e^2 \mathcal{E}_1^2 w_{0_1}^2}{4|m|! m_e \omega_{L_1}^2 [w_1(Z_0 + \hat{z}_e)]^2} \left[\frac{2[(X_0 + \hat{x}_e)^2 + (Y_0 + \hat{y}_e)^2]}{[w_1(Z_0 + \hat{z}_e)]^2}\right]^{|m|}$$

$$\times \exp\left\{\frac{-2[(X_0 + \hat{x}_e)^2 + (Y_0 + \hat{y}_e)^2]}{[w_1(Z_0 + \hat{z}_e)]^2}\right\} + \frac{e^2 \mathcal{E}_2^2 w_{0_2}^2}{4|m|! m_e \omega_{L_2}^2 [w_2(Z_0 + \hat{z}_e)]^2}$$

$$\times \left[\frac{2[(X_0 + \hat{x}_e)^2 + (Y_0 + \hat{y}_e)^2]}{[w_2(Z_0 + \hat{z}_e)]^2}\right]^{|m|} \exp\left\{\frac{-2[(X_0 + \hat{x}_e)^2 + (Y_0 + \hat{y}_e)^2]}{[w_2(Z_0 + \hat{z}_e)]^2}\right\}. \quad (9.5)$$

This term arises from elastic scattering of LG mode 1 into 1 and 2 into 2 through force provided by the first-order $\hat{A}^2$ interaction. At the single-photon level of field intensity, this interaction is analogous to Thomson scattering but with a superposition of plane waves that form LG modes. As a result of the elastic nature of this scattering interaction, potential $V_p(\mathbf{R}_0 + \hat{\mathbf{r}}_e)$ is time-independent. Fig. 9.2 depicts the energy strength of V_p along one axis of the $z = 0$-plane in the laboratory frame. In this plot, $\lambda_1 = 536$ nm and $\lambda_2 = 532$ nm with $\mathcal{E}_1 = 2.49 \times 10^6$ V/m and $\mathcal{E}_2 = 2.50 \times 10^6$ V/m. Gaussian beam waists are $w_{0_1} = 3.41$ μm and $w_{0_2} = 3.39$ μm.

Inelastic scattering of LG mode 2 into mode 1, reminiscent of a low-energy, non-relativistic Compton effect, results in population transfer from state $|n'F\rangle$ into $|nC\rangle$, the CS. This potential has the harmonic dependence of an azimuthally rotating optical lattice at rate ω_b and a spatial dependence (expressed in laboratory frame coordinates $\hat{\mathbf{r}} = \mathbf{R}_0 + \hat{\mathbf{r}}_e$) found in the coupling potential $\hat{V}_C$,

$$V_C(\hat{\mathbf{r}}, t) = 4^{|m|} \frac{(2|m|)!}{|m|!} \sqrt{\frac{4\pi}{(4|m| + 1)!}} \left(\frac{e^2 \mathcal{E}_1 \mathcal{E}_2 w_{0_1} w_{0_2}}{2 m_e \omega_{L_1} \omega_{L_2}}\right) \hat{r}^{2|m|} [w_1(\hat{r}\cos\hat{\theta}) w_2(\hat{r}\cos\hat{\theta})]^{-(|m|+1)}$$

$$\times \exp\left(-\hat{r}^2 \sin^2\hat{\theta}[w_1(\hat{r}\cos\hat{\theta})^{-2} + w_2(\hat{r}\cos\hat{\theta})^{-2}]\right) \left[Y_{2|m|}^{2m}(\hat{\theta}, \hat{\phi}) S(\hat{\mathbf{r}}) \exp(-i\omega_b t)\right.$$

$$\left. + Y_{2|m|}^{-2m}(\hat{\theta}, \hat{\phi}) S^*(\hat{\mathbf{r}}) \exp(i\omega_b t)\right]. \quad (9.6)$$

The position-dependent phase of the coupling potential, $S(\hat{\mathbf{r}})$, potentially leads to inhomogeneous broadening and a reduction in coupling strength depending on the wavelength
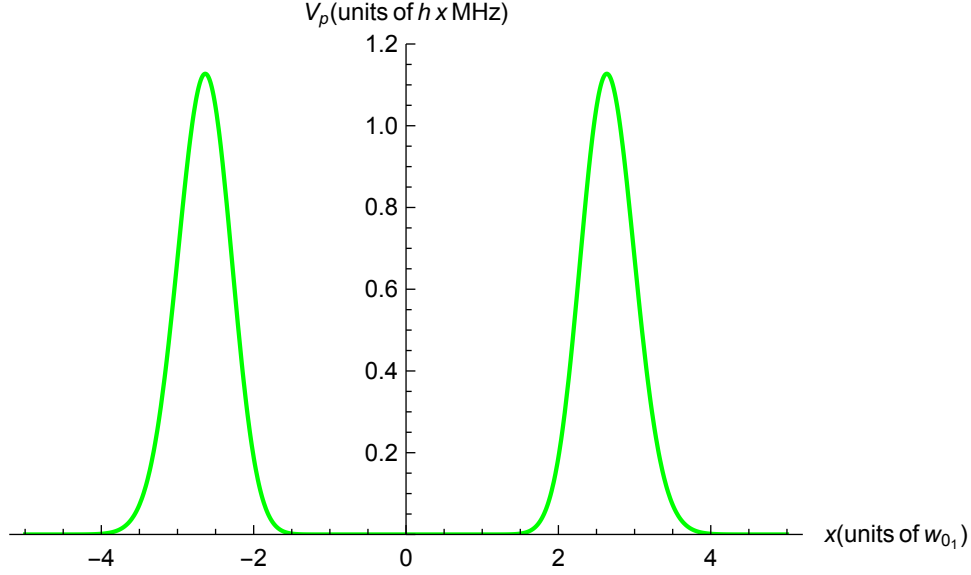
Figure 9.2: Figure taken from [9]. electron trapping potential as seen along the x-axis of the laboratory frame for $\lambda_1 = 536$ nm and $\lambda_2 = 532$ nm. A ponderomotive interaction from LG modes of $m = 14$ with $w_{0_1} = 3.41$ μm and $w_{0_2} = 3.39$ μm provides this potential. The field amplitudes here are $\mathcal{E}_1 = 2.49 \times 10^6$ V/m and $\mathcal{E}_2 = 2.50 \times 10^6$ V/m

difference of between mode 1 and 2. It can be expressed as

$$S(\hat{\mathbf{r}}) = \exp\left[\frac{i\hat{r}^2 \sin^2 \hat{\theta}}{2}\left(\frac{k_{L_2}}{R_2(\hat{r}\cos\hat{\theta})} - \frac{k_{L_1}}{R_1(\hat{r}\cos\hat{\theta})}\right)\right] \exp\{i[\psi_1(\hat{r}\cos\hat{\theta}) - \psi_2(\hat{r}\cos\hat{\theta})]\}$$
$$\times \exp\left[i(k_{L_2} - k_{L_1})\hat{r}\cos\hat{\theta}\right]. \quad (9.7)$$

However, the λ_1 and λ_2 used in this discussion makes $S(\hat{\mathbf{r}}) = 1$, so S can be ignored here.

9.1.2 Rabi Frequencies and Adiabatic Potentials

In order to achieve an observable coupling between $|n'F\rangle$ and $|nC\rangle$ through the potential $\hat{V}_C$, it is essential that $n' \neq n$. This restriction comes from the fact that high-l Rydberg states have an average radius approximately equal to $n^2 a_0$ while the low angular-momentum states are twice the size for the same n. If $n' = n$, the electron wave function overlap would be too weak to give a matrix element that could provide measurable population transfer. As a result, $n' \sim n/\sqrt{2}$. In this discussion, $n = 32$, $n' = 21$, and $\omega_b = 2\pi \times 4.2$ THz. The radial wave function overlap of $U_g(r_e)$ and $U_e(r_e)$ for states $|g\rangle = |21F\rangle$ and $|e\rangle = |32C\rangle$ respectively is shown in Fig. 9.3.

176
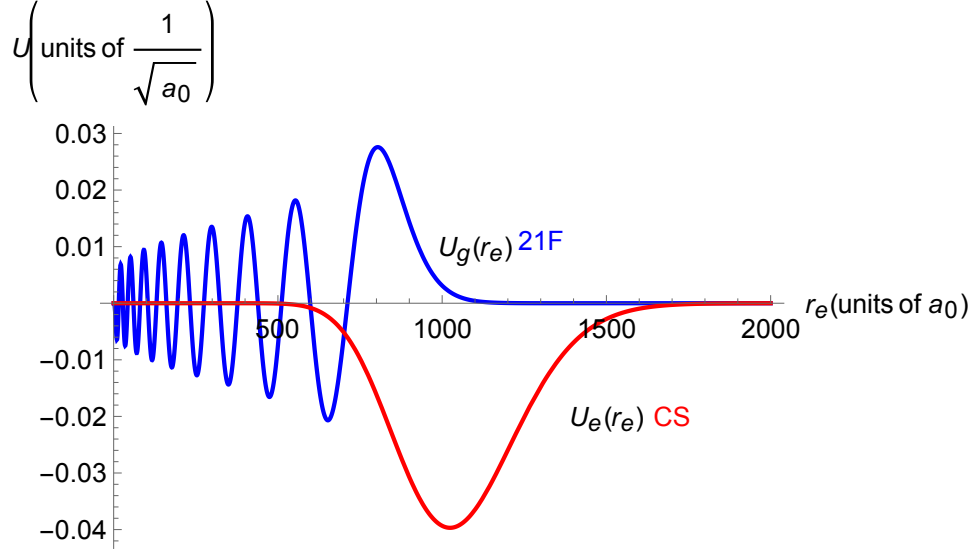
Figure 9.3: Figure taken from [9]. Depiction of electronic wave functions $|g\rangle = |21F\rangle$ (blue) and $|e\rangle = |32C\rangle$ (red) in the radial direction.

Because $\omega_b/(2\pi) = 4.2$ THz, which is the energy separation between $|g\rangle$ and $|e\rangle$, $\lambda_1 = 536$ nm and $\lambda_2 = 532$ nm. Therefore, the beams will focus at slightly different waists $w_{0_1} = 3.41$ μm and $w_{0_2} = 3.39$ μm at the position of the atoms. The matrix element $\hbar\Omega(\mathbf{R}_0)/2$ is computed at $Z_0 = 0$ along one dimension (X_0) of the plane normal to z. The following integral must be computed

$$\Omega(X_0) = \frac{2}{\hbar} \int \psi_e^*(\mathbf{r}_e)|V_C(X_0 + x_e, y_e, z_e)|\psi_g(\mathbf{r}_e)d^3\mathbf{r}_e. \tag{9.8}$$

I compute this integral along X_0 using the "NIntegrate" function of Mathematica with the quasi-Monte-Carlo method of 10^6 quasi-random samples. In this calculation $\mathcal{E}_1 = 2.49 \times 10^6$ V/m and $\mathcal{E}_2 = 2.50 \times 10^6$ V/m, which corresponds to an optical power measurement of 150.0 mW for each beam along the z-component of their Poynting vectors [202]. The results as a function of X_0 at $Z_0 = 0$ are represented with the black curve in Fig. 9.4.

The green curve in Fig. 9.4 represents the adiabatic trapping potential V_{ad} of the CS along X_0 that confines the atoms near the center of the tubular laser trap. If the application of DC electric and magnetic fields along z lifts the degeneracy of the hydrogenic manifold, I can assume that $\hat{V}_p$ does not induce any state mixing and that ψ_e retains its unperturbed spatial structure for all CM positions $\mathbf{R}_0$. The effects of $\hat{V}_p$ can thus be calculated with
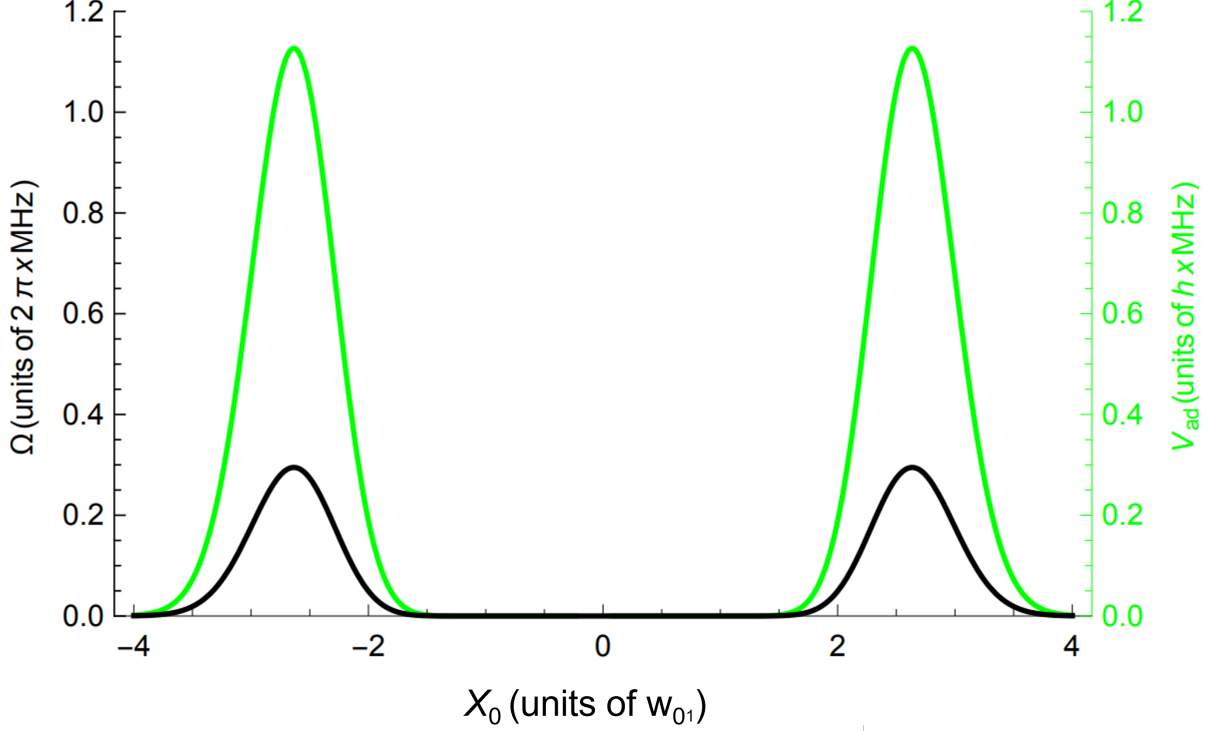
Figure 9.4: Figure taken from [9]. The Rabi frequency (black) for a coupling between $|21F\rangle$ and $|32C\rangle$ by $\hat{V}_C$. Calculated at $Y_0 = Z_0 = 0$ along X_0. The adiabatic trapping potential (green) of the CS brought on by the time-independent ponderomotive potential $\hat{V}_p$. Here, $w_{0_1} = 3.41$ μm with $\mathcal{E}_1 = 2.49 \times 10^6$ V/m and $\mathcal{E}_2 = 2.50 \times 10^6$ V/m

nondegenerate perturbation theory in the first order,

$$V_{ad}(X_0) = \int \psi_e^*(\mathbf{r}_e)|V_p(X_0 + x_e, y_e, z_e)||\psi_e(\mathbf{r}_e)d^3\mathbf{r}_e. \tag{9.9}$$

The diameters of the atomic states involved in this circularization technique are only ~ 90 nm while the diameter of the radial, LG optical trap is on the order of ~ 20 μm. Consequently, $V_{ad} \simeq V_p$ for both $|g\rangle$ and $|e\rangle$ due to weak spatial averaging of $\hat{V}_p$ over the electronic wave functions.

9.1.3 Experimental Implementation

Calculating Newton's equations to solve for $\mathbf{R}_0(t)$ for an atom with speed $V_0 = 5$ cm/s and adiabatic potential V_{ad} predicts that it will take ~ 0.6 ms to oscillate back and forth in this sort of radial trap with the optical parameters given above, which is about 60 times the lifetime of the $|g\rangle = |21F\rangle$ state, $\tau_{21F} = 11$ μm. An atom that is not prepared near the rim

of the tubular laser trap would be decayed before it is circularized. Only atoms initialized in the vicinity of the intensity maximum of the LG beams are able to be circularized. This area is approximated by a hollow disk of radius $r_0 \sim 10$ μs and infinitesimal width limited by the lifetime and speed of the atom $dr \sim V_0 \tau_{21F}$ (total area is $2\pi r_0 dr$). The fraction of atoms able to be circularized is this area divided by πr_0^2. Considering that the Rabi frequencies would allow about half the atoms in this fraction to be circularized with a 4 μs pulse duration of beam 1 $\lambda_1 = 536$ nm, the overall circularization efficiency would be about 5% for this method.

In a proposed experimental implementation of this circularization scheme, two tunable lasers giving several 100 mW of optical power at λ_1 (beam 1) and λ_2 (beam 2) would be locked to two modes of an optical frequency comb separated at 4.2 THz. Each Gaussian laser would then diffract off a spatial light modulator (SLM) or digital micromirror device (DMD) to yield LG lasers of large (> 10) winding numbers $-|m|$ and $|m|$ [205]. A microscope-objective lens focusing the lasers to the desired waists realizes the ponderomotive laser trap, and DC fields E_0 and B_0 are oriented longitudinally along the z-axis to lift the hydrogenic-state degeneracy. After laser cooling ^{87}Rb atoms in a gray optical molasses [206], field $\mathcal{E}_2$ is adiabatically ramped to prevent atom heating by the trap.

Once the ^{87}Rb atoms are cooled in their ground state, optical pumping would transfer the atoms in the stretched state, $F = 2, m_F = 2$. Detuned (~ 500 MHz) lasers at wavelengths 780 nm, 776 nm, and 1292 nm and large optical powers would prepare the atoms in the $|g\rangle = |21F, m_j = 7/2\rangle$ state for a maximum duration of 1 μs using an off-resonant, three-photon transition. Beam 1 and wavelength λ_1 would then be pulsed on for a duration not exceeding τ_{21F} to allow circularization to occur.

9.2 Adiabatic Rapid Passage with a Ponderomotive Optical Lattice

I will now consider a one-dimensional optical lattice at $\lambda = 532$ nm that provides several simultaneous even-parity ($\Delta n_2 = -\Delta m_l = -2$) couplings among the hydrogenic red states ($n_1 = 0$) for the $n = 32$ manifold. The lattice's propagation axis lies perpendicular to the quantization-axis-defining stabilization fields $E_0 = 2.736$ V/cm and $B_0 = 5$ G, meaning $\Delta m_l = 0$ transitions are forbidden by selection rules. Two optical frequencies ω_L and ω_L' with $\omega_L' - \omega_L = 2\pi \times 350$ MHz each have two beams ($\mathbf{k}_L, -\mathbf{k}_L, \mathbf{k}_L'$, and $-\mathbf{k}_L'$ in all) which together make up two co-aligned, optical standing waves. The two frequencies can be derived from an optical phase-locked loop between two separate lasers or from an acousto-optic modulator.

All four beams are equal in peak intensity $I^{(i)} = I^{(r)} = I'^{(i)} = I'^{(r)} = I$ and have a

carrier-wave optical power of 1.43 W that is focused to a waist of $w_0 = 10~\mu$m. One set of counter-propagating beams can be amplitude-modulated with a slowly-varying envelope of structure $f(t)$. In the case described here, $f(t) = e^{-\ln(16)t^2/(2\tau^2)}$, where τ is a parameter characterizing the duration of the envelope in time. Literally it is the time where $f(t)$ drops to a quarter of its maximum value. Here, I will set it to $\tau = 25~\mu$s in the following simulation.

9.2.1 Atom-Field Coupling

The atom-field interaction $\hat{U}_{AF}$ between hydrogenic states $|n, n_1 = 0, n_2 = n - m_l - 1, m_l\rangle$ and $|n, n_1 = 0, n_2 = n - |m_l| + 1, m_l + 2\rangle$ is given by

$$\frac{e^2 f(t) I}{m_e c \epsilon_0 \omega_L^2} \cos\left[(k_L + k_L')X_0\right]$$
$$\times \langle n, n_1 = 0, n_2 = n - |m_l| + 1, m_l + 2| \cos\left[(k_L + k_L')\hat{x}_e\right] |n, n_1 = 0, n_2 = n - m_l - 1, m_l\rangle.$$
$$(9.10)$$

For a trapped atom located at the intensity node of the lattice, in the first order expansion of the matrix element, this coupling can be approximated as a electric-quadrupole potential,

$$\frac{\sqrt{\pi}e^2 f(t) I (k_L + k_L')^2}{\sqrt{30} m_e c \epsilon_0 \omega_L^2}$$
$$\times \langle n, n_1 = 0, n_2 = n - |m_l| + 1, m_l + 2| \hat{r}_e^2 Y_2^2(\hat{\theta}_e, \hat{\phi}_e) |n, n_1 = 0, n_2 = n - m_l - 1, m_l\rangle.$$
$$(9.11)$$

As noted earlier, the parabolic states $|n, n_1, n_2, m_l\rangle$ can be written as a coherent superposition of the hydrogenic states in the spherical basis. Explicitly, this relation is given by [60],

$$|n, n_1, n_2, m_l\rangle = \sum_{l=0}^{n-1} (-1)^{(1-n+m_l+n_1-n_2)/2+l} \sqrt{2l+1} \begin{pmatrix} \frac{n-1}{2} & \frac{n-1}{2} & l \\ \frac{m_l+n_1-n_2}{2} & \frac{m_l-n_1+n_2}{2} & -m_l \end{pmatrix} |n, l, m_l\rangle,$$
$$(9.12)$$

where the terms in parentheses are the Wigner-3j symbols.

For this case, the possible couplings of the 532-nm optical lattice of two frequencies ω_L' and ω_L when atoms are initialized in $|n = 32, n_1 = 0, n_2 = 28, m_l = 3\rangle$ is shown in Fig. 9.5, where the solid lines are desired couplings conducive to circularization and the dashed arrows indicate "leakage" transitions that reverse the CS production. The strong Zeeman interaction given by the $B_0 = 5.0$ G magnetic field in this study, shifts the "leakage" transitions out of resonance throughout the entire ARP scheme, allowing only the bottom rung of states in

Fig. 9.5 to be considered. A similar technique for preventing the undesired couplings was performed in [75].
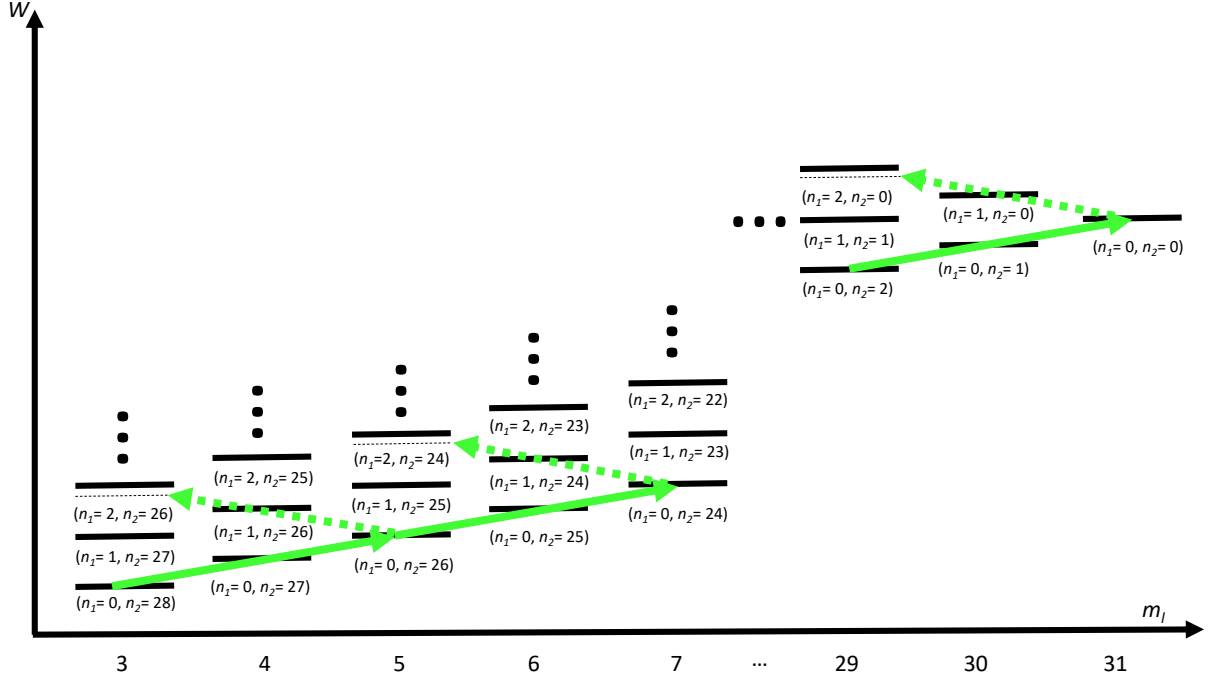
Figure 9.5: Figure taken from [9]. Hydrogenic manifold with stabilization fields E_0 and B_0 applied. A one-dimensional optical lattice consisting of two colors ω_L and ω'_L couples parabolic states of the same parity through the green arrows. The solid green arrows are useful for circularization while the the dashed arrows cause coherent population loss into the middle of the hydrogenic manifold.

The eigenenergies for the parabolic states, unperturbed by the laser field, are

$$W = -hc\left(\frac{m_+}{m_e + m_+}\right)\frac{R_\infty}{n^2} + \frac{3}{2}E_0 e a_0 n(n_1 - n_2) + \frac{e\hbar B_0}{2m_e}(m_l + g_s m_s)$$
$$- \frac{1}{4}\pi\epsilon_0 a_0^3 E_0^2 n^4[17n^2 - 3(n_1 - n_2)^2 - 9m_l^2 + 19], \quad (9.13)$$

where m_+ denotes the mass of the atom's ionic core, $M = m_+ + m_e$. Now, let's assume that the atoms are located exactly at the stable equilibrium positions of the lattice wells, i.e., the intensity minima. The energy lost by the laser field $\hbar(\omega'_L - \omega_L) = \hbar\omega_{RF,0} = h \times 350$ MHz due to the exchange in mode numbers taking place during the ponderomotive interaction can be added to the energy W. One can consider this addition of imparted energy from the laser to the atom as the *dressed-atom picture* [69; 66]. Specifically, when only considering

the $n_1 = 0$ states in the hydrogenic manifold, non-adiabatic energy levels are

$$W' = W + \frac{n_2}{2}\hbar\omega_{RF}(t) + U_{0,n_2}, \tag{9.14}$$

where U_{0,n_2} is the ponderomotive shift on the Rydberg state that changes as n_2 decreases. For the ARP method of circularization, the RF beat frequency, $\omega_{RF}(t)$, between the two co-aligned lattices is a linear function of time with $\omega_{RF}(t) = \omega_{RF,0} + \alpha t$, where $\alpha = \Delta\omega_{RF}/\tau$ is the chirp of the beat frequency. The simulation below has $\alpha = 2\pi \times 56.4$ kHz/μs.

Energies W' would be diagonal in the Hamiltonian if the previously introduced couplings were zero. Including the nonzero atom-field couplings between states of quantum numbers n_2, m_l and $n_2 - 2, m_l + 2$ implies that the parabolic basis is no longer good for this Hamiltonian. After diagonalization, there exists an adiabatic eigenstate $|j\rangle$ that is a time-dependent superposition of all parabolic states. At the beginning of the ARP sequence, this adiabatic state is the $|n, 0, n-4, 3\rangle$ parabolic state, which has $|nF\rangle$ admixture. Towards the end of the ponderomotive laser coupling and beat-frequency sweep, the system should approach population inversion to the $|nC\rangle$ state, provided that no diabatic transitions occur.

Adiabatic states $|j\rangle$, engendered by the mixing of parabolic states $|i\rangle = |n, n_1, n_2, m_l\rangle$ through the ponderomotive atom-field coupling, can be thought of as a unitary transformation $\hat{D}$ of $|i\rangle$. Thus, as explained in [66],

$$|j\rangle = \sum_i D_{ij} |i\rangle \tag{9.15}$$

and

$$|i\rangle = \sum_j D_{ji}^* |j\rangle, \tag{9.16}$$

which, under the Schrödinger equation,

$$\sum_j [i\hbar\partial_t(D_{ji}^* |j\rangle) = \hat{H}D_{ji}^* |j\rangle] \tag{9.17}$$

$$\sum_j [i\hbar\dot{D}_{ji}^* |j\rangle + i\hbar D_{ji}^*\partial_t |j\rangle = \hat{H}D_{ji}^* |j\rangle] \tag{9.18}$$

$$\sum_j [i\hbar \langle j'| D_{ij'}\dot{D}_{ji}^* |j\rangle + i\hbar \langle j'| D_{ij'}D_{ji}^*\partial_t |j\rangle = \langle j'| D_{ij'}\hat{H}D_{ji}^*\delta_{jj'} |j\rangle]. \tag{9.19}$$

Note that the diagonalized Hamiltonian $D_{ij}\hat{H}D_{ji}^* |j\rangle \langle j|$ has no off-diagonal terms. Term $i\hbar \langle j'| D_{ij'}\dot{D}_{ji}^* |j\rangle$ yields noticeable couplings between the adiabatic states $|j\rangle$ and $|j'\rangle$, provided that $D_{ij'}\dot{D}_{ji}^* \sim D_{ij}\hat{H}D_{ji}^*$. Such non-adiabatic couplings would threaten the fidelity in the ARP scheme for circularization, as a portion of atoms in the state $|j\rangle$ that evolves to $|nC\rangle$

at the end of the sequence would be transferred to state $|j'\rangle$. Ideally $D_{ij}\hat{H}D_{ji}^* \gg D_{ij'}\dot{D}_{ji}^*$, which, for a two-level system, is quantified by an adiabaticity parameter [207; 208],

$$\Gamma = \frac{|\langle i'|\,\hat{U}_{AF}\,|i\rangle\,|^2}{\hbar|d\Delta W'(t)/dt|},\tag{9.20}$$

where $\Delta W'(t) - W'_{i'}(t) - W'_i(t)$. If $\Gamma \geq 4$ (a good value for Γ), then the probability of a non-adiabatic transition from $|j\rangle$ to $|j'\rangle$, $P(j \to j')$, is $\ll 0.01$, as given by the Landau-Zener formula [207; 208],

$$P(j \to j') = e^{-2\pi\Gamma}.\tag{9.21}$$

Eq. 9.21 is usually only true if one is considering a two-level Hilbert space or a multi-level basis with a sequence of two-level ARP protocols isolated in time. Using the parameters I lay at the beginning of the section, where the maximum Rabi frequency is $2\pi \times 1.90$ MHz for the $|32, 0, 18, 13\rangle \to |32, 0, 16, 15\rangle$ coupling, multiple parabolic states can be populated at any given time throughout the ARP sweep, meaning the two-level Landau-Zener parameter is not valid in this case. However, ensuring that Γ is as large as possible for any of the couplings is good practice to minimize the non-adiabatic transitions.

9.2.2 Simulation

Now I will present the simulation of this type of ARP scheme using ponderomotive laser couplings among the hydrogenic states to see the sort of efficiencies this method would provide using the commonly accessible experimental parameters given at the beginning of the section.

Numerical integration of the time-dependent Schrödinger equation, consisting of every two of the bottom $n_1 = 0$, red states of the $n = 32$ hydrogenic manifold, from $m_l = 3$ to $m_l = 31$, the CS, is performed. Consideration of decay $\Gamma_{n,0,n_2,m_l}$ by spontaneous emission, blackbody radiation, and photoionization is included in the diagonal terms by introducing $-i\Gamma_{n,0,n_2,m_l}c_{n,0,n_2,m_l}(t)/2$ in the diagonals of the matrix. The Mathematica "NDSolve" algorithm is used to carry out the integration. Fig. 9.6(a) shows the results of this integration while Fig. 9.6(b) shows the time-dependent energies W' in the adiabatic basis. Each colored curve represents a parabolic state, with the leftmost red curve representing population P in $|32, 0, 28, 3\rangle$ and the rightmost green curve representing the population in $|32C\rangle = |32, 0, 0, 31\rangle$.

Note that there are still leftovers in the cyan curve, representing $|32, 0, 2, 29\rangle$, implying that the ARP efficiency (ignoring the decay), is 89%. When decay is considered, the absolute efficiency becomes 77%. Lower-angular-momenta Rydberg states at $n = 32$ have lifetimes
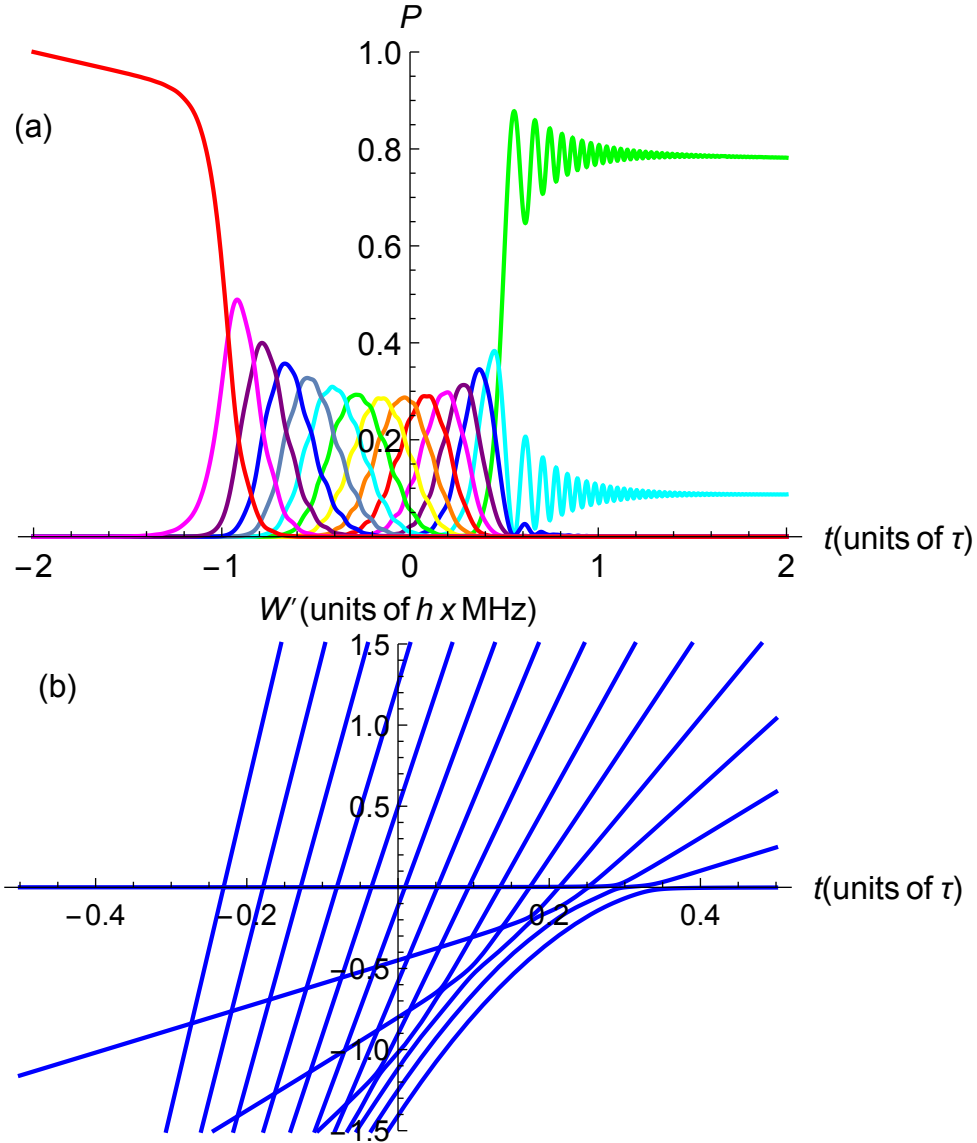
Figure 9.6: Figure taken from [9]. Probability P of atom starting in $|32, 0, 28, 3\rangle$ at the beginning of the sequence occupying each coupled parabolic state all the way to the circular state (green curve). Each parabolic state is also characterized by an integer number, $n_2/2$, of inelastic photon scatters through the ponderomotive effect. In (b), adiabatic energies of the dressed parabolic states are shown as a function of time. The bottom adiabatic energy evolves to $|32C\rangle$ at the end of the sequence.

of ~ 50 μs. Experimentally, the decay rate of the CS can be reduced through blackbody shielding and Purcell suppression [146], extending its lifetime to at least ~ 10 ms. Thus, one would want to sweep $\omega_{RF}(t)$ faster at the beginning of the ARP protocol and slower near the end, making α time dependent. Determining the best chirp rate could be done through

optimal-control methods [209].

I ignored the "leakage" couplings represented by the green, dashed lines in Fig. 9.5, as the magnetic field B_0 shifts the m_l to m_l-2 transitions out of resonance by 28 MHz. Additionally, the m_l-dependent second-order DC Stark shifts add to this detuning. If there was no B_0 field and/or the E_0 field was weak enough to make second-order DC Stark effects negligible, these "leakage" transitions would contribute to a great deal of population loss towards the center of the hydrogenic manifold. Engineering σ^+- or σ^-- polarized RF fields for the ARP scheme was a way to circumvent this inefficiency in [61; 200; 153]. But how can couplings reminiscent of σ^+- or σ^--polarized-RF transitions be realized with a ponderomotive optical lattice?

9.3 Atom-Field Couplings with Time-Orbiting Ponderomotive Optical Lattice

The answer to the question posed in the previous section is to add a second lattice orthogonal to both the x- and z-axis. Both lattices (1 and 2) would consist of counter-propagating fields, $\mathbf{E}_{1/2}^{(i)}$ and $\mathbf{E}_{1/2}^{(r)}$, with the incident fields i being phase modulated at a controllable RF frequency, ω_{RF}, that is swept over the frequency spacings of the hydrogenic states shifted by E_0 or B_0 (if a magnetic field is necessary). The modulation signals must have an equal RF amplitude η_1 and be out of phase by $\pi/2$. Therefore, the following fields must make up the lattice,

$$\mathbf{E}_1^{(i)}(x,t) = \hat{\epsilon}^{(1)}\mathcal{E}_1^{(i)}\cos\left[k_L x - \omega_L t + \eta_1 \cos\left(\omega_{RF}t\right)\right] \tag{9.22}$$

$$\mathbf{E}_2^{(i)}(x,t) = \hat{\epsilon}^{(2)}\mathcal{E}_2^{(i)}\cos\left[k_L y - \omega_L t + \eta_1 \sin\left(\omega_{RF}t\right)\right] \tag{9.23}$$

$$\mathbf{E}_1^{(r)}(x,t) = \hat{\epsilon}^{(1)}\mathcal{E}_1^{(r)}\cos\left(k_L x + \omega_L t\right) \tag{9.24}$$

$$\mathbf{E}_2^{(r)}(y,t) = \hat{\epsilon}^{(2)}\mathcal{E}_2^{(r)}\cos\left(k_L y + \omega_L t\right), \tag{9.25}$$

where $\hat{\epsilon}^{(1)} \perp \hat{\epsilon}^{(2)}$ to prevent cross-talk. Recall that $x = X_0 + x_e$ and $y = Y_0 + y_e$ are the coordinates in the lab-frame. When $\mathcal{E}_1^{(i)} = \mathcal{E}_2^{(i)} = \mathcal{E}_1^{(r)} = \mathcal{E}_2^{(r)} = \mathcal{E}$, with $\mathcal{E} = \sqrt{2I/(c\epsilon_0)}$, the Rydberg atom trapped at the intensity minimum of the two-dimensional lattice well sees a time-orbiting potential with a period at the order of the Kepler frequency.

On average, the orbiting potential has no net effect on the atom's CM dynamics but does induce dipole-allowed, odd-parity couplings between the internal hydrogenic states $|n,0,n_2,m_l\rangle$ and $|n,0,n_2-1,m_l+1\rangle$. After taking a time-average over the Kepler frequency, the ponderomotive potential takes the form of a typical two-dimensional lattice potential that exerts a conservative, sinusoidal force on the CM. The time-independent ponderomotive po-

tential is, considering the parameters mentioned above,

$$U_p(X_0+\hat{x}_e, Y_0+\hat{y}_e) = \frac{e^2 I}{c\epsilon_0 m_e \omega_L^2} \left[J_0(\eta_1) \cos\left[2k_L(X_0 + \hat{x}_e)\right] + J_0(\eta_1) \cos\left[2k_L(Y_0 + \hat{y}_e)\right] + J_0^2(\eta_1) + 1 \right]$$
(9.26)

This sort of system has parallels to the time-orbiting potential (TOP) trap that was used in generating the first Bose-Einstein condensate [210; 81], where there is no risk in heating the atom's CM by the orbit on average.

I shall show that the two-dimensional phase-modulation presented here provides only couplings from m_l to $m_l + 1$. At $X_0 = Y_0 = \lambda/4$, where the atom is trapped at the potential minimum of $\hat{U}_p$

$$U_{AF}(\lambda/4 + \hat{x}_e, \lambda/4 + \hat{y}_e, t) = -\frac{e^2 I J_1(\eta_1)}{c\epsilon_0 m_e \omega_L^2} \Big\{ \left[\sin\left(2k_L\hat{x}_e\right) - i\sin\left(2k_L\hat{y}_e\right) \right] e^{i\omega_{RF}t}$$
$$+ \left[\sin\left(2k_L\hat{x}_e\right) + i\sin\left(2k_L\hat{y}_e\right) \right] e^{-i\omega_{RF}t} \Big\}. \quad (9.27)$$

Under the rotating-wave approximation (RWA), the matrix element becomes

$$\langle n, 0, n_2 - 1, m_l + 1| \hat{U}_{AF} |n, 0, n_2, m_l\rangle = -\frac{e^2 I J_1(\eta_1)}{c\epsilon_0 m_e \omega_L^2} \sum_{p=0}^{\infty} \frac{(-1)^p (2k_L)^{2p+1}}{(2p+1)!}$$
$$\times \langle n, 0, n_2 - 1, m_l + 1| (\hat{x}_e^{2p+1} + i\hat{y}_e^{2p+1}) |n, 0, n_2, m_l\rangle e^{i(\Delta W/\hbar - \omega_{RF})t}. \quad (9.28)$$

For a first-order, $p = 0$ approximation of this matrix element, the matrix element is proportional to that of a σ^+-polarized RF wave,

$$\langle n, 0, n_2 - 1, m_l + 1| \hat{U}_{AF} |n, 0, n_2, m_l\rangle \simeq -\frac{2\sqrt{8\pi/3}e^2 I J_1(\eta_1)k_L}{c\epsilon_0 m_e \omega_L^2} \langle n, 0, n_2 - 1, m_l + 1|$$
$$\times \hat{r}_e Y_1^1(\hat{\theta}_e, \hat{\phi}_e) |n, 0, n_2, m_l\rangle e^{i(\Delta W/\hbar - \omega_{RF})t}. \quad (9.29)$$

Expressing the coupling of m_l with $m_l + 1$ in terms of a Rabi frequency

$\Omega_{m_l,m_l+1} = \frac{2}{\hbar} |\langle n, 0, n_2 - 1, m_l + 1| \hat{U}_{AF} |n, 0, n_2, m_l\rangle|$ results in the following approximation,

$$\Omega_{m_l,m_l+1} \simeq \frac{4\sqrt{2}e^2 I J_1(\eta_1) k_L}{\hbar c \epsilon_0 m_e \omega_L^2} \sum_{ll'} (-1)^{-n-n_2+l'+l} \langle n, l'| \hat{r}_e |n, l\rangle (2l+1)(2l'+1)$$

$$\times \begin{pmatrix} \frac{n-1}{2} & \frac{n-1}{2} & l \\ \frac{m_l-n_2}{2} & \frac{m_l+n_2}{2} & -m_l \end{pmatrix} \begin{pmatrix} l & 1 & l' \\ m_l & 1 & -m_l-1 \end{pmatrix} \begin{pmatrix} l & 1 & l' \\ 0 & 0 & 0 \end{pmatrix} \begin{pmatrix} \frac{n-1}{2} & \frac{n-1}{2} & l' \\ \frac{m_l-n_2}{2}+1 & \frac{m_l+n_2}{2} & -m_l \end{pmatrix}.$$

$$\tag{9.30}$$

Comparing the approximate Rabi frequencies of the two-dimensional POL with the one-dimensional lattice reveals that the 1D lattice scales as k_L^2 while the 2D scales as k_L. Because the electronic wave functions are still smaller than λ, quantity $k_L \langle n, l'| \hat{r}_e |n, l\rangle$ is less than one. Therefore, the odd-parity, atom-field coupling should fundamentally be stronger than the coupling for the even-parity case.

All of the above equations concerning the time-orbiting ponderomotive optical lattice are valid as long as all intensities are equal, all polarizations of counter-propagating beams are perfectly aligned parallel to each other and perpendicular to the orthogonal lattice, the modulation signal is evenly split in power between both arms, and the phase difference between the split modulation signals is $\pi/2$. Any imperfection in alignment or control of these parameters would introduce a coupling from m_l to m_l-1 and reverse the circularization.

The ponderomotive light shift applied to the atom's internal state when it is located exactly at $X_0 = Y_0 = \lambda/4$ differs as m_l changes. The general alignment of the electron's wave function transverse to the quantization axis increases with m_l, causing a weaker adiabatic energy deviation from the position-independent energy offset U_{offset} as the ponderomotive potential is averaged over the electron density. This deviation is not the weakest for the CS because the overall electron radius tends to decrease as l and m_l increases. Because these light shifts are state-dependent, they upset the efficiency of the ARP procedure.

The phase modulation of the optical lattice allows control over this state-dependent light shift, and the differences can be minimized by reducing the $J_0(\eta_1)$ mode of the EOM output. All the while, η_1 can be set such that $J_1(\eta_1)$ is maximized and the Rabi frequencies Ω_{m_l,m_l+1} reach the $2\pi \times 10$ MHz level.

In a comparison of the peak Rabi frequencies, Ω, and light shifts U_{0,n_2} provided by the 1D versus 2D, time-varying optical lattice, the $n = 32$ hydrogenic manifold is considered with $\lambda = 532$ nm and $I = 0.907$ MW/cm^2. Here $J_0(\eta_1) = 0.17$ and $J_1(\eta_1) = 0.57$. Fig. 9.7 shows the comparison using the same optical parameters that were used in the previous section for the one-dimensional lattice.
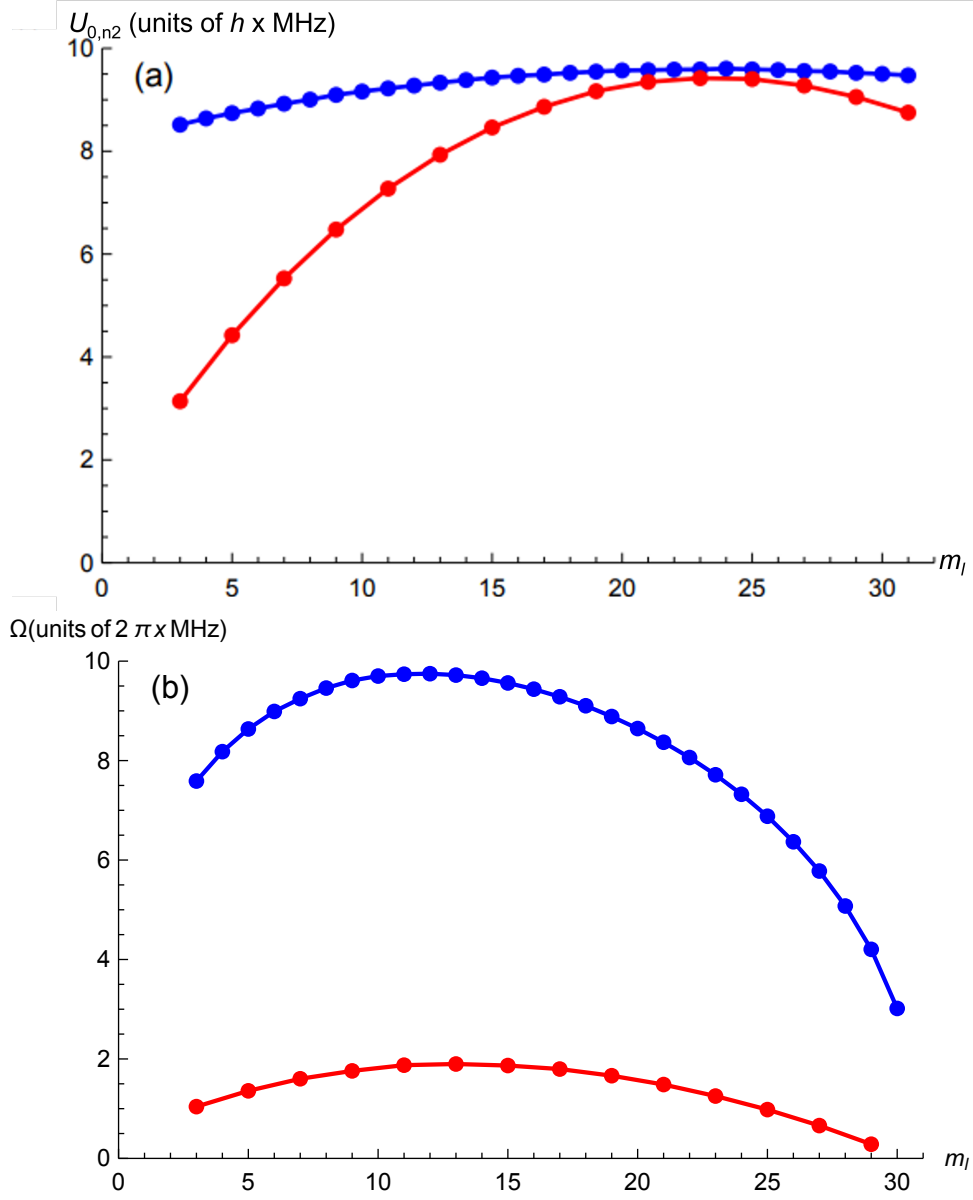
Figure 9.7: Figure taken from [9]. State-dependent light shift U_{0,n_2} for an atom located at $X_0 = Y_0 = \lambda/4$ in the lattice for the two-dimensional lattice (blue) and one-dimensional lattice (red) is shown in (a) as m_l is varied. Rabi frequencies coupling the parabolic states for $m_l \to m_l + 1$ transitions (blue) and $m_l \to m_l + 2$ transitions (red) by the two- and one-dimensional optical lattices respectively are depicted in (b).

Note that the Rabi frequencies are considerably stronger for the two-dimensional, time-orbiting ponderomotive optical lattice. Also note that the variations in U_{0,n_2} are less significant, as $J_0(\eta_1)$ has been reduced. Both effects, coupled with the fact that "leakage"

transitions are eliminated entirely, would result in faster and more efficient ARP. In fact, the Rabi frequencies provided by the time-orbiting lattice could even bypass ARP altogether and allow direct excitation to the CS through pulse engineering of the modulation signals using a quantum-optimal-control algorithm similar to the ones done in [200; 153]. The ultimate goal of that endeavour would be to initialize a sample of CSs within a few ns.

Even though reducing $J_0(\eta_1)$ lowers the state-to-state light shifts on the atom by the lattice, it greatly reduces the full-modulation lattice depth to ~ 1 MHz or less. This is not a problem if the Rydberg atom starts as a ground-state atom that is laser cooled to the lowest motional state, $\nu = 0$, of lattice and stays there as it is excited to Rydberg state. The use of optical tweezers on the atoms would also provide greater control on the atom's position and motion within the lattice well, making the weak lattice depth workable.

9.4   Discussion

I will now make a comparison of the laser-based circularizaiton procedures outlined in this chapter. All of the proposed circularization methods described in this chapter replace the in-vacuum, near-field RF antennas used in ARP [45; 75], which suffer more from inefficiencies in field polarization and homogeneity than at optical wavelengths, with laser fields that have cleaner spatial modes that can be focused down to the extent of the Rydberg wave function and be more easily aligned directly onto the atom. Thus, site-selective circularization is no longer prohibited by the diffraction limit of the field's spatial mode, and polarization inefficiencies can be neglected through the intensity-dependent behavior of the ponderomotive potential. Furthermore, the ease of working with laser beams outweigh the hassle of constructing and calibrating high-current and supreconducting magnets found in traditional circularization methods that require significant magnetic fields beyond 5 G, such as certain ARP schemes and the crossed-fields method [75; 71; 72; 73; 74], described in Chapter IV. The all-optical methods found in this chapter are expected to require fields no greater than the ~ 5 G level. Lastly, the latter two methods described involving rectilinear one- and two-dimensional ponderomotive optical lattices offer strong atom-field couplings at the $\sim$MHz level that would aid in the speed and efficiency of the ARP procedure compared to the one performed in [45].

Lasers can now have the functionality of cooling ground-state atoms, as well as exciting both low- and high-l Rydberg states up to the CS when considering the methods presented in this chapter. The first-discussed method of circularization involving LG beams of opposite winding numbers offers the advantage of generating a large-volume, low-density sample of CSs, based on the beam parameters. These conditions would ensure that the CSs are non-

interacting, making the system attractive for high-precision spectroscopy experiments and tests of fundamental physics [211; 26]. Additionally, there is the advantage of this method requiring a single, ponderomotive transition of large Δl rather than a sequence of transitions. A major drawback of this method is its large inefficiency of $\sim 95\%$, mainly due to increasing radius of the vortex mode with increasing $|m|$.

A much more efficient means of optically circularizing Rydberg states is to use a one-dimensional optical lattice of two laser frequencies ω'_L and ω_L that are separated by a tunable beat frequency $\omega_{RF}(t)$. This frequency is resonant with the Stark and Zeeman splitting of the hydrogenic manifold by parallel stabilization fields of strength E_0 and B_0 that are perpendicular to the lattice-propagation axis. ARP can be performed by sweeping ω_{RF} through the this resonant frequency and adding a Gaussian envelope to one of the lattice frequencies. With the conditions outlined in Section 2, the overall circularization efficiency is estimated to be $\sim 89\%$. However, a large magnetic field at 5 G is required to tune the $m_l \to m_l - 1$ de-circularizing, leakage transitions out of resonance. As mentioned in the paragraph above, larger magnetic fields are experimentally more of a nuisance to realize.

To combat the leakage transitions, $\Delta m_l = +1$-selection rules need to be introduced in the system. Traditionally, this has been done by designing RF electrodes that give rise to σ^+-polarized fields. Effecting atom-field couplings with the ponderomotive interaction and applied laser fields means that an optical lattice orthogonal to the first of equal potential depth. Both lattices must be phase modulated at ω_{RF} and equal modulation depths with one of the arms having a modulation out of phase by $pi/2$. Effectively, the laser's atom-field coupling would resemble a σ^+-polarized (or σ^--polarized) RF field like the ones found in [61; 152; 153]. Such a two-dimensional lattice would allow a reduction of B_0 and fundamentally have matrix elements stronger than the ones in the previous case. Presented in Fig. 9.7(b), the lattice conditions of the 2D-potential yield larger Rabi frequencies reaching 10 MHz. As a disadvantage for this method, any misalignment or mismatch in this time-dependent optical field could add a π or σ^- component to the atom-field coupling and de-circularize the sample throughout the ARP sequence.

A drawback for all the schemes presented in this chapter is the requirement of an ultracold Rydberg sample to begin with, as the atoms must be deeply trapped to prevent significant Doppler-shifted features [85; 7]. Experiments with CSs involving thermal atomic beams passing through superconducting, high-Q cavities [46] would find these methods largely inefficient.

In summary, I have presented an outline to achieve circular-state Rydberg atoms with novel optical lattice traps that are periodically driven. One method of driving these lattices, phase-modulation, has been experimentally demonstrated in the previous chapter through

spectroscopy of low-angular-momentum Rydberg levels [7]. Goals for obtaining these CSs include furthering the field of fundamental physics by making an accurate and precise measurement of the Rydberg constant [211; 26] and detecting axionic dark matter with CSs high-Q microwave cavities.

CHAPTER X

Outlook

The bulk of this dissertation highlights the role of optical lattices for applications in precision metrology and searches of fundamental physics. Rubidium offers a wide array of atomic states attractive for such endeavors. This dissertation discussed two sets of states in particular: the $5D_j$ levels, applicable for portable optical clocks [25; 28; 38; 39], and circular-state Rydberg atoms, suitable for high-precision spectroscopy of the Rydberg constant [211; 26] and searches of axions, a proposed dark-matter candidate [50; 1].

Integration of an optical-lattice potential or dipole trap with rubidium atoms in the $5D$ state could potentially enhance the performance by canceling the AC Stark shifts implemented by the two-photon transition and confining the atoms within a potential minimum. Accurate knowledge of the AC polarizability at various laser wavelengths for this use in the system is thus necessary. An experiment described in this dissertation measured the $5D_{3/2}$ polarizability with a deep, 1064-nm optical lattice enhanced by a near-concentric, in-vacuum cavity with a finesse of 600. Double-step, two-photon laser spectroscopy was performed and obtained a measurement of $\alpha_{5D_{3/2}}^S(\omega_L = 2\pi c/1.064~\mu\text{m}) = -524(17)$ atomic units with the tensor polarizability lying within the measurement uncertainty. The rate of photoionization of the $5D$ atoms, measurable by the spectral linewidths yielded an experimental cross-section of 44(1) Mbarn. AC polarizabilities of other optical wavelengths that can be introduced to the system in the form of lattices and dipole traps, conducive to better clock performance than $\lambda = 1064$ nm, could also be measured with similar methods.

Circular-state (CS) Rydberg atoms live the longest of all other levels within a principal quantum number n. Furthermore, their electronic structure is a simple torus around the inner ion core with a vanishing probability density towards the nucleus that scales with l as r_e^l. Therefore, no systematic effects from the nuclear charge density affect the accuracy of R_∞. Insensitivity to the nuclear charge density is important because there has been conflicting measurements of the proton charge radius in recent years[27; 17; 18; 47; 48] that

192

have been tied to possibly inaccurate values of R_∞ originating from spectroscopy of low-l atomic states.

In the past, the long lifetimes of CSs were useful in non-destructively measuring the time-evolution of microwave photons trapped in a resonator by reading out the phase shift the photon imprinted on the circular electronic wave function by the AC Stark effect [46]. Because such an apparatus offers sensitivity of RF and microwave fields at the single-photon level, it would be an ideal platform for sensing axion-converted microwaves [50].

A key procedure within these Rydberg-atom experiments is the initialization of exotic, high-l Rydberg states that have sufficiently long lifetimes. This thesis introduces periodically driven ponderomotive optical lattices as an alternate method for Rydberg atom circularization. Experimental work here has demonstrated the feasibility of phase-modulated optical lattices with low-angular-momentum Rydberg states, and proposed phase-modulated and moving lattices for circularization. My dissertation argues that the spatial-selectivity, electromagnetic mode purity, and insensitivity to orbital-angular-momentum selection rules make periodically driven ponderomotive laser traps a tool for circular-state engineering superior to some existing methods [45; 71; 75; 74].

As is typical in any scientific field, opportunities for new experiments blossom from the conclusions of a given experiment. Since this growing tree of experiments is infinite, and the tenure of a graduate student is finite, in the following sections, I briefly detail the possible future trajectories for the Rb optical lattice experiments in the Raithel Lab.

10.1 Future Directions: A Lattice-Tweezer Hybrid Trap for Engineering Circular States

As a means of making the circularization methods discussed in Chapter IX more efficient, optical tweezer arrays of Rydberg atoms [134; 105; 196] can restrict the CM motion by the tweezer beam's large trapping potential and allow freedom in atomic arrangement along the various wells of the optical lattice.

An exciting experimental construction, shown in Fig. 10.1, is a hybrid optical trap consisting of a two-dimensional tweezer array with trapping beams aligned along stabilization fields $\mathbf{E}_0$ and $\mathbf{B}_0$. Aligned transverse to the tweezer beams and stabilization fields are two arms of the two-dimensional, time-orbiting optical lattice. In each dimension, there are two lattice beams: a phase-modulated laser and an unmodulated laser. The phase differences of between the modulation signals of the beams is $\pi/2$, meaning the direction of the optical modulation is in a circular, "stirring" motion. When this stirring occurs at a rate equal to the DC Stark and Zeeman splittings effected by the stabilization fields, a low-l Rydberg

state may be transferred to the circular state through the methods described in Sections 9.2 & 9.3.
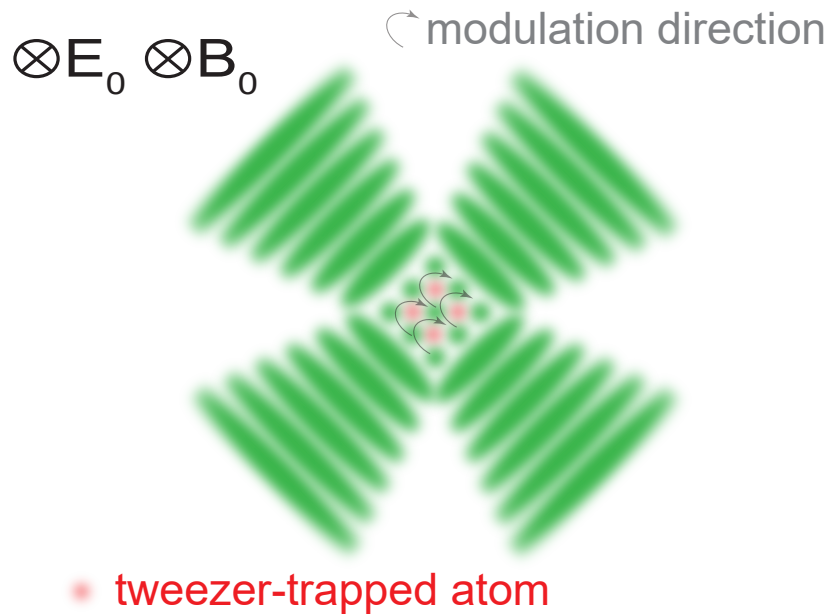
Figure 10.1: A hybrid trap featuring a time-orbiting optical lattice and two-dimensional tweezer array.

This "hybrid" trap of optical tweezers and a two-dimensional optical lattice grants the benefit of programmable initialization of atoms within the potential minimum of a specified lattice site before the circularization sequence. As discussed in Chapter VIII, an atom prepared near a potential maximum is subject to first-order Doppler shifts and makes Doppler-free $\Delta\nu = \pm 2$ sidebands to the energy level more probable. With this apparatus, it can be ensured that atoms are located exactly at the potential minima of the lattice. Also the tweezer array would allow a proposed non-demolition readout [133] of circular states by an ancillary atom in a low-l Rydberg state that is co-trapped along the longitudinal axis of the tweezer beams.

Programmable arrangement of the atoms would provide control over Rydberg-Rydberg interactions, which are undesirable for fundamental physics applications. The tweezer-trapped circular states, engineered by the circularization scheme mentioned above, could then be selectively loaded into the moving optical lattice that transports them through the high-Q cavity with the axion-converted microwaves entrapped inside. Alternatively, high precision spectroscopy with a microwave pulse applied to the circular Rydberg state would extract the Rydberg constant. Controlled loading and arrangement of circular-states is most

efficiently done with a single-atom optical trap.

10.2   Beyond Fundamental Physics: Quantum Processing and Simulation

The technology developed in Chapter 8 involving shaken optical lattices for Rydberg states has far-reaching applications beyond fundamental physics. Because $\Delta \nu = 0$ for odd-parity transitions in this means of ponderomotive laser manipulation, efficient quantum simulators consisting of $|nS\rangle$ and $|nP\rangle$ Rydberg states can now be realized [189; 135; 212].

In particular, the quantum walks described in [189] can now be simulated through site-selective excitation of $|nS\rangle$ or $|nP\rangle$ atoms trapped in tweezer arrays. The walking is based on dipole-dipole shifts and internal-state transitions between two atoms at different lattice sites. Lattice beams are able to be focused down to the similar waist sizes as the tweezer beams and be co-aligned with them. Additionally, these odd-parity ponderomotive transitions can realize the internal state couplings required for synthetic lattices [212]. In [212], a Su-Schrieffer-Heeger (SSH) Hamiltonian [213] is created through tunable microwave couplings among Rydberg $|nS\rangle$ and $|nP\rangle$ states. The couplings create a tunneling term in the Hamiltonian and allows distinctive "edge" and "bulk" states to appear in spectroscopy of the lattice's eigenstates. The laser interaction described in Chapter VIII has the ability to replace microwaves for the couplings and can be used in sync with a spatial-dimension lattice of atoms in tweezer arrays. Other proposals and experiments of Rydberg-atom simulators involving both odd- and even-parity interactions would also find use with this method [134; 214; 102; 136]

The long lifetimes of circular-state Rydberg atoms offer extended coherence times for low-error quantum computers. One- and two-qubit gates involving such atoms were proposed in [133]. Ponderomotive transitions were proposed as means of manipulating the internal states involved in the computation schemes for [133] with tightly focused Laguerre-Gaussian beams of opposite winding numbers.

The experiments I just described would require no inhomogeneous broadening from differential light shifts and near-perfect trapping efficiency. Advanced methods of laser cooling, including Raman sideband cooling to the $\nu = 0$ motional state [215] and gray optical molasses [216; 206] would be required to achieve a well-defined pulse area for quantum simulation and information processing. In addition to the appropriate choices of states in the transition (e.g., $|69S_{1/2}\rangle \rightarrow |69P_{1/2}\rangle$, $|69S_{1/2}\rangle \rightarrow |70S_{1/2}\rangle$, or $|85S_{1/2}\rangle \rightarrow |85P_{1/2}\rangle$), the angle between the lattice beams, $\theta \neq \pi$, and wavelength can be adjusted to give the appropriate lattice spacing that makes a given transition magic.

The time-orbiting ponderomotive optical lattice presented in Chapter IX is a suitable

platform for the engineering of Rydberg-electron wave packets [217]. The ARP sequence described in Section 9.2 does not need to end with $|nC\rangle$. Any of the intermediate states existing in the time frame from $-\tau$ to 0.5τ of the ARP sequence is a parabolic wave function that is elliptical in shape. Tests of the quantum-classical correspondence principle for Keplerian orbits would be an interesting investigative direction upon the creation of these wave packets [218]. Furthermore, observation high-l Rydberg-ground trilobite molecules [219] would be an exciting consequence of engineering these electronic wave functions.

While ponderomotive interactions with cold Rydberg atoms have been thoroughly observed in an experimental setting, as shown in this work and previous [199; 170; 154; 157; 62; 63], their compatibility with portable atomic sensors [140; 141; 143; 142] would require evidence of ponderomotive laser couplings with a room-temperature vapor.

APPENDIX

APPENDIX A

The Minimal Coupling Hamiltonian

In Chapter II, I give my description of tightly-bound atoms in optical lattices starting from the minimal coupling Hamiltonian on the valence electron. Chapter IV features some discussion on Rydberg atoms in the presence of RF and static electromagnetic fields for which a minimal-coupling Hamiltonian is necessary to model all resulting quantum-mechanical phenomena. Because these sections of this thesis rely so profoundly on this operator, I believe it is necessary to include its origins. Here I will discuss the derivation of minimal coupling Hamiltonian $\hat{H}$ using a free electron as the exemplary particle,

$$\hat{H} = \frac{1}{2m_e}[\hat{\mathbf{p}} + e\mathbf{A}(\hat{\mathbf{r}};t)]^2 - e\phi(\hat{\mathbf{r}}), \tag{A.1}$$

where $\hat{\mathbf{p}}$ is the canonical momentum operator that is conjugate to the electron's canonical position operator $\hat{\mathbf{r}}$ in the laboratory frame. ϕ and $\mathbf{A}$ are the scalar and vector potentials of the electromagnetic field, which can include a linear superposition of DC and AC $\mathbf{E}$- and $\mathbf{B}-$ fields.

A.1 Lagrangian Mechanics for an Electron in an Electromagnetic Field

An electron in an electromagnetic field of potential $A_\mu = (\phi, \mathbf{A})$ undergoes a Lorentz force, classically described by

$$m_e\ddot{\mathbf{r}} = e\nabla\phi(\mathbf{r}) + e\frac{\partial\mathbf{A}(\mathbf{r};t)}{\partial t} - e\dot{\mathbf{r}} \times \nabla \times \mathbf{A}(\mathbf{r};t), \tag{A.2}$$

Eq. A.2 can be rearranged using the time-derivative-operator identity $d/dt = (\dot{\mathbf{r}} \cdot \nabla) + \partial/\partial t$ and the vector identity $\dot{\mathbf{r}} \times \nabla \times \mathbf{A} = \nabla(\dot{\mathbf{r}} \cdot \mathbf{A}) - (\dot{\mathbf{r}} \cdot \nabla)\mathbf{A}$

$$m_e \ddot{\mathbf{r}} = e\nabla\phi(\mathbf{r}) - e\nabla[\dot{\mathbf{r}} \cdot \mathbf{A}(\mathbf{r};t)] + e\frac{d\mathbf{A}(\mathbf{r};t)}{dt} = e\nabla\phi(\mathbf{r}) - e\nabla[\dot{\mathbf{r}} \cdot \mathbf{A}(\mathbf{r};t)] + e\frac{d}{dt}\frac{\partial}{\partial\dot{\mathbf{r}}}(\dot{\mathbf{r}} \cdot \mathbf{A}(\mathbf{r};t))$$

$$= e\nabla\phi(\mathbf{r}) - e\nabla[\dot{\mathbf{r}}\cdot\mathbf{A}(\mathbf{r};t)] + e\frac{d}{dt}\frac{\partial}{\partial\dot{\mathbf{r}}}(\dot{\mathbf{r}}\cdot\mathbf{A}(\mathbf{r};t)) - e\frac{d}{dt}\frac{\partial}{\partial\dot{\mathbf{r}}}\phi(\mathbf{r}) = -\nabla U(\mathbf{r};\dot{\mathbf{r}};t) + \frac{d}{dt}\left[\frac{\partial}{\partial\dot{\mathbf{r}}}U(\mathbf{r};\dot{\mathbf{r}};t)\right],$$
(A.3)

where $-e\frac{d}{dt}\frac{\partial}{\partial\dot{\mathbf{r}}}\phi(\mathbf{r}) = 0$ and $U(\mathbf{r};\dot{\mathbf{r}};t)$ is the velocity-dependent, generalized potential associated with the generalized force (Q_x, Q_y, Q_z), where Q_j for $j = x, y, z$ follows

$$\frac{\partial T}{\partial r_j} - \frac{d}{dt}\left(\frac{\partial T}{\partial \dot{r}_j}\right) + Q_j = 0,$$
(A.4)

where, for the case of the electron, the kinetic energy is $T = \frac{1}{2}m_e\dot{\mathbf{r}} \cdot \dot{\mathbf{r}}$. The system is subject to the Euler-Lagrange equations for a given Lagrangian $L = T - U$,

$$\frac{\partial L}{\partial r_j} - \frac{d}{dt}\left(\frac{\partial L}{\partial \dot{r}_j}\right) = 0,$$
(A.5)

true for all coordinates of $\mathbf{r}$ and $\dot{\mathbf{r}}$. From Eqs. A.4 & A.5, I obtain

$$Q_j = -\frac{\partial U}{\partial r_j} + \frac{d}{dt}\left(\frac{\partial U}{\partial \dot{r}_j}\right).$$
(A.6)

For the Lorentz force,
$$U(\mathbf{r};\dot{\mathbf{r}};t) = -e\phi(\mathbf{r}) + e\dot{\mathbf{r}} \cdot \mathbf{A}(\mathbf{r};t),$$
(A.7)

which results in the following Lagrangian,

$$L = \frac{1}{2}m_e\dot{r}^2 + e\phi(\mathbf{r}) - e\dot{\mathbf{r}} \cdot \mathbf{A}(\mathbf{r};t).$$
(A.8)

When we find the canonical momentum, $\mathbf{p} = \frac{\partial L}{\partial\dot{\mathbf{r}}}$, I arrive at

$$\mathbf{p} = \mathbf{p}_{kinetic} - e\mathbf{A}(\mathbf{r};t),$$
(A.9)

where $\mathbf{p}_{kinetic} = m_e\dot{\mathbf{r}}$ is known as the kinetic momentum of the system. Because the Hamiltonian is a sum of the kinetic energy due to the kinetic momentum and a velocity-independent

potential V, we can write

$$H = \frac{1}{2m_e}[\mathbf{p} + e\mathbf{A}(\mathbf{r};t)]^2 - e\phi(\mathbf{r}). \tag{A.10}$$

In operator form, we have Eq. A.1.

BIBLIOGRAPHY

BIBLIOGRAPHY

[1] G. Raithel, R. Cardman, and A. Duspayev, Rydberg atoms for precision measurement in science and technology, in *Quantum Sensing, Imaging, and Precision Metrology*, volume 12447, pages 184–190, SPIE, 2023.

[2] J. Dalibard and C. Cohen-Tannoudji, J. Opt. Soc. Am. B **6**, 2023 (1989).

[3] R. Cardman, X. Han, J. L. MacLennan, A. Duspayev, and G. Raithel, Phys. Rev. A **104**, 063304 (2021).

[4] S. K. Dutta, J. R. Guest, D. Feldbaum, A. Walz-Flannigan, and G. Raithel, Phys. Rev. Lett. **85**, 5551 (2000).

[5] R. Cardman, J. L. MacLennan, S. E. Anderson, Y.-J. Chen, and G. A. Raithel, New J. Phys. **23**, 063074 (2021).

[6] A. Ramos, *Precision Measurements with Rydberg States of Rubidium*, PhD thesis, 2019.

[7] R. Cardman and G. Raithel, Phys. Rev. Lett. **131**, 023201 (2023).

[8] R. Cardman and G. Raithel, Phys. Rev. A **106**, 052810 (2022).

[9] R. Cardman and G. Raithel, Phys. Rev. A **101**, 013434 (2020).

[10] W. Li, I. Mourachko, M. W. Noel, and T. F. Gallagher, Phys. Rev. A **67**, 052502 (2003).

[11] F. Bloch, Zeitschrift für physik **52**, 555 (1929).

[12] C. Kittel, *Introduction to solid state physics Eighth edition*, 2021.

[13] P. D. Lett et al., Phys. Rev. Lett. **61**, 169 (1988).

[14] C. I. Westbrook et al., Phys. Rev. Lett. **65**, 33 (1990).

[15] P. S. Jessen et al., Phys. Rev. Lett. **69**, 49 (1992).

[16] P. Verkerk et al., Phys. Rev. Lett. **68**, 3861 (1992).

[17] A. Beyer et al., Science **358**, 79 (2017).

[18] H. Fleurbaey et al., Phys. Rev. Lett. **120**, 183001 (2018).

[19] L. Morel, Z. Yao, P. Cladé, and S. Guellati-Khélifa, Nature **588**, 61 (2020).

[20] S. Sturm et al., Nature **506**, 467 (2014).

[21] A. Bauch, Measurement Science and Technology **14**, 1159 (2003).

[22] T. J. Quinn, Metrologia **40**, 103 (2003).

[23] C. L. Holloway et al., AVS Quantum Science **4**, 034401 (2022).

[24] D. B. Newell et al., Metrologia **55**, L13 (2018).

[25] K. W. Martin et al., Phys. Rev. Applied **9**, 014019 (2018).

[26] A. Ramos, K. Moore, and G. Raithel, Phys. Rev. A **96**, 032513 (2017).

[27] R. Pohl et al., Nature **466**, 213 (2010).

[28] K. W. Martin et al., Phys. Rev. A **100**, 023417 (2019).

[29] H. Lyons, Scientific American **196**, 71 (1957).

[30] D. A. Steck, Cesium D line data, available online at https://steck.us/alkalidata/cesiumnumbers.1.6.pdf year=2003.

[31] H. M. Goldenberg, D. Kleppner, and N. F. Ramsey, Phys. Rev. Lett. **5**, 361 (1960).

[32] D. Kleppner, H. M. Goldenberg, and N. F. Ramsey, Phys. Rev. **126**, 603 (1962).

[33] A. Clairon et al., IEEE Transactions on Instrumentation and Measurement **44**, 128 (1995).

[34] A. Derevianko and H. Katori, Rev. Mod. Phys. **83**, 331 (2011).

[35] T. Bothwell et al., Metrologia **56**, 065004 (2019).

[36] B. J. Bloom et al., Nature **506**, 71 (2014).

[37] T. Bothwell et al., Nature **602**, 420 (2022).

[38] V. Maurice et al., Optics Express **28**, 24708 (2020).

[39] Z. L. Newman et al., Optics Letters **46**, 4702 (2021).

[40] S. Eustice et al., arXiv preprint arXiv:2301.13363 (2023).

[41] K. Weng et al., JOSA B **37**, 1637 (2020).

[42] S. Dyer et al., Phys. Rev. Appl. **19**, 044015 (2023).

[43] Y.-J. Chen, S. Zigo, and G. Raithel, Phys. Rev. A **89**, 063409 (2014).

[44] Y.-J. Chen, L. F. Gonçalves, and G. Raithel, Phys. Rev. A **92**, 060501(R) (2015).

[45] R. G. Hulet and D. Kleppner, Phys. Rev. Lett. **51**, 1430 (1983).

[46] S. Haroche, Rev. Mod. Phys. **85**, 1083 (2013).

[47] N. Bezginov et al., Science **365**, 1007 (2019).

[48] A. Grinin et al., Science **370**, 1061 (2020).

[49] E. Tiesinga, P. J. Mohr, D. B. Newell, and B. N. Taylor, Rev. Mod. Phys. **93**, 025010 (2021).

[50] F. Chadha-Day, J. Ellis, and D. J. E. Marsh, Science Advances **8**, eabj3618 (2022).

[51] I. Ogawa, S. Matsuki, and K. Yamamoto, Phys. Rev. D **53**, R1740 (1996).

[52] R. Bradley et al., Rev. Mod. Phys. **75**, 777 (2003).

[53] A. R. Zhitnitskii, Sov. J. Nucl. Phys. **31** (1980).

[54] M. Dine, W. Fischler, and M. Srednicki, Phys. Lett. B **104**, 199 (1981).

[55] J. E. Kim, Phys. Rev. Lett. **43**, 103 (1979).

[56] M. Shifman, A. Vainshtein, and V. Zakharov, Nucl. Phys. B **166**, 493 (1980).

[57] M. S. Turner, Phys. Rep. **197**, 67 (1990).

[58] L. Zhong et al., Phys. Rev. D **97**, 092001 (2018).

[59] C. Boutan et al., Phys. Rev. Lett. **121**, 261302 (2018).

[60] T. F. Gallagher, *Rydberg Atoms*, volume 3, Cambridge University Press, 2005.

[61] A. Signoles et al., Phys. Rev. Lett. **118**, 253603 (2017).

[62] K. R. Moore, S. E. Anderson, and G. Raithel, Nature communications **6**, 6090 (2015).

[63] K. R. Moore and G. Raithel, Phys. Rev. Lett. **115**, 163003 (2015).

[64] K. Moore, A. Duspayev, R. Cardman, and G. Raithel, Physical Review A **102**, 062817 (2020).

[65] H. A. Bethe and E. E. Salpeter, *Quantum mechanics of one-and two-electron atoms*, Springer Science & Business Media, 2012.

[66] P. R. Berman and V. S. Malinovsky, *Principles of Laser Spectroscopy and Quantum Optics*, Princeton University Press, 2010.

[67] T. W. Hänsch, S. A. Lee, R. Wallenstein, and C. Wieman, Phys. Rev. Lett. **34**, 307 (1975).

[68] J. D. Jackson, *Classical Electrodynamics, Third Edition*, John Wiley & Sons, 1999.

[69] J. Dalibard and C. Cohen-Tannoudji, J. Opt. Soc. Am. B **2**, 1707 (1985).

[70] M. L. Zimmerman, M. G. Littman, M. M. Kash, and D. Kleppner, Phys. Rev. A **20**, 2251 (1979).

[71] D. Delande and J. C. Gay, EPL (Europhysics Letters) **5**, 303 (1988).

[72] J. Hare, M. Gross, and P. Goy, Phys. Rev. Lett. **61**, 1938 (1988).

[73] D. A. Anderson, A. Schwarzkopf, R. E. Sapiro, and G. Raithel, Phys. Rev. A. **88**, 031401(R) (2013).

[74] A. A. Morgan, V. Zhelyazkova, and S. D. Hogan, Phys. Rev. A **98**, 043416 (2018).

[75] P. Nussenzveig et al., Phys. Rev. A **48**, 3991 (1993).

[76] R. R. Freeman, T. J. McIlrath, P. H. Bucksbaum, and M. Bashkansky, Phys. Rev. Lett. **57**, 3156 (1986).

[77] P. H. Bucksbaum, R. R. Freeman, M. Bashkansky, and T. J. McIlrath, J. Opt. Soc. Am. B **4**, 760 (1987).

[78] P. H. Bucksbaum, D. W. Schumacher, and M. Bashkansky, Phys. Rev. Lett. **61**, 1182 (1988).

[79] D. L. Freimund, K. Aflatooni, and H. Batelaan, Nature **413**, 142 (2001).

[80] C. J. Foot, *Atomic Physics*, Oxford University Press, 2005.

[81] M. H. Anderson et al., Science **269**, 198 (1995).

[82] K. B. Davis et al., Phys. Rev. Lett. **75**, 3969 (1995).

[83] B. DeMarco and D. S. Jin, Science **285**, 1703 (1999).

[84] A. G. Truscott, K. E. Strecker, W. I. McAlexander, G. B. Partridge, and R. G. Hulet, Science **291**, 2570 (2001).

[85] V. S. Malinovsky, K. R. Moore, and G. Raithel, Phys. Rev. A **101**, 033414 (2020).

[86] T. Topcu and A. Derevianko, Phys. Rev. A **88**, 042510 (2013).

[87] A. Ashkin, J. M. Dziedzic, J. E. Bjorkholm, and S. Chu, Opt. Lett. **11**, 288 (1986).

[88] H. J. Metcalf and P. van der Straten, *Laser Cooling and Trapping*, Springer Science+Business Media, 1999.

[89] S. J. Blundell and K. M. Blundell, *Concepts in Thermal Physics, Second Edition*, Oxford University Press, 2010.

[90] J. P. Gordon and A. Ashkin, Phys. Rev. A **21**, 1606 (1980).

[91] C. Cohen-Tannoudji, Atomic motion in laser light, in *Systèmes Fondamentaux en Optique Quantique, Les Houches, 1990*, edited by J. Dalibard, J. M. Raimond, and J. Zinn-Justin, Session LIII, Amsterdam, Netherlands, 1992, Elsevier.

[92] D. A. Steck, Rubidium 85 D line data, available online at https://steck.us/alkalidata/rubidium85numbers.pdf, 2008.

[93] D. A. Steck, Sodium D line data, available online at https://steck.us/alkalidata/sodiumnumbers.pdf, 2000.

[94] S. Chu, L. Hollberg, J. E. Bjorkholm, A. Cable, and A. Ashkin, Phys. Rev. Lett. **55**, 48 (1985).

[95] A. Ashkin and J. P. Gordon, Opt. Lett. **8**, 511 (1983).

[96] E. L. Raab, M. Prentiss, A. Cable, S. Chu, and D. E. Pritchard, Phys. Rev. Lett. **59**, 2631 (1987).

[97] N. Thaicharoen, A. Schwarzkopf, and G. Raithel, Phys. Rev. A **92**, 040701(R) (2015).

[98] V. Bendkowsky et al., Nature **458**, 1005 (2009).

[99] S. Hollerith et al., Science **364**, 664 (2019).

[100] K. Mølmer, Y. Castin, and J. Dalibard, J. Opt. Soc. Am. B **10**, 524 (1993).

[101] W. D. Phillips, Rev. Mod. Phys. **70**, 721 (1998).

[102] T. L. Nguyen et al., Phys. Rev. X **8**, 011032 (2018).

[103] M. Saffman and T. Walker, Phys. Rev. A **72**, 022347 (2005).

[104] M. S. Safronova, C. J. Williams, and C. W. Clark, Phys. Rev. A **67**, 040303 (2003).

[105] S. Ma et al., Phys. Rev. X **12**, 021028 (2022).

[106] M. A. Viray, E. Paradis, and G. Raithel, New J. Phys. **23**, 063022 (2021).

[107] D. A. Steck, Quantum and atom optics, available online at http://steck.us/teaching, 2022.

[108] A. Neuzner, M. Körber, S. Dürr, G. Rempe, and S. Ritter, Phys. Rev. A **92**, 053842 (2015).

[109] P. Barakhshan et al., *Portal for High-Precision Atomic Data and Computation* (version 2.0). University of Delaware, Newark, DE, USA. URL: https://www.udel.edu/atom [February 2022].

[110] H. Friedrich, *Theoretical atomic physics*, volume 3, Springer, 2006.

[111] T. K. Langin, G. M. Gorman, and T. C. Killian, Science **363**, 61 (2019).

[112] N. Zuber et al., Nature **605**, 453 (2022).

[113] S. Olmschenk et al., Phys. Rev. A **76**, 052314 (2007).

[114] P. S. Barklem, Astron. Astrophys. Rev. **24**, 9 (2016).

[115] L. Zhao, W. Eissner, S. N. Nahar, and A. K. Pradhan, arXiv:1801.02188 (2018).

[116] T. P. Dinneen, C. D. Wallace, K.-Y. N. Tan, and P. L. Gould, Opt. Lett. **17**, 1706 (1992).

[117] B. C. Duncan, V. Sanchez-Villicana, P. L. Gould, and H. R. Sadeghpour, Phys. Rev. A **63**, 043411 (2001).

[118] B. Arora and B. Sahoo, Physical Review A **86**, 033416 (2012).

[119] Y.-J. Chen, *Atom trapping and spectroscopy in cavity-generated optical potentials*, PhD thesis, 2015.

[120] J. MacLennan, *Rydberg Molecules and Excitation of Lattice-Mixed Rydberg States in a Deep Ponderomotive Optical Lattice*, PhD thesis, 2021.

[121] E. D. Black, Am. J. Phys. **69**, 79 (2001).

[122] L. Barbier, A. Pesnelle, and M. Cheret, Journal of Physics B: Atomic and Molecular Physics (1968-1987) **20**, 1249 (1987).

[123] L. Barbier and M. Cheret, Journal of Physics B: Atomic and Molecular Physics (1968-1987) **20**, 1229 (1987).

[124] M. A. Mahmoud, Central European Journal of Physics **6**, 530 (2008).

[125] J. C. Tully and R. K. Preston, The Journal of Chemical Physics **55**, 562 (1971).

[126] J. C. Tully, The Journal of Chemical Physics **93**, 1061 (1990).

[127] J. E. Sansonetti, Journal of physical and chemical reference data **35**, 301 (2006).

[128] M. S. Safronova, C. J. Williams, and C. W. Clark, Phys. Rev. A **69**, 022509 (2004).

[129] M. S. Safronova and U. I. Safronova, Phys. Rev. A **83**, 052508 (2011).

[130] A. Reinhard, T. C. Liebisch, B. Knuffman, and G. Raithel, Phys. Rev. A **75**, 032712 (2007).

[131] M. Marinescu, H. R. Sadeghpour, and A. Dalgarno, Phys. Rev. A **49**, 982 (1994).

[132] M. Saffman, T. G. Walker, and K. Mølmer, Rev. Mod. Phys. **82**, 2313 (2010).

[133] S. R. Cohen and J. D. Thompson, PRX Quantum **2**, 030322 (2021).

[134] H. Bernien et al., Nature **551**, 579 (2017).

[135] A. Browaeys and T. Lahaye, Nature Physics **16**, 132 (2020).

[136] P. Scholl et al., Nature **595**, 233 (2021).

[137] A. Ramos, R. Cardman, and G. Raithel, Phys. Rev. A **100**, 062515 (2019).

[138] S. J. Berl, C. A. Sackett, T. F. Gallagher, and J. Nunkaew, Physical Review A **102**, 062818 (2020).

[139] F. Ripka, H. Kübler, R. Löw, and T. Pfau, Science **362**, 446 (2018).

[140] C. L. Holloway et al., IEEE Transactions on Antennas and Propagation **62**, 6169 (2014).

[141] D. A. Anderson, R. E. Sapiro, and G. Raithel, IEEE Aerospace and Electronic Systems Magazine **35**, 48 (2020).

[142] D. H. Meyer, P. D. Kunz, and K. C. Cox, Phys. Rev. Appl. **15**, 014053 (2021).

[143] D. Anderson, R. Sapiro, L. Gonçalves, R. Cardman, and G. Raithel, Phys. Rev. Appl. **17**, 044020 (2022).

[144] J. Lee, J. Nunkaew, and T. F. Gallagher, Phys. Rev. A **94**, 022505 (2016).

[145] J. Han, Y. Jamil, D. V. L. Norum, P. J. Tanner, and T. F. Gallagher, Phys. Rev. A **74**, 054502 (2006).

[146] D. Kleppner, Phys. Rev. Lett. **47**, 233 (1981).

[147] X. Han et al., Phys. Rev. A **97**, 031403(R) (2018).

[148] K. R. Overstreet, A. Schwettmann, J. Tallant, D. Booth, and J. P. Shaffer, Nature Physics **5**, 581 (2009).

[149] A. Schwarzkopf, R. E. Sapiro, and G. Raithel, Physical Review Letters **107**, 103001 (2011).

[150] R. Damburg and V. Kolosov, Journal of Physics B: Atomic and Molecular Physics **12**, 2637 (1979).

[151] I. V. Komarov, T. P. Grozdanov, and R. K. Janev, Journal of Physics B: Atomic and Molecular Physics **13**, L573 (1980).

[152] E. K. Dietsche et al., Nature Physics **15**, 326 (2019).

[153] A. Larrouy et al., Phys. Rev. X **10**, 021058 (2020).

[154] S. E. Anderson and G. Raithel, Nature communications **4**, 1 (2013).

[155] G. Leuchs, S. J. Smith, S. N. Dixit, and P. Lambropoulos, Phys. Rev. Lett. **56**, 708 (1986).

[156] U. Fano, Phys. Rev. A **32**, 617 (1985).

[157] S. E. Anderson, *Trapping Rydberg Atoms in Ponderomotive Optical Lattices.*, PhD thesis, 2014.

[158] A. Giusti-Suzor and P. Zoller, Physical Review A **36**, 5178 (1987).

[159] K. C. Younge, S. E. Anderson, and G. Raithel, New J. Phys. **12**, 023031 (2010).

[160] M. L. Zimmerman, J. C. Castro, and D. Kleppner, Phys. Rev. Lett. **40**, 1083 (1978).

[161] J. C. Gay and D. Delande, Comments At. Mol. Phys. **13**, 275 (1983).

[162] P. Cacciani, E. Luc-Koenig, J. Pinard, C. Thomas, and S. Liberman, Phys. Rev. Lett. **56**, 1124 (1986).

[163] T. Van der Veldt, W. Vassen, and W. Hogervorst, J. Phys. B: At. Mol. Opt. Phys. **26**, 1945 (1993).

[164] A. D. Cronin, J. Schmiedmayer, and D. E. Pritchard, Rev. of Mod. Phys. **81**, 1051 (2009).

[165] M. Abe et al., Quantum Science and Technology **6**, 044003 (2021).

[166] J. Bateman, S. Nimmrichter, K. Hornberger, and H. Ulbricht, Nature communications **5**, 4788 (2014).

[167] K. Dieckmann, R. J. C. Spreeuw, M. Weidemüller, and J. T. M. Walraven, Phys. Rev. A **58**, 3891 (1998).

[168] J. J. Sakurai, *Advanced Quantum Mechanics*, Addison-Wesley, 1967.

[169] E. Hansis, T. Cubel, J.-H. Choi, J. R. Guest, and G. Raithel, Review of scientific instruments **76**, 033105 (2005).

[170] S. E. Anderson, K. C. Younge, and G. Raithel, Phys. Rev. Lett. **107**, 263001 (2011).

[171] B. P. Stoicheff and E. Weinberger, Canadian Journal of Physics **57**, 2143 (1979).

[172] D. Meschede, JOSA B **4**, 413 (1987).

[173] A. Tauschinsky, R. Newell, H. B. van Linden van den Heuvell, and R. J. C. Spreeuw, Phys. Rev. A **87**, 042522 (2013).

[174] G. Belin and S. Svanberg, Physics Letters A **47**, 5 (1974).

[175] G. Belin, L. Holmgren, and S. Svanberg, Physica Scripta **13**, 351 (1976).

[176] G. Belin, L. Holmgren, and S. Svanberg, Physica Scripta **14**, 39 (1976).

[177] J. Farley, P. Tsekeris, and R. Gupta, Phys. Rev. A **15**, 1530 (1977).

[178] A. Duspayev et al., Phys. Rev. Research **3**, 023114 (2021).

[179] M. Deiß, S. Haze, and J. Hecker Denschlag, Atoms **9**, 34 (2021).

[180] T. Niederprüm et al., Nature communications **7**, 12820 (2016).

[181] T. Niederprüm, O. Thomas, T. Eichert, and H. Ott, Phys. Rev. Lett. **117**, 123002 (2016).

[182] C. Boisseau, I. Simbotin, and R. Côté, Phys. Rev. Lett. **88**, 133004 (2002).

[183] S. Hollerith et al., Phys. Rev. Res. **3**, 013252 (2021).

[184] W. Li, P. J. Tanner, and T. F. Gallagher, Phys. Rev. Lett. **94**, 173001 (2005).

[185] S. Ravets et al., Nature Physics **10**, 914 (2014).

[186] F. Ripka, C. Lui, M. Schmidt, H. Kubler, and J. P. Shaffer, Rydberg atom-based radio frequency electrometry: hyperfine effects, in *Optical and Quantum Sensing and Precision Metrology II*, volume 12016, pages 102–107, SPIE, 2022.

[187] M. Allegrini, E. Arimondo, and L. A. Orozco, Journal of Physical and Chemical Reference Data **51**, 043102 (2022).

[188] M. Saffman, T. G. Walker, and K. Mølmer, Rev. Mod. Phys. **82**, 2313 (2010).

[189] M. Khazali, Quantum **6**, 664 (2022).

[190] R. M. Jopson, R. R. Freeman, W. E. Cooke, and J. Bokor, Phys. Rev. Lett. **51**, 1640 (1983).

[191] R. R. Jones and T. F. Gallagher, Physical Review A **38**, 2846 (1988).

[192] R. R. Jones, C. J. Dai, and T. F. Gallagher, Physical Review A **41**, 316 (1990).

[193] H. Lehec, X. Hua, P. Pillet, and P. Cheinet, Phys. Rev. A **103**, 022806 (2021).

[194] K.-L. Pham, T. F. Gallagher, P. Pillet, S. Lepoutre, and P. Cheinet, PRX Quantum **3**, 020327 (2022).

[195] A. Muni et al., Nature Physics **18**, 502 (2022).

[196] A. P. Burgers et al., PRX Quantum **3**, 020326 (2022).

[197] J. T. Wilson et al., Phys. Rev. Lett. **128**, 033201 (2022).

[198] A. Yariv and P. Yeh, *Optical waves in crystals*, volume 5, Wiley New York, 1984.

[199] K. C. Younge, B. Knuffman, S. E. Anderson, and G. Raithel, Phys. Rev. Lett. **104**, 173001 (2010).

[200] S. Patsch et al., Phys. Rev. A **97**, 053418 (2018).

[201] A. E. Siegman, *Lasers*, University Science Books, 1986.

[202] L. Allen, M. W. Beijersbergen, R. J. C. Spreeuw, and J. P. Woerdman, Phys. Rev. A **45**, 8185 (1992).

[203] J. D. Rodrigues, L. G. Marcassa, and J. T. Mendonça, J. Phys. B: At. Mol. Opt. Phys. **49**, 074007 (2018).

[204] K. Mukherjee, S. Majumder, P. K. Mondal, and B. Deb, J. Phys. B: At. Mol. Opt. Phys. **51**, 015004 (2018).

[205] M. Mirhosseini et al., Opt. Express **21**, 30204 (2013).

[206] S. Rosi et al., Scientific reports **8**, 1301 (2018).

[207] J. R. Rubbmark, M. M. Kash, M. G. Littman, and D. Kleppner, Phys. Rev. A **23**, 3107 (1981).

[208] C. Zener, Proc. R. Soc. London Ser. A **137**, 696 (1932).

[209] V. S. Malinovsky and J. L. Krause, The European Physical Journal D-Atomic, Molecular, Optical and Plasma Physics **14**, 147 (2001).

[210] W. Petrich, M. H. Anderson, J. R. Ensher, and E. A. Cornell, Phys. Rev. Lett. **74**, 3352 (1995).

[211] J. Hare et al., IEEE Transactions on Instrumentation and Measurement **42**, 331 (1993).

[212] S. K. Kanungo et al., Nature Communications **13**, 972 (2022).

[213] W. P. Su, J. R. Schrieffer, and A. J. Heeger, Phys. Rev. Lett. **42**, 1698 (1979).

[214] M. M. Aliyu, A. Ulugöl, G. Abumwis, and S. Wüster, Phys. Rev. A **98**, 043602 (2018).

[215] A. J. Kerman, V. Vuletić, C. Chin, and S. Chu, Phys. Rev. Lett. **84**, 439 (2000).

[216] M. Weidemüller, T. Esslinger, M. A. Ol'shanii, A. Hemmerich, and T. W. Hänsch, Europhysics Letters **27**, 109 (1994).

[217] D. W. Schumacher, J. H. Hoogenraad, D. Pinkos, and P. H. Bucksbaum, Physical Review A **52**, 4719 (1995).

[218] E. A. Shapiro and P. Bellomo, Phys. Rev. A **60**, 1403 (1999).

[219] D. Booth, S. T. Rittenhouse, J. Yang, H. R. Sadeghpour, and J. P. Shaffer, Science **348**, 99 (2015).